

Aerodynamics of wind-assisted ships

Interaction effects on the aerodynamic performance of multiple wind-propulsion systems

Bordogna, Giovanni

DOI

[10.4233/uuid:96eda9cd-3163-4c6b-9b9f-e9fa329df071](https://doi.org/10.4233/uuid:96eda9cd-3163-4c6b-9b9f-e9fa329df071)

Publication date

2020

Document Version

Final published version

Citation (APA)

Bordogna, G. (2020). *Aerodynamics of wind-assisted ships: Interaction effects on the aerodynamic performance of multiple wind-propulsion systems*. [Dissertation (TU Delft), Delft University of Technology]. <https://doi.org/10.4233/uuid:96eda9cd-3163-4c6b-9b9f-e9fa329df071>

Important note

To cite this publication, please use the final published version (if applicable).
Please check the document version above.

Copyright

Other than for strictly personal use, it is not permitted to download, forward or distribute the text or part of it, without the consent of the author(s) and/or copyright holder(s), unless the work is under an open content license such as Creative Commons.

Takedown policy

Please contact us and provide details if you believe this document breaches copyrights.
We will remove access to the work immediately and investigate your claim.

AERODYNAMICS OF WIND-ASSISTED SHIPS

**INTERACTION EFFECTS ON THE AERODYNAMIC PERFORMANCE
OF MULTIPLE WIND-PROPULSION SYSTEMS**

Dissertation

for the purpose of obtaining the degree of doctor
at Delft University of Technology
by the authority of the Rector Magnificus prof. dr. ir. T. H. J. J. van der Hagen
chair of the Board of Doctorates
to be defended publicly on
Monday 27 January 2020 at 10:00 o'clock

by

Giovanni BORDOGNA

Master of Science in Marine Technology
Delft University of Technology, The Netherlands
born in Como, Italy

This dissertation has been approved by the promotors.

Composition of the doctoral committee:

Rector Magnificus,	chairperson
Prof. dr. ir. R.H.M. Huijsmans,	Delft University of Technology, promotor
Dr. ir. I. Akkerman,	Delft University of Technology, copromotor

Independent members:

Prof. dr. ir. L.L.M. Veldhuis,	Delft University of Technology
Prof. ir. J.J. Hopman,	Delft University of Technology
Prof. dr. ir. H.W.M. Hoeijmakers,	University of Twente
Prof. dr. M. Belloli,	Polytechnic University of Milan, Italy
Dr. ir. J.A. Keuning,	Delft University of Technology
Prof. dr. ir. M.L. Kaminski,	Delft University of Technology, reserve member

This research was funded by De Bijlboeg Fonds and De Samenwerkende Maritieme Fondsen and supported by Damen Shipyards, Dykstra Naval Architects and Maritime Research Institute Netherlands.

Keywords: Wind-assisted ship propulsion, Aerodynamic interaction, Dynarig, Wingsail, Flettner rotor

Cover by: Ilse Modder, www.ilsemodder.nl

Printed by: Gildeprint Enschede, www.gildeprint.nl

Copyright © 2020 by G. Bordogna

ISBN 978-94-6323-977-6

An electronic version of this dissertation is available at:

<http://repository.tudelft.nl/>.

To my parents



SUMMARY

The shipping industry is currently under pressure to reduce its pollutant emissions and, thus, to alleviate its negative impact on the environment and human health. With this aim, in the last years, the International Maritime Organization issued significant measures to improve the energy efficiency of ships (see the Energy Efficiency Design Index) as well as restrictive regulations to limit the amount of contaminating emissions from seaborne transport. Arguably one of the most impactful measures will be enforced at the commence of 2020 when the world fleet will have to use cleaner fuels or otherwise will need to install expensive exhaust gas cleaning systems (known as scrubbers) to comply with the new regulations. The use of cleaner and more expensive fuels will increase the ship operating costs and this, in turn, will make investments into fuel-saving devices more attractive.

In this evolving situation, the use of wind energy as an auxiliary form of propulsion for commercial ships has again become of interest as it has the potential to deliver significant fuel savings. However, one of the bottlenecks for the further uptake of wind-assisted propulsion is the uncertainty related to the performance prediction of these hybrid ships. In fact, the amount of fuel savings deliverable by a wind-assist technology has a direct impact on its economic and environmental attractiveness. An accurate performance estimate is, therefore, a necessary condition before any sound evaluation of wind-assisted propulsion can be made.

At the Delft University of Technology, the Sail Assist project was started with the aim to investigate the physics of wind-assisted propulsion. The project was divided into two parts with focus, respectively, on the aerodynamics and hydrodynamic aspects of wind-assisted vessels. The final objective of the project was to combine the two components into a computer tool (named Performance Prediction Program) capable of predicting the performance of a given wind-assisted ship in a quick yet reliable manner. In this framework, this dissertation deals with the aerodynamics of wind-assisted propulsion with the goal to contribute to the realization of the aerodynamic component of the Performance Prediction Program.

From an aerodynamic perspective, previous research indicates that the most necessary improvement to the performance estimate of wind-assisted vessels is to account for the aerodynamic interaction effects occurring between the multiple wind-propulsion systems installed on the ship. These effects, although proven to have a significant influence on the overall performance of the ship, are typically neglected or oversimplified.

Based on these observations and considering the goal of the Sail Assist project (developing a quick yet accurate performance prediction tool), the following main research question can be formulated:

After understanding the physical phenomena associated with the aerodynamic interaction of different wind-assist devices, does a simple and computationally inexpensive

method exist that is able to accurately predict the interaction effects on the aerodynamic performance of a generic arrangement of wind-propulsion systems?

To provide an answer to this research question, in this dissertation the effects of the aerodynamic interaction on the performance of different wind-propulsion systems are investigated. In particular, the core of this doctoral work comprises a series of experimental studies on two wind-assist devices, namely the Dynarig and the Flettner rotor. In regards to the Flettner rotor, special attention was given to its performance with respect to scale effects. The influence of the Reynolds number on the aerodynamic coefficients of rotating cylinders, in fact, was still a matter of debate. Finally, the experimental data were used to validate the capabilities of a simple mathematical model to predict the effects of the aerodynamic interaction between two generic wind-propulsion systems.

The experimental work comprised three different series of wind-tunnel tests. The first experiments were carried out on a single Dynarig and on a two-sail arrangement in which force and pressure measurements were taken on each sail. The effects of the aerodynamic interaction were investigated by varying the distance between the sails while considering apparent wind angles ranging all typical sailing conditions. The results of the study showed that for a considerable range of moderate apparent wind angles the aerodynamic interaction has a positive effect on both sails. On the contrary, at smaller and at larger angles the interaction effects are detrimental for the downstream sail.

The second series of tests aimed at investigating the influence of the Reynolds number on the aerodynamic performance of rotating cylinders. In fact, to achieve a reliable performance prediction of multiple Flettner rotors, that is part of the final goal of the Sail Assist project, it is first necessary to have a thorough understanding of the aerodynamic characteristics of a single Flettner rotor device. The wind-tunnel experiments were conducted on a large-scale Flettner rotor in which the forces and pressures acting on the cylinder were measured for Reynolds numbers as large as $Re = 1.0 \cdot 10^6$. The results indicated that the lift coefficient is affected by the Reynolds number only in the critical flow region and below a certain value of velocity ratio, that is the ratio between the tangential speed of the rotating cylinder and the freestream velocity. On the other hand, the drag coefficient appeared to be influenced by the Reynolds number over the entire range of flow conditions analyzed.

The last experimental effort dealt with the effects of the aerodynamic interaction on the performance of two Flettner rotors. Similarly to the Dynarig, also in this case the interaction effects were investigated for different distances between the Flettner rotors as well as for apparent wind angles ranging all typical sailing conditions. The study suggested that the aerodynamic performance of the two Flettner rotors is affected by their interaction, and, generally, this is most noticeable when the devices are set closer to each other and when they are aligned with the wind direction. The velocity ratio appeared to play a fundamental role: it is the key parameter that determines how the aerodynamic interaction affects the performance of multiple Flettner rotors.

The data gathered during the experimental campaigns were used for the validation of a mathematical found in the literature and previously applied to predict the aerodynamic performance of two sailing yachts competing in a match race. The mathematical model, that is based on the horseshoe vortex theory, had features compatible with the

requirements of the Sail Assist Performance Prediction Program as it could assure quick and inexpensive calculations. The results of the validation indicated that, in its current form, the considered mathematical model is not able to properly predict the interaction effects occurring between two Dynarigs or two Flettner rotors. In the former case, this is due to the simplifying assumptions proper of the mathematical model analyzed. In the latter case, on the other hand, it was proven that a more refined version of the aerodynamic interaction model would be suited to predict the performance of two interacting Flettner rotor devices.

In conclusion, the experimental studies carried out in this doctoral work were a first step towards a more thorough understanding of the physical phenomena associated with the aerodynamic interaction between multiple wind-propulsion systems. The considered mathematical model proved to be currently unfit to be used in the aerodynamic module of the Performance Prediction Program, although it was demonstrated that, in the case of Flettner rotors, a more refined interaction model would be able to deliver a satisfactory degree of accuracy. Given these conditions, to (partially) fulfil the goal of the Sail Assist project, the force coefficients derived from the experimental studies were directly used in the aerodynamic module of the Performance Prediction Program. This allowed investigating vessels with wind-propulsion installations comparable to those tested in the wind-tunnel experiments. The Performance Prediction Program, that comprises the results of this dissertation and those of an analogous doctoral thesis on the hydrodynamics of wind-assisted ships, was successfully employed to carry out studies on various wind-assisted ship designs. A significant example is a study conducted in collaboration with Damen Shipyards and Norsepower Oy Ltd, in which the benefits of using one or two Flettner rotors on a general cargo ship were analyzed. The results of the investigation indicated that after deducting the penalties of an increased hydrodynamic resistance and non-optimal engine operating point due to the sailing condition of the ship, considerable fuel savings can still be attained.

This type of analysis, accomplished with the use of the Performance Prediction Program, can support shipowners in comparing and evaluating different wind-assist technologies and guide them in making an informed investment in wind-assisted propulsion.



SAMENVATTING

De scheepvaartsector staat momenteel onder grote druk om de uitstoot van verontreinigende stoffen en de daarmee gerelateerde negatieve impact op het milieu en de menselijke gezondheid te verkleinen. Met dit als doel heeft de Internationale Maritieme Organisatie in de afgelopen jaren belangrijke maatregelen genomen om de energie-efficiëntie van schepen te verbeteren (te zien in bijvoorbeeld de Energy-Efficiency-Design-Index), en beperkende voorschriften opgesteld om de hoeveelheid vervuulende emissies door zeetransport te beperken. Een van de meest bepalende maatregelen zal worden ingevoerd aan het begin van 2020. Vanaf dit moment is de wereldvloot verplicht schonere brandstoffen te gaan gebruiken of te kiezen voor de installatie van dure uitlaatgasreinigingssystemen (zogenoeten scrubbers) om aan de nieuwe voorschriften te voldoen. Het gebruik van schonere en duurere brandstoffen zal de operationele kosten van het schip verhogen en dit zal op zijn beurt investeringen in brandstof besparende apparaten aantrekkelijker maken.

Met deze aanstaande ontwikkelingen is het gebruik van windenergie, als een ondersteunende vorm van voortstuwing voor de scheepvaart, opnieuw interessant geworden. Windenergie heeft grote potentie tot het besparen van brandstof. Echter een van de knelpunten voor de verdere invoering van ondersteunende voortstuwing door wind is de onzekerheid met betrekking tot de prestatievoorspelling van deze hybride schepen. De hoeveelheid brandstofbesparing die door deze technologie kan worden geleverd, heeft een directe invloed op de economische en ecologische aantrekkelijkheid ervan. Een nauwkeurige schatting van de prestaties is daarom noodzakelijk voordat een degelijke evaluatie van ondersteunende voortstuwing door wind kan worden gemaakt.

Aan de Technische Universiteit Delft is het Sail Assist-project gestart met als doel het onderzoeken van de fysica gerelateerd aan ondersteunende voortstuwing door wind. Het project was opgedeeld in twee delen met aandacht voor de aerodynamische en hydrodynamische aspecten van gedeeltelijk door wind voortgestuwde schepen, respectievelijk. Het uiteindelijke doel van het project was om de twee componenten te combineren tot een computerprogramma (Performance Prediction Program genaamd) dat in staat is om de prestaties van een willekeurig door wind ondersteund schip op een snelle maar betrouwbare manier te voorspellen. In dit kader behandelt dit proefschrift de aerodynamica van ondersteunende voortstuwing door wind met als doel het bijdragen aan de realisatie van de aerodynamische component van het Performance Prediction Program.

Vanuit aerodynamisch perspectief geeft eerder onderzoek aan dat de meest noodzakelijke verbetering in de schatting van de prestaties van door wind ondersteunde schepen ligt in het meenemen van de aerodynamische interactie-effecten die optreden tussen de meerdere windvoortstuwingssystemen die op het schip zijn geïnstalleerd. Hoewel deze effecten een significante invloed hebben op de algehele prestaties van het schip, worden ze meestal verwaarloosd of anders sterk vereenvoudigd.

Op basis van deze observaties en rekening houdend met het doel van het Sail Assist-project (het ontwikkelen van een snelle maar nauwkeurige tool voor het voorspellen van prestaties), kan de volgende hoofdonderzoeksvraag worden geformuleerd:

Na het beter begrijpen van de fysische fenomenen samenhangend met de aerodynamische interactie tussen verschillende wind voorstuwers, bestaat er een eenvoudige en reken technisch goedkope methode welke in staat is om de effecten van interactie tussen verschillende wind voorstuwers op de aerodynamische prestaties van een generieke opstelling van windaandrijfsystemen nauwkeurig te voorspellen??

Om een antwoord te kunnen geven op deze onderzoeksvraag, worden in dit proefschrift de effecten van de aerodynamische interactie op de prestaties van verschillende windvoortstuwingssystemen onderzocht. In het bijzonder omvat de kern van dit doctoraatswerk een reeks experimentele onderzoeken naar twee windvoortstuwingssystemen, namelijk de Dynarig en de Flettner-rotor. Wat de Flettner-rotor betreft, is speciale aandacht besteed aan de prestaties met betrekking tot schaafeffecten. De invloed van het Reynolds-getal op de aerodynamische coëfficiënten van roterende cilinders was in feite nog steeds een kwestie van discussie. Ten slotte werden de experimentele gegevens gebruikt om de mogelijkheden van een eenvoudig wiskundig model te valideren zodanig de effecten van de aerodynamische interactie tussen twee generieke windvoortstuwingssystemen te voorspellen.

Het experimentele werk omvatte drie verschillende series windtunneltests. De eerste experimenten werden uitgevoerd op een enkele Dynarig en op een opstelling met twee zeilen waarin kracht- en drukmetingen werden uitgevoerd op elk zeil. De effecten van de aerodynamische interactie werden onderzocht door de afstand tussen de zeilen te variëren terwijl rekening werd gehouden met schijnbare windhoeken variërend tussen alle typische zeilomstandigheden. De resultaten van het onderzoek toonden aan dat voor een aanzienlijk bereik van gematigde schijnbare windhoeken de aerodynamische interactie een positief effect heeft op beide zeilen. Integendeel, bij kleinere en grotere hoeken zijn de interactie-effecten schadelijk voor het zeil stroomafwaarts.

De tweede serie testen was gericht op het onderzoeken van de invloed van het Reynolds-getal op de aerodynamische prestaties van roterende cilinders. Voor een betrouwbare prestatievoorspelling van meerdere Flettner-rotors, wat deel uitmaakt van het uiteindelijke doel van het Sail Assist-project, is het eerst noodzakelijk om een grondig begrip te hebben van de aerodynamische eigenschappen van een enkele Flettner-rotor. De windtunnelexperimenten werden uitgevoerd op een grootschalige Flettner-rotor waarin de krachten en drukken die op de cilinder werkten werden gemeten voor Reynolds-getallen zo groot als $Re = 1.0 \cdot 10^6$. De resultaten gaven aan dat de liftcoëfficiënt alleen wordt beïnvloed door het Reynolds-getal in het kritische stroomgebied en onder een bepaalde waarde van snelheidsverhouding, dat wil zeggen de verhouding tussen de tangentiële snelheid van de roterende cilinder en de ongestoorde stroomsnelheid. Anderzijds leek de weerstandcoëfficiënt te worden beïnvloed door het Reynolds-getal over het gehele bereik van de geanalyseerde stroomomstandigheden.

De laatste experimentele inspanning had betrekking op de effecten van de aerodynamische interactie op de prestaties van twee Flettner-rotors. Net als de Dynarig werden

ook in dit geval de interactie-effecten onderzocht voor verschillende afstanden tussen de Flettner-rotors en voor schijnbare windhoeken, variërend tussen alle typische zeilomstandigheden. De studie suggereerde dat de aerodynamische prestaties van de twee Flettner-rotors worden beïnvloed door hun interactie, en in het algemeen is dit het meest merkbaar wanneer de rotoren dichter bij elkaar worden geplaatst en wanneer ze zijn uitgelijnd met de windrichting. De snelheidsverhouding leek een fundamentele rol te spelen: het is de belangrijkste parameter die bepaalt hoe de aerodynamische interactie de prestaties van meerdere Flettner-rotors beïnvloedt.

De data verzameld tijdens de experimentele campagnes, werd gebruikt voor de validatie van een wiskundig model gevonden in de literatuur en eerder toegepast om de aerodynamische prestaties van twee zeiljachten die aan een matchrace deelnemen te voorspellen. Het wiskundige model, dat is gebaseerd op de hoefijzer vortextheorie, had functies die compatibel zijn met de vereisten van het Sail Assist Performance Prediction Program, omdat het snelle en goedkope berekeningen kon garanderen. De resultaten van de validatie gaven aan dat het wiskundige model in zijn huidige vorm niet in staat is om de interactie-effecten tussen twee Dynarigs of twee Flettner-rotors goed te voorspellen. In het eerste geval is dit te wijten aan de vereenvoudigende veronderstellingen van het geanalyseerde wiskundige model. In het laatste geval echter, werd bewezen dat een meer verfijnde versie van het aerodynamische interactiemodel geschikt zou zijn om de prestaties van twee interacterende Flettner-rotoren te voorspellen.

Concluderend, de experimentele studies die werden uitgevoerd in dit doctoraatswerk waren een eerste stap in de richting van een grondiger begrip van de fysische fenomenen die samenhangen met de aerodynamische interactie tussen meerdere windvoortstuwingssystemen. Het beschouwde wiskundige model bleek momenteel ongeschikt om te worden gebruikt in de aerodynamische module van het Performance Prediction Program, hoewel werd aangetoond dat, in het geval van Flettner-rotors, een verfijnder interactiemodel een bevredigende mate van nauwkeurigheid zou kunnen leveren. Gezien deze omstandigheden, om (gedeeltelijk) het doel van het Sail Assist-project te bereiken, werden de krachtcoëfficiënten afgeleid uit de experimentele studies direct gebruikt in de aerodynamische module van het Performance Prediction Program. Dit maakte het mogelijk om schepen met wind-voortstuwingssystemen te onderzoeken vergelijkbaar met die getest in de windtunnel-experimenten. Het Performance Prediction Program, dat de resultaten van dit proefschrift en die van een vergelijkbaar proefschrift over de hydrodynamica van door wind ondersteunde schepen omvat, werd met succes gebruikt om studies uit te voeren naar verschillende door wind ondersteunde scheepsontwerpen. Een belangrijk voorbeeld is een studie uitgevoerd in samenwerking met Damen Shipyards en Norsepower Oy Ltd, waarin de voordelen van het gebruik van een of twee Flettner-rotors op een vrachtschip zijn geanalyseerd. De resultaten van het onderzoek gaven aan dat na aftrek van de nadelige effecten van een verhoogde hydrodynamische weerstand en niet-optimaal motorbedrijfspunt als gevolg van de zeilconditie van het schip, nog steeds aanzienlijke brandstofbesparingen kunnen worden bereikt.

Dit type analyse, uitgevoerd met behulp van het Performance Prediction Program, kan scheepseigenaren helpen bij het vergelijken en evalueren van verschillende technologieën aangaande windondersteuning en hen helpen bij het maken van een geïnformeerde investering in door wind ondersteunde voortstuwing.



CONTENTS

Summary	v
Samenvatting	ix
1 Introduction	1
1.1 Background of wind-assisted propulsion	1
1.2 Renewed interest in wind assist	4
1.3 The Performance Prediction Program	5
1.4 Research outline	6
2 Aerodynamics of wind-assisted ships	9
2.1 State-of-the-art	10
2.2 Research focus	13
2.3 Research questions	15
3 Aerodynamic interaction between two rigid sails	17
3.1 Introduction	18
3.2 Sail design and experimental method	21
3.3 Test setup	24
3.4 Results	26
3.4.1 Reynolds number effect on single sail performance	26
3.4.2 Measurements of the velocity field past the Dynarig	27
3.4.3 Interaction: force measurements	29
3.4.4 Interaction: pressure measurements	34
3.4.5 Interaction effects: ship performance	38
3.5 Conclusions	40
4 Reynolds number effect on Flettner rotor aerodynamic performance	41
4.1 Introduction	42
4.2 Experimental setup	45
4.2.1 The Delft Rotor	45
4.2.2 Flow characteristics	47
4.3 Results	48
4.3.1 Lift coefficient	49
4.3.2 Drag coefficient	51
4.3.3 Pressure coefficient	53
4.3.4 Power consumption	56
4.4 Conclusions	57

5	Aerodynamic interaction between two Flettner rotors	59
5.1	Introduction	60
5.2	Experimental setup	62
5.2.1	Wind tunnel and flow characteristics	62
5.2.2	The Flettner rotor	63
5.2.3	Single Flettner rotor setup	64
5.2.4	Double Flettner rotor setup	64
5.3	Results	65
5.3.1	Single Flettner rotor	65
5.3.2	Interaction: lift and drag coefficients	68
5.3.3	Interaction: driving and heeling force coefficients	73
5.3.4	Reynolds number effect on aerodynamic interaction	77
5.4	Conclusions	80
6	Validation of an aerodynamic interaction model	83
6.1	Introduction	84
6.2	Mathematical model	85
6.3	Results of the aerodynamic model	88
6.3.1	Comparison with Dynarig experiments	88
6.3.2	Comparison with Flettner rotor experiments	91
6.4	Forces from velocity field measurements	97
6.4.1	Dynarig case	97
6.4.2	Flettner rotor case	102
6.5	Conclusions	107
7	Conclusions and recommendations	109
7.1	Conclusions	109
7.2	Recommendations for future work	111
A	Dynarig experiments	113
A.1	Measurements of the velocity field	114
A.2	Measurement uncertainty	116
B	Delft Rotor experiments	119
B.1	Further information on the experimental setup	120
B.2	Pressure measurement correction	121
B.3	Measurement uncertainty	123
C	Double Flettner rotor experiments	127
C.1	Measurements of the velocity field	128
C.2	Driving and heeling force coefficients	132
C.3	Measurement uncertainty	137
D	Aerodynamic model	141
D.1	Horseshoe vortex method	141
D.2	Flettner rotor coefficients from velocity field	143

Bibliography	159
Acknowledgements	167
Curriculum Vitæ	169
List of Publications	171



1

INTRODUCTION

1.1. BACKGROUND OF WIND-ASSISTED PROPULSION

The possibility to use wind energy as an auxiliary form of propulsion for commercial ships arose to the surface during the oil crisis of the 1970s. In October 1973, after the end of the Arab-Israeli War, the Organization of Arab Petroleum Exporting Countries proclaimed an oil embargo against the states suspected to support Israel in the conflict. The consequence of this decision was that, in a matter of months, the price of oil increased fourfold, causing a shock to the worldwide economy. The shipping industry was strongly hit and it had to seek solutions to reduce the fuel expenses of its fleet. In this political and economical frame, the academia and the maritime sector alike turned their attention towards wind energy.

Until the end of the nineteenth century, seaborne trade was still mainly operated by large sailing ships like the clippers and the windjammers (Figure 1.1). These ships, that typically measured more than 100 meters in length and sailed at a speed as high as 15 knots, were employed on routes from Europe to Asia and Oceania as well as on transatlantic routes. In 1869, however, the opening of the Suez canal permanently changed the maritime trading routes followed so far: a ship sailing from Europe eastbound could avoid travelling around the Cape of Good Hope in South Africa and thus could save a considerable amount of time. Sailing ships were unable to navigate across the Suez canal whereas steamships, that had recently come into appearance, could fully take advantage of this strategic shortcut. Steamships started to be preferred over sailing ships and when, at the beginning of the twentieth century, the diesel engine came into use, commercial sailing ships became obsolete.

An important aspect to consider is that at the time steamships made their first appearance, commercial sailing vessels were still attractive from an economic point of view and this condition persisted over many years. There were two main factors, however, for which sailing ships could not compete with mechanically driven ships: reliability and versatility. In fact, the propulsive power of mechanical ships was independent on the wind conditions and this allowed them to have a more reliable trade schedule as well

as to sail along new routes that were inconvenient for sailing vessels. Mechanical ships were also more manoeuvrable and less bulky (e.g. they did not have tall sailing masts), thus they could sail across the Suez and the Panama Canal (opened in 1914) and they only needed a reduced crew.



Figure 1.1: The windjammer *Pamir*. It operated commercially until 1949. (Photo: Public Domain)

It was undeniable that the introduction of mechanical ships brought considerable advantages to the maritime industry, even more so in a world that was rapidly becoming more industrialized and more connected. When in the 1980s the idea of using wind energy in the shipping sector became more consistent, it was evident to most observers that a return to pure sailing ships was unfeasible. In fact, hybrid ships were considered instead, ships that could ensure the same trade schedule and the same number of crew as standard mechanical ships did, onboard which wind energy was used as a form of assistance to the main propulsive power.



Figure 1.2: The Fijian ferry *Na Mata-i-sau* retrofitted with soft sails. (Photo: [Nuttall et al., 2014](#))

In the years of the oil crisis, several examples of wind-assisted ships began to appear. In response to the high fuel price of that period, that put at stake the whole inter-island transport system of its country, the government of Fiji invested in the retrofit project of

the *Na Mata-i-sau*, a 27-meter long ferry (Figure 1.2). The ship was retrofitted with two masts and soft sails and it serviced until its sinking occurred in 1985. Nonetheless, the rig was salvaged and it was subsequently installed onboard a similar ship, the *Cagidonu*. The University of Southampton, that partnered in the project, after analysing the log data of the *Cagidonu*, concluded that the ship achieved an average of 37% fuel savings compared to an analogous ship (Satchwell, 1986).



Figure 1.3: *Shin Aitoku Maru*, the first ship to be fitted with the JAMDA-NKK wing sails. (Photo: MK)

In Japan, the classification society NKK and the Japanese Marine Machinery Development Association (JAMDA) developed rigid, foldable wing sails for assisted propulsion. The rigid sails were fully automated and they trimmed themselves according to the local wind conditions to maximize the wind-generated thrust. The first ship to be fitted with two 96 square-meter sails was the product tanker *Shin Aitoku Maru* in 1980 (Figure 1.3). In 1984, similar sails were installed onboard two larger ships, the bulk carriers *Aqua City* and *Usuki Pioneers*. In the following years, there was a total of 17 ships of different type and size that employed the JAMDA-NKK wing sails. Nuttall et al. (2014) report that the Japanese wing sails ensured fuel saving as high as 30% as well as better stability and reduced engine wear.

New wind-propulsion systems were also invented. For example, the Cousteau Foundation proposed the innovative Turbosail, that is a boundary-layer control system that makes use of a suction fan to increase the pressure difference between the sides of the airfoil. The first ship to be fitted with Turbosails was the *Alcyone*, a Research Expedition Vessel of 30 meters in length used by the French foundation. As reported by Charrier et al. (1985), two other ships were going to be fitted with this device: a new, larger oceanographic ship for the Cousteau Foundation and a chemical carrier, that would have been the first commercial installation of the Turbosail.

Already at the beginning of the 1980s however, the price of oil began to drop and, in a matter of a few years, it settled to a near prior-crisis level. Despite the proven technology and the promising fuel savings reported, wind-assisted propulsion became unappealing from an economic perspective: the many wind-assist initiatives that took place during the years of the oil crisis were dismissed and those planned for the following years were halted.

1.2. RENEWED INTEREST IN WIND ASSIST

Since the commencement of the new millennium, wind-assisted propulsion is again gathering attention as an attractive possibility to reduce the dependence of the shipping sector on fossil fuels. While during the oil crisis, wind assistance was considered merely as a way to cut fuel expenses, the reason behind the renewed interest towards it is now twofold: economic and environmental.

Shipping is responsible to carry as much as 90% of the world trade volume (Smith et al., 2015) and, according to Nelissen et al. (2016), its carbon dioxide (CO₂) emissions account for about one billion tons per year. In the current frame, this represents circa 3% of the total anthropogenic emissions, nonetheless, the same study indicates that emissions due to maritime transport are expected to increase by 50-250% by 2050. In case the emissions from other sources were reduced to avoid an intolerable increase in global average temperature, while ship emissions continued to increase along the projected path, in the year 2050 the shipping industry could account for up to 15% of the total global emissions (Nelissen et al., 2016). Another issue arises from the type of fuel that is still largely used by most of the global fleet, that is Heavy Fuel Oil (HFO). Being an unrefined, residual oil, it contains high percentages of sulphur and once it is burnt it produces enormous quantities of nitrogen oxides (NO_x) and sulphur oxides (SO_x) that are proven to be harmful to human health (Sofiev et al., 2018). Smith et al. (2015) report that shipping represents respectively about 13% and 15% of the global SO_x and NO_x emissions caused by human activities. For the reasons above discussed, in the last years, the maritime transport industry is under pressure to alleviate its negative impact on the environment and on human health and this is pursued by the issuing ever stricter emission regulations.

As for the beginning of 2013, the IMO (International Maritime Organization) Energy Efficiency Design Index (EEDI) enforces new merchant ships of 400 gross tonnage and above to improve their efficiency regarding CO₂ emissions with respect to comparable ships built between 2000 and 2010. The reduction level is tightened every five years until the period 2025-2030, in which a 30% energy efficiency improvement will need to be met. At European level, the MRV (Monitoring Reporting Verification) regulation requires vessels larger than 5000 gross tonnage to annually monitor and report to an independent body their CO₂ emissions. This measure was enforced on 1 January 2018 and it applies to ships calling at any EU (including Iceland and Norway) port. Other regulations were issued over the years to restrain SO_x and NO_x emissions. Since 2015, in the so-called Emission Control Areas (Baltic Sea, North Sea, North America Area, United States and Caribbean Sea Area), the limit for sulphur content in the fuel burnt by ships transiting these areas must not exceed 0.1%. On the other hand, outside these protected areas, the global limit was decreased by the IMO from 4.5% to 3.5% sulphur content as for 1 January 2012 (Smith et al., 2015). Despite being an improvement, this means that ships sailing in open waters are still allowed to use HFO. A significant tightening of this measure, however, will enter into force at the commence of 2020, when more than 70000 ships will have to use fuels that do not exceed 0.5% sulphur content or otherwise will need to install exhaust gas cleaning systems (known as scrubbers) to comply with the regulation. Lastly, an initial strategy to reduce greenhouse gas (GHG) emissions by international shipping was adopted by the IMO's Marine Environment Protection Committee (MEPC) during

its 72nd session held in April 2018 in London. The IMO initial strategy identified levels of ambition which have the aim to lead to a reduction in total annual GHG emissions by at least 50% by 2050 compared to 2008 and to pursue efforts towards phasing them out. This significant decision follows the pathway of CO₂ emissions reduction established in the Paris Agreement signed in 2015 by the parties of the UNFCCC (United Nations Framework Convention on Climate Change). In fact, the Paris Agreement on climate change, in which international shipping was not included, has the objective to adopt measures necessary to keep the global temperature rise in this century well below 2 degrees Celsius compared to pre-industrial levels and to prosecute efforts to limit the temperature rise even further to 1.5 degrees Celsius.

The economic and environmental motives behind the renewed attraction for wind assist technologies are tightly intertwined. In fact, as [Argyros \(2015\)](#) reports, the demand for cleaner fuels is likely to lead to an increase in fuel price and this, in turn, will make investments into energy-saving devices more attractive. In this evolving situation, wind-assisted propulsion, that has the potential to ensure double-digit percentages in fuel savings, can play an important role.

1.3. THE PERFORMANCE PREDICTION PROGRAM

Following the growing interest towards wind-assisted propulsion, the Sail Assist project was started at the Delft University of Technology with the aim to investigate the physics of wind-assisted ships. The project was divided into two main parts: one part focused on the aerodynamics of wind-assisted vessels, while the other part focused on their hydrodynamic aspects. The final goal of the project was to combine the aerodynamic and the hydrodynamic components into a computer program capable of predicting the performance of a given wind-assisted ship.

In the context of sailing yachts, a software with similar features exists since the late 1970s. In 1976, in fact, [Kerwin \(1976\)](#) presented the so-called Velocity Prediction Program (VPP), a computer program that calculates the sailing speed of a yacht of known characteristics, for a selected range of wind conditions (wind speeds and wind angles). The software, that is divided into an aerodynamic and a hydrodynamic module, comprises sets of regression formulas derived from systematic series of dedicated towing-tank tests (the Delft Systematic Yacht Hull Series; [Kerwin, 1976](#)) and full-scale sail performance measurements (originally) or wind-tunnel tests (in a later phase). The aerodynamic forces and moments are expressed with nondimensional coefficients dependent on the sail type and the sail angle of attack, whereas the hydrodynamic forces and moments are described with nondimensional coefficients based on the hull geometry, the Froude number or the Reynolds number, depending on the force component considered. In this manner, the experimental results can be applied to any yacht, irrespective of its size, provided that its hull and sail characteristics are compatible with the models used in the systematic series. The core of the software is an algorithm that finds the balance between the aerodynamic and the hydrodynamic forces and moments acting on the yacht. This is attained with an iterative process during which the sailing parameters of the yacht (e.g. the reef and the flattening of the sails) are adjusted to reach the optimal boat speed for a given combination of wind speed and wind angle. The typical output of a VPP is a polar diagram in which the optimized yacht speed is plotted

for the entire range of selected wind conditions.

Nowadays, VPPs are commonly used by yacht designers to readily compare different prototypes during the project of a new sailing boat as well as by sail racing organizations to create rating systems that allow boats of different sizes and characteristics to fairly compete in one same regatta. In either case, what assures a quick, yet enough accurate performance prediction, are the sets of built-in force models that provide for an instantaneous estimate of the forces and moments acting on the yacht under consideration.

As underlined by [Argyros \(2015\)](#), one fundamental prerequisite for the uptake of wind assistance in the shipping industry is to establish a common method able to reliably predict the potential fuel savings of different wind assist designs. In the wake of the successful application of VPPs in the sailing yacht framework, the rationale of the Sail Assist project is to adapt the concept of a Velocity Prediction Program for sailing yachts to a Performance Prediction Program (PPP) for wind-assisted ships. The two computer programs are based on a similar structure but have some significant differences. In the first place, wind assistance means that, unless some exceptional cases, the ship propulsion is hybrid: the thrust to move the ship at the desired forward speed is provided simultaneously by the engine and by the wind-generated thrust. Thus, the balance between the aerodynamic and hydrodynamic forces and moments can be solved either by fixing the ship speed, while optimizing the percentage of thrust generated by the wind propulsion systems, or by fixing the amount of thrust delivered by the engine, while optimizing the ship speed. The name Performance Prediction Program stems from the possibility to set different optimization routines. The other key difference between a VPP and a PPP is that the built-in force models derived from sailing yacht testing need to be replaced by force models based on data of wind-assisted ships.

In the frame of the Sail Assist project, this dissertation deals with the aerodynamic aspects of wind-assisted ships. More specifically, the aim of the present work is to contribute to the realization of the aerodynamic built-in force model of the Performance Prediction Program.

1.4. RESEARCH OUTLINE

The structure of the present doctoral dissertation is given here below.

Chapter 2 deals with the aerodynamics of wind-assisted ships. First, the state-of-the-art is presented, paying particular attention to the characteristics of the different propulsion systems most commonly considered for wind assistance. The attention is then directed to the limitations of the performance prediction methods presented over the years while the importance of considering the effects of the aerodynamic interaction on the overall performance of the ship is discussed. The last section of the chapter includes the reasoning behind the selection of the research focus. The research questions are finally presented.

In Chapter 3 the experimental research carried out on the Dynarig is described. The first part of the chapter includes a literature review on the effects of the aerodynamic interaction occurring between multiple sails. The results of the wind-tunnel experiments are then introduced. Firstly, the discussion regards the results of the tests conducted on a single Dynarig. These experiments aim at providing a term of comparison for the results presented in the second part of the chapter. The attention, in fact, is then directed to

the effects of the aerodynamic interaction on the performance of an arrangement of two similar Dynarigs. In support of this discussion, the results include the aerodynamic force coefficients and pressure coefficients measured on each Dynarig for a range of different wind angles and two different gap-distances between the sails. Lastly, the aerodynamic performance of a ship equipped with one or two Dynarigs is analysed in terms of overall driving and heeling force coefficients.

Chapter 4 provides a thorough analysis of the Reynolds number effects on the aerodynamic coefficients of a large-scale rotating cylinder. The chapter begins with a comprehensive review of the studies conducted on this topic and it evidences the need for further research, especially at high Reynolds numbers. After the description of the setup used in the experiments, the results of the wind-tunnel tests on the large-scale rotating cylinder are presented. In particular, the influence of the Reynolds number on the lift and drag coefficients is investigated. To support the discussion, the pressure measurements taken at the cylinder mid-span are reported and analyzed in detail. Measurements of the power consumption necessary to rotate the cylinder are also included at the end of the chapter.

The effects of the aerodynamic interaction on the performance of two similar Flettner rotors are discussed in Chapter 5. A literature review is provided at the beginning of the chapter, in which the lack of research on this topic is underlined. The attention is then directed to the results of the experimental study. Firstly, the results of the wind-tunnel experiments conducted on a single Flettner rotor are presented. The results of the measurements of the lift and drag coefficients as well as those of the velocity field past the Flettner rotor are reported with the aim of providing useful data to better understand the effects of the aerodynamic interaction. In the second part of the chapter, in fact, the results of the experiments carried out on two similar Flettner rotors are introduced. The tests include measurements performed at a range of different wind angles for three gap distances between the two rotors. Moreover, for each of these conditions, the Flettner rotors were spun at different combinations of velocity ratios. The effects of the interaction are studied by comparing the results of the aerodynamic coefficients of the two Flettner rotor and those measured on the single device. This chapter ends with a discussion on the possible influence of the Reynolds number on the aerodynamic interaction occurring between multiple Flettner rotors.

In Chapter 6 the capabilities of a simple mathematical model to predict the aerodynamic interaction effects are analysed. The chapter begins with a discussion regarding the features that the aerodynamic module of the Performance Prediction Program should have. The focus is then directed to a mathematical model found in the literature that was employed to estimate the effects of the aerodynamic interaction on the performance of two competing sailing yachts. The second part of the chapter deals with the validation of the mathematical model against the experimental results of the Dynarig and Flettner rotor tests presented in Chapter 3 and Chapter 5. In support of the analysis, the results of the computed and the measured velocity fields past the considered wind-propulsion system are compared.

Finally, the main conclusions of this dissertation are presented in Chapter 7 together with a number of recommendations for future work.



2

AERODYNAMICS OF WIND-ASSISTED SHIPS

The concept of wind-assisted propulsion was born during the years of the oil crisis. In those years, the scientific community was involved in an active debate regarding which wind-propulsion system would have been most suitable for adoption in the shipping sector. Several wind assist devices were presented and compared in terms of aerodynamic performance as well as in terms of practical features, i.e. deck space occupancy, operability, easiness of employment, etc. Nonetheless, due to the end of the crisis, and the consequent normalization of the oil price, the topic of wind assist practically disappeared from the scientific literature until the first years of the new millennium when it again attracted a considerable attention. In this chapter, the state-of-the-art for the aerodynamic performance prediction of wind-assisted ships is discussed. In particular, the focus is directed to the limitations of the performance prediction methods presented over the years while the need for a thorough physical model is underlined. At the end of the chapter, the research questions related to the present work are introduced keeping in consideration the scope of the Sail Assist project.

2.1. STATE-OF-THE-ART

The 1980s were a dynamic period for wind-assisted propulsion. This is testified by two large international symposia held on the topic in those years (RINA, 1981; Satchwell, 1985b). In these conferences, the possibility to use wind energy as a form of assistance for ship propulsion was debated from different perspectives. Among these, most relevant to the present dissertation are the studies dedicated to the various wind-propulsion systems and their aerodynamic performance. In those years, in fact, several different wind assist devices were analysed and compared with the aim to find which the shipping industry would have been more likely to consider for adoption.

In the years of the oil crisis, soft sails were often regarded as a viable solution for wind assistance. In particular, being a well-established technology, the application of traditional fore-and-aft rigs to small coasters (Scott, 1981; Gifford, 1981) or fishing vessels (Jaquemin, 1981) was seen as an effective manner to reduce the operational costs of the ship with a limited investment. The *Na Mata-i-sau* and *Cagidonu* projects of Fiji are an important example of this. Nonetheless, more innovative wind-propulsion systems were also considered. For example, the Flettner rotor and the Turbosail, that are mechanical devices capable of delivering a high lift force with a limited “sail” area, were a popular matter of discussion. A common characteristic of these boundary-layer control devices is that some energy input is required for their functioning. In fact, the Flettner rotor (Flettner, 1925) is a cylinder that, rotated by an electric engine, generates a lift force due to the Magnus effect, while, in the Turbosail (Charrier et al., 1985), a suction fan is used to aspire the boundary-layer air in order to increase the pressure difference.



Figure 2.1: *Alcyone*, the Research Expedition Vessel of the French Cousteau Foundation equipped with two Turbosails. (Photo: David Merrett)

Another mechanical system that was deemed an appealing solution for wind assist was the wind turbine. The main advantage of using this technology is that it is able to operate in any relative wind direction, even when the ship sails straight into the wind (Rainey, 1981). Differently from any other wind-propulsion system, the wind turbine functions by converting wind energy into mechanical energy, thus it needs to be mechanically coupled with the water propeller. To prove this concept, in the early 1980s, several small windmill-driven prototype boats were launched (Bose, 1981; Bose and Small, 1985; Blackford, 1985).

Some considerable improvements were also made in sail technology. Kite sails, for example, attracted the interest of many researchers in the years of the oil crisis (Schaefer and Allsopp, 1981; Stewart, 1985). Compared to the other wind-propulsion systems, in fact, kites have some important advantages: they experience higher wind speeds by flying high above the sea surface and by being dynamically operated, they occupy marginal deck space, and being the traction force connected at the deck level, they generate a minimal heeling moment.

Other innovative sail types came also into appearance, in particular, two should be mentioned: the Dynarig and the wingsail. The Dynarig (or, originally, Prölls rig), was considered a modernized version of the square rig with improved aerodynamic performance. Moreover, compared to its predecessor, the Dynarig, that is a self-standing and automated rig, was also more practical from a sailing perspective. The wingsail, on the other hand, is a rigid sail built with an airfoil-shaped cross-section. The main advantage of the wingsail is that it has enhanced aerodynamic efficiency, i.e. a higher lift over drag ratio, than soft sails, thus it is particularly suited for upwind sailing. In those years, several types of wingsails were considered, based on different airfoil sections (for example, Fiorentino et al., 1985) or comprised by a set of multiple wings like, for example, the Walker wingsail (Walker, 1985).



Figure 2.2: A ship sailing with the assistance of a kite sail. (Photo: Skysails)

As mentioned at the beginning of this chapter, during this first period of wind-assisted propulsion, the scientific discussion was mainly orientated to seek what wind assist device had most merits compared to the others and therefore was most suitable to be used on commercial ships. To pursue this goal, and to help ship owners with their investment decisions, several performance prediction methods were proposed. Nance (1981), for example, reports the amount of auxiliary power that different wind assist devices are able to deliver given a certain ship speed and wind conditions (wind speed and wind angle). Based on these performance data, the payback periods relative to each considered wind auxiliary system are then derived. A similar method was proposed by Smulders (1985). According to this procedure, first, a certain wind assist device and the

route to be sailed by the ship are chosen. Consequently, the necessary sail area to reach the desired amount of fuel savings is calculated taking into account the performance of the chosen wind-propulsion system and the wind conditions of the selected route. The economic assessment is then based on the results of this procedure. Finally, [Wellicome \(1985\)](#) compares the performance of the kite, the wingsail, the wind turbine, the Flettner rotor and the Dynarig using formulas of classic aerodynamic theory and assuming arbitrary operating conditions for each considered device.

The methods above briefly introduced have the aim to directly compare the merits of the various wind-propulsion systems solely being based on their idealized aerodynamic performance. In fact, it is assumed that the overall aerodynamic performance of the rig is not influenced by whether the sail area necessary to reach a certain amount of fuel savings is comprised by one single device or whether it needs to be spread over multiple devices. This assumption implies that the interaction effects that are likely to occur in case multiple devices are employed do not alter the aerodynamic performance and, therefore, also the relative merits of the various wind-propulsion systems analysed.

On the other hand, other studies introduce a more refined performance prediction method ([Satchwell, 1985a](#); [Schenzle, 1985](#); [Fiorentino et al., 1985](#)). In these investigations, in fact, the performance merits of the wind-propulsion systems are analysed taking into account certain effects caused by the coupling between the aerodynamic and hydrodynamic forces acting on the ship. For example, the induced resistance caused by the hydrodynamic sideforce necessary to compensate the aerodynamic heeling force, is accounted for. It should be mentioned, however, that these effects are calculated by using simple linear theory or empirical formulas. Although these studies introduce a new layer of reality, similarly to the methods previously discussed, there is no indication regarding the influence of the aerodynamic interaction on the overall performance of the wind-propulsion systems.

The last performance prediction method that should be mentioned is that one described by [Shenzle \(1981\)](#) and by [Bradbury \(1981\)](#). These studies deal with dedicated wind-tunnel tests on a ship model equipped with Dynarigs ([Shenzle, 1981](#)) or with wingsails ([Bradbury, 1981](#)). The aerodynamic coefficients gathered during the experiments were then used to compute the overall performance of the considered ship. In these cases, the effects of the interaction on the overall aerodynamic performance of the rig are taken into account, as they are already included in the measured coefficients. It should be noted, however, that the results of these experiments are only valid for sail arrangements comparable to those tested in these studies.

After the end of the oil crisis, the research on wind-assisted propulsion was practically halted until the early years 2000s, when it again attracted the attention of the scientific community and the shipping industry alike. Since the commencement of the new millennium, in fact, several studies were published on this topic, and the interest grew stronger over the years. This new era for wind-assisted propulsion inherited an important legacy from the research conducted on wind assist in the 1980s. In particular, a part of some exceptions, the main wind-propulsion systems that are currently considered for adoption are the same as those proposed decades earlier. The kite, the Flettner rotor, the Dynarig and several different types of wingsails, in fact, are nowadays commonly considered suitable devices for wind assistance. On the other hand, the interest

in traditional soft sail rigs and in the wind turbine now appears to be decreased.

Since the years of the oil crisis, important advancements were made regarding the knowledge of the aerodynamic performance of wind-propulsion systems. In fact, a significant amount of research efforts was directed to gain a better understanding of the lift and drag characteristics of the most common wind assist devices. The numerical investigation of [De Marco et al. \(2016\)](#) on Flettner rotors, the studies of [Fujiwara et al. \(2003\)](#), [Burden et al. \(2010\)](#), [Li et al. \(2015\)](#) and [Li \(2017\)](#) on certain types of wingsails and the wind-tunnel experiments on the Dynarig mentioned by [Smith et al. \(2013\)](#), are notable examples of this. Nonetheless, limited progress was made regarding the methods used to estimate the fuel savings achievable by a wind-assisted ship. The scientific literature, in fact, shows that considerable simplifying assumptions are still typically made. For example, from an aerodynamic perspective, [Luyu et al. \(2010\)](#), [Shukla and Gosh \(2009\)](#) and [Viola et al. \(2015\)](#) assume that the overall thrust generated by a set of multiple wing sails is not affected by their aerodynamic interaction. A similar assumption is made also by [Traut et al. \(2012\)](#), [Traut et al. \(2014\)](#) and [De Marco et al. \(2016\)](#), in which the thrust of a set of Flettner rotors is calculated as the arithmetic sum of the thrust generated by each installed device. A partial improvement is provided by [Eggers \(2016\)](#). To partially account for the interaction effects occurring between the two Flettner rotors installed on the ship under analysis, the author assigns a reduction in lift to the leeward Flettner rotor when the ship is sailing in the conditions in which the aerodynamic interaction is assumed to be most detrimental.

Similarly to some studies carried out in the 1980s, also in more recent times, a certain number of investigations were conducted to obtain the aerodynamic coefficients of specific vessels. For example, this is the case of [Smith et al. \(2013\)](#). In this study, the authors used data obtained by means of wind-tunnel tests carried out on a ship equipped with a set of Dynarigs. The aerodynamic data were then used to estimate the amount of fuel savings achievable by the considered ship. In the work of [Burden et al. \(2010\)](#) and [Ouchi et al. \(2013\)](#) a similar approach is used. In these cases, the vessels under consideration are equipped with sets of wingsails. As previously mentioned, however, although these methods do take into account the complex interaction effects that alter the aerodynamic performance of the rig, the results of these studies are only applicable to the specific cases considered.

2.2. RESEARCH FOCUS

The state-of-the-art of the research carried out on the aerodynamic aspects of wind-assisted propulsion shows that, since the years of the oil crisis, some significant progress was made. In particular, it appears that, during these past years, the scientific community gained a considerable amount of knowledge regarding the aerodynamic characteristics of the most popular wind assist devices. Nowadays, in fact, the literature offers numerous studies in which the lift and drag coefficients of these devices are investigated. The same literature, however, also indicates that, to estimate the performance of a wind-assisted ship, either dedicated (and expensive) experimental or numerical investigations are conducted or substantial simplifying assumptions are still typically made.

From an aerodynamic perspective, it appears that the most remarkable assumption is to neglect the complex interaction effects that alter the aerodynamic performance

of the rig and that, in turn, would influence the fuel savings achievable by the ship. A key study on this topic is that of [Fujiwara et al. \(2005\)](#). This research, in fact, is a rare example of investigation dedicated to understanding the influence of the aerodynamic interaction effects on the overall thrust of a wind-assisted vessel. In the work of [Fujiwara et al. \(2005\)](#), the authors carry out a series of wind-tunnel experiments on a bulk carrier model equipped with four hybrid sails (a combination of a wingsail and a soft sail), with the aim of investigating the influence of two types of interaction effects on the overall aerodynamic performance of the ship. Such effects are the interaction effects occurring between the multiple sails installed on the ship and the interaction effects caused by the ship hull on the sails. The results of the study indicate that, for the case considered, the driving force coefficient is reduced by up to 18% in case the interaction effects are taken into account. Moreover, it appears that, generally, the “sail-sail” interaction effects are the most influential for the overall aerodynamic performance of the vessel. In line with the results of their investigation, the authors conclude that, to properly assess the performance of a wind-assisted vessel, the aerodynamic interaction effects cannot be neglected.

Taking into account the outcome of the literature review here discussed, and the scope of the Sail Assist project, it appears that a better understanding of the “sail-sail” interaction effects is most needed in order to develop a method able to reliably predict the aerodynamic performance of a generic wind-assisted ship. Based on these considerations, the present work focuses on improving the performance estimate of wind-propulsion systems and, in particular, on gaining a better understanding of the aerodynamic interaction effects occurring between the multiple propulsion systems installed on a wind-assisted vessel.



(a) The DNA sailing yacht *Black Pearl*.
(Photo: Dykstra Naval Architects)



(b) The general cargo vessel *E-ship 1*.
(Photo: Lpele)

Figure 2.3: The two wind-assist devices analysed in this dissertation, the Dynarig (a) and the Flettner rotor (b)

The core of this doctoral thesis comprises a series of experimental studies on two wind-propulsion systems, namely the Dynarig and the Flettner rotor. The reason to focus on these devices is threefold. Firstly, from a practical perspective, these devices proved to be feasible options. The Dynarig, in fact, is now successfully employed on several large sailing yachts while, regarding the Flettner rotor, a few significant examples of ships equipped with this device and regularly operated can be found in the past as well as nowadays. Secondly, at the time in which this work began, the Dynarig and the Flettner rotor, together also with the kite, were arguably the wind-assist devices most likely to be adopted by the shipping industry. This was justified by a number of com-

panies that offered commercial solutions involving these technologies. The reason why the kite was eventually not considered in the present work is because, due to the fact that typically only a single kite sail is used, and being operated at a high altitude above the ship's deck, this wind-assist device is not affected by the aerodynamic interaction effects above discussed and that are the main focus of the present dissertation. The third and final reason is that in Chapter 6 of the present work, the capabilities of a simple mathematical model to predict the effects of the aerodynamic interaction between two generic wind-propulsion systems are investigated. In this respect, to better understand the potential of the considered mathematical model, it was deemed necessary to test two substantially different types of wind-propulsion systems. The Dynarig, in fact, is a "passive" device that functions on the same principles of a sail or a wingsail while, on the other hand, the Flettner rotor is an "active" device, i.e. it requires an energy input to function and its rotational speed determines its flow characteristics (e.g. the separation point and, thus, its lift and drag force).

Within the scope of the Sail Assist project, the experimental campaigns were designed in such a way that, although the validation of the mathematical model proved unsuccessful, the results of the experiments on the Dynarigs and the Flettner rotors could be directly used to, at least partially, fulfill the requirements of the aerodynamic model of the Performance Prediction Program.

Before elaborating the research questions of this work, it should be pointed out that in the current dissertation special attention was given to the aerodynamic performance of the Flettner rotor with respect to scale effects. In fact, as further elaborated in the literature review presented in Chapter 4, the Reynolds number influence on the lift and drag coefficients of rotating cylinders was still a matter of debate. To achieve an accurate performance prediction of multiple Flettner rotors, that is part of the final goal of this thesis, a thorough understanding of the aerodynamic characteristics of a single Flettner rotor was a necessary requirement.

2.3. RESEARCH QUESTIONS

The work presented in this dissertation aims at answering a series of research questions that are presented here below. The first two research questions deal with the interaction effects occurring between a set of two similar Dynarigs (rigid sails) or Flettner rotors. These research questions read:

- What is the effect of the aerodynamic interaction on the performance of a wind-assist arrangement comprised of two similar rigid sails?
- What is the effect of the aerodynamic interaction on the performance of a wind-assist arrangement comprised of two similar Flettner rotors?

The third research question tackles the influence of scale effects on the aerodynamic performance of a single Flettner rotor, namely:

- How does the Reynolds number influence the aerodynamic coefficients of a rotating cylinder in the critical and supercritical flow regime?

Finally, the last research question treats the capability of a simple mathematical model to predict the aerodynamic interaction effects occurring between multiple wind assist devices. This research question reads as follows:

- Is a simple mathematical method, based on the horseshoe vortex theory, capable to predict the effects of the aerodynamic interaction occurring between two rigid sails or two Flettner rotors?

3

AERODYNAMIC INTERACTION BETWEEN TWO RIGID SAILS

The research presented in this chapter deals with the aerodynamic interaction between two rigid sails. Wind-tunnel experiments were carried out on a single sail and on a two-sail arrangement, during which force and pressure measurements were taken on each sail. For the two-sail arrangement, two gap distances between the sails were investigated and the tests were performed at apparent wind angles ranging all typical sailing conditions. The results show that for an extended interval of moderate apparent wind angles the aerodynamic interaction has a positive effect on both sails. On the contrary, at smaller and at larger angles the interaction effects are detrimental for the downstream sail. The outcome of the present work indicates that the number of sails employed and their gap distance are important parameters to determine the aerodynamic interaction effects.

This chapter is based on the journal article: G. Bordogna, J.A. Keuning, R.H.M. Huijsmans and M. Belloli. Wind-tunnel experiments on the aerodynamic interaction between two rigid sails used for wind-assisted propulsion. *International Shipbuilding Progress*, 65(1):93-125, 2018.

3.1. INTRODUCTION

The soundness of the performance prediction of a wind-assisted ship lies in the fact that all the complex effects caused by the aerodynamic force acting on the ship are considered. Such effects comprise the sailing behaviour of the ship (e.g. sailing at a constant heel and leeway angle) as well as the fact that the engine and the propeller are operated in a lightly loaded, off-design, condition. From an aerodynamic perspective, one of the main challenges is to accurately estimate the amount of thrust that can be generated considering the effects caused by the interaction of the several wind-propulsion systems (sails, wingsails, Flettner rotors, etc.) that might be installed on the ship. While in any Velocity Prediction Program (VPP) for sailing yachts the sail interaction effects are taken into account, in the performance prediction of wind-assisted ships, assumptions are generally made to simplify or neglect altogether any effect of the aerodynamic interference occurring between the installed wind-propulsion systems. Some notable examples of this are the works of [Schenzle \(1985\)](#), [Shukla and Gosh \(2009\)](#), [Traut et al. \(2012\)](#), [Viola et al. \(2015\)](#) and [De Marco et al. \(2016\)](#). Arguably, the main reason to be so is that, differently from sailing yachts, for which within a certain yacht category (e.g. a sloop) different yachts have a similar sail plan (one single mast with a mainsail and a headsail), the wind-propulsion systems that could be installed on board of commercial ships might vary considerably in terms of type (e.g. sails versus Flettner rotors), in terms of quantity and in terms of their relative distance and position on the deck. All these degrees of freedom make it necessary to study each case by means of dedicated wind-tunnel experiments or CFD simulations.

The concept of wind assistance for commercial ships is not new. In fact, already in the 1980s, to take action against the high fuel prices of that time, several studies on different wind-assist devices were conducted. Among the numerous studies on the topic published in that time, arguably, the most relevant to the present work are the publications of [Bradbury \(1981\)](#) and [Ingham and Terslov \(1985\)](#). Bradbury carried out a two-dimensional analysis using potential flow as well as wind-tunnel experiments on a ship with a rig composed of eight identical NACA 0018 wings. During the experimental campaign, only the total forces acting on the ship and on the rig were measured. The author concluded that a graduated sail trim gave considerably better performance than a parallel one. On the other hand, Ingham and Terslov conducted a wind-tunnel campaign on a bulk carrier equipped with six wingsails. Once again just the total forces acting on the ship and the rig were measured and no details about the performance of each wingsail were given.

The first thorough analysis of the physics behind the aerodynamic interaction effects of sails is attributable to Boeing engineer Arvel Gentry. To the author knowledge, he was the first one to analyse using of CFD tools the effects of the interaction between the jib and the mainsail of a sailing yacht. In the publications of Gentry ([Gentry, 1971](#); [Gentry, 1981](#)) the yacht under consideration had an overlapping jib (the jib leech was laying at half chord length of the mainsail) and the boat was considered to be sailing close-hauled (the sails were set at a small angle of attack) so that flow separation could be neglected. In such condition, it was proven that there is a beneficial interaction between the two sails, i.e. the two sails together are more aerodynamically efficient than the sum of the two single sails. More precisely, the mainsail generates an upwash on the jib causing its

stagnation point to be shifted windward, thus the boat needs to be sailed closer to the wind to prevent the jib to stall. The trailing edge of the overlapping jib (leech) is in a high flow speed region, meaning that the Kutta condition needs to be fulfilled at a higher speed and this increases the efficiency of the whole sail. From the mainsail perspective, the downwash generated by the jib causes the peak suction velocities on the lee side of the main to be strongly reduced. The reduced pressure gradient allows the mainsail to be operated at higher angles of attack without stalling.

[Gentry \(1973\)](#) introduces a third sail, i.e. a staysail between the jib and the mainsail, and the yacht was again sailing in such a way that the sails were set at a small angle of attack so that separation could be ignored. The most relevant result about the aerodynamic behaviour of a three-sail arrangement is that whether there is a positive or negative interaction strongly depends on the relative position of the sails and their trim. The author points out how in case the sails were wrongly trimmed the advantage of adding extra sail area would be wasted by the efficiency loss of the whole sail plan. On the contrary, if the sails are properly positioned and trimmed, a so-called bootstrap effect may occur: the mainsail increases the efficiency of the staysail that, in turn, it increases the efficiency of the jib. Gentry underlines how, theoretically, the bootstrap effect could occur also when a much larger number of sails is used. Still in the context of sailing yacht aerodynamics, it should be mentioned the work of [Chapin and Neyhousser \(2006\)](#). The work deals with the optimization of a double-rig in terms of sail camber and sail trim angle by means of CFD RANS. Similarly to the results of Gentry, the outcome of this study underlines the importance of a proper sail setting in order to take advantage of the interaction effects.

Another field of research that deals with the aerodynamic interaction of sails is that one of competitive sailing for which it is important to understand how two yachts interfere with each other during a match race. In this case, the mainsail and the jib of each yacht are considered as one large sail and the interference (change in driving force) generated by each boat on the other is studied in terms of change in velocity field (wind angle and wind speed). Typically, the velocity field around the flow-perturbing boat is calculated with a CFD software ([Caponnetto, 1997](#); [Roncin and Kobus, 2004](#)) or measured with wind-tunnel experiments ([Richards and Pelley, 2014](#)) at several positions. Using the computed (or measured) change in wind angle and wind speed, the change in driving force the second boat would experience at all considered positions in space is calculated.

In the context of wind-assisted propulsion for commercial ships, the first relevant study that tackled the aerodynamic interaction between several sails is the work presented by [Fujiwara et al. \(2005\)](#). In this research, the performance of a single soft sail, expressed in terms of driving force coefficient, is compared to the performance of a sail plan composed of four equal sails. The sails tested had a rectangular or a triangular shape and, for each sail shape, two different arrangements were used: a) the four sails were aligned along the centreline of the ship and they were all trimmed with the same angle of attack, b) the four sails had a goose-winged arrangement (they were zig-zag shifted about the centreline) and each sail was trimmed independently during the wind-tunnel experiments in order to increase the driving force of the entire sail plan. The tests were carried out at apparent wind angles ranging from 20° (sailing upwind) to 180°

(sailing downwind) and the forces were measured on each sail and compared to the results of the single-sail experiment. The results show how, in general, the aerodynamic interaction occurring between the four sails has a negative effect on the efficiency of the sails. This is particularly so for large apparent wind angles ($AWA = 150^\circ - 180^\circ$) at which the downstream sails are in the wake of the upstream ones, the former experiencing a reduced wind speed. The goose-winged arrangement, on the other hand, largely reduces this negative effect. Regarding the tests conducted at smaller apparent wind angles ($AWA = 20^\circ - 90^\circ$), whether the effects of the aerodynamic interaction are positive or negative, it depends on the position of the sail under consideration relative to the others and on whether the sails are all trimmed equally or independently with the aim of increasing the driving force. For both cases, only the most upstream sail (the first one from the bow) experiences an increase in driving force compared to the single sail. Conversely, the performance of the other sails is decreased, and this effect is stronger moving towards the most downstream sail (the last one from the bow). Trimming each sail independently has an overall positive effect: the increase in driving force experienced by the first sail is enhanced and the decrease in performance of the remaining sails is reduced. Another interesting output of the research is that the multiple-sail bootstrap effect as suggested by Gentry did not occur for any sail arrangement tested by [Fujiwara et al. \(2005\)](#).

More recently, the research inspired by the University of Tokyo “Wind Challenger” project ([Ouchi et al., 2011](#); [Ouchi et al., 2013](#)) gave more insights into the interaction effects occurring between two or more wingsails. In the work of [Nakashima et al. \(2011\)](#) and [Li et al. \(2015\)](#), the authors studied by means of wind-tunnel experiments as well as with CFD simulations the performance of a cascade of wingsails. In the publication of [Nakashima et al. \(2011\)](#), the sail under consideration was a wingsail 50 m in span, 20 m in chord length and its wing section was a NACA 0021 profile. The rig was composed of three of such sails set 23.6 m apart from one another. Wind-tunnel experiments were carried out on a 1:100 scale model and the forces were measured on each sail. The apparent wind angles tested varied between 30° and 150° and the angle of attack (AOA) of the three wingsails was kept constant for all conditions at $AOA = 15^\circ$. In these conditions, the authors found that the upstream wingsail increased its lift compared to the single wingsail up to $AWA = 60^\circ$, whereas the second and third sails decreased their performance due to the aerodynamic interaction. For larger apparent wind angles, all sails showed a lower lift coefficient compared to the single sail. To understand the effect of the trim angle on the performance of each sail, the authors also tested two wingsails set at different angles of attack. Interesting to mention is the case in which the apparent wind angle was $AWA = 30^\circ$ and the sails were set at $AOA = 15^\circ$ (upstream sail) and $AOA = 20^\circ$ (downstream sail). In this condition, both sails showed an increase in lift compared to the single sail set respectively at the same angle of attack. Unfortunately, no results were reported about the change in drag.

In the work of [Li et al. \(2015\)](#), the sail design was improved to a wingsail with a foldable flap named “Variable-Camber Sail”. Once again, three identical sails were tested, this time at three different distances between them, namely 1, 1.5 and 2 chord lengths. The apparent wind angles tested ranged from 30° to 150° and the angle of attack of each sail was first set the same and then set to maximize the driving force coefficient of the

whole sail cascade. The results show that the distance between the sails play a key role in the way the aerodynamic interaction affects the sail performance and that the thrust generated by the sail cascade is improved when each sail is trimmed independently. Nonetheless, considering the same conditions, the performance of the sail cascade is still worse than the single sail in terms of driving force coefficient even when the sail trim is optimized,

The works of Jo et al. (2013) and Lee et al. (2016) are also related to the sail cascade concept proposed in the “Wind Challenger” project. In these studies, the authors made use of a CFD code connected to a genetic algorithm to optimize the angle of attack, the flap length and the flap deflection angle of three identical wingsails set 1.5 chord lengths apart. As reference case the wingsails were all set at the same angle of attack and the results of the optimization referred to such condition. Compared to the reference case, the optimized wingsails were modified to increase their lift while preventing flow separation. For example, for $AWA = 45^\circ$, the results of the optimization process show how the angle of attack, the flap length and flap deflection angle increases moving from the upstream sail to the downstream one. The optimization process does increase the thrust generated by the sail cascade compared to the reference case, but it is still worse than the single wingsail.

The output of the studies above summarized indicates that the aerodynamic interaction occurring between two or more sails might strongly affect the performance of the whole sail plan. Moreover, the same studies suggest that design parameters such as the number of sails and their gap distance and relative position, and operational parameters such as the apparent wind angle and the sail trim, play a fundamental role in the determination of the strength of the interaction effects and whether they have a positive or negative influence on the performance.

The work presented in this chapter deals with the aerodynamic interaction of two similar rigid sails exposed at apparent wind angles covering the typical range of sailing conditions of a ship ($AWA = 20^\circ - 180^\circ$). For similar conditions, the lift and drag forces, as well as the pressure measured on each sail, were compared with the results of measurements carried out on an analogous single sail. These results are eventually used to compare the performance, expressed in terms of driving and heeling force coefficients, of a “ship” equipped with one or two rigid sails.

In the framework of this doctoral dissertation, the scope of the present experiments is twofold. In the first place, the purpose is to gain a better understanding of the physics of the sail aerodynamic interaction. Secondly, considering the aim of the Sail Assist project, the purpose is to gather useful data to build the aerodynamic module of the Performance Prediction Program. In this respect, the data obtained during this experimental campaign are used to validate a simple aerodynamic model based on the horseshoe vortex method to predict the effects of the aerodynamic interaction on the performance of multiple sails (see Chapter 6).

3.2. SAIL DESIGN AND EXPERIMENTAL METHOD

The sail type chosen for the experiments is a square sail mounted on a self-standing mast with horizontal yards commonly referred to as Dynarig (Figure 3.1). The reason for choosing this type of sail is that it became one popular option for wind-assisted ship

propulsion due to its ease of operation. In fact, differently from soft sails typically employed on sailing yachts, the Dynarig allows for only one trimming option: the rotation about its vertical axis in order to change its angle of attack with respect to the wind.



Figure 3.1: Sail model used during the experiments

The span of the chosen sail is $H = 1.3$ m, its chord length is $c = 0.7$ m, (leading to an aspect ratio $AR = 1.85$) and its camber is 10%. The total height of the sail, including the mast, is 1.5 m. The sails were manufactured using carbon fibre sandwich, making it a rigid construction. Although full-scale Dynarigs are made of soft sails, the sails are constrained to the yards in such a way that deformations in terms of sail camber are minimized. Under high loads, other deformations like mast bending and torsion might occur, but otherwise, the carbon-fibre model and a full-scale Dynarig can be considered to behave similarly.



Figure 3.2: Assembly of the pressure taps in the sail

Within the two outer carbon fibre skins, in the core of the sail, 128 pressure taps were located (Figure 3.2). Each pressure tap had two holes, one on each side of the sail, allowing to measure the pressure at the extrados (low pressure side of the sail) and the intrados

(high pressure side of the sail) simultaneously. Due to the presence of the inner pressure taps, the thickness of the sail reached 10 mm. Although its edges were smoothed to compensate as much as possible its oversized dimension, it is conceivable that it had a negative effect on the performance of the single sail compared to soft-sail Dynarigs. More specifically, it is likely that for small angles of attack the larger thickness of the sail might cause leading edge separation to occur and that would reduce the suction area on the extrados of the sail. This issue was not further analysed since the present research focuses on sail interaction rather than on the performance of the single sail.

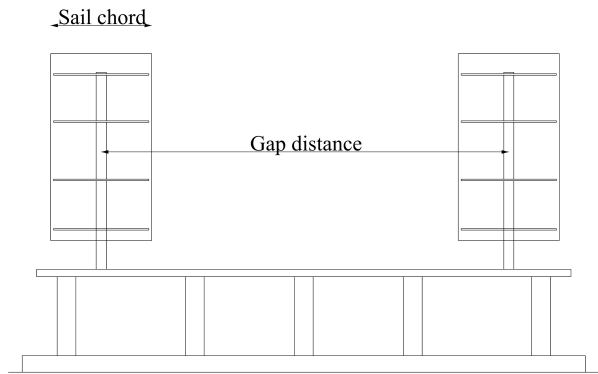


Figure 3.3: The gap distance (GD) is here defined as the horizontal distance between the two sail masts' vertical axis expressed in terms of sail chord c .

The pressure taps were divided into eight rows, i.e. sixteen taps per row, and they were more densely distributed at the leading and at the trailing edge as well as at the top and at the bottom of the sail (see Figure 3.2). The diameter of the mast was oversized to allow to accommodate all the pressure-tap tubes in its interior.

Considering the scarcity of published results on the topic of sail interaction on board of wind-assisted ships, it was decided to carry out wind-tunnel experiments keeping the number of sails to the minimum (two sails) and to investigate the influence of only one design parameter on the results. The design parameter that was deemed more interesting to be studied was the sail gap distance, that is the horizontal distance between the two sail masts' vertical axis (Figure 3.3) expressed in terms of sail chords. The single-sail experiments, used as the reference for the two-sail tests, included the test of the single Dynarig at angles of attack ranging from 0° to 90° . Conversely, in the two-sail experiments, the Dynarigs were aligned on a table that mimicked the ship's deck and they were trimmed independently to maximize the driving force of the whole sail plan. This procedure was repeated for apparent wind angles varying between 20° to 180° and for two different gap distances between the sails.

To better understand the nature of the interaction effects, during the single-sail experiments, the velocity field past the single Dynarig was measured for various conditions. The tests were conducted using four Cobra Probes mounted on a vertical bar at different heights from the ground (Figure 3.4). The Cobra Probe is a multi-hole pressure probe capable to measure the three velocity components within an angle of $\pm 45^\circ$ at a

frequency of 2000 Hz. The vertical bar on which the probes were installed could displace laterally to a maximum of ± 1.5 m from the Dynarig's vertical axis of symmetry. Tests were carried out for three angles of attack, $AOA = 5^\circ, 45^\circ, 90^\circ$, and for three distances, namely 1.5, 2.5 and 4 chord lengths downstream the sail.

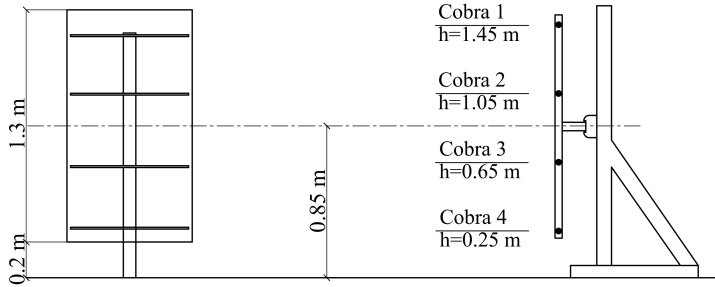


Figure 3.4: Position of the Cobra Probes with respect to the single Dynarig

3.3. TEST SETUP

The experiments were carried out in the boundary-layer test section of the Polytechnic University of Milan wind tunnel. The test section is 13.84 m wide and 3.84 m high (Figure 3.6) and the maximum reachable wind speed is 16 m/s.

The test section has a large turntable of 13 m diameter that can be manually adjusted to change the angle of incidence of the tested model. For the single-sail experiments, the Dynarig was positioned in the middle of the turntable and it was mounted on a balance fixed to a platform laying below the wind-tunnel floor in such a way that the total height of the sail from the floor was 1.5 m (Figure 3.5). Rigid aluminum foils were used to cover the hole in the floor to prevent air leakage (see Figure 3.1).

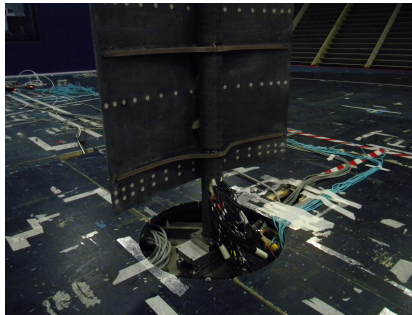


Figure 3.5: Single sail mounted on the force balance

For the two-sail experiments, a different setup was adopted. The two sails were mounted on a table that was positioned in the centre of the wind-tunnel turntable (Figure 3.6). Each sail was mounted on an independent balance that was connected to

an electric engine that was remotely controlled to rotate each sail around its vertical axis. Similarly to the single-sail setup, also in this case the sails were mounted in such a manner that the total height of the sails from the table was 1.5 m.

The balance used throughout the experiments was a RUAG 192 whose design loads are: $F_{(X)} = 1500$ N, $F_{(Y)} = 1000$ N, $F_{(Z)} = 5000$ N, $M_{(X)} = 500$ Nm, $M_{(Y)} = 1000$ Nm and $M_{(Z)} = 600$ Nm. In both the single-sail and the two-sail experiments the X -axis of the balance was aligned with the sail's chord while the Y -axis was perpendicular to it. The Z -axis of the balance was positive pointing upwards.

All the experiments were carried out at a nominal wind speed of $V = 10$ m/s, however, during the single-sail experiments, two different wind speeds ($V = 6$ m/s and $V = 12$ m/s) were also tested to check the influence of the Reynolds number on the lift and drag forces generated by the sail. This procedure was repeated for angles of attack $AOA = 5^\circ$, $AOA = 45^\circ$ and $AOA = 90^\circ$. The three chosen wind speeds correspond to Reynolds numbers $Re = 2.8 \cdot 10^5$ ($V = 6$ m/s), $Re = 4.7 \cdot 10^5$ ($V = 10$ m/s) and $Re = 5.6 \cdot 10^5$ ($V = 12$ m/s).



Figure 3.6: Two-sail arrangement mounted on the wind-tunnel turntable

The declared boundary-layer height of the wind tunnel is 0.2 m and the turbulence intensity index is $I_u = 2\%$. Before the beginning of the experiments, however, four Cobra Probes were placed in the centre of the wind-tunnel turntable in order to check these quantities. The probes were mounted on a vertical support as described in Section 3.2. The difference in mean longitudinal velocity between the lowest (0.25 m) and uppermost (1.45 m) probe was found to be 7% whereas the difference between the uppermost probe with respect to the second (0.65 m) and third (1.05 m) probe from the ground was 1% and 3% respectively. This indicates that the measured wind-tunnel boundary-layer height was slightly larger than the declared one, but nevertheless comparable to the height of the mast of the single Dynarig measured from the wind-tunnel floor to the bottom of sail planform (0.2 m). It can be concluded that during the single-sail and the two-sail experiments the Dynarigs were tested in a comparable wind profile. Furthermore, the values of turbulence intensity measured by the four probes were: $I_u = 1.99\%$ (at 0.25 m), $I_u = 1.55\%$ (at 0.65 m), $I_u = 1.23\%$ (at 1.05 m) and $I_u = 1.19\%$ (at 1.45 m). This leads to an averaged turbulence intensity index $I_u = 1.49\%$, that is slightly lower than the declared one.

Given the Dynarig sail area (0.91 m²) and the wind tunnel cross-section area (53.14

m²), the blockage ratio was 1.71% for the single-sail tests and 3.42% for the two-sail tests. For both cases, the blockage ratio was deemed small enough not to adopt any correction factor.

The experiments of the single Dynarig began starting with the angle of attack $AOA = 0^\circ$ and after every run, the angle of attack of the sail was increased by manually turning the wind-tunnel turntable. During this operation, the wind was switched off. Before and after every run, zero measurements (wind switched off) were taken. The two zero-measurements were then averaged and subtracted from the measurements taken during each corresponding run. For each angle of attack, the forces and the pressures on the sail were recorded during 60 seconds at a sampling frequency of 500 Hz, leading to 30000 samplings per run. The air temperature and the air density were constantly recorded during the experiments. The wind speed was measured by two different pitot tubes, one fixed to the wind-tunnel ceiling and one positioned in front of the turntable (Figure 3.6). The pitot tubes had a vertical distance of 1.0 m and 1.2 m from the ground and the ceiling respectively. The wind speed used to calculate the force and pressure coefficients was the average of these two measurements. The single Dynarig was tested at the following angles of attack: $AOA = 0^\circ, 2.5^\circ, 5^\circ, 7.5^\circ, 10^\circ, 12.5^\circ, 15^\circ, 17.5^\circ, 20^\circ, 22.5^\circ, 25^\circ, 30^\circ, 35^\circ, 40^\circ, 45^\circ, 50^\circ, 60^\circ, 70^\circ, 80^\circ, 90^\circ$. For the two-sail experiments, a different procedure was used. First, the wind-tunnel turntable was rotated to the desired angle of incidence that, in fact, corresponds to the apparent wind angle the ship would sail at.

For each apparent wind angle, the sails were remotely trimmed via a computer connected to the electric engines used to rotate the balances and the sails bolted on top of them. The computer was placed in the control room outside the wind tunnel and it displayed in real time the nominal angle of attack, the lift and drag forces and the driving and heeling forces of each sail. After having switched the wind on, the sails were trimmed in an iterative process: first, the trim of the upstream sail was adjusted to maximize its driving force, subsequently the same was done with the downstream sail. Before taking the measurement, the trim of both sails was carefully perfected to check whether the driving force of the whole sail plan could be further increased. A wool tell-tale placed at half-span at the trailing edge of each Dynarig helped during the trimming process of the sails. Once the sails were deemed properly trimmed, the forces and the pressures on each Dynarig were measured in the same manner used for the single-sail tests. The two-sail arrangement was tested at the following apparent wind angles: $AWA = 20^\circ, 30^\circ, 35^\circ, 45^\circ, 60^\circ, 75^\circ, 90^\circ, 105^\circ, 120^\circ, 135^\circ, 150^\circ, 165^\circ, 180^\circ$. For each apparent wind angle, the experiments were carried out at two different gap distances between the sails, namely 2.5 chord lengths (i.e. 1.75 m) and 4 chord lengths (i.e. 2.8 m).

3.4. RESULTS

The measurement uncertainties relative to the results presented in this chapter can be found in Appendix A.2.

3.4.1. REYNOLDS NUMBER EFFECT ON SINGLE SAIL PERFORMANCE

The study of the influence of the Reynolds number on the lift and drag coefficients of the single Dynarig is reported in Figure 3.7.

In this chapter, the Dynarig lift and drag coefficients are defined as:

$$C_L = \frac{F_L}{\frac{1}{2} \cdot \rho \cdot A \cdot V^2} \quad (3.1)$$

$$C_D = \frac{F_D}{\frac{1}{2} \cdot \rho \cdot A \cdot V^2} \quad (3.2)$$

where F_L and F_D are, respectively, the lift and drag force, ρ is the air density, A is the projected area of the Dynarig's planform ($A = H \cdot c$) and V is the wind speed.

The Reynolds number (here based on the sail chord length) was decreased by 40% and increased by 20% respect to the reference Reynolds number ($Re = 4.7 \cdot 10^5$) corresponding to the nominal wind speed of 10 m/s. The results show that the effect of increasing or decreasing the Reynolds number does not significantly affect the lift and the drag coefficients. Although these results indicate that the influence of the Reynolds number on the aerodynamic performance of the Dynarig is negligible, it should be considered that the full-scale Reynolds number is expected to be about 20 times larger the model-scale Reynolds number and this might lead to some deviations from the experimental results in terms of both single sail and multiple sail performance.

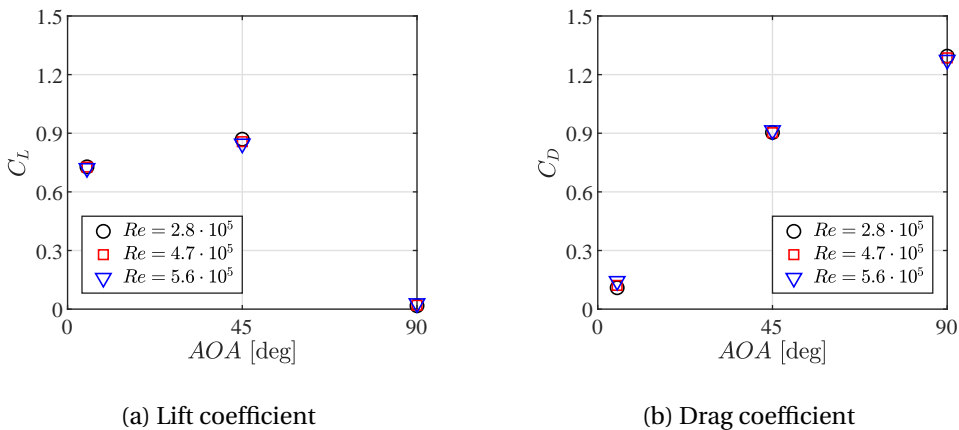


Figure 3.7: Influence of the Reynolds number on the single Dynarig lift and drag coefficient

3.4.2. MEASUREMENTS OF THE VELOCITY FIELD PAST THE DYNARIG

The results of the velocity field measurements past the single Dynarig are reported given in Figure 3.8. For the sake of conciseness, only the results of Cobra Probe 2 are provided herewith. The results of Cobra Probe 2 and Cobra Probe 3, in fact, show a similar trend and they can be considered representative for most of the sail plan. Cobra Probe 1 and Cobra Probe 4, on the other hand, captured a more peculiar trend due to their position closer to the sail top and bottom tip vortices (see Figure 3.4). The full velocity field measurements can be found in Appendix A.1.

Figure 3.8 illustrates the mean velocity magnitude and the mean direction of the flow. The velocity magnitude, that is normalized with the free stream velocity, is indicated by

the colourmap and the vector size. Conversely, the direction of the flow is suggested by the vector orientation. The results are given in terms of longitudinal (X -axis) and transversal (Y -axis) distance from the Dynarig's vertical axis of symmetry, normalized with the sail chord length.

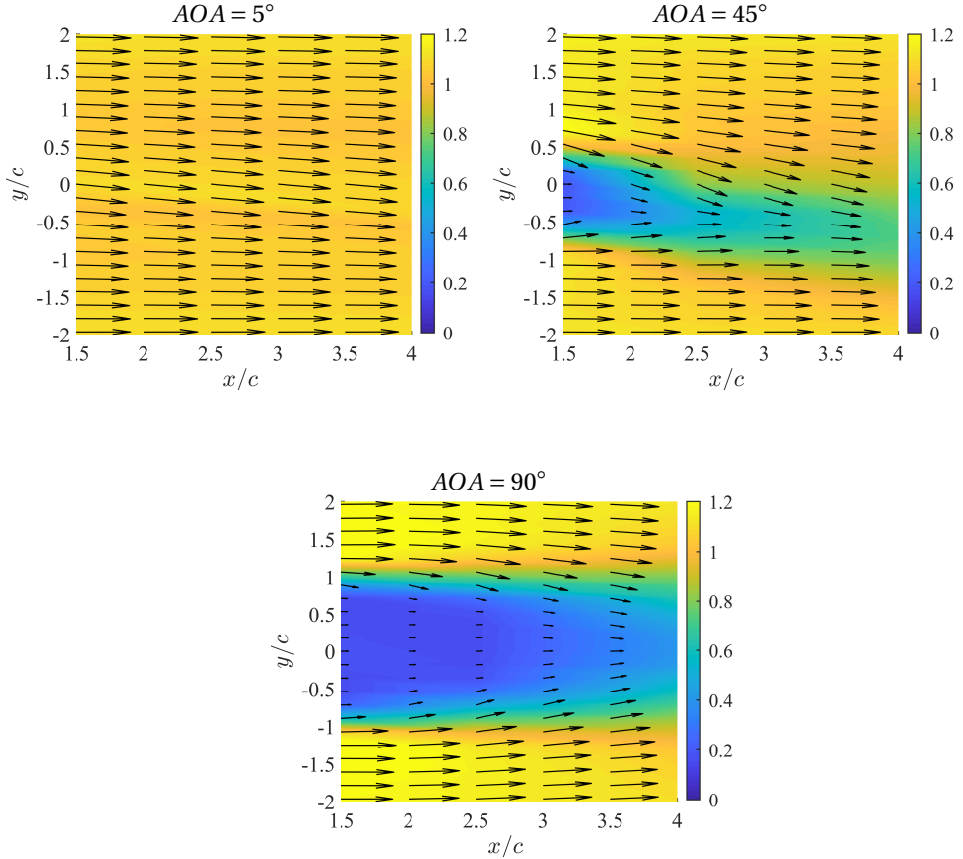


Figure 3.8: Velocity field past the Dynarig at different angles of attack. Measurements of Cobra probe 2 taken at a height of 1.05 m from the ground. The results show the velocity field in a plane parallel to the floor

The results of the investigation show that for $AOA = 5^\circ$ the most noticeable effect is a moderate change of the flow direction while a limited wake is measured. For this condition, in fact, the flow over the sail is predominantly attached so that the lift, that is directly dependent on the circulation (that is the cause of the change in flow direction), is dominant. At $AOA = 45^\circ$, on the other hand, the lift and drag generated by the Dynarig are equally relevant and this reflects on the velocity field in two ways: the flow is largely deviated (due to the circulation) and it presents a large area in which it is decelerated (due to the flow separation on the sail). Lastly, at angle of attack $AOA = 90^\circ$, the sail is fully stalled and this causes a strong flow speed reduction directly downstream the Dynarig.

Although these results only cover a limited number of angles of attack, and no measurements were taken upstream the Dynarig, they nevertheless can be used to support the analysis of the force measurements carried out in the following section of the present work.

3.4.3. INTERACTION: FORCE MEASUREMENTS

The forces measured during the experiments had to be transformed from the balance reference system into lift and drag and, successively, into driving and heeling force. To do so, the nominal angle of attack, i.e. the angle of attack of the sail with respect to the undisturbed flow, had to be derived from the apparent wind angle, that is the angular position of the turntable with respect to the wind direction, and the brace angle, that is the angular position recorded by the electric engines and it is the angle of the sail chord with respect to the central axis of the “ship” (Figure 3.9). The actual angle of attack of the sails, i.e. the angle of attack considering the effects of upwash and downwash on the local velocity field, is unknown.

The driving force (F_X) was considered to be aligned with the central axis of the “ship” and positive pointing towards its bow. On the other hand, the heeling force (F_Y) was perpendicular to the central axis of such ship and positive pointing towards starboard (Figure 3.9). The driving and heeling force coefficients were derived according to:

$$C_X = \frac{F_X}{\frac{1}{2} \cdot \rho \cdot A \cdot V^2} \quad (3.3)$$

$$C_Y = \frac{F_Y}{\frac{1}{2} \cdot \rho \cdot A \cdot V^2} \quad (3.4)$$

The wind speed V used to calculate the non-dimensional coefficients was the averaged wind speed measured by the ground pitot tube and by the ceiling pitot tube during each run. On average, the wind speed measured by ground pitot tube was 1% higher than the wind speed measured by the pitot tube fixed to the wind-tunnel ceiling and the lowest and highest wind speeds measured during the whole experimental campaign were $V = 10.00$ m/s (ground pitot tube) and $V = 10.16$ m/s (ceiling pitot tube) respectively. Likewise, the air density ρ measured during each test was used for the calculations.

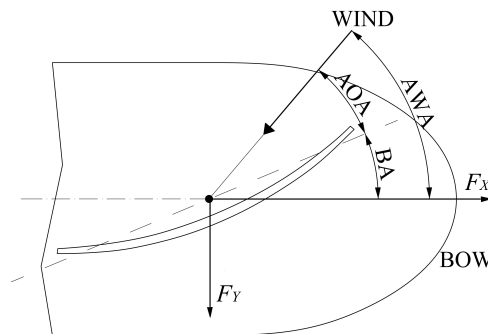


Figure 3.9: Apparent Wind Angle (AWA), Brace Angle (BA) and Angle of Attack (AOA). The direction of the driving (F_X) and heeling (F_Y) force is also indicated.

The results of the nominal angles of attack for all considered apparent wind angles and for gap distances 2.5 and 4 chord lengths are reported in Figure 3.10. For the same gap distance, the results show how, in general, the sails were set at different angles of attack. More precisely, up to $AWA = 120^\circ$, the stern sail (Dynarig at the stern of the “ship”) is trimmed at larger angles of attack to compensate the effects of the downwash (reduction in apparent wind angle) generated by the bow sail (Dynarig at the bow of the “ship”). This trend, clearly visible for gap distance 2.5, it becomes less noticeable when the gap distance between the sails is increased to 4 chord lengths. This indicates that the effect of the downwash becomes less pronounced with the increase of the separation between the sails.

For both gap distances analysed, the bow and the stern sails are trimmed at moderate angles of attack up to $AWA = 120^\circ$. This means that up to such apparent wind angle the flow on the sails is predominantly attached and that most of the driving force is generated by the lift. From $AWA = 135^\circ$, the angle of attack of both sails rapidly increases and at $AWA = 180^\circ$ it reaches the value of $AOA = 90^\circ$: the ship is sailing fully downwind and the sails are set perpendicular to the wind direction. For this range of apparent wind angles, flow separation plays a fundamental role and the driving force is generated almost exclusively by the drag.

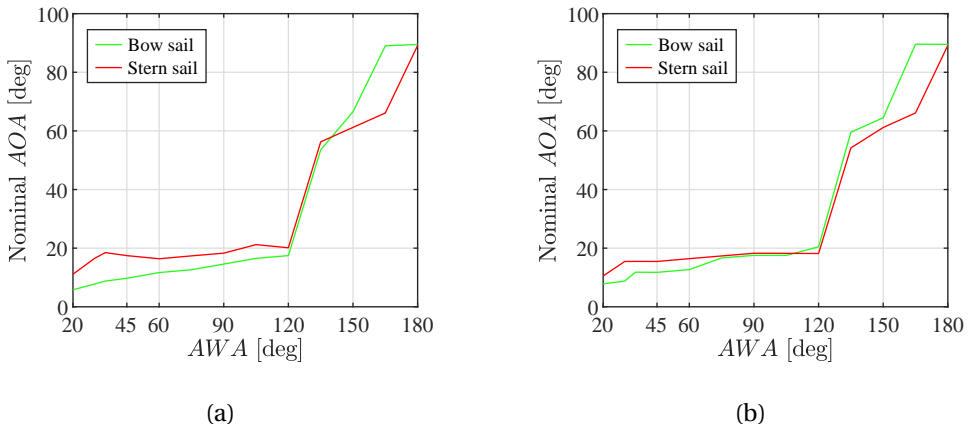


Figure 3.10: Nominal angles of attack. Gap distance $GD = 2.5$ (a) and $GD = 4$ (b)

The results obtained during the two-sail experiments were compared with the results of the single-sail tests in terms of lift and drag and in terms of driving force and heeling force, generated at the same nominal angle of attack. The nominal angles of attack given in Figure 3.10 were used to linearly interpolate the results of the single-sail tests to derive the values of lift and drag corresponding to the desired angles and, consequently, the driving and heeling force were calculated. Using this procedure, a fair comparison between the results of the single-sail experiments and the results of the two-sail experiments could be achieved.

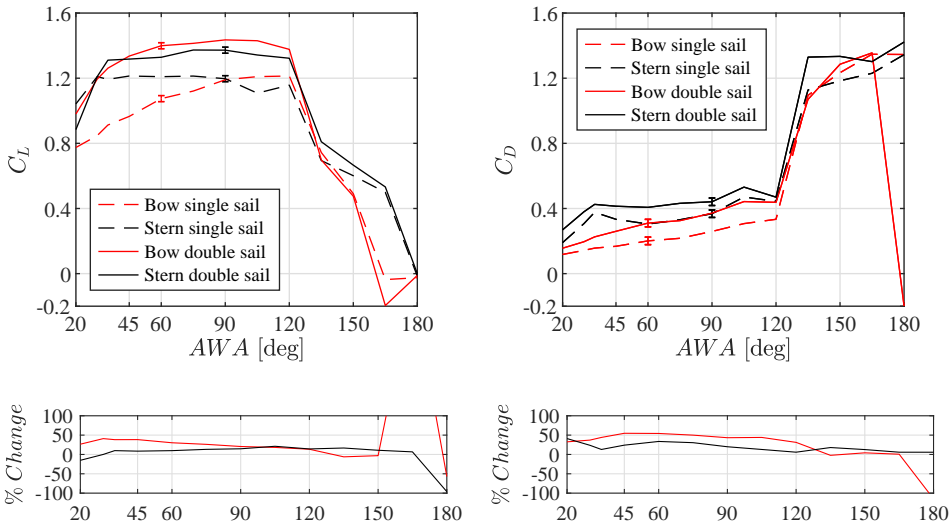


Figure 3.11: Lift and drag coefficients (top) and the percentage change of the double Dynarig results with respect to the single Dynarig (bottom). Gap distance $GD = 2.5$

In Figure 3.11 the lift and drag coefficients of the single-sail and of the two-sail experiments, obtained during the tests with a gap distance of 2.5 chord lengths, are given. In general, there is a considerable difference between the coefficients of the two-sail arrangement compared to their single-sail counterparts. More precisely the following differences are identified.

- For $AWA = 20^\circ$, C_L of the stern sail (two-sail arrangement) is smaller than C_L of the corresponding single sail. This effect is arguably due to the unfavourable downwash (reduction in angle of attack) caused by the bow Dynarig (see Figure 3.8, $AOA = 5^\circ$).
- In the range $35^\circ < AWA < 120^\circ$, the two sails tend to be no longer in each other's wake. In this condition, they experience the effect of the circulation on the flow, i.e. a change in flow angle and an increase in flow speed. This change causes an increase in lift and drag of both sails.
- For $135^\circ < AWA < 180^\circ$, it is more difficult to identify a clear trend, although it appears that the drag generated by the stern sail, that for this range of apparent wind angles is the upstream sail, is moderately increased.
- At $AWA = 180^\circ$, both sails are set at $AOA = 90^\circ$, i.e. they are perpendicular to the wind direction to maximize their drag. In this situation, the flow separates and recirculates and this causes the bow Dynarig (that for this AWA is the downstream sail) to generate a negative drag force. In Figure 3.8, $AOA = 90^\circ$, the recirculating flow cannot be appreciated since negative longitudinal flow velocities cannot be measured by the Cobra Probe.

The effects caused by the aerodynamic interaction on the lift and drag generated by the two sails also affect their driving and heeling force. Apart for $AWA \leq 30^\circ$ and $AWA = 180^\circ$, at which the downstream sail is penalized for being in the wake of the upstream one, for all the other angles, both sails show an increase in driving force due to the positive effect of their aerodynamic interaction (Figure 3.12).

As reported in Figure 3.12, for apparent wind angles between $AWA = 20^\circ$ and $AWA = 75^\circ$, the bow Dynarig increased its driving force up to 40% and in the range $90^\circ < AWA < 120^\circ$, the sails show a similar increase of about 15-20%. Regarding the heeling force, in the range of apparent wind angles in which it plays a significant role in the sailing behaviour of a ship ($20^\circ < AWA \approx 100^\circ$), the aerodynamic interaction between the two sails has the effect of increasing C_Y , being the heeling force generated by the stern Dynarig at $AWA = 20^\circ$ the only exception (Figure 3.12).

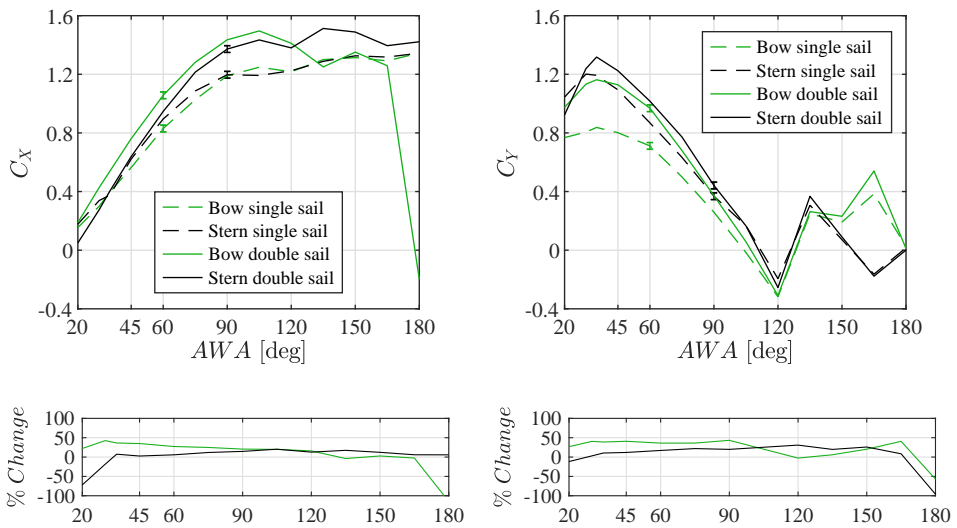


Figure 3.12: Driving and heeling force coefficients (top) and the percentage change of the double Dynarig results with respect to the single Dynarig (bottom). Gap distance $GD = 2.5$

In Figure 3.13 the results of the lift and drag coefficients obtained at the larger gap distance are presented. In general, the results follow the same trend evidenced for the shorter gap distance, nevertheless, a few differences should be mentioned.

- In the range $75^\circ < AWA < 105^\circ$, there is practically no difference between the lift coefficients of the stern and bow sail. The same holds true for the drag coefficients. However, the coefficients of the two-sail arrangement are larger than their single-sail counterparts. This result indicates that both sails are affected by the aerodynamic interaction to a similar extent.
- At $AWA = 180^\circ$, due to the larger gap distance, the effects of flow separation and recirculation are strongly reduced. The bow sail is able to generate a positive drag force although it is still considerably lower than the force produced by the stern sail.

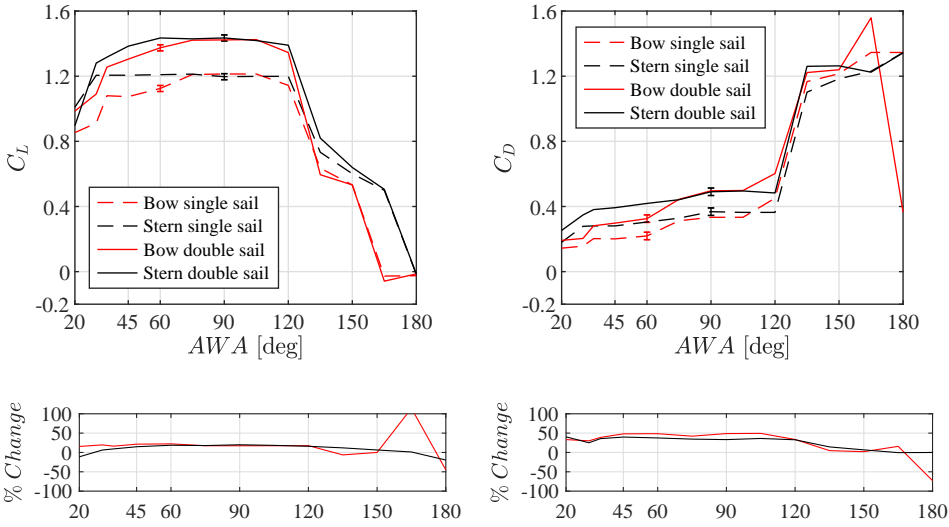


Figure 3.13: Lift and drag coefficients (top) and the percentage change of the double Dynarig results with respect to the single Dynarig (bottom). Gap distance $GD = 4$

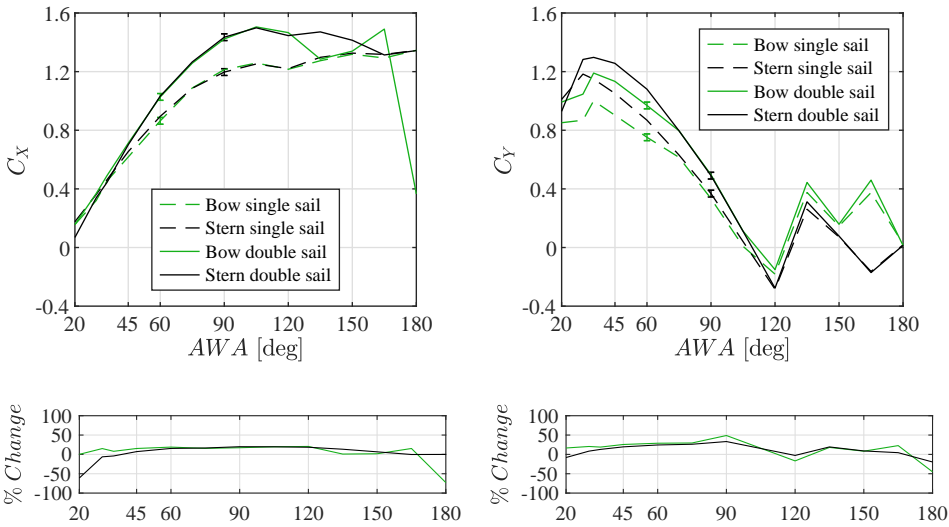


Figure 3.14: Driving and heeling force coefficients (top) and the percentage change of the double Dynarig results with respect to the single Dynarig (bottom). Gap distance $GD = 4$

The differences above discussed also reflect in the driving and heeling force coefficients. The results reported in Figure 3.14 show how for apparent wind angles varying from 75° to 105° there is practically no difference in C_X and C_Y of the bow and the stern sail respectively. The results of the percentage change reported in Figure 3.14 also indicate that the effects caused by the aerodynamic interaction are attenuated by the

increased gap distance. In fact, for $20^\circ < AWA < 45^\circ$, the downstream sail benefits from a reduced wake (likewise it occurs for $AWA = 180^\circ$). However, at the same time, the upstream sail experiences a weakened upwash, leading to a lower increase in driving force compared to the single sail. Finally, similarly to the shorter gap distance, in the range $75^\circ < AWA < 120^\circ$ it appears that C_X of the bow and stern sail are equally increased by about 15 – 20% compared to the single sail.

3.4.4. INTERACTION: PRESSURE MEASUREMENTS

During the experiments, pressure measurements were taken along with the force measurements discussed in Section 3.4.3. The pressure was measured at the intrados and at the extrados of the sails at the positions indicated in Figure 3.15. For the sake of conciseness, only the results of the pressure taps of row 5 (see Figure 3.15) are herewith discussed. The sixteen pressure taps of row 5 were located about 120 mm below half sail span and, apart from the rows at the upper and lower edges of the sail that were influenced by the tip vortices, the pressure distribution at the selected row could be deemed representative of most of the sail planform.

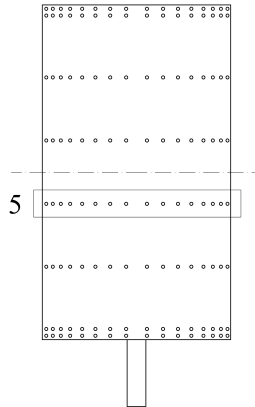


Figure 3.15: Distribution of the pressure taps on the Dynarig

The pressure distribution over the single sail and over the two sails of the double-Dynarig arrangement was compared in terms of pressure coefficient. The results of C_p were plotted against the non-dimensional position along the chord length x/c , being $x/c = 0$ the leading edge and $x/c = 1$ the trailing edge of the sail. Let p being the measured pressure, the pressure coefficient is defined as:

$$C_p = \frac{p}{\frac{1}{2} \cdot \rho \cdot V^2} \quad (3.5)$$

A comparison between the pressure measurements taken during the single-sail tests and during the two-sail tests was possible only for a limited number of cases. In fact, differently from the force measurements for which the results of the single Dynarig were linearly interpolated to find values of lift and drag at the required nominal angles of

attack, it is not a standard procedure to interpolate the results of the pressure distributions. Thus, a fair analysis could only be accomplished when the single sail and the bow and stern sail of the two-sail arrangement had a comparable nominal angle of attack. A selection of significant cases was elaborated and it is reported in Table 3.1.

Table 3.1: Pressure distribution comparison: cases analysed

Gap distance	AWA [deg]	AOA Bow		AOA Stern	
		Double sail	Single sail	Double sail	Single sail
		[deg]	[deg]	[deg]	[deg]
2.5	75	12.6	12.5	17.4	17.5
2.5	120	17.5	17.5	20.1	20.0
4	20	7.8	7.5	10.5	10.0
4	60	12.7	12.5	-	-
4	90	17.5	17.5	-	-
4	180	89.5	90.0	89.2	90.0

The results of the pressure distributions are given in Figure 3.16 to Figure 3.20 in order of increasing apparent wind angles. The results reported in Figure 3.17, Figure 3.18 and Figure 3.19 show the beneficial effects of the aerodynamic interaction on the bow and stern Dynarig for different apparent wind angles and for both the considered gap distances.

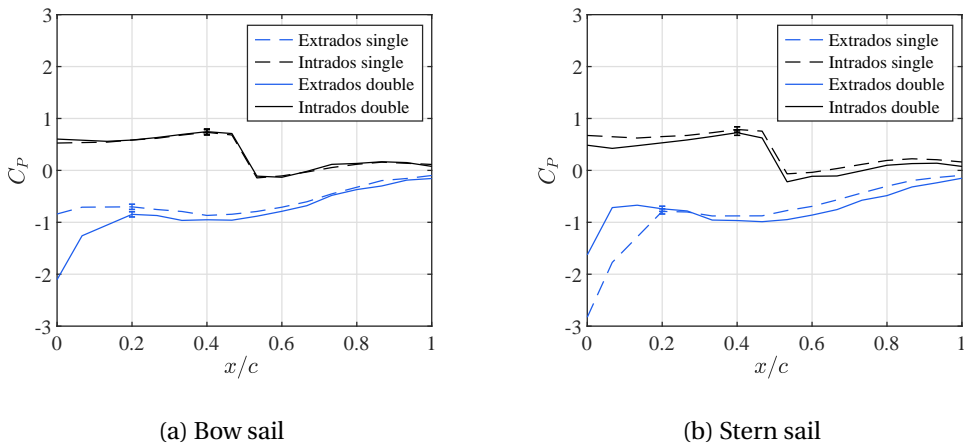


Figure 3.16: Difference in pressure distribution at $AWA = 20^\circ$. Gap distance $GD = 4$

The most significant result is the suction increase, i.e. a lower C_p , with respect to the single sail. It appears that for the stern Dynarig the suction increase predominantly occurs near the leading edge of the sail, whereas for the bow sail, it extends until the trailing edge. Following the reasoning of Gentry reported in the Section 3.1, the upwash generated by the stern Dynarig allows the upstream sail to be operated at a higher angle

of attack than it otherwise would by itself. Moreover, the upstream sail extrados experiences a flow speed increase caused by the downstream Dynarig, meaning that the Kutta condition at its trailing edge needs to be fulfilled at a higher speed, causing an efficiency increase of the whole sail. It must be remembered, however, that the analysis of Gentry referred to a mainsail and an overlapping jib of a sailing yacht, on the contrary, the sails herewith under consideration do not overlap but, instead, they are set 2.5 or even 4 chord lengths apart. This difference could limit the applicability of Gentry's theory to the present case.

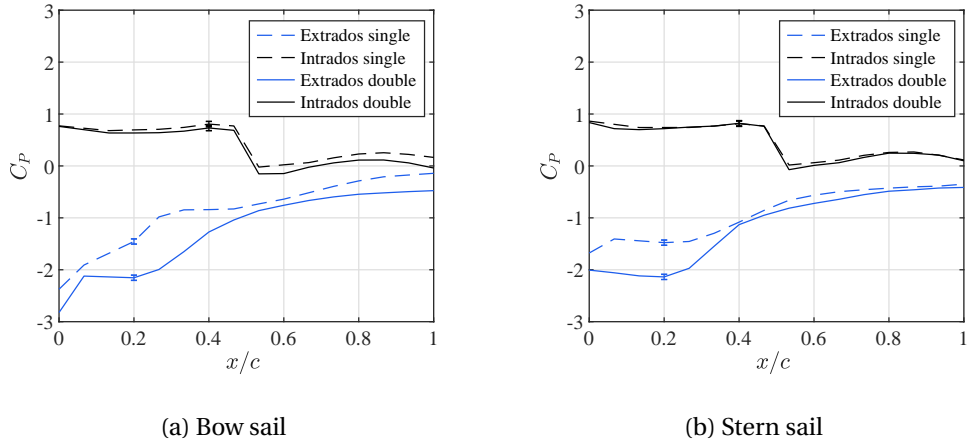


Figure 3.17: Difference in pressure distribution at $AWA = 75^\circ$. Gap distance $GD = 2.5$

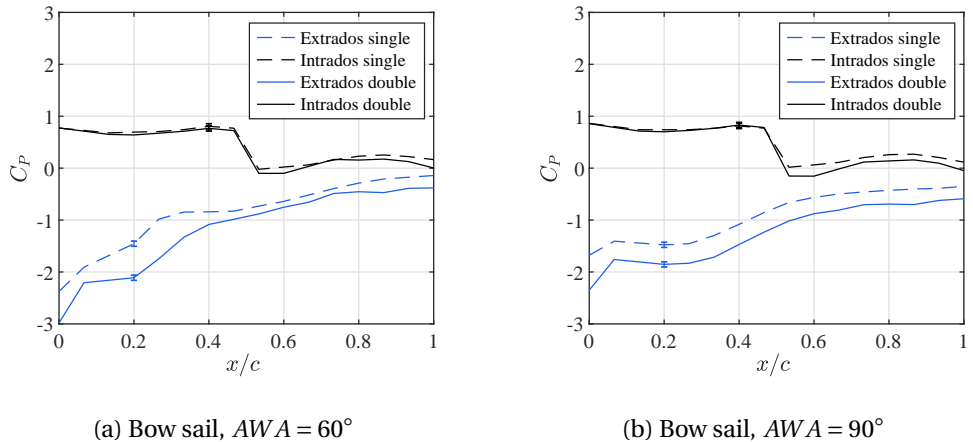


Figure 3.18: Difference in pressure distribution at $AWA = 60^\circ$ (a) and $AWA = 90^\circ$ (b). Gap distance $GD = 4$

Regarding the downstream Dynarig, the sail appears to benefit from the downwash and, arguably, the turbulence caused by the upstream sail. In fact, the leading-edge separation, that is visible in the single-sail results, appears to be strongly reduced.

At $AWA = 20^\circ$, a different condition is found. While the bow sail shows an increased leading edge suction peak compared to the single sail, the stern Dynarig appears to be adversely affected by the (small) wake and the disadvantageous downwash generated by the upstream sail (Figure 3.16). Another situation in which the interaction effects are detrimental for the downstream Dynarig occurs at $AWA = 180^\circ$. For this apparent wind angle, the flow separation and the wake generated by the upstream sail (the stern Dynarig in this case) causes the downstream (bow) sail to have a dramatic pressure decrease at its intrados. On the other hand, for the same apparent wind angle, the upstream sail is practically unaffected by the interaction effects (Figure 3.20).

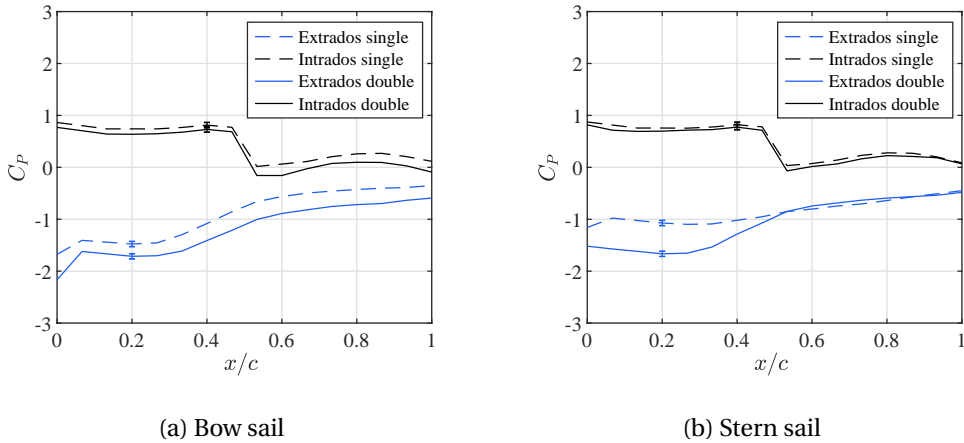


Figure 3.19: Difference in pressure distribution at $AWA = 120^\circ$. Gap distance $GD = 2.5$

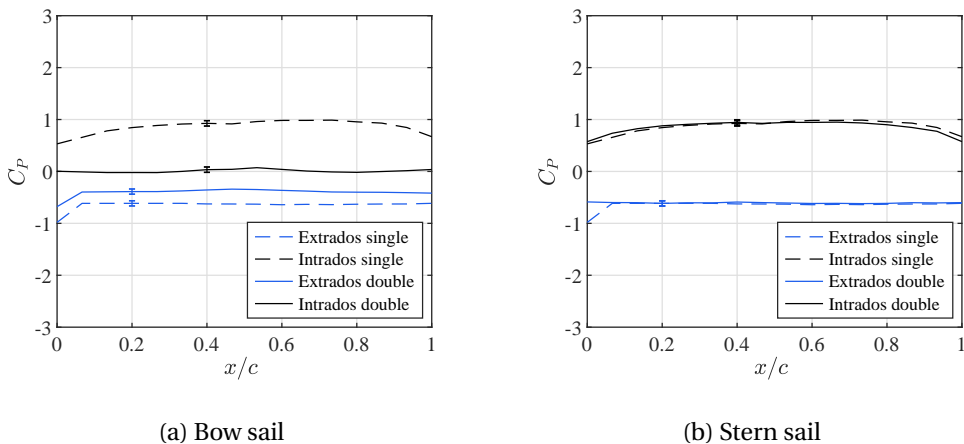


Figure 3.20: Difference in pressure distribution at $AWA = 180^\circ$. Gap distance $GD = 4$

Regarding the pressure distribution on the sail intrados, the abrupt pressure drop around $x/c=0.5$, that occurs for the cases reported in Figure 3.16, Figure 3.17, Figure 3.18,

Figure 3.19, is caused by the shielding effect of the sail mast on the nearby pressure taps. Moreover, up to an apparent wind angle of 120° , it seems that the pressure difference at the intrados between the single-sail and the double-sail results is considerably less pronounced compared to the differences measured at the sail extrados.

3.4.5. INTERACTION EFFECTS: SHIP PERFORMANCE

In Section 3.4.3 and Section 3.4.4 the bow and the stern Dynarig of the two-sail arrangement were compared to the single Dynarig to investigate the performance difference when the sails were set at the same nominal angle of attack. In the present section, the focus is on the performance difference between a ship equipped with two Dynarigs and a ship equipped with one Dynarig expressed in terms of driving and heeling force coefficients. To do so, the single sail had to be trimmed to maximize C_X for each apparent wind angle, meaning that the single Dynarig and the Dynarigs of the two-sail arrangement might be trimmed with different angles of attack. The single sail was virtually trimmed via a computer programme. In fact, for each apparent wind angle ($20^\circ < AWA < 180^\circ$), the driving force coefficient C_X was calculated for each pair of C_L and C_D values corresponding to all the angles of attack tested during the single-sail experiments ($0^\circ \leq AOA \leq 90^\circ$). This procedure led to a group of driving force coefficients among which the highest C_X was selected for each apparent wind angle. The heeling force coefficients were chosen accordingly. About the results of the two-sail arrangement, for each apparent wind angle, the results of C_X and C_Y of the two sails were respectively averaged to derive the driving and the heeling force coefficients of the whole sail plan. It must be pointed out that the performance comparison of the two “ships” herewith presented only comprises the differences due to the sail aerodynamic interaction. Any other difference that might occur on board of real ships is not taken into account.

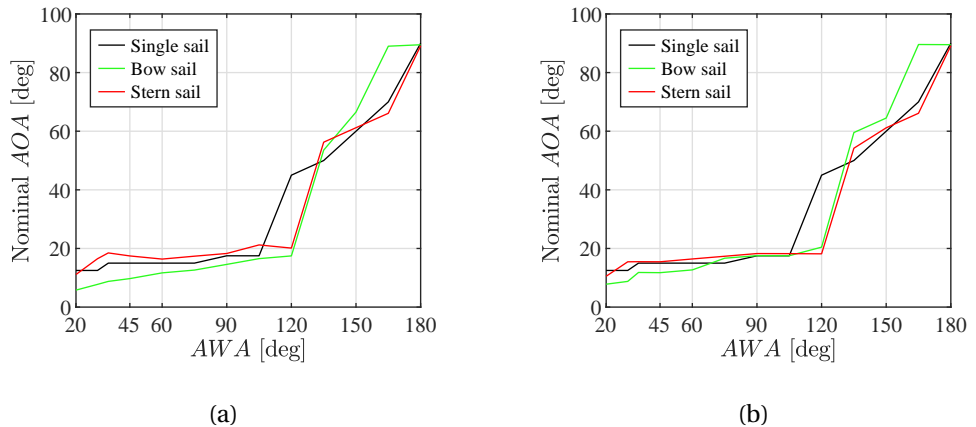


Figure 3.21: Double Dynarig vs Single Dynarig ship - nominal angles of attack. Gap distance $GD = 2.5$ (a) and $GD = 4$ (b)

In Figure 3.21 the nominal angles of attack of the sails of the single-Dynarig ship and double-Dynarig ship are presented for gap distance 2.5 and 4 chord lengths respectively.

For the shorter distance, it can be seen that for $30^\circ < AWA < 105^\circ$, the nominal angle of attack of the single Dynarig lays in between those of the bow and stern sail of the ship with two Dynarigs. When the gap distance is increased to 4 chord lengths, this trend becomes less visible and, for $75^\circ < AWA < 105^\circ$, there is practically no difference between the compared nominal angles of attack. The results here presented agree with the reasoning on the effects of upwash and downwash on the sail angles of attack elaborated in Section 3.4.3.

The comparison of the driving and heeling force coefficient of the ship with one Dynarig and the ship with two Dynarigs is depicted in Figure 3.22. In the interval $45^\circ \leq AWA \leq 165^\circ$, the two sails benefit from their aerodynamic interaction leading to an averaged C_X larger than the C_X of the single sail. More specifically, in the range $60^\circ \leq AWA \leq 120^\circ$, the ship with the sails set 4 chord lengths apart appears to have a somewhat larger C_X than the ship with the sails separated by the shorter distance. For $AWA < 35^\circ$ and $AWA = 180^\circ$, the aerodynamic interaction has a negative effect on the performance of the double-Dynarig ship that, in fact, it is outperformed by the ship equipped with one sail only. About the heeling force coefficient C_Y (Figure 3.22), a similar trend can be identified; in the range of apparent wind angles of interest (up to $AWA \approx 100^\circ$), the double-Dynarig ship has a larger C_Y than the ship with only one Dynarig, being the results of apparent wind angle $AWA = 20^\circ$ the only exception. It should be pointed out that the results of the percentage change relative to the heeling force coefficients were limited to $AWA = 90^\circ$ since the results obtained at larger apparent wind angles are of limited interest and out of scale for the type of graphical representation used (see Figure 3.22).

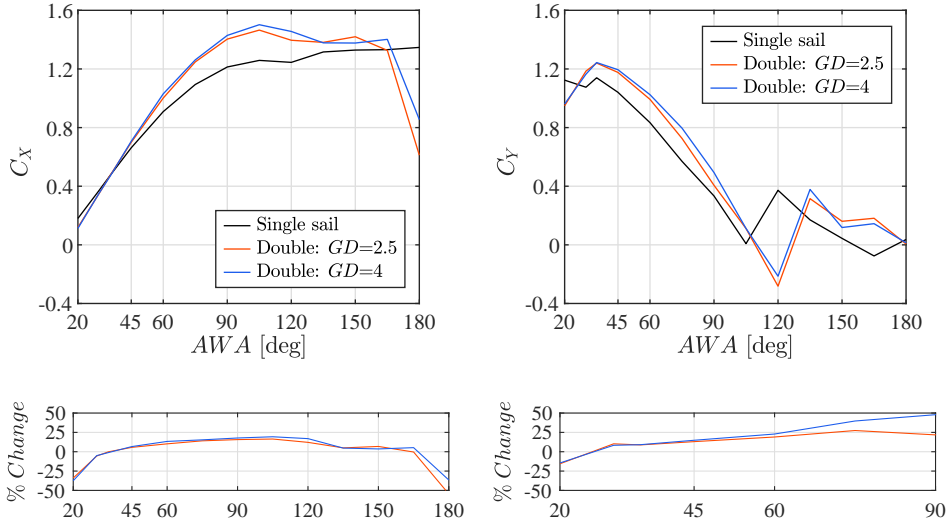


Figure 3.22: Double Dynarig vs Single Dynarig ship - driving and heeling force coefficients (top) and the relative percentage change (bottom)

In this section, the discussion about the performance of the ship with one Dynarig and of the ship with two Dynarigs was based on the driving force coefficient that each

rig was able to achieve in the wind conditions considered. Nonetheless, it should be mentioned that to conclude on which solution is the best in terms of ship performance, the heeling force and its effects on the sailing behaviour of the ship (e.g. heel angle and leeway angle) should also be taken into account. For this purpose, a thorough balance of all the aero/hydrodynamic forces acting on the ship should be evaluated.

3.5. CONCLUSIONS

The effects of the aerodynamic interaction occurring between two rigid sails were analysed by comparing the performance of a two-sail arrangement and a single sail. The performance difference was investigated for two gap distances between the sails and for apparent wind angles covering all typical sailing conditions. Two different methods were used for the comparison: in one case, the aerodynamic coefficients of the single sail were obtained at the same nominal angles of attack at which the two Dynarigs were trimmed during the experiments in order to maximise their driving force. In the other case, also the single sail was trimmed for the maximum driving force, leading to a performance comparison between two fictitious ships equipped with one and two Dynarigs respectively. Regardless of the method applied, for a large interval of apparent wind angles, both the bow and the stern sail of the two-Dynarig arrangement benefited from their aerodynamic interaction. This finding, validated with force and pressure measurements taken on each sail, is in agreement with the results relative to the interaction of two wingsails reported by [Nakashima et al. \(2011\)](#). Considering the outcome of the current research and the results of previous works, it can be concluded that the number of sails employed, and their gap distance, are key parameters in the determination of the effects of the aerodynamic interaction on the performance of multiple sails.

4

REYNOLDS NUMBER EFFECT ON FLETTNER ROTOR AERODYNAMIC PERFORMANCE

The Flettner rotor is attracting increasing attention as a viable technology for wind-assisted ship propulsion. Nonetheless, the influence of the Reynolds number on the aerodynamic performance of rotating cylinders is still unclear and under debate. The present chapter deals with a series of wind-tunnel experiments on a large-scale Flettner rotor in which the forces and pressures acting on the cylinder were measured for Reynolds numbers as large as $Re = 1.0 \cdot 10^6$. The rotating cylinder used in the experimental campaign had a diameter of 1.0 m and span of 3.73 m. The results indicate that the lift coefficient is only affected by the Reynolds number in the critical flow region and below velocity ratio $k = 2.5$. Conversely, in the velocity ratio range $1 < k < 2.5$, the drag coefficient is markedly influenced by the Reynolds number over the entire range of flow conditions analysed. The power consumption scales with the cube of the tangential velocity and it appears to be insensitive to the Reynolds number or whether the cylinder is spun in an air stream or in still air.

This chapter is based on the journal article: G. Bordogna, S. Muggiasca, S. Giappino, M. Belloli, J.A. Keuning, R.H.M. Huijsmans and A.P. van 't veer. Experiments on a Flettner rotor at critical and supercritical Reynolds numbers. *Journal of Wind Engineering and Industrial Aerodynamics*, 188:19-29, 2019.

4.1. INTRODUCTION

The Flettner rotor is a rotating cylinder that generates an aerodynamic lift due to the Magnus effect. Invented by German engineer Anton Flettner (Flettner, 1925), it was first used in 1925 onboard the *Backau* ship as a form of propulsion. The *Backau* was equipped with two Flettner rotors and it successfully completed its first voyage across the Atlantic in 1926. The same year, following the success of the first rotor ship, the *Barbara* was launched. The vessel had three Flettner rotors and it served as a freighter in the Mediterranean between 1926 and 1929. Despite the proven concept, the rotor ship was fast abandoned since it could not compete with the increasing adoption of diesel engines and with the low oil price of that time. In present years, however, the possibility to use wind energy as an auxiliary form of propulsion for commercial ships has again become of interest due to the volatile fuel prices and to the ever-stringent environmental regulations.

Since its inception the Flettner rotor was seldom used for real-life applications in the maritime field, nonetheless, the physical phenomena associated with rotating cylinders attracted the interest of many scientists over the years. Among the several parameters that were proven to affect the aerodynamic performance of a Flettner rotor (the velocity ratio, the aspect ratio, the use of endplates and the endplate's size), the influence of the Reynolds number is still a matter of debate as it emerges from the studies conducted on this topic until today.

Reid (1924) carried out a systematic series of experiments on a rotating cylinder of physical aspect ratio, $AR = 13$, without endplates, at Reynolds numbers varying between $Re = 3.9 \cdot 10^4$ and $Re = 1.1 \cdot 10^5$. The results of Reid (1924) indicate that for the range considered, the Reynolds number has a marginal influence on C_L and C_D . The work of Thom represents an important contribution to the research on Flettner rotors. The author, in fact, conducted a large series of force and pressure measurements of rotating cylinders, studying the influence of surface roughness, aspect ratio as well as endplates on the aerodynamic forces. Concerning the topic of scale effects, in the work of Thom (1934), the lift and drag coefficients were measured on a rotating cylinder of aspect ratio $AR = 12.5$ at $Re = 5.3 \cdot 10^4$ and $Re = 8.8 \cdot 10^4$. The results indicate that the effects of different Reynolds numbers on the aerodynamic coefficients is negligible.

Several years after, Swanson (1961) provided a detailed summary of the experiments on rotating cylinders carried out until that time. Results of a set of two-dimensional tests performed by the author in the Reynolds number range $3.5 \cdot 10^4 < Re < 5.0 \cdot 10^5$ for velocity ratios $0 \leq k \leq 1$, were also reported. A remarkable output of this investigation is that, for $0 \leq k \leq 0.5$ and $1.3 \cdot 10^5 < Re < 5.0 \cdot 10^5$, the lift coefficient becomes negative and the drag coefficient appears to be considerably affected by the variation of the Reynolds number up to $k = 0.75$.

During the oil crisis in the 1980s, wind assistance for ship propulsion was considered an appealing manner to cut operational costs and this led to several publications on the topic. Relevant to the present study is the work of Clayton (1985) and Bergeson and Greenwald (1985). The former author performed experiments at two different Reynolds numbers, namely $Re = 1.7 \cdot 10^4$ and $Re = 4.9 \cdot 10^4$, on a rotating cylinder of aspect ratio $AR = 10.4$ equipped with two endplates of size $1.4D$ and, subsequently, $2D$. The study indicates that when the larger endplate size is adopted the results seem to be insensitive

to the different Reynolds numbers considered. Nonetheless, for the smaller endplate size, the author concludes that a lower Reynolds number causes a decrease in C_L and an increase in C_D . This effect is noticed until velocity ratio $k = 2$. Conversely, Bergeson and Greenwald mounted a rotating cylinder with diameter $D = 1.16$ m and $H = 7.2$ m on aboard a small motor yacht. Using a combination of mooring lines and spring dynamometers, the authors could measure the forces generated by the rotor for a variety of velocity ratios. The authors report that the tests were conducted with a wind speed ranging between 9–16 knots, meaning that, on average, the Reynolds number achieved was in the order of $Re = 5.0 \cdot 10^5$. The results show that, for velocity ratio $k < 3$, C_L is larger than the lift coefficients obtained in other experiments carried out on rotating cylinders of similar aspect ratios but at lower Reynolds numbers. No results of the drag coefficients are provided.

In 1993, Tokumaru and Dimotakis (1993) completed a series of tests on a rotating cylinder of aspect ratio $AR = 18.7$, with no endplates, at $Re = 3.8 \cdot 10^3$. The authors report that, for low velocity ratios, their results overestimate the lift coefficient compared with the data provided by Reid (1924), and they attribute the discrepancy to a lower Reynolds number used in their experimental campaign.

More recent are the studies of Badalamenti (2010) and Zhang and Bensow (2011). The former conducted a series of tests on a cylinder of aspect ratio $AR = 5.1$ with no endplates, at Reynolds numbers ranging between $Re = 1.9 \cdot 10^4$ and $Re = 9.6 \cdot 10^4$. The results partially disagree with those of Clayton (1985): a decrease in Reynolds number entails an increase in C_L as well as in C_D . This is particularly noticeable for $k < 1.5$ (C_L) and for $k > 2.5$ (C_L and C_D). For a similar Reynolds number ($Re = 4.0 \cdot 10^4$), the latter author carried out wind-tunnel experiments on a rotating cylinder with $AR = 6$. The data show a similar trend compared to the results of Badalamenti (2010).

Besides the experimental studies, several CFD simulations on the topic of rotating cylinders were also published over the years. Among these, research efforts as those of Badr et al. (1989), Ingham and Tang (1990), Chew et al. (1995), Mittal and Kumar (2003) and Padrino and Joseph (2006) dealt with two-dimensional flows at low Reynolds numbers ($Re < 1.0 \cdot 10^3$). In the work of Badr et al. (1989) is shown that simulations conducted at $Re = 60$ lead to a lower lift coefficient than when $Re = 5$ is used. These results also agree with the findings of Ingham and Tang (1990). Mittal and Kumar (2003) and Padrino and Joseph (2006) conducted simulations at $Re = 200$ and, at $k = 4$, both studies indicate that $C_L \approx 18$ and $C_D \approx 0$. Conversely, in the study of Chew et al. (1995), whose computations were carried out at $Re = 1.0 \cdot 10^3$, is reported that, at velocity ratio $k = 4$, $C_L \approx 9$ and $C_D \approx 3.5$. Arguably, such significant discrepancy between the results of Mittal and Kumar (2003) and those of Padrino and Joseph (2006) is, at least partially, due to the different Reynolds numbers used in their computations.

Karabelas (2010) carried out Large Eddy Simulations on a cylinder at $Re = 1.4 \cdot 10^5$ up to velocity ratio $k = 2$. The results are compared with experimental data obtained at $Re = 6.0 \cdot 10^4$ and reported in the investigation of Aoki and Ito (2001). The comparison indicates that the drag coefficient is generally unaffected by the Reynolds number, whereas, at $k = 1$, the lift coefficient achieved at $Re = 1.4 \cdot 10^5$ is approximately twice as large that one obtained at $Re = 6.0 \cdot 10^4$. In another study, Karabelas et al. (2012) completed a series of two-dimensional CFD simulations on a rotating cylinder at $Re =$

$5.0 \cdot 10^5$, $Re = 1.0 \cdot 10^6$ and $Re = 5.0 \cdot 10^6$ for velocity ratio range $2 \leq k \leq 8$. The results suggest that the lift and drag coefficients are only marginally affected by the Reynolds number and that, in general, a higher Reynolds number leads to lower force coefficients. On the other hand, Everts et al. (2014), who conducted a study at the same Reynolds numbers as Karabelas et al. (2012), concludes that the Reynolds number has a marked influence on C_l and C_d : an increase in Reynolds number produces a sharp increase in lift coefficient and a decrease in drag coefficient.

The works of Zhang and Bensow (2011), Craft et al. (2012), Li et al. (2012) and De Marco et al. (2014) deal with rotating cylinders immersed in a three-dimensional flow at relatively high Reynolds numbers. Zhang and Bensow (2011) show that for the two Reynolds numbers considered ($Re = 5.0 \cdot 10^4$ and $Re = 1.0 \cdot 10^5$) the lift and drag coefficients are substantially insensitive to scale effects. Craft et al. (2012) carried out a series of computations on a Flettner rotor at three different Reynolds numbers: $Re = 1.4 \cdot 10^5$, $Re = 8.0 \cdot 10^5$ and $Re = 1.0 \cdot 10^6$. The outcome of the investigation is that the effect of the Reynolds number on the lift coefficient is marginal, both for the bare cylinder and when endplates are used. No results for the drag coefficient are reported. Li et al. (2012) performed simulations on a series of Flettner rotors with aspect ratios 3, 6, 9 and 12 at $Re = 1.6 \cdot 10^6$. Comparing the results for the case with $AR = 6$ and the experimental data of Badalamenti (2010), in which $AR = 5.1$ and $Re = 9.6 \cdot 10^4$, it appears that, for velocity ratios $k < 3$, the higher Reynolds number leads to higher lift coefficients. Conversely, the drag coefficient seems unaffected by the change in the flow regime. Finally, the study of De Marco et al. (2014) deals with CFD simulations at $Re = 5.11 \cdot 10^6$ of a Flettner rotor of aspect ratio $AR = 3.5$, with and without endplates. For the case with endplates (size = $2D$), and for $1 < k < 3$, it is shown that both C_L and C_D are larger than the results reported by Reid (1924), Thom (1934), Badalamenti (2010) and Zhang and Bensow (2011). It should be noticed, however, that a direct comparison of these results is hindered by the use of different aspect ratios.

From an operational perspective, another important aspect of Flettner rotors is the power necessary to spin the cylinder at the desired rotational velocity. In the study of Reid (1924) is reported that the power consumption of the rotating cylinder was greater in still air than in an air stream. Zhang and Bensow (2011) also indicate that, for a given cylinder, the freestream velocity influences the power requirement, being lower for a higher freestream velocity. The results of Clayton (1985) and Badalamenti (2010) disagree with these findings as their data show that the power necessary to spin the cylinder is insensitive to the Reynolds number.

For the interested reader, other studies on rotating cylinders not included in this summary can be found in the exhaustive work of Zdravkovich (2003).

The review here presented indicates that, despite the numerous publications, the influence of the Reynolds number on the aerodynamic coefficients of a rotating cylinder is still unclear. This is due to two main reasons. The first reason is that most of the available experimental data were obtained at Reynolds numbers in the subcritical regime or lower. Only Swanson (1961) carried out experiments at higher Reynolds numbers but, in this case, the velocity ratio was limited to $k = 1$. On the other hand, the computational investigations that did extend to the supercritical regime show contradictory results. Arguably, engineering challenges as, for instance, having the possibility to make

use of an adequate facility both in terms of dimensions and maximum reachable flow speed, as well as having to deal with large aerodynamic forces and moments, hindered the executions of experiments in the supercritical regime. Different complexities, but certainly not less troublesome, are those related to the CFD simulations of a rotating cylinder at high Reynolds numbers. In this respect, the results of [Zhang and Bensow \(2011\)](#) are exemplary: for a same condition, the lift and drag coefficients show a considerable scatter depending on the type of flow solver employed for the computations.

In this context, the present chapter deals with a series of wind-tunnel experiments aimed at the understanding of the Reynolds number effect on the aerodynamic coefficients of a rotating cylinder in a critical and supercritical flow regime. The tests were carried out on a large-scale Flettner rotor (referred to as Delft Rotor in the text) and the aerodynamic forces, as well as the pressures on the cylinder's surface, were measured at all tested conditions. A set of different Reynolds numbers was investigated, being, respectively, $Re = 1.8 \cdot 10^5$ the lowest and $Re = 1.0 \cdot 10^6$ the highest Reynolds numbers achieved.

In the frame of this doctoral work, the scope of the present chapter is to gain insights into the performance of Flettner rotors at full scale.

4.2. EXPERIMENTAL SETUP

4.2.1. THE DELFT ROTOR

The experiments were carried out in the boundary-layer test section of Polytechnic University of Milan wind tunnel. The test section is 13.84 m wide, 3.84 m high and 35 m long. During the experimental campaign, the Delft Rotor was mounted in the centre of the test chamber as shown in Figure 4.1.

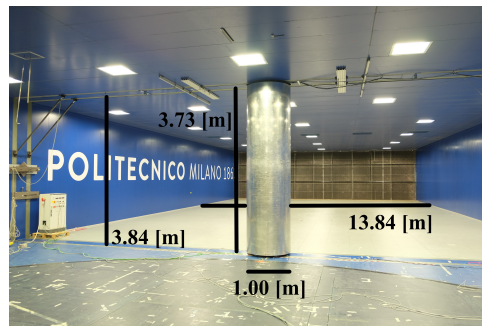


Figure 4.1: The Delft Rotor in Polytechnic University of Milan wind tunnel

The Delft Rotor is a rotating cylinder with diameter $D = 1.0$ m and span $H = 3.73$ m and it is comprised of three main parts: a fixed structure, an internal frame and an outer skin. The fixed structure consisted of a lower and an upper assembly made of four threaded bars screwed into the wind-tunnel ground and ceiling structural beams. Two purpose-built force balances were placed at the extremity of the threaded bars, on top of which the bearing housings were bolted. The proximity of the balances to the bearings minimized the bending moment and allowed to use a three-component force

balance built to measure lift, drag and torque. The outer skin was composed of four calendered aluminum sheets bolted to the internal frame. The frame, composed of three equal wheels and a set of vertical bars, was rotated by an electric engine hung to the lower bearing housing (Figure 4.2).

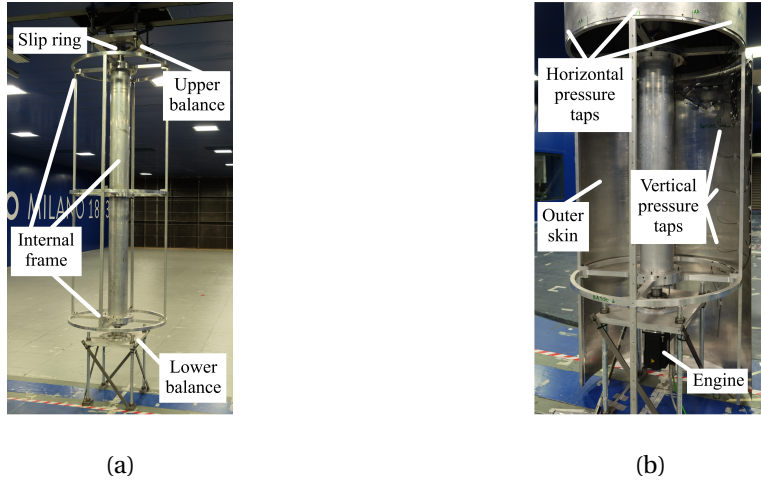


Figure 4.2: Structure of the Delft Rotor without (a) and with (b) outer skin

The Delft Rotor was equipped with two different pressure measurement systems, namely one high sample-rate pressure scanner (PSI ESP-32HD) and one AMS4711 sensor. The reason to use two different measurement systems is that limited literature was found on techniques for dynamic pressure measurements. Therefore, it was decided to use two measurement systems with different characteristics. The ESP scanner, that has a pressure range of ± 2500 Pa, has 32 channels, and this allows to take several pressure measurements simultaneously. Due to its dimensions, it had to be fixed to the central shaft of the internal frame of the cylinder, meaning that, during the tests, it was only marginally affected by the centripetal acceleration but also that, to reach all the pressure taps, long pneumatic connections had to be made. Conversely, the AMS system, that has a pressure range of ± 2000 Pa, is a very compact instrument with only one pressure tap and thus could be directly placed on the internal face of the cylinder outer skin. This means that the AMS system was more affected by the centripetal acceleration, but it had a very short pneumatic connection. Although in a different manner, both the centripetal acceleration and the pneumatic connection influence the pressure measurements, and, in general, such influence increases with the rotational speed. Corrections were made to compensate for these effects as far as possible, nonetheless, the errors that could have derived from such effects are taken into account in the measurement uncertainty analysis. Further information on the experimental setup and the pressure correction methods employed can be found in Appendix B.1 and Appendix B.2.

The experimental campaign on the Delft Rotor comprised two distinct series of tests. During the first series of tests, all the 32 ESP scanner pressure taps were equally distributed around the cylinder circumference at 1.85 m from the ground (horizontal pres-

sure taps). Doing so, it was possible to measure the pressure distribution around an entire section at the cylinder mid-height during the tests carried out at $k = 0$ (static experiments). During the second series of tests, 16 taps were removed from the circumference and they were equally spaced along the span of the cylinder (vertical pressure taps). This second type of arrangement was used to measure the pressure distribution on the Delft Rotor at different heights. Similarly to the ESP system, also the AMS4711 sensor was placed at 1.85 m from the ground (cylinder mid-height).

The pressure systems installed on the Delft Rotor use a piezoresistive silicon chip as sensing element and they both work as differential transducers. Thus, to obtain the actual pressure acting on the outer skin, it was necessary to measure also the static pressure in the interior of the cylinder. This was achieved using a single pressure tube located above the lower force balance. To pass the signal of both the ESP scanner and the AMS4711 sensor to the readout instrumentation, a slip ring connected to the upper hollow shaft was installed (Figure 4.2). The slip ring was also equipped with a transducer to measure the instantaneous velocity and angular position. The angular position of the cylinder was therefore in phase with the pressure measurements.

The experimental setup of the Delft Rotor was designed to find a good compromise between the possibility to achieve as high as possible high Reynolds numbers and the structural constraints related to the large aerodynamic forces involved.

4.2.2. FLOW CHARACTERISTICS

The boundary layer test section of Polytechnic University of Milan wind tunnel has a standard turbulent intensity $I_u = 2\%$ while the boundary layer thickness is about 0.2 m. Considering this turbulent intensity level, the critical Reynolds number region for a circular cylinder is anticipated with respect to smooth flow conditions. The lowest Reynolds number tested, $Re = 1.8 \cdot 10^5$, is in fact already experiencing the drag coefficient reduction typical of the critical flow region.

The flow velocity, used to calculate all the aerodynamic coefficients, was measured with a pitot tube placed 5 m in front of the Delft Rotor at the height of 1.85 m from the ground. The clearance between the cylinder and the wind-tunnel floor and ceiling was 55 mm (Figure 4.1). These gaps were necessary to let enough room (considering also a safety margin) for the instrumentation cables. Considering the flow velocity reduction due to the boundary layer and that a gap of 55 mm corresponds to about 1.5% of the cylinder span, it can be assumed that the tip vortices were (at least largely) suppressed by the wind-tunnel upper and lower walls. In this respect, the experiments were conducted in a two-dimensional flow condition. However, the wind-tunnel boundary layer caused the flow to have non-two-dimensional features. In fact, the boundary layer, besides the decrease of the incoming flow velocity near the walls, it also caused a change in pressure distribution around the cylinder ends. On the other hand, outside of the boundary layer, the flow presented a straight profile and no effects caused by the wind-tunnel walls were measured. The effects of such testing conditions are noticeable by comparing the results of the force coefficients obtained using the pressure distribution measured at the cylinder mid-height (sectional C_l and C_d), and the coefficients obtained from the force balances and the pressure integration along the entire span of the Delft Rotor (overall C_L and C_D). In fact, it can be noticed that, due to the wind-tunnel boundary layer, the

sectional lift and drag coefficients are, in general, larger than the corresponding overall coefficients.

The sectional force coefficients are here defined as:

$$C_l = \frac{F_l}{\frac{1}{2} \cdot \rho \cdot D \cdot V^2}, C_d = \frac{F_d}{\frac{1}{2} \cdot \rho \cdot D \cdot V^2} \quad (4.1)$$

where F_l and F_d are, respectively, the sectional lift and drag force, D is the cylinder diameter and V is the wind speed.

Conversely, the overall force coefficients were calculated according to:

$$C_L = \frac{F_L}{\frac{1}{2} \cdot \rho \cdot A \cdot V^2}, C_D = \frac{F_D}{\frac{1}{2} \cdot \rho \cdot A \cdot V^2} \quad (4.2)$$

where F_L and F_D are, respectively, the overall lift and drag force and A is the cylinder's projected area ($A = H \cdot D$).

Finally, following the definitions commonly used in the literature on this subject, the Reynolds number is here calculated based on the cylinder's diameter ($Re = D \cdot V/\nu$) and the velocity ratio k is defined as the ratio between the tangential velocity of the rotating cylinder and the wind speed ($k = U_{tan}/V$).

4.3. RESULTS

The results of the experimental campaign on the Delft Rotor are presented in this section. For each velocity ratio, every measurement carried out is reported, apart from $k = 0$ for which just the averaged result is shown for the sake of clarity. It should be noticed that the results of the static measurements ($k = 0$) given in Figure 4.4 – Figure 4.9 use the same colour legend as used for all other cases to indicate the corresponding Reynolds number. All measurement techniques employed in the experiments are indicated in the result figures: force balances (F. Balance), integration of the results of ESP scanner vertical pressure sensors (Press. Int.), AMS4711 pressure sensor (AMS47), ESP scanner horizontal pressure sensors (Scanner) and, finally, (Engine) for the engine controller used to measure the power consumption. As stated in Section 4.2.1, two separate series of tests were carried out on the Delft Rotor. This is specified in the result figures with the terminology “Exp. 1” (first test series) and “Exp. 2” (second test series). Regarding the integration of the pressure results of the vertical ESP scanner sensors, the pressures measured by the 16 taps installed along the cylinder span were used in the calculations. The integrated pressure was then transformed into non-dimensional coefficients by using the reference wind speed V measured by the pitot tube placed at a height of 1.85 m from the ground (see Section 4.2.2). A summary of the cases investigated is given in Table 4.1.

Table 4.1: Summary of the experiments carried out on the Delft Rotor

#Test	Re [$\cdot 10^5$]	Velocity ratio k													
		0	0.5	1.0	1.25	1.5	1.75	2.0	2.25	2.5	3.0	3.5	4.0	4.5	5.0
Exp. 1	1.8	x	-	x	x	x	x	x	x	x	-	-	-	-	-
Exp. 1	3.6	x	-	x	x	x	x	x	x	x	-	-	-	-	-
Exp. 1	5.5	x	-	x	x	x	x	x	x	x	-	-	-	-	-
Exp. 1	10.0	x	-	x	x	x	x	x	-	-	-	-	-	-	-
Exp. 2	1.8	x	x	x	-	x	-	x	-	x	-	-	-	-	-
Exp. 2	2.5	x	x	x	x	x	x	x	x	x	x	x	x	x	x
Exp. 2	3.6	x	x	x	x	x	x	x	x	x	x	x	x	x	x
Exp. 2	10.0	x	x	x	-	x	-	x	-	-	-	-	-	-	-

To better understand the results reported in the following sections, the cylinder direction of rotation and the conventions used in the present analysis are depicted in Figure 4.3.

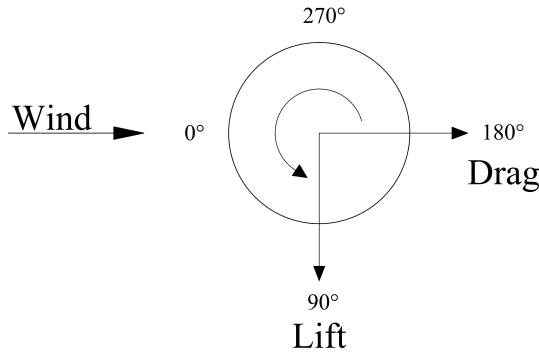


Figure 4.3: Cylinder direction of rotation and conventions used

The measurement uncertainties relative to the results presented in this chapter can be found in Appendix B.3.

4.3.1. LIFT COEFFICIENT

The overall and sectional lift coefficients (Figure 4.4 and Figure 4.5) show a similar trend, as C_L (obtained from measurements taken over the entire cylinder's span) and C_l (obtained from measurements taken only at the cylinder's mid-section) appear to be affected by the Reynolds number in a similar manner. In the range $0 < k < 2.5$, higher Reynolds numbers lead to higher lift coefficients. This holds true until $Re = 2.5 \cdot 10^5$, in fact for the higher Reynolds numbers considered such difference is no longer appreciable. On the other hand, for velocity ratios $k > 2.5$, the lift coefficient does not seem affected by the Reynolds number. This is also supported by the fact that the influence of the Reynolds number on the lift coefficient appears to decrease with the increase of the velocity ratio.

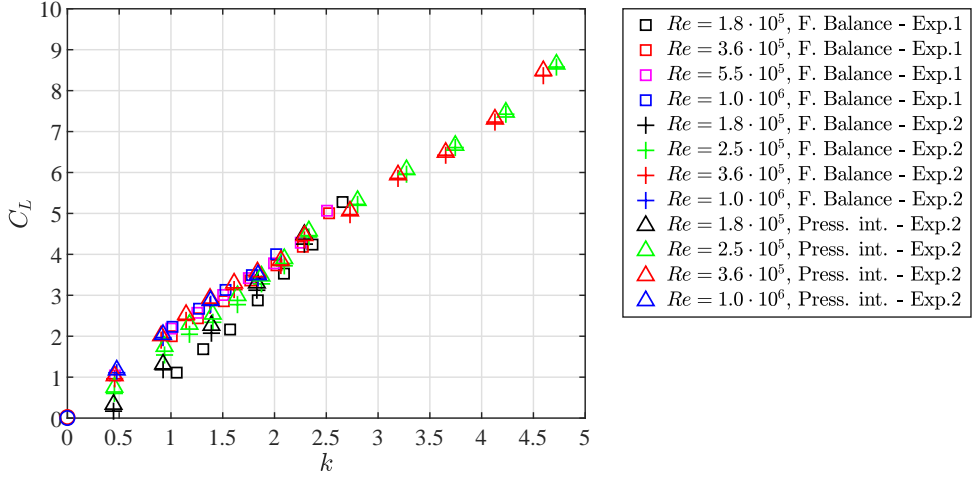


Figure 4.4: Overall lift coefficient vs velocity ratio

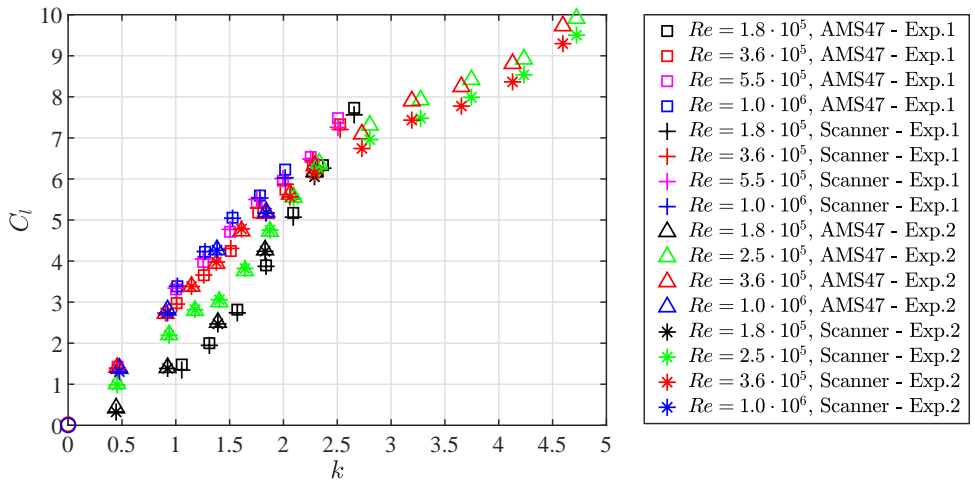


Figure 4.5: Sectional lift coefficient vs velocity ratio

Studies on three-dimensional cylinders without endplates as for example, [Badalamenti \(2010\)](#), [Li et al. \(2012\)](#) and [De Marco et al. \(2016\)](#) indicate that the lift coefficient ceases to increase after a certain velocity ratio and that this depends on the aspect ratio of the cylinder. In the work of [De Marco et al. \(2014\)](#) simulations on a cylinder with an aspect ratio similar to the present study ($AR = 3.5$) are carried out at $Re = 5.11 \cdot 10^6$. The results show that, for the case without endplates, the lift coefficient reaches a plateau at $k = 2$ (Fig. 6). In the present results, for the range of velocity ratios considered, such plateau is not found, and this is because the tip vortices that generate on a free-standing cylinder are in the current case largely suppressed by the wind-tunnel walls. In fact, as

shown in the studies of Li et al. (2012) and Zhang et al. (2013) the tip vortices decrease the pressure difference and thus reduce the lift generated by the rotating cylinder. On the other hand, for the same aspect ratio $AR = 3.5$, the lift coefficient results of the cylinder with endplates reported by De Marco et al. (2014) are more comparable with the results of the present study, especially for $k < 1.5$.

Although for a larger aspect ratio ($AR = 5.1$), the results of Badalamenti (2010) regarding a Flettner rotor with two non-rotating endplates of size $2D$ show a similar trend compared to the results of the lift coefficients obtained in the present study (Figure 4.6). In fact, also in the work of Badalamenti (2010) the slope of the lift coefficient curve decreases at $k = 2.5$ and until $k = 5.0$ no plateau is found. On the other hand, compared to the present work, the lift coefficients measured by Badalamenti (2010) are considerably lower. It is tenable that this is due to the substantially lower Reynolds number used in the experiments ($Re = 1.9 \cdot 10^4$).

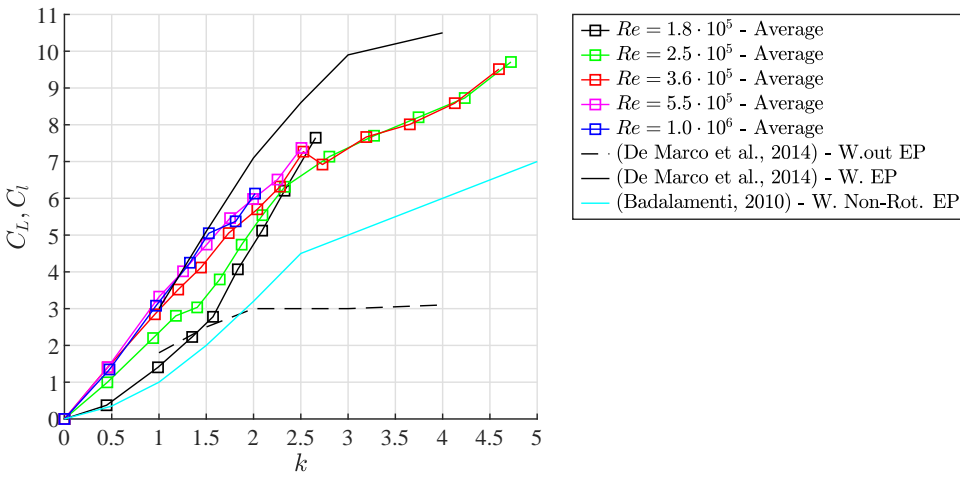


Figure 4.6: Comparison of averaged sectional lift coefficient with other similar studies

4.3.2. DRAG COEFFICIENT

The large scatter in the overall drag results (Figure 4.7) is arguably due to the effect of the wind-tunnel boundary layer on the pressure distributions at the cylinder extremities mentioned in Section 4.2.2. This scatter is not found in the overall lift coefficient results and this is because the drag coefficient is more sensitive to changes in pressure distribution. In fact, looking at Figure 4.10, it can be noticed that a minor shift of the suction (that occurs at about 90° with respect to the wind direction) towards the front or the rear of the cylinder would cause a noticeable change in drag force but a marginal change in lift force. The effect of the Reynolds number on the drag coefficient is thus more appreciable in Figure 4.8, where the sectional results are reported.

The Reynolds number influence that is evident at $k = 0$ (static cylinder) is suppressed by the rotation at velocity ratio $k = 0.5$. At higher velocity ratios, until $k = 2.5$, the Reynolds number shows a marked influence on the drag coefficient: similar to the lift coeffi-

cient, a higher Re entails a higher drag coefficient. Nonetheless, differently from the lift coefficient, the Reynolds number effect is noticed throughout the entire range of Re considered. At $k > 2.5$, the sectional drag coefficients obtained for $Re = 2.5 \cdot 10^5$ and $Re = 3.6 \cdot 10^5$ do not show any remarkable difference. At $k = 2.5$, however, the difference between the drag coefficient obtained at $Re = 1.8 \cdot 10^5$ and $Re = 5.5 \cdot 10^5$ is still substantial.

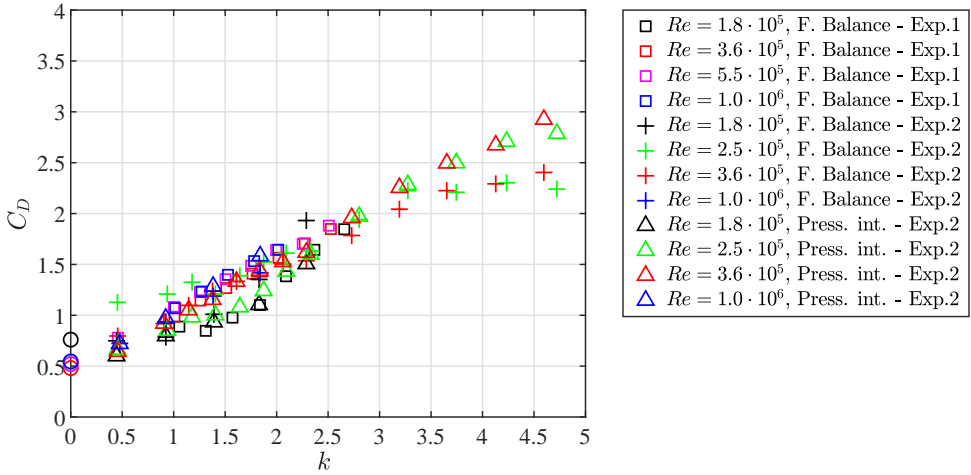


Figure 4.7: Overall drag coefficient vs velocity ratio

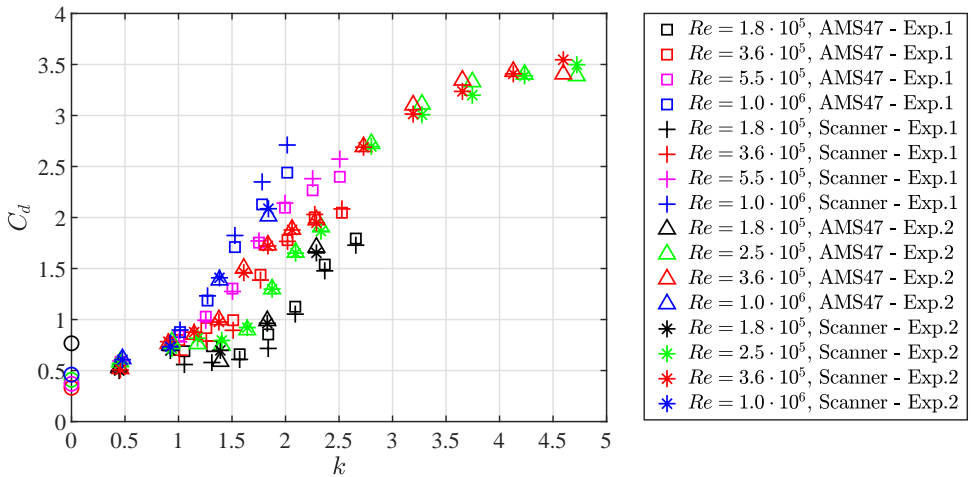


Figure 4.8: Sectional drag coefficient vs velocity ratio

The findings of [De Marco et al. \(2014\)](#) show that in case the cylinder does not have endplates, similarly to the lift coefficient, the drag coefficient ceases to increase at $k = 2$ (Figure 4.9). On the contrary, in case the cylinder is equipped with endplates, the drag

coefficient keeps increasing with the increase of the velocity ratio. This is also supported by the fact that, according to Badalamenti (2010) and Zhang et al. (2013), for velocity ratios $k > 3$, rotating endplates generate more drag than otherwise a cylinder without or with non-rotating endplates. The results of Badalamenti (2010) for the cylinder with two non-rotating endplates show that the slope of the drag coefficient curve decreases at $k = 3$ but no plateau is found up to $k = 5$ (Figure 4.9). The results of the present investigation show a similar trend compared to the findings of Badalamenti (2010) for the case of a cylinder with non-rotating endplates. Similarly to the lift coefficient, the differences in drag coefficients of the present study and that of Badalamenti (2010), arguably, are at least in part due to the different Reynolds numbers employed.

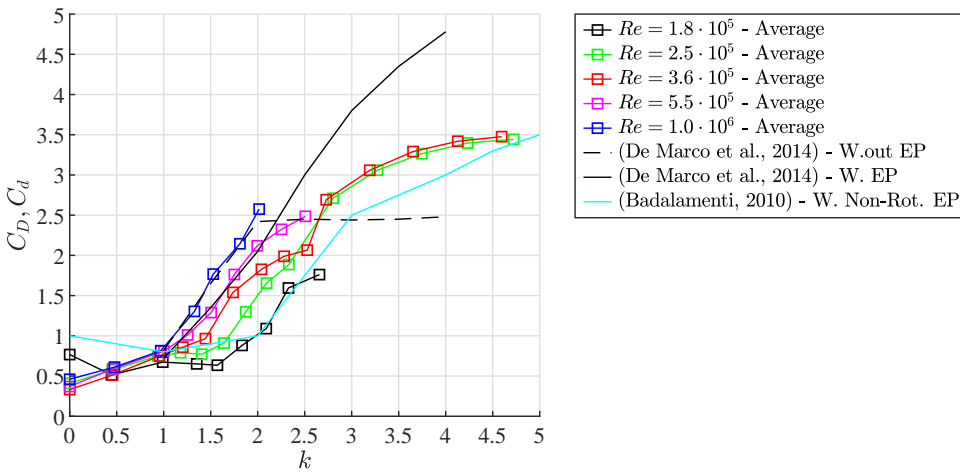
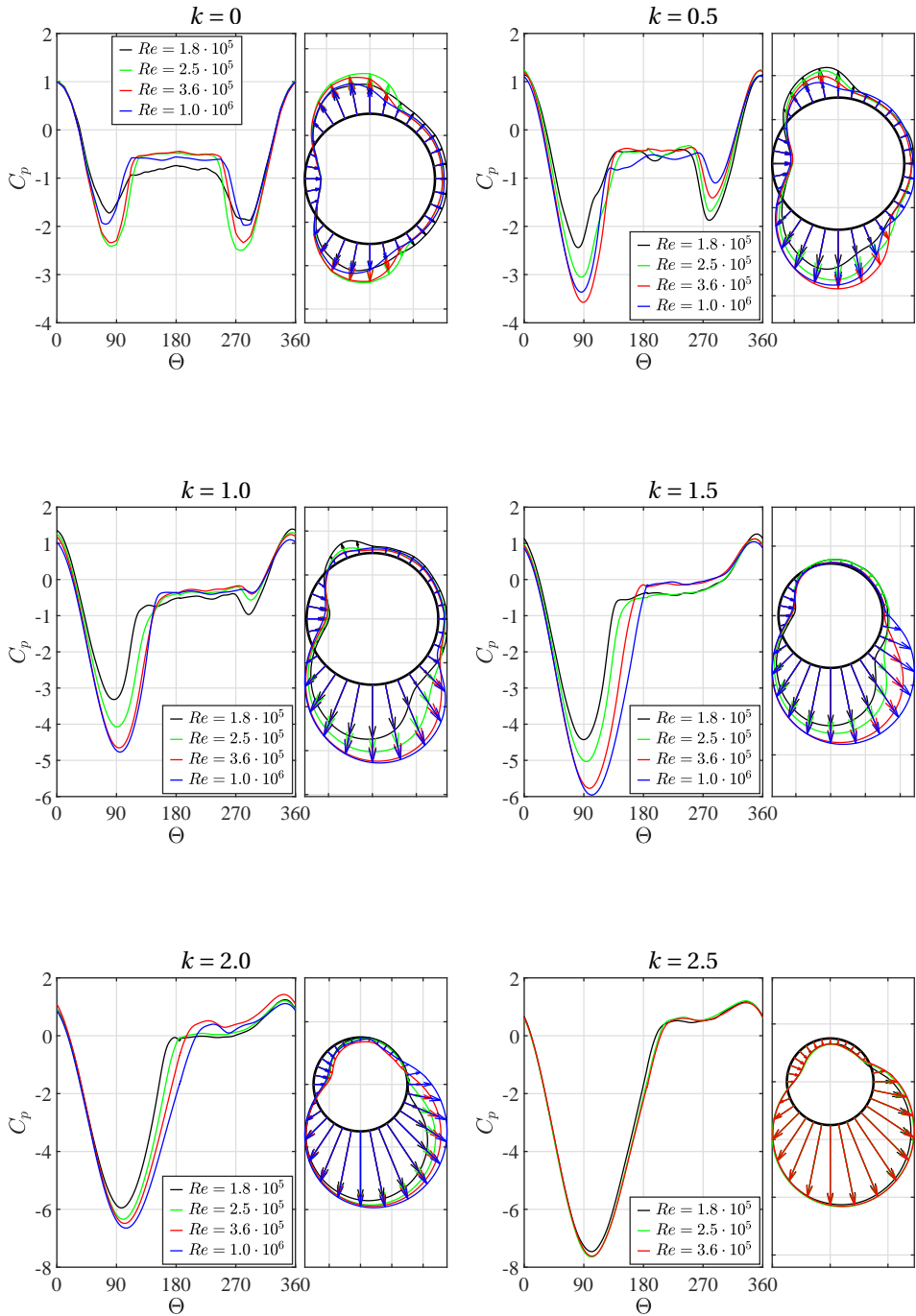


Figure 4.9: Comparison of averaged sectional drag coefficient with other similar studies

4.3.3. PRESSURE COEFFICIENT

The results of sectional pressure coefficient C_p , obtained by averaging the data of the AMS4711 sensor and those of the horizontal pressure taps of the ESP scanner, support the findings of the lift and drag coefficients discussed in Section 4.3.1 and 4.3.2. The cylinder rotation causes an asymmetry in the pressure distribution on the sides of the Flettner rotor that results in the generation of lift (Figure 4.10, $k = 0$ and $k = 0.5$). In the range $0.5 \leq k \leq 2$, a higher Reynolds number leads to a larger $C_{p_{min}}$ and to a lower $C_{p_{max}}$. For $Re = 3.6 \cdot 10^5$ and $Re = 1.0 \cdot 10^6$, this change is balanced in such a way that it results in similar lift coefficients, whereas for the lower Reynolds numbers the change in $C_{p_{min}}$ and $C_{p_{max}}$ leads to different lift coefficients as reported in Section 4.3.1.

In the velocity ratio range $1 < k \leq 2.5$, the drag increase at higher Reynolds numbers is caused by the shift of the suction peak and the separation point towards the rear of the cylinder. For velocity ratios $k > 2.5$, the C_p curves of the two Reynolds numbers tested practically overlap, leading to similar lift and drag coefficients (Figure 4.5 and Figure 4.8). Finally, with the increase of the velocity ratio the stagnation point shifts in the direction opposite to the direction of rotation of the cylinder (Figure 4.3 and Figure 4.10).



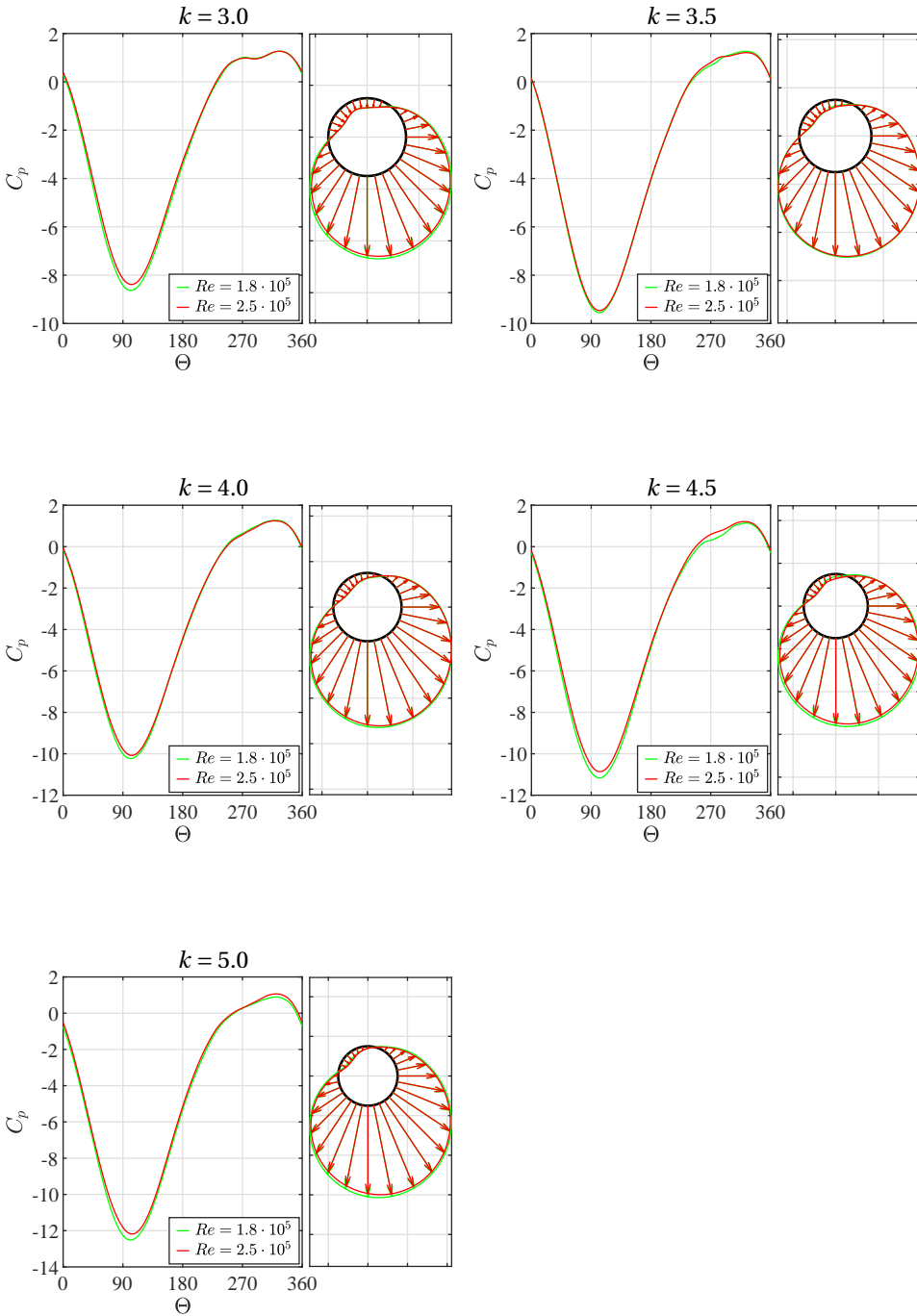


Figure 4.10: Averaged sectional pressure coefficients measured at the cylinder mid-span for increasing velocity ratio k . The wind comes from the left side of the plots and the cylinder rotates anticlockwise as depicted in Figure 4.3.

4.3.4. POWER CONSUMPTION

The power necessary to spin the cylinder at a given rotational speed was measured during experiments carried out in an air stream as well as in still air. The results are reported in Figure 4.11 and Figure 4.12 respectively. Considering the rather large measurement uncertainties (see Appendix B.3), in particular, associated to considerable scatter of the case in which the cylinder rotates in an air stream (Figure 4.11), it can be concluded that the Reynolds number has a negligible influence on the power necessary to spin the Flettner rotor. These findings agree with the results of Clayton (1985) and Badalamenti (2010).

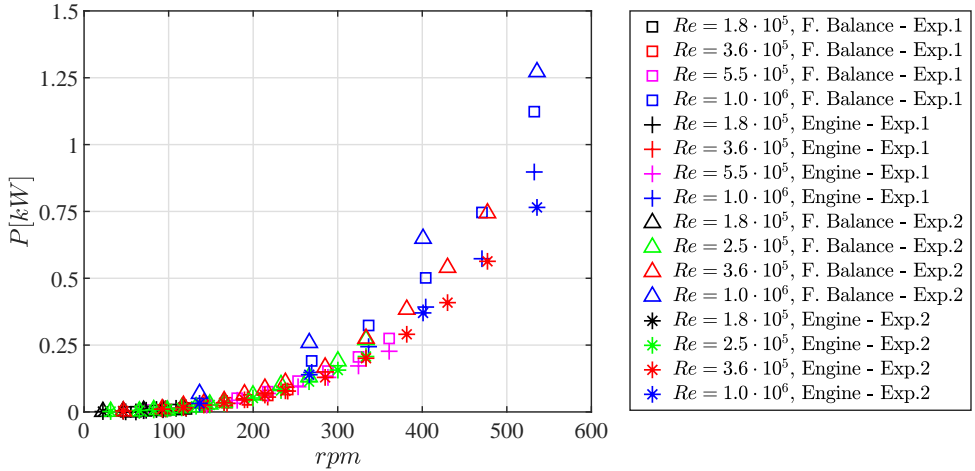


Figure 4.11: Delft Rotor power consumption in an air stream at increasing rotational speeds

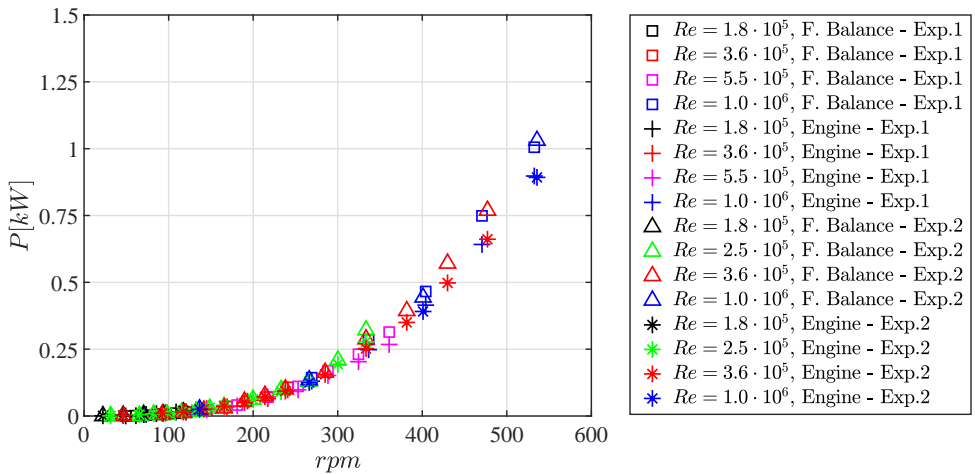


Figure 4.12: Delft Rotor power consumption in still air at increasing rotational speeds

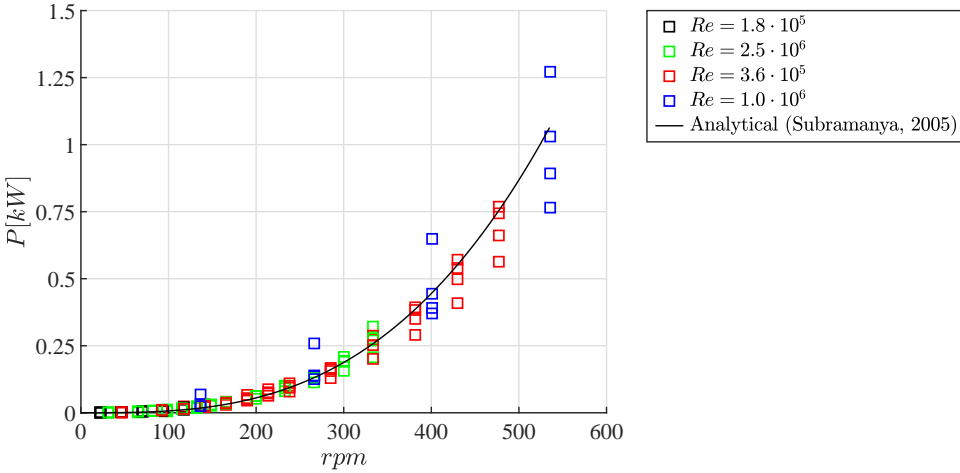


Figure 4.13: Comparison of the Delft Rotor power consumption with the analytical formula of [Subramanya \(2005\)](#)

Another interesting finding shown in [4.11](#) and [Figure 4.12](#) is that the power necessary to rotate the Delft Rotor scales with the cube of its rotational speed. [Subramanya \(2005\)](#) proposes an analytical formula to calculate the power consumption of a rotating cylinder based on its tangential velocity U_{tan} , its lateral surface area A_s ($A_s = \pi \cdot D \cdot H$) and a friction coefficient C_f . The formula reads:

$$P = C_f \cdot \rho \cdot U_{tan}^3 / 2 \cdot A_s \quad (4.3)$$

In [Figure 4.13](#) is shown that a close agreement with the experimental results is found by setting $C_f = 0.007$, that can be considered a reasonable value for the friction coefficient. It should be noticed, however, that the actual power consumption of a Flettner rotor is arguably also affected by the functioning of its mechanical systems.

4.4. CONCLUSIONS

The present chapter deals with a series of wind-tunnel experiments aimed at a better understanding of the Reynolds number effects on the aerodynamic performance of Flettner rotors. The results indicate that within the range considered, there is a remarkable influence of the Reynolds number on the lift and drag coefficients below velocity ratio $k = 2.5$. The lift coefficient, in fact, appears to be affected for the two lowest Reynolds numbers tested (critical flow region), but it is insensitive to the Reynolds number in the supercritical flow region ($Re = 3.6 \cdot 10^5$, $Re = 5.5 \cdot 10^5$ and $Re = 1.0 \cdot 10^6$). Also, it appears that the effect of the Reynolds number on the lift coefficient decreases with the increase of the velocity ratio. On the other hand, the drag coefficient is affected by the Reynolds number for all flow conditions analysed. For velocity ratios until $k = 2.5$, a higher Reynolds number leads to a higher lift and drag coefficient. Conversely, for velocity ratios $k > 2.5$, the results suggest that the effect of the Reynolds number on the lift coefficient becomes limited. Considering that the drag coefficient at $k = 2.5$

appears to be strongly influenced by the different Reynolds numbers tested, the current data arguably do not permit to conclude whether the Reynolds number affects the drag coefficient also for velocity ratios $k > 2.5$.

The results of the present investigation were also compared with similar studies. Despite the discrepancies caused by the substantially different Reynolds numbers used, a qualitative agreement is found with the findings of [Badalamenti \(2010\)](#) for the case of a Flettner rotor with two non-rotating endplates.

The power consumption is found to scale with the cube of the cylinder tangential velocity and it appears to be unaffected by the Reynolds number and on whether the cylinder is spun in an air stream or in still air.

5

AERODYNAMIC INTERACTION BETWEEN TWO FLETTNER ROTORS

To increase the fuel savings potential of the ship on which Flettner rotors are installed, multiple devices are typically used. However, in the performance estimate of these hybrid ships, it is currently assumed that Flettner rotors operate independently, regardless of the number of devices employed and their relative position on the ship's deck. The present investigation deals with a wind-tunnel experimental campaign aimed at understanding the aerodynamic interaction effects on the performance of two similar Flettner rotors. The study indicates that the aerodynamic performance of the two Flettner rotors is affected by their interaction, and, generally, this is most noticeable when the devices are set closer to each other and when they are aligned with the wind direction. It is demonstrated that, depending on the apparent wind direction, the layout of the Flettner rotors on the ship's deck has a remarked influence on the driving and heeling force coefficients of the entire rig. Lastly, the velocity ratio is found to play a key role in the determination of how the interaction affects the Flettner rotor aerodynamic performance.

This chapter is based on the journal article: G. Bordogna, S. Muggiasca, S. Giappino, M. Belloli, J.A. Keuning and R.H.M. Huijsmans. The effects of the aerodynamic interaction on the performance of two Flettner rotors. *Journal of Wind Engineering and Industrial Aerodynamics*, (2019), doi.org/10.1016/j.jweia.2019.104024

5.1. INTRODUCTION

The physical phenomena associated with Flettner rotors and, more broadly, to rotating cylinders, were studied quite extensively over the past years. As a result of these research efforts, it was possible to identify the influence of several parameters as, for example, the velocity ratio, the endplate size, the aspect ratio and the Reynolds number, on the aerodynamic performance of a single Flettner rotor. However, to increase the fuel-saving potential of the designated vessel, in real-life applications, multiple Flettner rotors are often used (see Figure 5.1). The use of multiple Flettner rotors in a confined space as it is the deck of a ship is likely to lead to a change in performance of each of the installed device due to their aerodynamic interaction.



Figure 5.1: The *E-ship 1* is a wind-assisted ship equipped with four Flettner rotors. Photo: Alan Jamieson

Although it is tenable that, in general, this situation would be the norm, this phenomenon is nowadays largely neglected. In fact, the aerodynamic thrust generated by a set of Flettner rotors is now commonly calculated as the simple arithmetic sum of the thrust produced by each of the installed devices, i.e. the aerodynamic interaction effects are fully disregarded (Li et al., 2012; Traut et al., 2012; Pearson, 2014; Traut et al., 2014; De Marco et al., 2016). On the other hand, in other cases in which the interaction effects are taken into account, an arbitrary reduction in aerodynamic force is assumed. Eggers (2016), for example, assigns a reduction in lift force to the leeward Flettner rotor when the ship is sailing in certain conditions in which the aerodynamic interaction effects are assumed to be most relevant.

The reason for these simplifications in modelling the aerodynamic thrust generated by a set of Flettner rotors is because, substantially, the literature lacks publications on this topic. This is also remarked by De Marco et al. (2016) and Badalamenti (2010). There are, in fact, numerous publications on the phenomena associated with arrangements of two or more steady cylinders, whereas considerably fewer studies focused on sets of rotating cylinders. As it will be argued herewith, in either case, the literature currently available is of limited practical use for real-life Flettner rotor applications.

Due to its importance in many engineering fields, the problem of interference between two or more steady cylinders in tandem, staggered or side-by-side arrangement, was largely studied during the years. Comprehensive summaries on this topic can be found in the works of Zdravkovich (2003) and Sumner (2010), in which details on the forces and pressures of each cylinder are provided together with extensive analyses of the

flow pattern. The same research topic attracted considerable attention also for problems related to wake-induced vibrations, see, for example, the studies of [Bearman \(2011\)](#), [Assi et al. \(2010\)](#) and [Diana et al. \(2014\)](#), in which cases, the focus is on the dynamic response of the analysed structures. Although the current research shares the aim of studies on multiple steady cylinders, i.e. how two or more cylinders interfere depending on their relative position, the forces and flow patterns generated by rotating cylinders are not comparable to those of steady cylinders. The findings relative to steady cylinders have, therefore, limited utility in the context of the present work.

Regarding studies on multiple rotating cylinders, considerable fewer publications can be found in the literature. [Prandtl \(1926\)](#), joint with his extensive research on the single Flettner rotor, provided flow visualizations of two side-by-side counter-rotating cylinders. Unluckily, no results regarding the interaction effects on the aerodynamic forces were reported. The research efforts of [Ueda et al. \(2003\)](#) and [Watson \(1995\)](#) deal with analytical solutions for two rotating cylinders in Stokes flows. In particular, [Ueda et al. \(2003\)](#) provide the drag coefficients for several velocity ratios and gap distances between cylinders. For the same type of flow, [Garzon and Figueroa \(2017\)](#) analytically calculated the velocity field generated by an array of four rotating cylinders. The results for four different rotation sets are compared with PIV measurements and show good agreement. [Sungnul and Moshkin \(2009\)](#), [Yoon et al. \(2009\)](#) and [Fallah et al. \(2011\)](#) conducted numerical studies on two counter-rotating cylinders in side-by-side and staggered arrangement. The computations were carried out in laminar flow, i.e. $Re < 100$, and the effects of the velocity ratios and the cylinders' relative positions on the lift and drag coefficients were computed. The studies agree in indicating that both the cylinders' relative positions and velocity ratios strongly influence their lift and drag coefficients. On the other hand, the work of [Guo et al. \(2009\)](#) comprised a series of PIV measurements for Reynolds numbers ranging between $425 < Re < 1130$ and for velocity ratios $0 \leq k \leq 4$. The cylinders were set in a side-by-side arrangement and, also in this case, they were counter rotating. The study does not include any result regarding the effects of the aerodynamic interference on the cylinders' lift and drag coefficients. However, in line with [Sungnul and Moshkin \(2009\)](#), [Yoon et al. \(2009\)](#) and [Fallah et al. \(2011\)](#), the author concludes that the gap distance and the cylinders' velocity ratios are important parameters to determine the flow pattern. This is supported by the finding that the vortex shedding of the cylinders is suppressed as the velocity ratio increases. The characteristics of the numerical and experimental investigations carried out until today on multiple rotating cylinders limit the applicability of the available literature to the present work. In fact, the research efforts here discussed were typically conducted in the laminar or creeping flow regime as well as using counter-rotating cylinders. Apart to the flow regime that, for the scope of this research it is a limit on its own, to generate positive thrust Flettner rotors typically spin in the same direction.

The present study aims to be the first attempt in investigating the effects of the interaction on the aerodynamic performance of multiple Flettner rotors. The experimental campaign comprised two distinct series of experiments: first, tests on a single Flettner rotor were carried out in order to establish a baseline for comparison. For these experiments, measurements of the velocity field were also taken at several locations in the wake of the single Flettner rotor. At a later time, two analogous Flettner rotors were

tested for a range of different relative positions and velocity ratios. In this series of tests, their lift and drag coefficients were measured and then compared to those of the single Flettner rotor to investigate the effects of the aerodynamic interaction. These results were eventually used to study the performance, expressed in terms of driving and heeling force coefficients, of different Flettner rotor layouts when installed on the deck of a ship.

In the framework of this doctoral thesis, the results of the experiments discussed in this chapter are also used to validate the capabilities of a simple aerodynamic model to predict the aerodynamic interaction effects on the performance of multiple Flettner rotors (see Chapter 6).

5.2. EXPERIMENTAL SETUP

5.2.1. WIND TUNNEL AND FLOW CHARACTERISTICS

The experiments were carried out in the boundary layer test section of Polytechnic University of Milan wind tunnel. The test section is 13.84 m wide, 3.84 m high and 35 m long. It has a standard turbulent intensity $I_u = 2\%$ and the boundary layer thickness is about 0.2 m. Considering the wind-tunnel boundary layer and the height of the Flettner rotor bottom static endplate (0.3 m) from the ground (Figure 5.3), it can be assumed that the Flettner rotors experienced a straight wind profile throughout the experimental campaign.

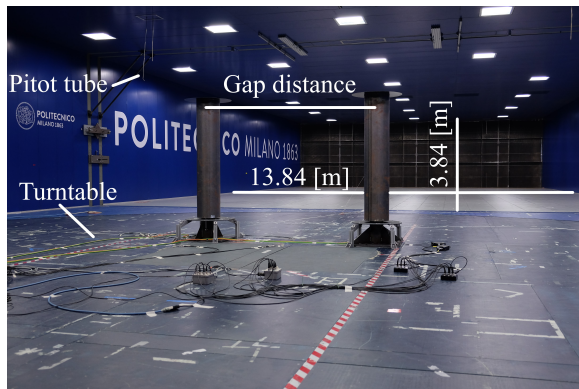


Figure 5.2: The Flettner rotor gap distance (GD) is here defined as the horizontal distance between the two cylinders' vertical axis of symmetry expressed in terms of cylinder diameter D .

The flow velocity, used to calculate all the aerodynamic coefficients, was measured with the wind-tunnel pitot tube that is hung at a distance of 1.2 m from the ceiling (Figure 5.2). All tests were conducted at a wind speed of $V = 5$ m/s, leading to a Reynolds number $Re = 1.0 \cdot 10^5$. Nonetheless, some tests were carried out at lower and higher Reynolds numbers. In fact, some experiments on the single Flettner rotor were conducted at a wind speed $V = 3.5$ m/s ($Re = 7.0 \cdot 10^4$) and $V = 10$ m/s ($Re = 1.8 \cdot 10^5$). No corrections were made due to blockage effects as the blockage ratio was less than 1%.

In this chapter, the Reynolds number, the velocity ratio k and the lift and drag coefficients C_L and C_D follow the same definitions provided in Chapter 4.

5.2.2. THE FLETTNER ROTOR

The Flettner rotor type used throughout the experimental campaign had a diameter $D = 0.3$ m, a span $H = 1.5$ m and a physical aspect ratio $AR = 5$, that is comparable to the aspect ratio of Flettner rotors commonly used for wind-assisted propulsion. Two endplates, of diameter $D_E/D = 2$, were used. The top endplate rotated with the cylinder while the bottom endplate was fixed at a height of 0.3 m from the ground (Figure 5.3).

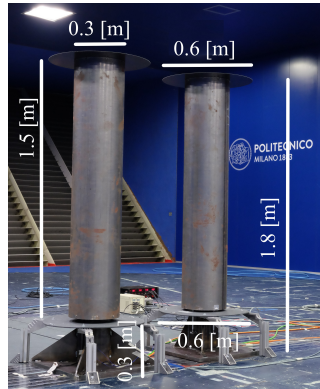


Figure 5.3: Main dimensions of the Flettner rotors used in the experiments

The rotating cylinder comprised three different main parts: a hollow square section beam welded to a steel ground plate, an aluminum static cylinder and a thin steel rotating cylinder on top of which the carbon fibre endplate was attached. The electric engine used to spin the cylinder was hung on a plate secured to the top of the static cylinder. The rotation was passed to the external cylinder through a flexible joint that connected the engine shaft with the top plate shaft, to which the external rotating cylinder was bolted (Figure 5.4).

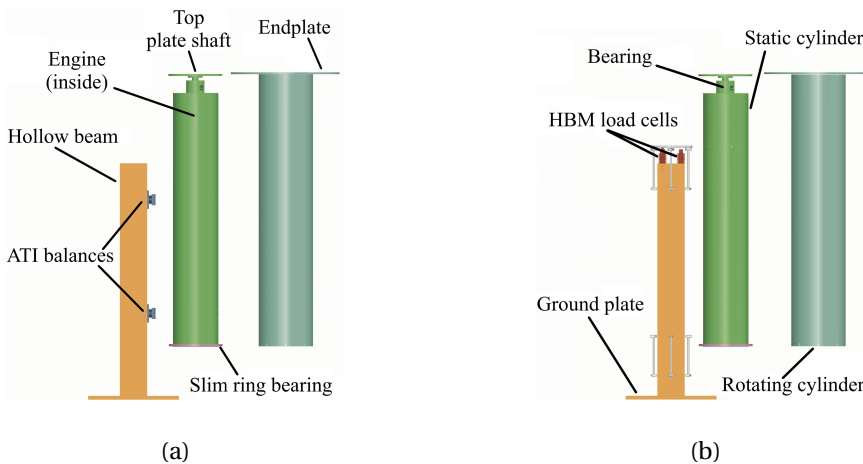


Figure 5.4: Flettner rotor components with ATI balances (a) and HBM load cells (b)

The two cylinders used in the experiments were analogous except for the measurement instruments employed. In fact, one cylinder was equipped with two ATI Mini45 F/T balances, that are 6-axis sensors, while the other with three HBM Z6FD1 load cells, that are mono-directional sensors. The internal arrangement of the two cylinders, specifically the connection between the hollow beam and the static cylinder, had to be modified to fit the different measurement instruments used. This is shown in Figure 5.4.

5.2.3. SINGLE FLETTNER ROTOR SETUP

During the experiments, the single Flettner rotor was positioned in the centre of the wind-tunnel turn table and the lift and drag forces were measured for all velocity ratios considered. For velocity ratios $k = 0$, $k = 1$, $k = 1.5$ and $k = 2$, moreover, measurements of the velocity field were taken at several positions in the wake of the rotating cylinder.

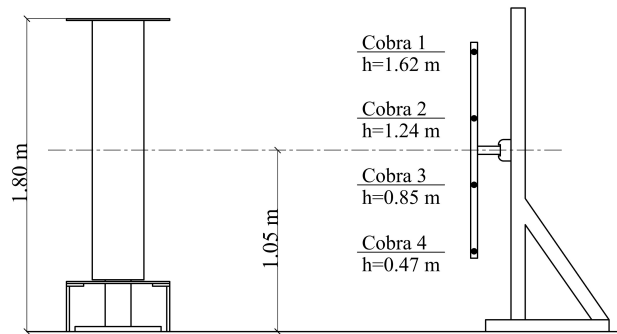


Figure 5.5: Vertical position of the Cobra Probes with respect to the Flettner rotor

Four Cobra Probes were used to measure the velocity field. The Cobra Probe is a multi-hole pressure probe capable to measure the three velocity components within an angle range of $\pm 45^\circ$ at a frequency of 2000 Hz. The Cobra Probes were mounted on a vertical bar at four different heights, namely 0.47 m (Cobra 4), 0.85 m (Cobra 3), 1.24 m (Cobra 2) and 1.62 m (Cobra 1) from the ground (Figure 5.5). Measurements of the velocity field were taken at four longitudinal distances downstream the Flettner rotor, corresponding to 1.5, 3, 7.5 and 15 diameters. At each longitudinal position, the vertical bar was automatically displaced from -1.5 m to +1.5 m with respect to the cylinder centreline, in steps of 0.15 m.

For this series of tests, the Flettner rotor equipped with the ATI balances was used.

5.2.4. DOUBLE FLETTNER ROTOR SETUP

The two Flettner rotors were tested for three different gap distances, defined as the horizontal distance between the two cylinders' vertical axis of symmetry, non-dimensionalised with the cylinder diameter D (Figure 5.2), corresponding to $GD = 3, 7.5$ and 15. For each gap distance GD , the wind-tunnel turntable was rotated at various angles between 15° and 180° in order to change the cylinders' relative position with respect to the incoming wind direction.

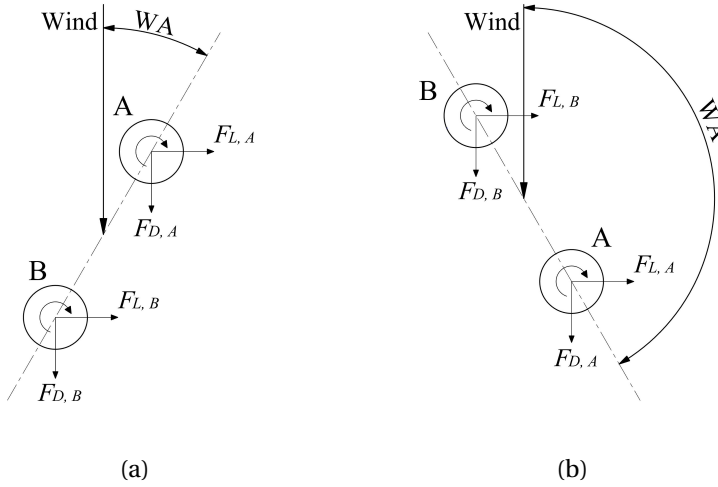


Figure 5.6: Conventions used for two-Flettner rotor experiments for $W_A < 90^\circ$ (a) and $W_A > 90^\circ$ (b)

For each case, the Flettner rotors were spun for all combinations of velocity ratios generated by $k = 1$, $k = 1.5$ and $k = 2$, leading to a matrix of nine velocity ratios. Throughout the experiments, the cylinders rotated clockwise and the lift and drag forces of Flettner rotor A and Flettner rotor B were measured following the conventions depicted in Figure 5.6.

5.3. RESULTS

The measurement uncertainties relative to the results presented in this section can be found in Appendix C.3.

5.3.1. SINGLE FLETTNER ROTOR

This section deals with the results of the experiments carried out on the single Flettner rotor. The aim of these tests was twofold: on one hand, the force measurements were necessary to create reference data for the comparison with the results of the double Flettner rotor tests whereas, on the other hand, the measurements of the velocity field provided a useful insight to understand the nature of the aerodynamic interaction effects. As already mentioned in Section 5.2.1, the tests were carried out at $Re = 10^5$, however, experiments at $Re = 7.0 \cdot 10^4$ and at $Re = 1.8 \cdot 10^5$ were also performed. In the former case, the reason was to better compare the results of the single Flettner rotor with the available literature data. In the latter case, the aim was to investigate, within the possibilities offered by the setup employed, whether a higher Reynolds number would affect the lift and drag coefficients in the same manner described in Chapter 4.

The results of the single Flettner rotor are provided in Figure 5.7 and compared with the results of Badalamenti and Prince (2008), who performed tests at Reynolds number $Re = 1.9 \cdot 10^4$ on a Flettner rotor of similar aspect ratio ($AR = 5.1$), and using a similar configuration (one rotating and one fixed endplate of $D_E/D = 2$). Although due to the setup used in the current work, it was unfeasible to reach such a low Reynolds num-

ber, the results of the current experiments obtained at $Re = 7.0 \cdot 10^4$ show an excellent agreement with the results of [Badalamenti and Prince \(2008\)](#). The differences between the results obtained at lower and higher Reynolds numbers are in line with the findings reported in Chapter 4.

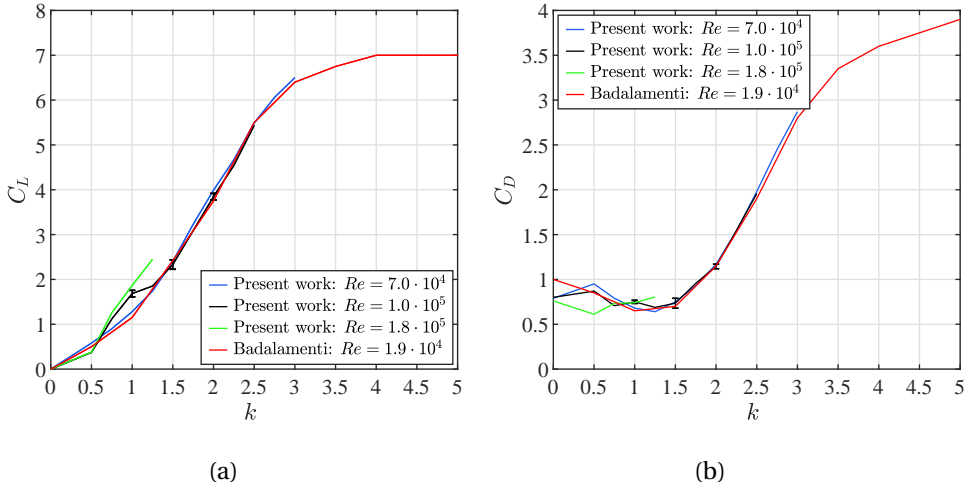


Figure 5.7: Lift (a) and drag (b) coefficients of the single Flettner rotor compared with the results of [Badalamenti and Prince \(2008\)](#)

Figure 5.9 shows the results of the velocity field measurements obtained at velocity ratios $k = 0$, $k = 1$, $k = 1.5$ and $k = 2$. For the sake of conciseness, only the results of Cobra Probe 2 are reported. The results of Cobra Probe 2 and Cobra Probe 3, in fact, show a similar trend and they can be considered representative for most of the cylinder's span. Cobra Probe 1 and Cobra Probe 4, on the other hand, captured a more peculiar trend due to their position closer to the Flettner rotor top and bottom tip vortices (see Figure 5.5). The full velocity field measurements can be found in Appendix C.1.

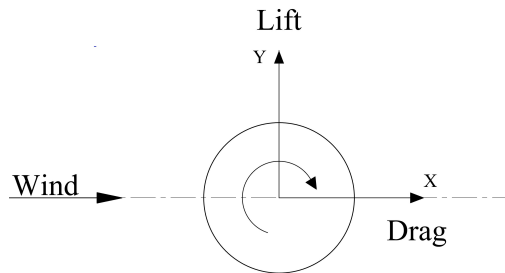


Figure 5.8: Direction of rotation and reference system used for the single Flettner rotor tests

The results depicted in Figure 5.9 illustrate the mean velocity magnitude and the mean direction of the flow. The velocity magnitude, that is normalized with the free

stream velocity, is indicated by the colourmap and the vector size. Conversely, the direction of the flow is suggested by the vector orientation. The results are given in terms of longitudinal (X -axis) and transversal (Y -axis) distance from the cylinder's vertical axis of symmetry, normalized with the cylinder diameter. The Flettner rotor rotates clockwise as shown in Figure 5.8, and it is located at the centre of the reference system ($x/D = 0$, $y/D = 0$).

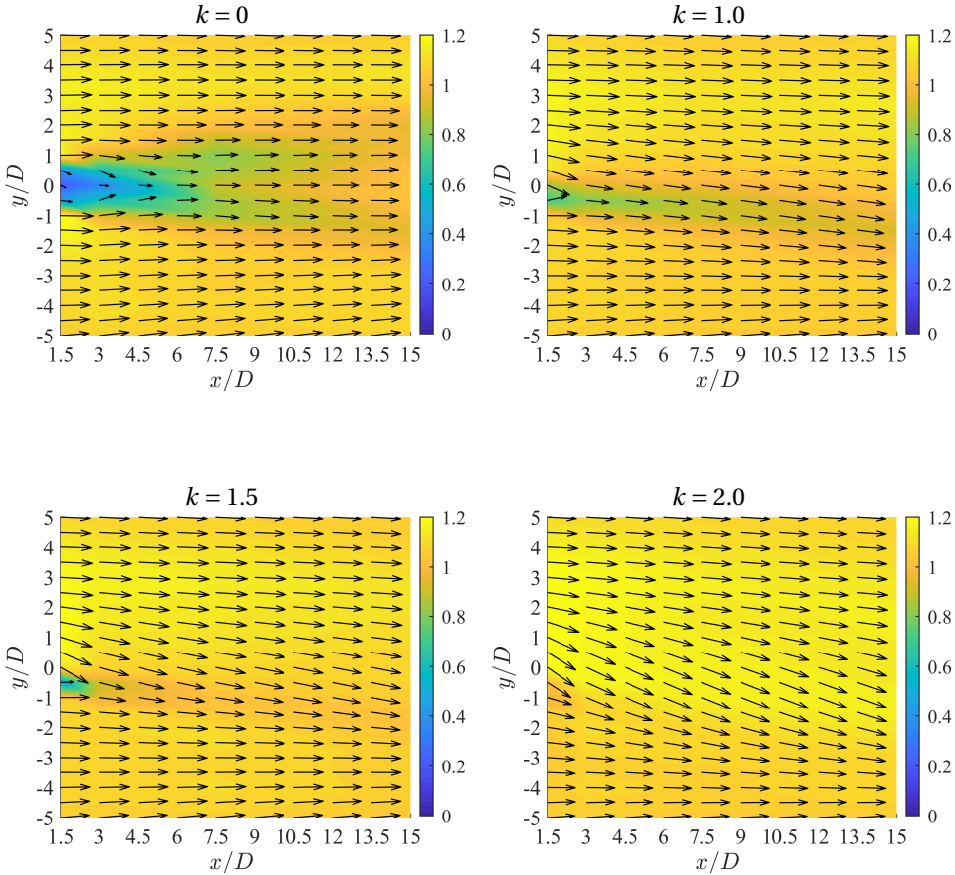


Figure 5.9: Velocity field past the single Flettner rotor at different velocity ratios k . Measurements of Cobra probe 2 taken at a height of 1.24 m from the ground. The results show the velocity field in a plane parallel to the floor

As it can be appreciated from the results report in Figure 5.9, the cylinder wake, that is clearly visible for $k = 0$, is reduced with the increase of the velocity ratio. At $k = 1$, the wake is already strongly reduced and deviated due to the downwash caused by the Flettner rotor's circulation. At $k = 2$, the wake is fully suppressed and the flow is heavily deviated, up to an angle of about 40° at the distance $x/D = 1.5$. It should also be noted that, in general, the downwash is mainly appreciable in the range $-3 < y/D < 3$ and that, in the range $1 < y/D < 4$, the circulation causes the flow speed to increase compared

to the free stream velocity. Higher velocity ratios mean a stronger circulation and, in turn, this leads to a more noticeable downwash and a more steep increase in wind speed in the range $1 < y/D < 4$. On the other hand, the circulation does not seem to cause any appreciable decrease in flow speed on the opposite side of the cylinder, in the range $-1 < y/D < -4$, where, in fact, the flow appears to have speed comparable to the free stream velocity.

5.3.2. INTERACTION: LIFT AND DRAG COEFFICIENTS

The lift and drag coefficients C_L and C_D of the two Flettner rotors were measured for several wind angles ranging between 15° and 180° (see conventions in Figure 5.6) to investigate the influence of different relative positions with respect to the incoming wind on the cylinders' aerodynamic coefficients. Depending on the gap distance, different wind angles were tested. These are reported in Table 5.1.

Table 5.1: Summary of the wind angles tested depending on the considered gap distance

Gap distance (GD)		Wind Angle (WA) [deg]						
$3D$	15 30 45	60 90 120 150 180						
$7.5D$	15 30 45	60 90 120 150 180						
$15D$	15 30 -	60 - 120 150 180						

The reason why no experiments were conducted for gap distance $GD = 15$ and wind angle $WA = 90^\circ$, is because, in this condition, the Flettner rotor positioned closer to the edge of the turntable would have been too near the wind-tunnel walls and this, arguably, would have jeopardized the measurements. Moreover, for the largest gap distance, it was decided not to perform experiments at $WA = 45^\circ$.

For each considered gap distance and wind angle, the experiments on the two Flettner rotors comprised a matrix of nine tests generated by all combinations of velocity ratios $k = 1$, $k = 1.5$ and $k = 2$. During the experiments, in fact, one Flettner rotor spun at a given velocity ratio, while the other spun for the entire set of velocity ratios $k = 1$, $k = 1.5$ and $k = 2$. Lift and drag were measured for all velocity ratio combinations. The results reported in Figure 5.10, Figure 5.11 and Figure 5.12 are also structured in this manner. In fact, the results for Flettner rotor A and Flettner rotor B show how, for the velocity ratio of interest, their lift and drag coefficients change due to the velocity ratio of the other Flettner rotor. The results of the single Flettner rotor used for the comparison are also reported for the same velocity ratio of interest. Following the conventions depicted in Figure 5.6, when analyzing the results, it should be borne in mind that Flettner rotor A is windward with respect to Flettner rotor B until $WA = 90^\circ$, whereas the opposite is true for wind angles $WA > 90^\circ$.

The results reported in Figure 5.10, Figure 5.11 and Figure 5.12 show that the Flettner rotors' relative position has a considerable influence on how C_L and C_D are affected by the aerodynamic interaction. This is in agreement with the findings of the literature discussed in Section 5.1. It appears evident, in fact, that, generally, the effects of the Flettner rotors' aerodynamic interaction become less pronounced with the increase of

the gap distance. This holds true for any considered velocity ratio considered.

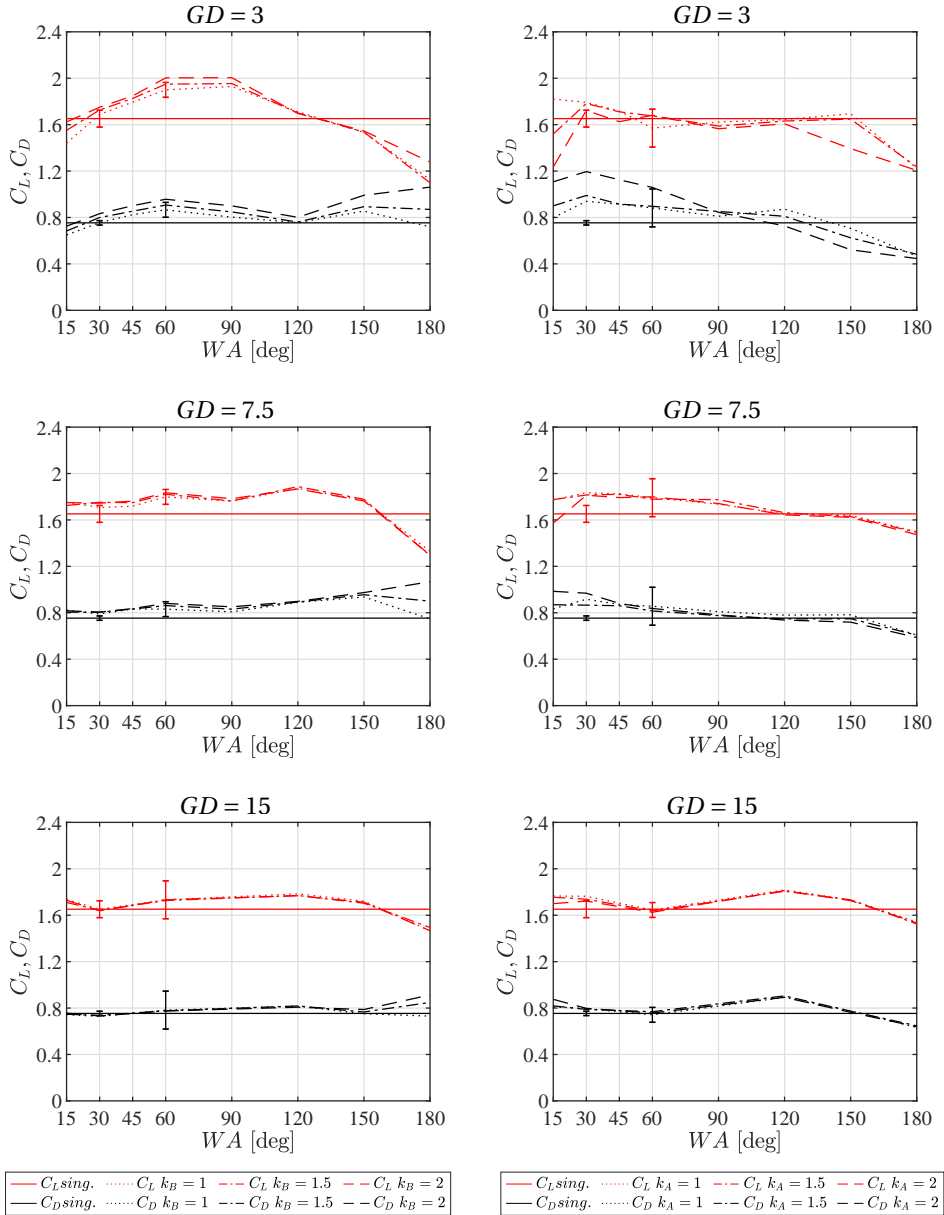


Figure 5.10: Lift and drag coefficients of Flettner rotor A (left) and Flettner rotor B (right) for different gap distances GD . Velocity ratio considered $k = 1$

The position of the two Flettner rotors with respect to the incoming wind direction, i.e. the wind angle, also appears to play an important role. When the two cylinders

come close to being aligned with the incoming wind direction, in fact, C_L and C_D of the downstream Flettner rotor are strongly influenced by the interaction effects. This can be noticed looking at the results of Flettner rotor A for $150^\circ \leq WA \leq 180^\circ$ as well as those of Flettner rotor B for $15^\circ \leq WA \leq 30^\circ$. In these wind angle ranges, in fact, the downstream Flettner rotor is, at least partially, immersed in the wake generated by the upstream one and these are, generally, the regions where the most prominent variations of lift and drag coefficients occur.

As suggested by the results of the velocity field measurements shown in Figure 5.9, the variations of lift and drag coefficients are mainly caused by two phenomena: a change in direction of the flow and a change of the flow velocity. The change in flow direction has an opposite effect on the lift and drag coefficient, i.e. when C_L increases C_D decreases and vice-versa. In particular, the circulation of the upstream Flettner rotor generates a downwash (unfavourable change in flow direction) that causes the lift coefficient of the downstream device to decrease and its drag coefficient to increase. Conversely, the upwash (favourable change in flow direction) generated by the downstream Flettner rotor on the upstream one has the opposite effect. It should be pointed out that during the experiments only the velocity field past the Flettner rotor was measured, meaning that the effects of the upwash on the velocity field were not appreciated. The change of the flow velocity, on the other hand, affects the lift and drag coefficient in a similar way: for a given change of flow speed, C_L and C_D are increased or decreased to the same extent. Ultimately, the magnitude of these phenomena depends on the velocity ratio, that, therefore, is the key parameter that regulates how the aerodynamic interaction affects the Flettner rotor lift and drag coefficients.

Let us now analyze the results more in detail. When Flettner rotor A is in the wake of Flettner rotor B, i.e. $150^\circ \leq WA \leq 180^\circ$, its C_L decreases while its C_D increases. Although to a different extent, this is the case for all gap distances considered (see Figure 5.10, Figure 5.11 and Figure 5.12). As previously explained, the reason why this occurs is due to the change in direction of the flow, i.e. the downwash caused by the circulation of Flettner rotor B. As it can be noticed from the results, this trend becomes more pronounced with the increase of the velocity ratio (stronger circulation) of this device. The results here analysed, however, are also influenced by the change of the flow velocity. This is particularly the case when Flettner rotor B is set at velocity ratios $k = 1$ or $k = 1.5$, for which, as shown Figure 5.9, a decrease of the flow velocity in the Flettner rotor's wake is still appreciable. Ultimately, the lift and drag coefficients are affected by the change in flow direction and velocity simultaneously. This can be observed in Figure 5.10, for example, looking at the results of Flettner rotor A for $150^\circ \leq WA \leq 180^\circ$ and for the three considered gap distances. At $WA = 180^\circ$, when the velocity ratio of Flettner rotor B is $k = 1$, the drag coefficient of Flettner rotor A decreases with respect to $WA = 150^\circ$. In fact, at $WA = 180^\circ$ the two Flettner rotors are aligned with the wind direction and, in this condition, the flow velocity reduction appears to be a more prominent effect compared to the downwash. When the velocity ratio of Flettner rotor B is increased, however, this effect is no longer appreciable because at velocity ratios $k = 1.5$ and $k = 2$ the flow velocity reduction in the wake of Flettner rotor B is less impactful compared to the change in flow angle and, as previously explained, this leads to an increase of the drag coefficient.

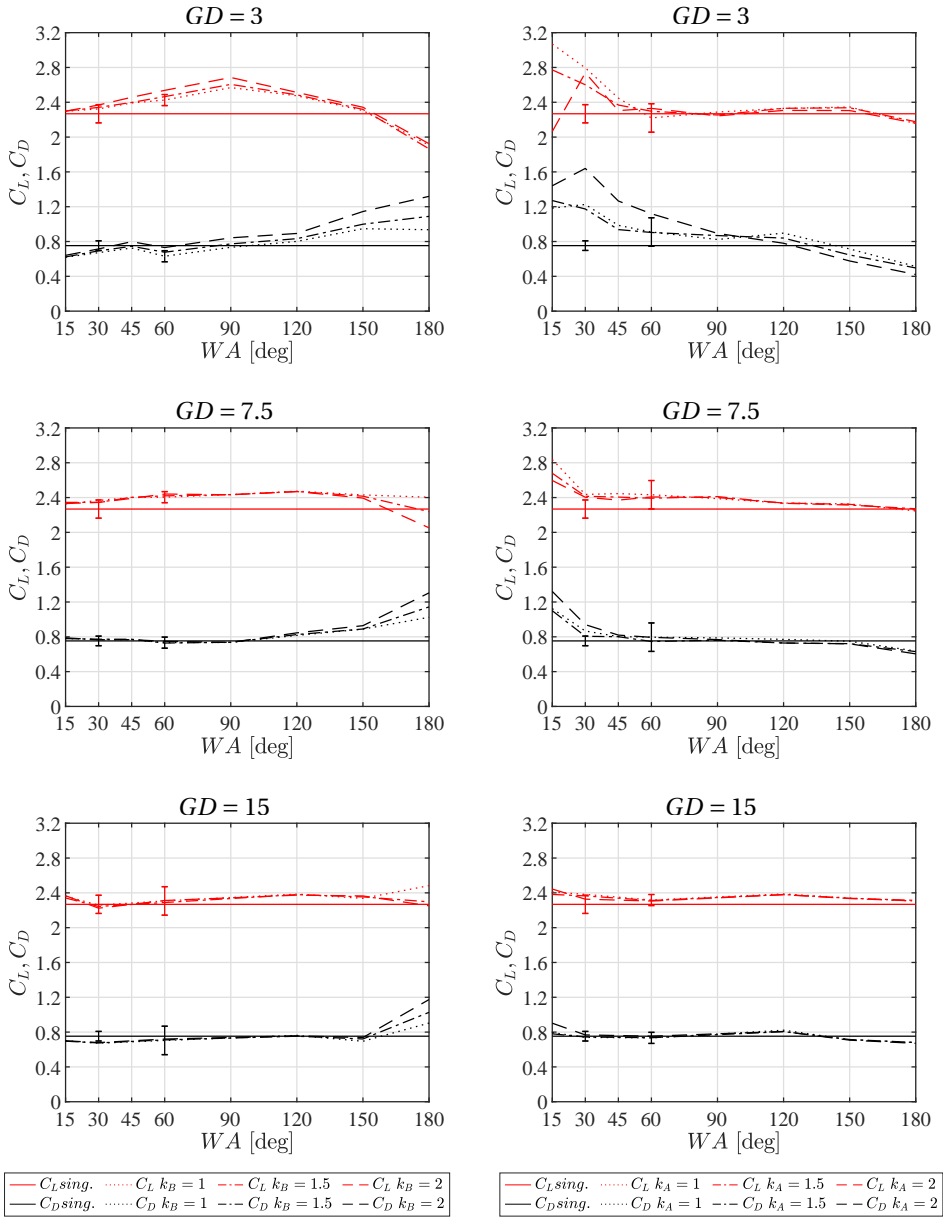


Figure 5.11: Lift and drag coefficients of Flettner rotor A (left) and Flettner rotor B (right) for different gap distances GD . Velocity ratio considered $k = 1.5$

Noticeable interaction effects do not only occur on the Flettner rotor that is in the wake of the other, but they also occur when the Flettner rotors are in other relative positions. In the range $45^\circ \leq WA \leq 120^\circ$, in fact, the aerodynamic coefficients of Flettner rotor A appear to be considerably affected by the behaviour of Flettner rotor B. In Figure

5.10, the drag coefficient and, more noticeably, the lift coefficient of Flettner rotor A is increased with respect to the corresponding coefficients of the single Flettner rotor.

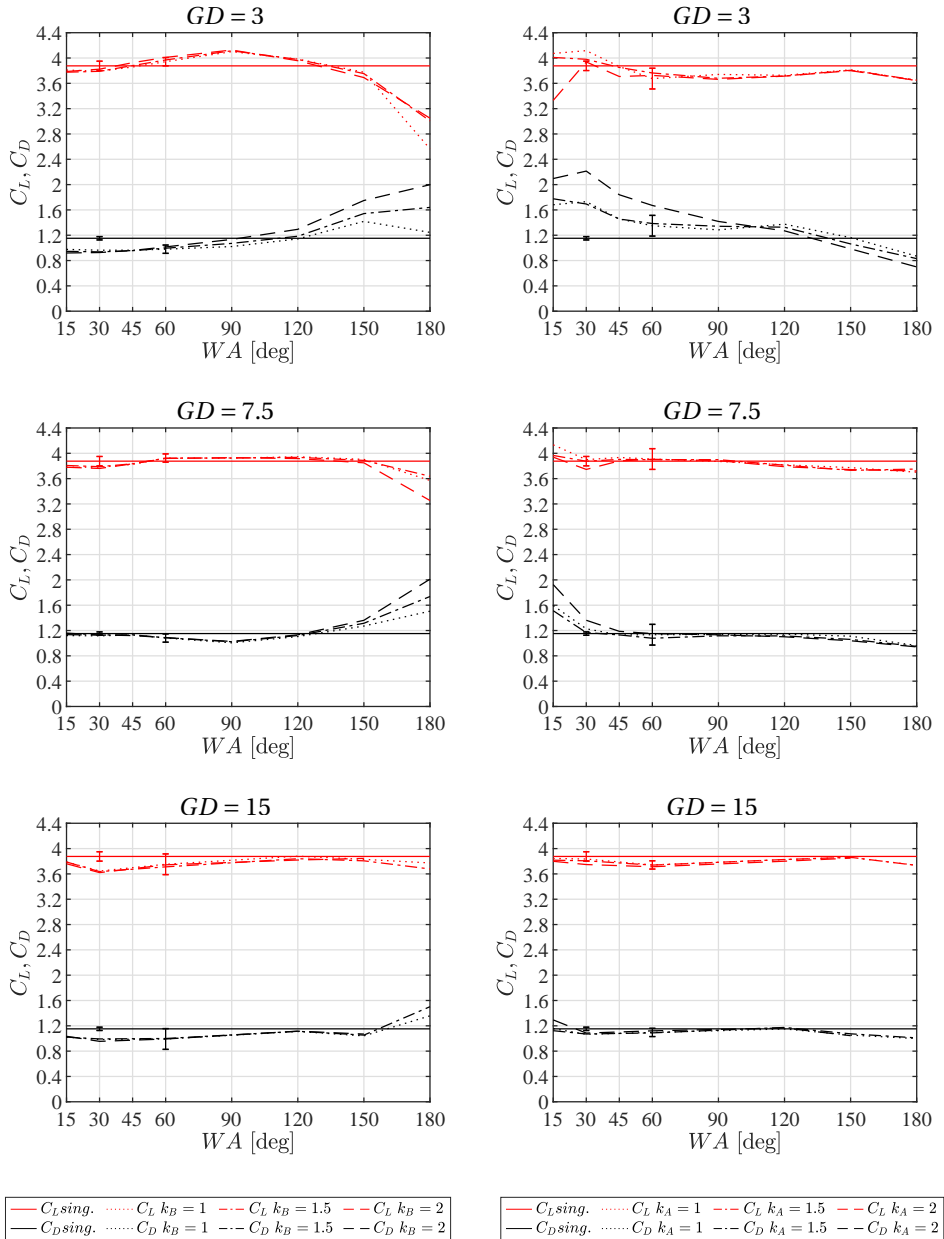


Figure 5.12: Lift and drag coefficients of Flettner rotor A (left) and Flettner rotor B (right) for different gap distances GD . Velocity ratio considered $k = 2$

For $WA > 90^\circ$, this is arguably due to the increase in flow speed caused by the circulation (of Flettner rotor B) as suggested by the results of the velocity field in Figure 5.9 (see range $1 < y/D < 4$). This phenomenon becomes less pronounced with the increase of the gap distance as well as with the increase of the velocity ratio considered (see results of Flettner rotor A in Figure 5.11 and Figure 5.12). On the other hand, when Flettner rotor B is windward to Flettner rotor A ($WA = 180^\circ$), it appears to be influenced by the proximity of the latter. This effect is most prominent for the considered velocity ratio $k = 1$ and the shortest gap distance (see results of Flettner rotor B in Figure 5.10). Once again, this phenomenon becomes less evident with the increase of the gap distance and, in general, also with the increase of the considered velocity ratio (see results of Flettner rotor B in Figure 5.11 and Figure 5.12).

5.3.3. INTERACTION: DRIVING AND HEELING FORCE COEFFICIENTS

As discussed in Section 5.3.2, the Flettner rotors' lift and drag coefficients depend on their velocity ratios as well as on their relative position with respect to the incoming wind direction. The driving and heeling force coefficients, on the other hand, are influenced by the Flettner rotors' velocity ratios, by their relative position with respect to the incoming wind direction but also by their layout on the ship's deck with respect to its heading. This means that, for one same gap distance, the location where the Flettner rotors are installed on the ship's deck affect their resulting driving and heeling force coefficients. The Flettner rotors can be installed in any desired arrangement on the ship, however, in the current study, two arrangements that, arguably, are nowadays the most commonly used for real-life applications, are analysed. These are the tandem (Figure 5.13) and the side-by-side arrangement (Figure 5.14). An example of a wind-assisted ship with two pairs of Flettner rotors installed, respectively, in side-by-side and tandem arrangement can be seen in Figure 5.1.

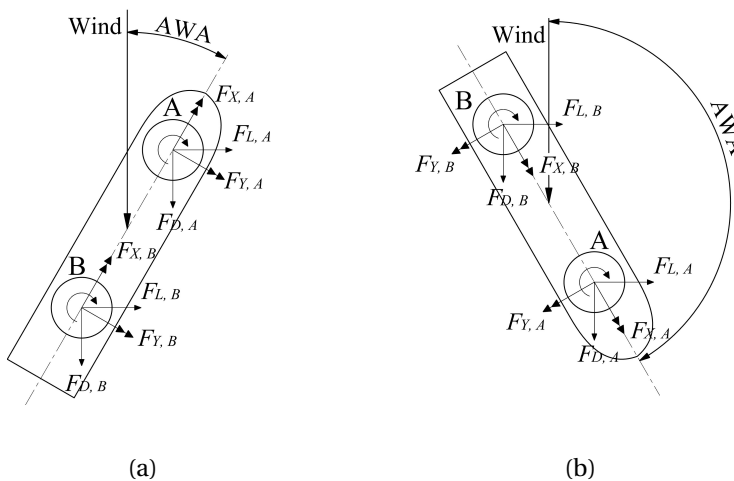


Figure 5.13: Flettner rotors in tandem arrangement. Conventions for $AWA < 90^\circ$ (a) and $AWA > 90^\circ$ (b)

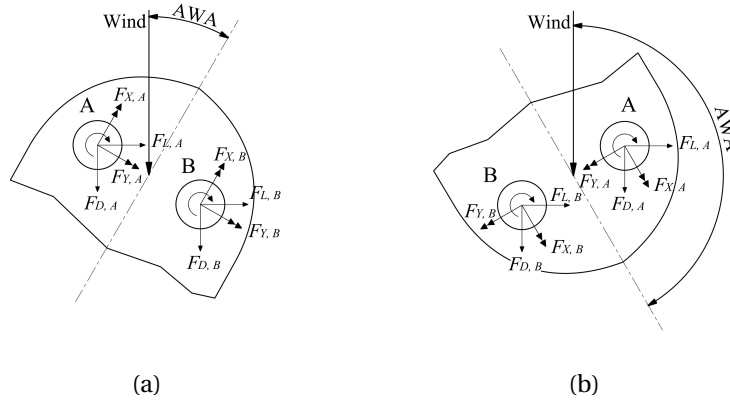


Figure 5.14: Flettner rotors in side-by-side arrangement. Conventions for $AWA < 90^\circ$ (a) and $AWA > 90^\circ$ (b)

Due to the setup used during the experiments on the two Flettner rotors (see Figure 5.6), the driving and heeling force coefficients were calculated from the results of C_L and C_D (Section 5.3.2) for a different set of apparent wind angles depending on the type of arrangement considered. These are reported in Table 5.2. Irrespective to the Flettner rotor arrangement, the driving and heeling force coefficients were derived according to:

$$\bar{C}_X = C_L \cdot \sin(AWA) - C_D \cdot \cos(AWA) \quad (5.1)$$

$$\bar{C}_Y = C_L \cdot \cos(AWA) + C_D \cdot \sin(AWA) \quad (5.2)$$

The present section aims at investigating the influence of the aerodynamic interaction on the performance of the considered Flettner rotor arrangements with respect to similar sets for which the interaction effects are neglected. To do so, the driving and heeling force coefficients of the analysed arrangement are calculated as the average, respectively, of C_X and C_Y of the two Flettner rotors belonging to such arrangement. These coefficients are then compared with those obtained for an analogous arrangement composed of two non-interacting devices whose data are derived from the results of the single Flettner rotor experiments.

Table 5.2: AWA at which C_X and C_Y are calculated depending on the Flettner rotor arrangement

Arrangement type	Apparent Wind Angle (AWA)							
	[deg]							
Tandem	30	45	60	90	120	150	180	-
Side by side	30	60	90	105	120	135	150	180

Considering the most common Flettner rotor installations currently in existence, the driving and heeling force coefficients when the two devices are in tandem arrangement are calculated for the three gap distances tested during the experiments. Conversely, when the Flettner rotors are in side-by-side arrangement, C_X and C_Y are calculated only

for the shortest gap distance. Figure 5.15 to Figure 5.18 show the results of the present analysis. Each case is investigated both in terms of C_X and C_Y coefficients and in terms of percentage change with respect to the case of two non-interacting Flettner rotors. For the sake of conciseness, only the most relevant results are reported herewith. The complete results can be found in Appendix C.2.

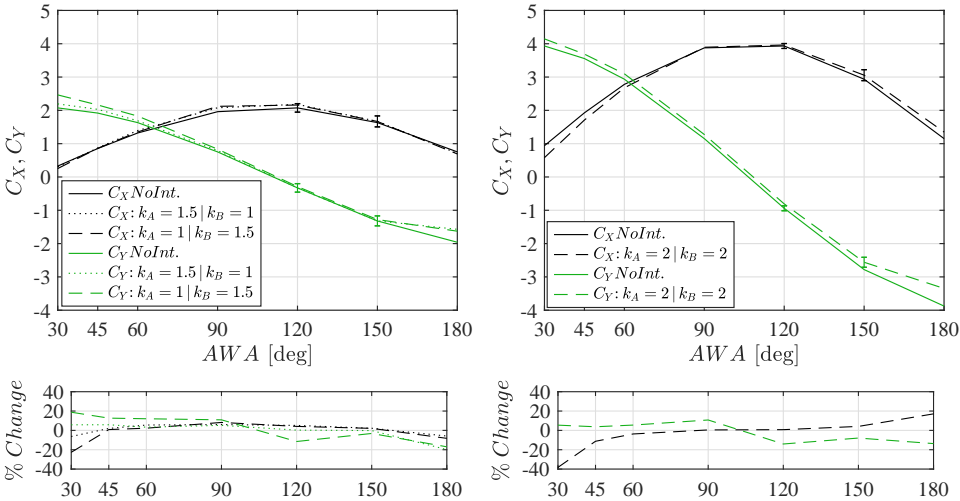


Figure 5.15: Driving and heeling force coefficients (top) and the percentage change of the double Flettner rotor results with respect to two non-interacting Flettner rotors (bottom). Velocity ratios: $k = 1$, $k = 1.5$ (left) and $k = 2$, $k = 2$ (right). Devices installed in tandem arrangement at gap distance $GD = 3$

In Figure 5.15 and Figure 5.16 the results of the two Flettner rotors placed at a distance of three diameters are given. For this condition, the most noticeable finding is that the driving and heeling force coefficients largely differ depending on whether the devices are installed in tandem or side-by-side arrangement. In fact, when the two Flettner rotors are in tandem arrangement the most relevant interaction effects occur when the ship is sailing close-hauled ($AWA = 30^\circ$) or downwind ($AWA = 180^\circ$). Conversely, for the side-by-side installation, the most evident interaction effects occur when the ship is sailing beam reach ($90^\circ \leq AWA \leq 120^\circ$). The magnitude of the interaction effects can be better appreciated by looking at the percentage change graphs reported at the bottom of the corresponding C_X and C_Y results.

Another substantial finding is that, for the same set of velocity ratios, the aerodynamic performance of the Flettner rotor ensemble varies depending on whether the windward Flettner rotor spins faster than the leeward one, or vice versa. This is evident, for example, for the side-by-side arrangement when the Flettner rotors spin at velocity ratios $k = 1$ and $k = 1.5$ and $AWA = 105^\circ$ (Figure 5.16). In this condition, if the windward device (Flettner rotor A) spins at a higher velocity ratio than the leeward one (Flettner rotor B), the driving force coefficient of the Flettner rotor ensemble increases by nearly 20% with respect to the non-interacting Flettner rotors. On the other hand, this increment does not occur when Flettner B spins faster than Flettner rotor A.

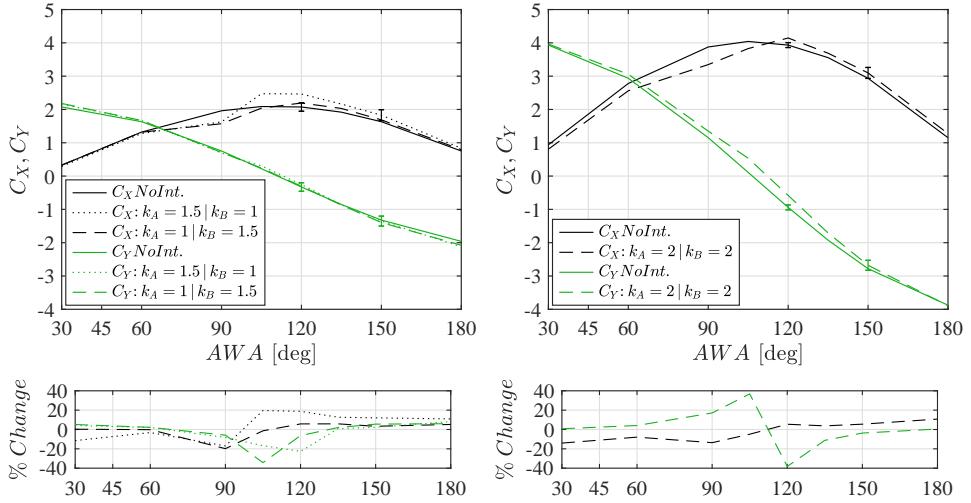


Figure 5.16: Driving and heeling force coefficients (top) and the percentage change of the double Flettner rotor results with respect to two non-interacting Flettner rotors (bottom). Velocity ratios: $k = 1, k = 1.5$ (left) and $k = 2, k = 2$ (right). Devices installed in side-by-side arrangement at gap distance $GD = 3$

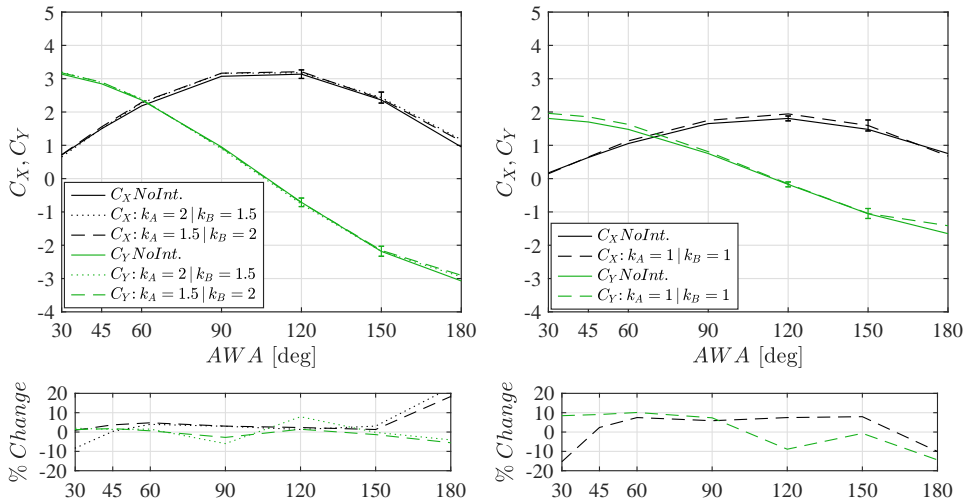


Figure 5.17: Driving and heeling force coefficients (top) and the percentage change of the double Flettner rotor results with respect to two non-interacting Flettner rotors (bottom). Velocity ratios: $k = 1.5, k = 2$ (left) and $k = 1, k = 1$ (right). Devices installed in tandem arrangement at gap distance $GD = 7.5$

Except for the largest gap distance and, in particular, for the tandem arrangement, the interaction effects occurring between the two Flettner rotors at $AWA < 45^\circ$ worsen the aerodynamic efficiency of the entire rig, i.e. C_X decreases and C_Y increases. This is caused by the decrease in C_L and the increase in C_D of the leeward Flettner rotor due to the downwash generated by the windward device (see relative figures in Section 5.3.2).

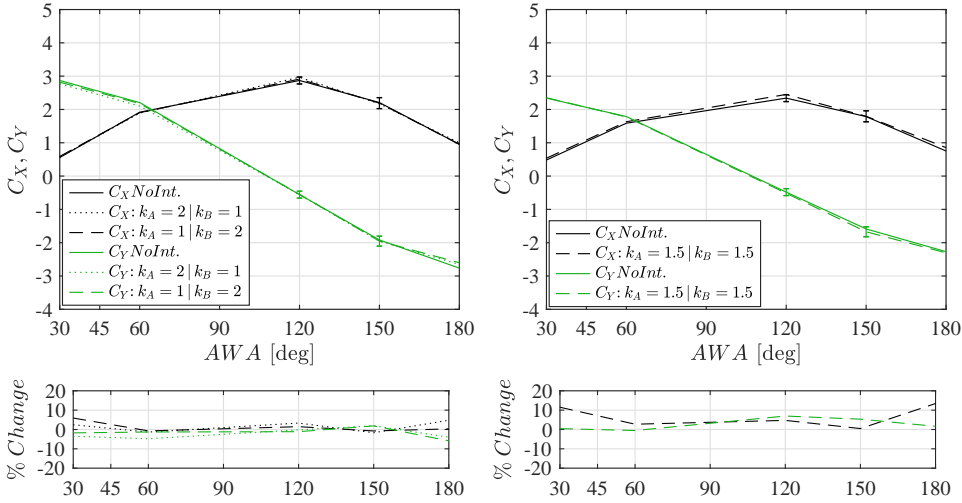


Figure 5.18: Driving and heeling force coefficients (top) and the percentage change of the double Flettner rotor results with respect to two non-interacting Flettner rotors (bottom). Velocity ratios: $k = 1$, $k = 2$ (left) and $k = 1.5$, $k = 1.5$ (right). Devices installed in tandem arrangement at gap distance $GD = 15$

The same phenomenon, however, often has a positive effect on the overall performance of the rig when the apparent wind angle is $AWA = 180^\circ$. This can be appreciated, for example, in Figure 5.15 when both devices spin at velocity ratio $k = 2$ as well as in Figure 5.17 for velocity ratios $k = 1.5$ and $k = 2$. In these conditions, in fact, the decrease in C_L and increase in C_D of the leeward Flettner rotor causes a rise of the driving force coefficient and a reduction of the heeling force coefficient of the Flettner rotor ensemble.

Following the trend of the results of the lift and drag coefficients, also for the driving and heeling force coefficients, the effects of the Flettner rotor aerodynamic interaction diminish with the increase of their gap distance. When the Flettner rotors are set 15 diameters apart, the two devices operate more independently, and their aerodynamic coefficients become closer to those of two non-interacting Flettner rotors. The results given in Figure 5.18, in fact, show that for apparent wind angles $60^\circ \leq AWA \leq 150^\circ$, the aerodynamic interaction has a minor influence on the driving and heeling force coefficients. Conversely, for $AWA < 60^\circ$ and $AWA > 150^\circ$, there is still a noticeable effect of the interaction on the aerodynamic performance of the considered Flettner rotors.

5.3.4. REYNOLDS NUMBER EFFECT ON AERODYNAMIC INTERACTION

As discussed in Section 5.2.1, the experiments to investigate the aerodynamic interaction were carried out at Reynolds number $Re = 1.0 \cdot 10^5$, meaning that the flow experienced by the two Flettner rotors was in the subcritical regime. As demonstrated in Chapter 4, however, the Reynolds number influences the drag and, within certain conditions, the lift coefficient of a Flettner rotor. Arguably, it should be expected that this also plays a role in the way multiple Flettner rotors interact. To investigate whether this is the case, during the tests conducted on the Delft Rotor discussed in Chapter 4, measurements of the velocity field were taken in the wake of the large-scale rotating cylinder. The Delft

Rotor had a diameter $D = 1.0$ m and a span $H = 3.73$ m. Due to its span, and considering that height of the wind-tunnel test section, the tip vortices were suppressed and, in this sense, the tests can be deemed two-dimensional. See Chapter 4 for further details.

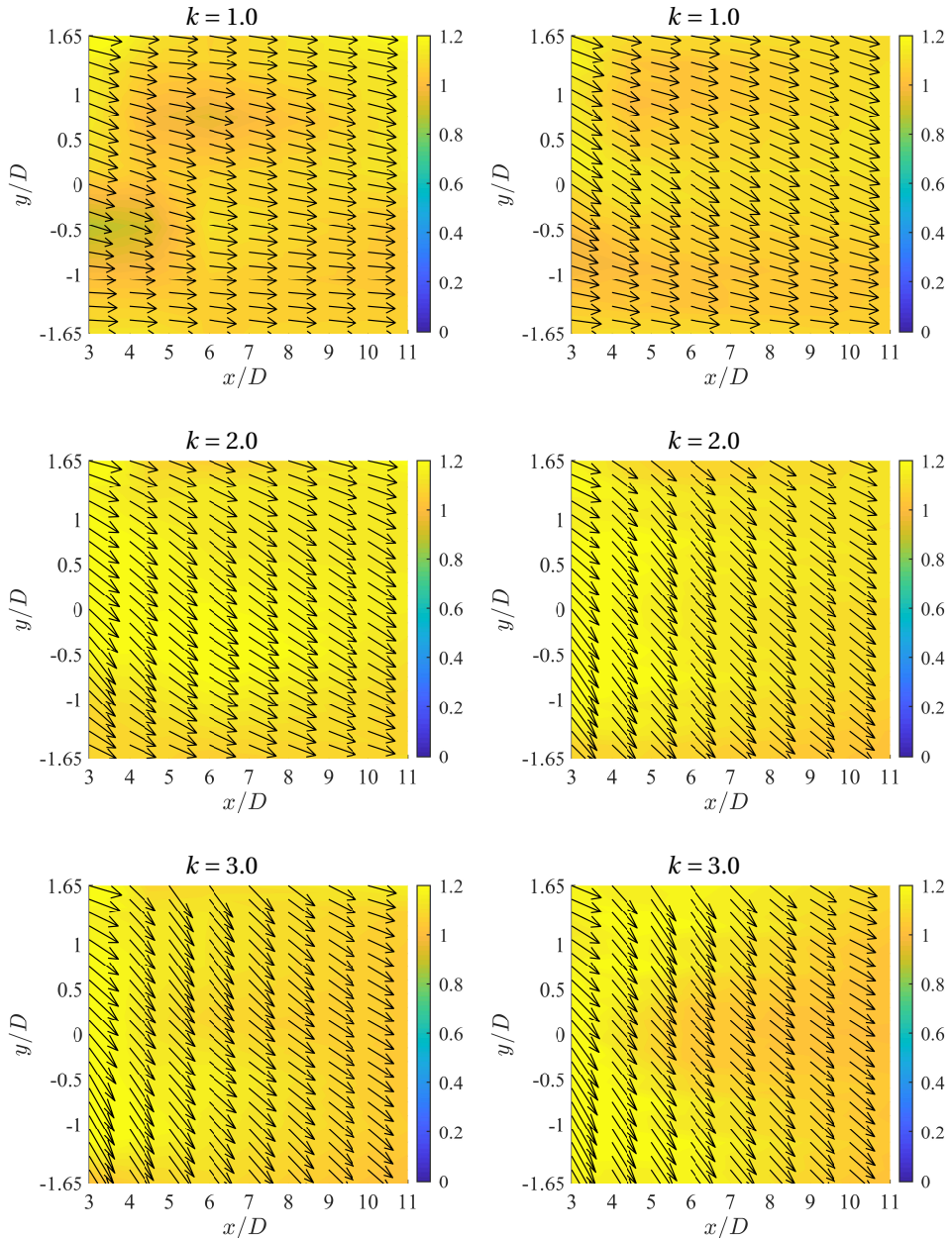


Figure 5.19: Velocity field past the Delft Rotor at different velocity ratios: Reynolds number $Re = 2.5 \cdot 10^5$ (left) and $Re = 5.5 \cdot 10^5$ (right). The measurements were taken at the cylinder mid-span height

The velocity field was measured using the same type of equipment described in Section 5.2.3, however, in this case, being the flow two-dimensional, measurements were only taken at the Flettner rotor mid-span height. Tests were carried out for two Reynolds number, namely $Re = 2.5 \cdot 10^5$ (critical regime) and $Re = 5.5 \cdot 10^5$ (supercritical regime), and for three different velocity ratios, i.e. $k = 1$, $k = 2$ and $k = 3$. Following the same conventions used in Figure 5.9, the results of the velocity field measurements are reported in terms of mean velocity magnitude and mean direction of the flow. The velocity magnitude, that is normalized with the free stream velocity, is indicated by the colourmap and the vector size. On the other hand, the direction of the flow is suggested by the vector orientation. Also for the results reported in Figure 5.19 it should be assumed that the Flettner rotor is located at the centre of the reference system ($x/D = 0$, $y/D = 0$) and it rotates clockwise. It should be pointed out, however, that due to the major dimensions of the large-scale Flettner rotor, a reduced number of positions in terms of x/D and y/D were tested compared to the experiments carried out on the smaller Flettner rotor used in the present work (see Figure 5.9 and Figure 5.19).

The results reported in Figure 5.19 show a trend comparable to the results depicted in Figure 5.9. In fact, it can be appreciated that the increase of the velocity ratio reduces the velocity deficit in the wake of the Flettner rotor while it intensifies the deflection of the flow. The Reynolds number appears to have a similar effect. At velocity ratio $k = 1$, in fact, an area of reduced velocity can be found at $y/D = -0.5$ and $3 \leq x/D \leq 4$ for $Re = 2.5 \cdot 10^5$. At Reynolds number $Re = 5.5 \cdot 10^5$, however, this is no longer visible. Also, at the higher Reynolds number, the flow appears to be more deflected. This is the case both for $k = 1$ and for $k = 2$, while for $k = 3$ this does not occur. A plausible explanation of this phenomenon can be found by looking at the results of the influence of the Reynolds number on the Flettner rotor lift coefficient (see Figure 5.20).

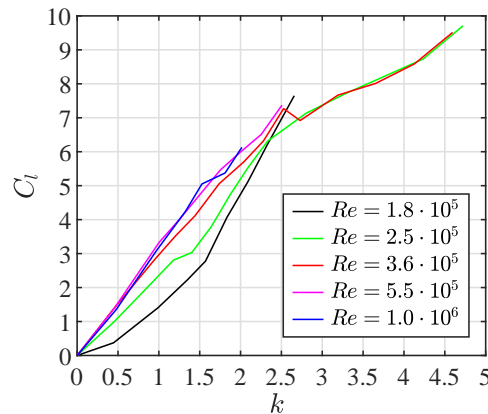


Figure 5.20: Delft rotor lift coefficient for different Reynolds numbers obtained from the results of Chapter 4

As discussed in Section 5.3.1, in fact, the circulation in the flow caused by the Flettner rotor spin alters the velocity field: the circulation tends to deflect the direction of the flow and to suppress the velocity deficit in the Flettner rotor's wake. Since lift is directly dependent on circulation, looking at Figure 5.20, it can be appreciated the reason why

a higher Reynolds number causes a larger flow deflection and a more noticeable suppression of the velocity deficit in the Flettner rotor's wake. It appears, in fact, that a higher Reynolds number entails a higher lift coefficient. Nonetheless, this is the case up to velocity ratio $k = 2.5$, above which the Reynolds number influence seems to be negligible. This is reflected in the results of the velocity field measurements depicted in Figure 5.19. For velocity ratio $k = 3$, in fact, no significant differences can be noticed for the results obtained at $Re = 2.5 \cdot 10^5$ and at $Re = 5.5 \cdot 10^5$. Moreover, Figure 5.20 also indicates that above $Re = 3.6 \cdot 10^5$ the lift coefficient seems to be insensitive to scale effects. Using the same rationale, therefore, it could be assumed that above this threshold the Reynolds number does not influence the velocity field past a Flettner rotor. In turn, it can be argued that, in the supercritical flow regime, the Reynolds number does not affect the aerodynamic interaction occurring between multiple Flettner rotors.

5.4. CONCLUSIONS

The present investigation deals with a series of wind-tunnel experiments on two similar Flettner rotors aimed at gaining more insights regarding the effects of the aerodynamic interaction on their performance. To provide a baseline for comparison, previous tests were carried out on a single Flettner rotor for analogous conditions. The results of the experimental campaign are reported in terms of lift and drag coefficients, as well as in the form of driving and heeling force coefficients. In the former case, the effects of the aerodynamic interaction occurring between the two Flettner rotors are shown on the lift and drag coefficients of each device. For the latter case, conversely, the driving and heeling force coefficients are presented for the combination of the two Flettner rotors and compared for similar sets of two non-interacting devices

From the results of the lift and drag coefficients, it is understood that the velocity ratio of each Flettner rotor and their relative position (gap distance and wind angle) are determining factors for the influence of the aerodynamic interaction on the Flettner rotor performance. In particular, it is shown that the interaction effects are, generally, most noticeable for shorter gap distances and when the two Flettner rotors come close to being aligned with the wind direction. The role of the velocity ratio appears to be more complex but, nonetheless, distinguishable trends can be identified with the aid of the velocity field measurements carried out in the wake of the single Flettner rotor. From these results, two main phenomena could be detected: the change of the incoming wind speed and the deflection of the incoming flow angle. For the former, a decrease of the incoming wind speed is found at lower velocity ratios whereas higher k values lead to an increase of the wind speed with respect to the freestream velocity. For the latter, it is understood that the downwash gains strength with the increment of the velocity ratio. For most cases, sensible conclusions can be drawn by applying the findings of the velocity field measurements to the results of the lift and drag coefficients.

The output of C_X and C_Y is the consequence of the trends of the lift and drag coefficients. In this case, however, it is demonstrated that the Flettner rotor layout on the ship's deck (in the current study, tandem versus side-by-side arrangement) is a key factor for the aerodynamic performance of the entire rig. Depending on the type of arrangement, the control of the velocity ratio of each Flettner rotor, i.e. whether the windward device rotates faster or slower than the leeward one, has the capacity to mitigate the detrimental

effect of the aerodynamic interaction or, in some cases, to increase the performance of the entire rig with respect to a comparable set of non-interacting devices. In general, it can be concluded that the best overall aerodynamic performance (that does not necessarily coincide with the best performance of the ship due to the coupling between its aero/hydrodynamic forces) is reached when the Flettner rotors are set furthest apart, i.e. when their aerodynamic interaction is minimized. In case this condition is not achievable due, for example, to a limited deck space, it is shown that for the shortest gap distance a higher aerodynamic efficiency is attained when the Flettner rotors are set in side-by-side arrangement for $AWA < 60^\circ$, and, for $AWA > 60^\circ$, when the devices are installed in a tandem arrangement.

To conclude, it is argued that the Reynolds number may affect the aerodynamic interaction occurring between multiple Flettner rotors. For the conditions analysed, it appears that scale effects may become marginal for velocity ratios $k \geq 2.5$ and when the flow is in a supercritical regime. Further research should be conducted on this topic to investigate the veridicality of these assumptions.



6

VALIDATION OF AN AERODYNAMIC INTERACTION MODEL

The ultimate goal of the Sail Assist project is to deliver a tool capable of predicting the aerodynamic performance of a generic wind-assisted ship in a quick yet reliable manner. To accomplish this mission, like Velocity Prediction Programs commonly used to assess the performance of sailing yachts, such tool should be based on inexpensive calculations that, nevertheless, can assure a sufficient degree of accuracy to properly differentiate between one ship design and the other. From the literature, it emerges that a mathematical model with characteristics compatible with the desired features was already employed to compute the performance of two competing sailing yachts. This chapter deals with the validation of this mathematical model against the experimental results previously presented in this dissertation. The results of the validation indicate that the mathematical model under analysis is currently not able of properly predicting the effects of the interaction on the resulting overall aerodynamic forces. Nonetheless, it is argued that the considered method could represent a useful starting point from which develop a more sophisticated aerodynamic model.

6.1. INTRODUCTION

The final objective of the Sail Assist project is to deliver a tool capable of estimating the performance of a generic wind-assisted ship. As argued in Chapter 1, such a tool should follow the same rationale on which Velocity Prediction Programs for sailing yachts were developed. To reach this goal, the aerodynamic module of the Sail Assist Performance Prediction Program should be able to deal with wind-propulsion systems of different types, employed in any desired number of devices and installed at any desired location on the ship's deck. Moreover, to be suitable for the scope of the Performance Prediction Program, the aerodynamic module should be capable to provide quick yet reliable results, meaning that it should be based on inexpensive calculations.

From the literature, it appears that a method with characteristics compatible with those above discussed can be found in the work of [Roncin and Kobus \(2004\)](#). This study, in fact, deals with the simulation of two sailing yachts competing in a match race. For the aerodynamic component of the simulation model, the authors assume that the aerodynamic force generated by each boat's rig can be calculated by considering the rig own aerodynamic characteristics, i.e. the lift and drag forces generated by the sails in a given wind condition, and the effects of the aerodynamic interaction occurring between the rigs of the two competing yachts. More specifically, this method assumes that the aerodynamic characteristics of each boat's rig are known while the effect of the interaction on their resulting aerodynamic forces is calculated. In the context of wind-assisted propulsion, this approach could be applied to calculate the aerodynamic performance of a ship's rig composed by multiple wind-assist devices. In fact, from the literature review reported in Chapter 2, it appears that the performance data, i.e. the lift and drag coefficients, of a large number of wind-assist devices are nowadays available or, nevertheless, can be obtained with a limited effort (e.g. a limited number of CFD computations or experiments). Conversely, the same literature also indicates that, when multiple wind-assist devices are used, the effect of the aerodynamic interaction on their overall performance is typically neglected.

In the method proposed by [Roncin and Kobus \(2004\)](#), the effects of the aerodynamic interaction are calculated assuming that the perturbation of the velocity field caused by the sails is represented by a single horseshoe vortex and a self-preserved viscous plane wake. The simplicity of the mathematical model employed assures quick and inexpensive calculations, making it suitable to be used in the aerodynamic module of the Performance Prediction Program. Moreover, this approach can, theoretically, be able to deal with any passive (sail, wingsails, Dynarig, etc.) and active (Flettner rotor and Turbosail) wind-assist device, employed in any desired number and installed in any generic arrangement on the ship's deck. These features meet the requirements for the aerodynamic module of the performance prediction tool.

In this scenario, the final chapter of the present doctoral dissertation deals with the validation of the aerodynamic mathematical model proposed by [Roncin and Kobus \(2004\)](#). In particular, the results of the experiments carried out on two rigid sails and two Flettner rotors, reported in Chapter 3 and Chapter 5 respectively, are used to validate the capability of this mathematical model to properly estimate the effects of the aerodynamic interaction on the performance of two generic wind-propulsion systems.

6.2. MATHEMATICAL MODEL

The mathematical model proposed by [Roncin and Kobus \(2004\)](#) to calculate the effects of the aerodynamic interaction on two competing sailing boats is comprised of two separated components, i.e. an inviscid component, based on the horseshoe vortex theory, and a viscous component, based on semi-empirical formulas. The vortex model is a function of lift while the viscous component is a function of drag. In particular, the lift generated by the boat's sail plan or, in the present case, by the wind-propulsion system under consideration, depends on the circulation. The circulation, in turn, generates a change in the flow field by altering the speed and direction of the flow. On the other hand, the drag of the wind-assist device determines the magnitude of its wake, i.e. the reduction in flow speed. Finally, the inviscid and viscous components are superimposed, meaning that the perturbation in the velocity field around the considered wind-propulsion system depends on the amount of lift and drag it generates. More specifically, the method here discussed is based on the following assumptions:

- The wind-propulsion system, regardless of its nature¹, is simplified as a mere generator of lift and drag. Depending on a controlling parameter (e.g. the angle of attack for a wingsail or the velocity ratio for the Flettner rotor), the wind-propulsion system under consideration generates a certain amount of lift and drag.
- Due to the previous assumption, the details that differentiate between one wind-propulsion system and another are neglected. For example, in the present mathematical model, the fact that two Flettner rotors have different aspect ratios is taken into account only in the measure of having a different lift and drag coefficient.
- The lift and drag generated by the wind propulsor affect the velocity field around itself in two ways: they cause a change in flow speed and flow angle.
- The effects of aerodynamic interaction are consequential to the change in the velocity field, i.e. the perturbation of the velocity field affects the aerodynamic forces of the wind-propulsion systems immersed in the perturbed velocity field.

Mathematically, the velocity field resulting from the perturbations caused by the n wind propulsion systems employed on the ship can be calculated as:

$$\mathbf{V}_{perturbed} = \mathbf{V}_{\infty} + \sum_{n=1}^N \mathbf{V}_{HSV_n} + \sum_{n=1}^N \mathbf{V}_{viscous_n} \quad (6.1)$$

where the change in the velocity field due to the horseshoe vortex system of each wind propulsor reads:

$$\mathbf{V}_{HSV} = \mathbf{V}_{AB} + \mathbf{V}_{A\infty} + \mathbf{V}_{B\infty} \quad (6.2)$$

The horseshoe vortex system, as shown in [Figure 6.1](#), comprises the bound vortex \mathbf{V}_{AB} and the two trailing vortices $\mathbf{V}_{A\infty}$ and $\mathbf{V}_{B\infty}$. The vortex strength (circulation) Γ is defined as:

¹As explained in [Chapter 2](#), due to its peculiarities, the kite sail is not considered in this work.

$$\Gamma = \frac{F_L}{\rho \cdot H \cdot V_\infty} \quad (6.3)$$

This indicates that \mathbf{V}_{HSV} is solely dependent on the lift force (F_L) generated by the wind-propulsion system of span H . Further details on the horseshoe vortex method employed in the current work can be found in Appendix D.1.

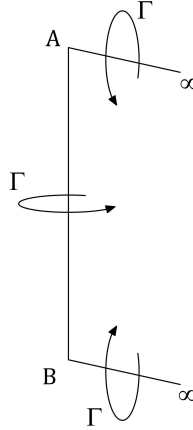


Figure 6.1: The horseshoe vortex system

The perturbation caused by the viscous component $\mathbf{V}_{viscous}$ is calculated according to a semi-empirical formula as proposed by Schlichting (1979). It should be noticed that in the study of Roncin and Kobus (2004) the viscous component is obtained using a different formulation proposed by Tennekes and Lumley (1974). In the present work, however, following the procedure of van Walree and Willemsen (1988) to calculate the velocity field around offshore structures, the formulation of Schlichting was preferred. Therefore, for each wind-assist device, $\mathbf{V}_{viscous}$ is computed as:

$$\mathbf{V}_{viscous} = \mathbf{V}_\infty \cdot \left(1 - 0.98 \cdot \left[\frac{x}{C_D \cdot d_w} \right]^{-0.5} \cdot \left[1 - \left(\frac{2y}{b} \right)^{1.5} \right]^2 \right) \quad (6.4)$$

where b is defined as:

$$b = 1.14 \cdot [C_D \cdot d_w \cdot x]^{0.5} \quad (6.5)$$

and d_w is the chord length or diameter of the wind propulsor considered. From Eq. 6.4, it can be seen that the viscous component $\mathbf{V}_{viscous}$ is solely dependent on the drag generated by the wind-assist device.

Once the perturbed velocity field $\mathbf{V}_{perturbed}$ is calculated, the resulting aerodynamic forces of each installed wind-propulsion system can be computed. In particular, the following procedure is used:

- First, the new lift and drag forces are calculated using the lift and drag coefficients of the single (undisturbed) wind-assist device and the magnitude of the velocity $V_{perturbed}$.
- Using the components of $V_{perturbed}$ perpendicular and parallel to the undisturbed wind direction, the downwash (upwash) is calculated at the coordinates where the wind-assist devices are placed.
- The calculated downwash (upwash) angles are then used to reorient the new lift and drag force vectors of each wind-assist device to be respectively perpendicular and parallel to $V_{perturbed}$.
- Finally, the resulting lift and drag coefficients are obtained by non-dimensionalising the new lift and drag force with the undisturbed flow velocity.

This procedure has a twofold aim. Firstly, apart from a number of simplifications proper of the method, it aims at mimicking the physics that causes the change in aerodynamic forces due to a perturbation in the velocity field. Secondly, to ensure a fair comparison between the calculations and the measurements, it resembles the way the resulting lift and drag coefficients were obtained during the experiments.

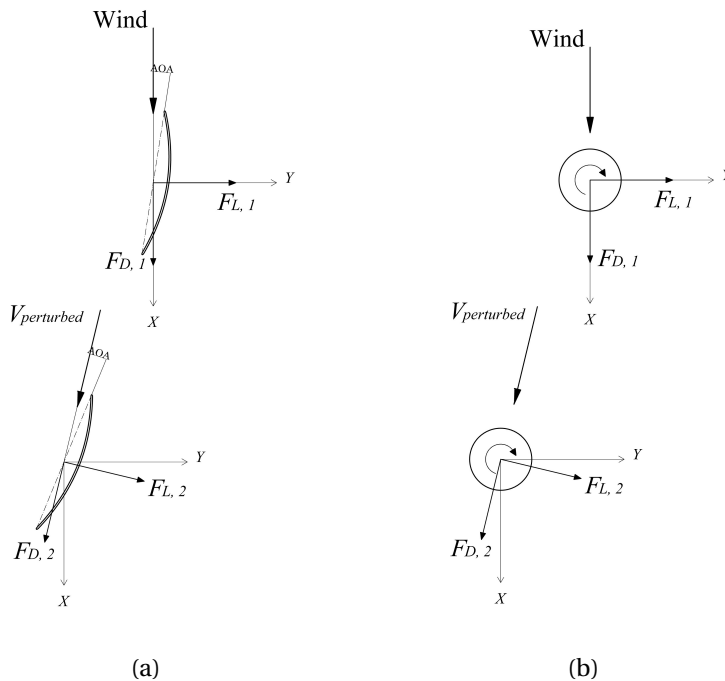


Figure 6.2: Change in aerodynamic forces of a Dynarig (a) and a Flettner rotor (b) due to a perturbation in the velocity field

To clarify the procedure above presented, Figure 6.2 shows how the aerodynamic

forces of a Dynarig and a Flettner rotor change due to the perturbed velocity field generated by a nearby wind-propulsion system. In the case of Flettner rotors, being cylinders axisymmetric, the magnitude of the lift and drag vectors is independent on the incoming wind direction. The orientation of the lift and drag vectors, conversely, follows the direction of the incoming wind so that they are respectively perpendicular and parallel to it. On the other hand, in the case of Dynarigs, lift and drag depend on the wind direction since a change in the orientation of the incoming wind would generate a change in the sail angle of attack. It should be noticed, however, that this in real-life applications does not occur since Dynarigs are trimmed for optimum performance: they are adjusted according to the perturbed wind direction in order to maintain the best angle of attack for each apparent wind angle the ship is sailing at. In view of these conditions, the results presented in Section 6.3 are obtained using the procedure above described both for Dynarigs and Flettner rotors.

6.3. RESULTS OF THE AERODYNAMIC MODEL

6.3.1. COMPARISON WITH DYNARIG EXPERIMENTS

In this section, the results obtained with the mathematical model are compared with the results of the experiments carried out on the two Dynarigs. More specifically, the results expressed in terms of overall driving and heeling force coefficients, as reported in Chapter 3, are herewith used for validation.

The results of the mathematical model were obtained in a similar fashion to the procedure used to collect the sails' aerodynamic force data during the experiments. In fact, for a given gap distance and wind angle, the trimming of the two Dynarigs (to achieve the largest driving force) was mimicked by calculating C_X and C_Y for all combinations of the wind propulsors' angles of attack. This procedure was carried out taking into account the effects of the aerodynamic interaction caused by the lift and drag forces corresponding to each angle of attack of the two wind-propulsion systems. At the end of this procedure, the largest overall driving force coefficient, and the corresponding heeling force coefficient were selected.

Figure 6.3 shows the comparison between the calculations and the experimental results obtained at a gap distance of 2.5 chord lengths. The results indicate that the mathematical model is only partially able to predict the effects of the aerodynamic interaction on the overall driving and heeling force coefficients. In particular, it is shown that for $AWA \leq 45^\circ$ and $AWA > 165^\circ$ the mathematical model predicts a decrease of C_X that is in agreement with the experimental results. On the other hand, in the interval $45^\circ < AWA < 165^\circ$, the calculations fail to match the increase of driving force coefficient measured during the wind-tunnel tests on the two rigid sails. In this range, the results of the mathematical model practically coincide with the results obtained by omitting the aerodynamic interaction effects (Exp. Single sail), meaning that, for this range of apparent wind angles, the benefits introduced by using this mathematical model are negligible.

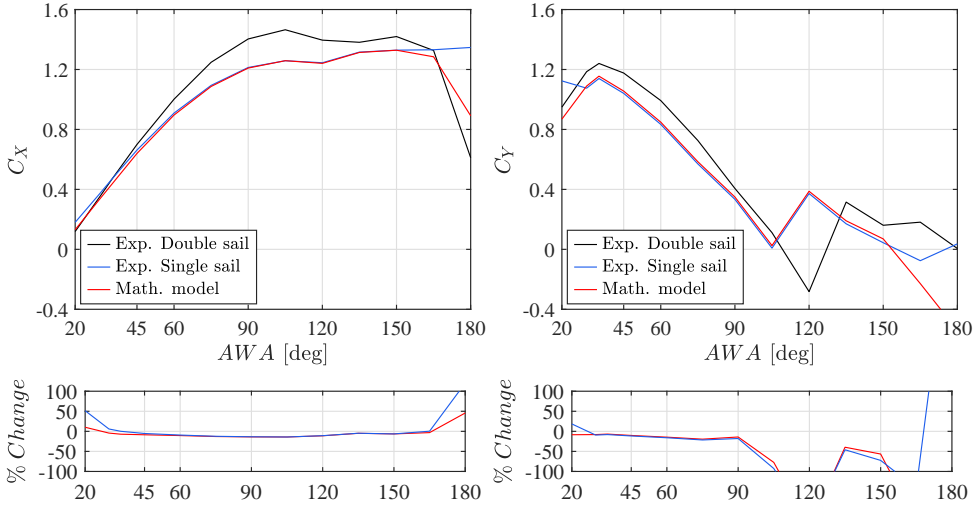


Figure 6.3: Comparison of the calculations and the single sail results with respect to the double sail (top) and their relative percentage change (bottom). Driving (left) and heeling (right) force coefficients. $GD = 2.5$

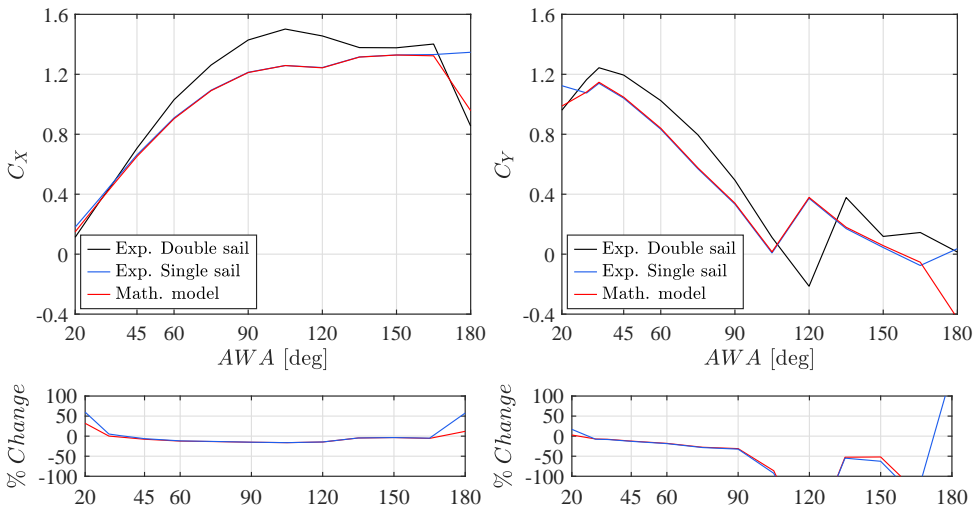
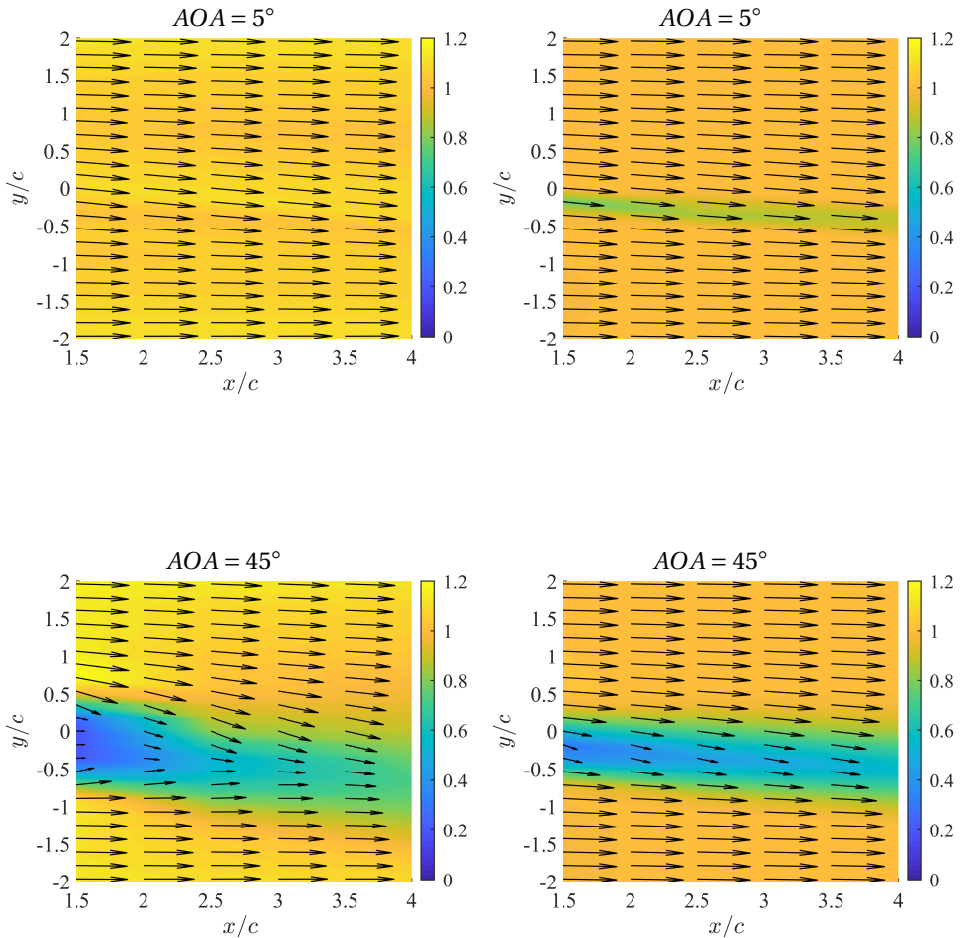


Figure 6.4: Comparison of the calculations and the single sail results with respect to the double sail (top) and their relative percentage change (bottom). Driving (left) and heeling (right) force coefficients. $GD = 4$

Regarding the results of the heeling force coefficient, compared to the case in which the interaction is neglected, the use of the aerodynamic mathematical model improves the performance estimate only for $AWA \leq 30^\circ$. For larger apparent wind angles, and until the heeling force is a concern for the overall performance of the ship (upwind sailing, typically $AWA \approx 100^\circ$), the computational results and the results obtained by neglecting the effects of the aerodynamic interaction equally underestimate C_y . Apart

from some minor differences, the analysis of the results here reported also holds true for the case in which the sails are set four chord lengths apart (see Figure 6.4).

To better understand the differences between the experimental results and the calculations, the velocity fields obtained using the mathematical model and measured during the single-sail tests are compared in Figure 6.5. The results of the comparison indicate that, at $AOA = 5^\circ$, the mathematical model appears to overpredict the magnitude of the wake, while for $AOA = 45^\circ$ and $AOA = 90^\circ$ the opposite holds true. Conversely, the results of the calculations indicate that the mathematical model underpredicts the increase of flow speed that occurs mainly on the low-pressure side of the sail ($0.5 \leq y/D \leq 2$). Similarly, the downwash appears to be underestimated and to be mostly confined in the wake area, whereas in the experiments noticeable changes of the flow direction are also registered outside the Dynarig's wake.



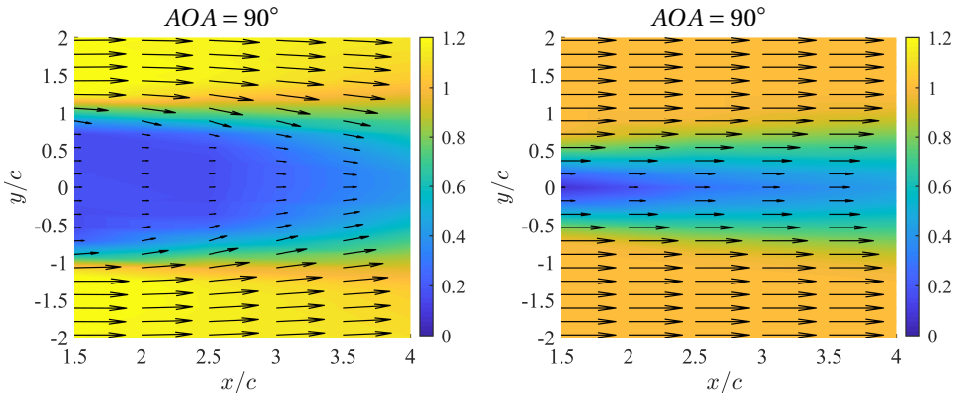


Figure 6.5: Velocity field past the Dynarig at different angles of attack: experimental results (left) and calculations (right). The experimental results were taken with Cobra probe 2 at a height of 1.05 m from the ground

6.3.2. COMPARISON WITH FLETTNER ROTOR EXPERIMENTS

The tests on the interaction between the two Flettner rotors were conducted in a different manner compared to the experiments on the two rigid sails discussed in Section 6.3.1. In fact, the Flettner rotor experiments were not conducted with the aim of maximizing the driving force for each considered condition, instead, in this case, the goal was to investigate the effects of the aerodynamic interaction when the two Flettner rotors were spun for a given set of different velocity ratios. Following a similar approach, the mathematical model was used to compute the resulting driving and heeling force coefficients for the same cases considered during the experimental campaign. In this section, the most relevant results are reported.

Also for Flettner rotors, the mathematical model is only partially able to predict the effects of the aerodynamic interaction on the overall driving and heeling force coefficients. In particular, it appears that, for several velocity ratio combinations, the model properly estimate a decrease of C_X that occurs at apparent wind angles $AWA \leq 60^\circ$. This can be seen in Figure 6.6, Figure 6.8, Figure 6.10, Figure 6.11 and Figure 6.12. Similarly, at apparent wind angles $AWA > 150^\circ$, the agreement between the computational results and the experimental results of the two Flettner rotors (Exp. Double FR) is, generally, satisfactory. Some exceptions can be noticed in Figure 6.8 and Figure 6.13, in which the mathematical model overpredicts the driving force coefficient.

In the range $60^\circ < AWA < 150^\circ$, the results of the mathematical model are contradictory. This can best be noticed looking at the results of the two Flettner rotors in side-by-side arrangement (Figure 6.9, Figure 6.10 and Figure 6.11). In this condition, in fact, the model does predict a strong influence of the interaction on the aerodynamic forces, but this does not always agree with the experimental results. In fact, for $60^\circ < AWA \leq 90^\circ$, the computational results show that there is a considerable decrease of C_X and this is in qualitative agreement with the results of the two Flettner rotor tests. On the other hand, in the range $90^\circ < AWA \leq 120^\circ$, the weaknesses of the mathematical model become evident. In Figure 6.9, it can be seen that the model fails to predict the recovery of the driving force coefficient measured during the experiments. Figure 6.10 shows that, for

the range of apparent wind angles considered, the aerodynamic interaction occurring between the two Flettner rotors has a positive effect on the overall driving force. The mathematical model, however, appears not to be able to predict such a favourable effect. Lastly, in Figure 6.11, the computational results indicate a strong reduction of C_X at $AWA = 105^\circ$ that does not occur in the experimental results.

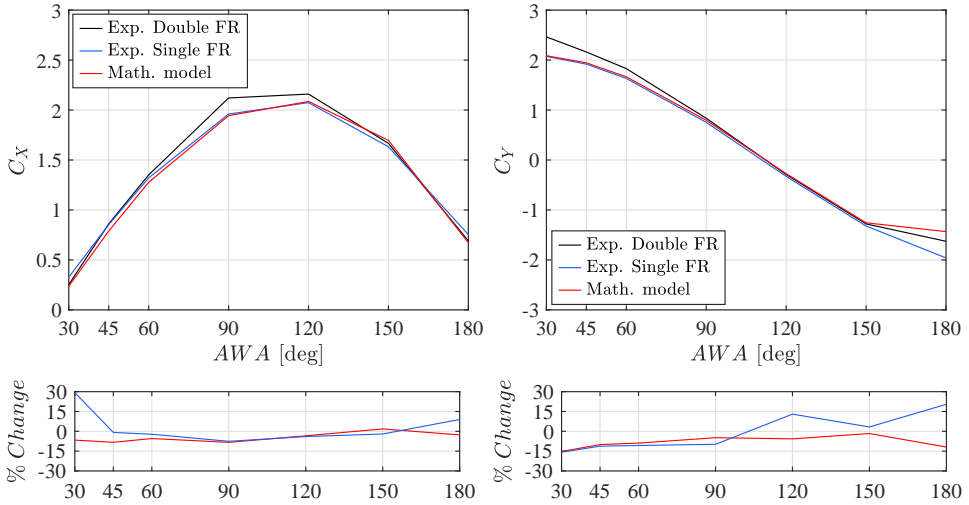


Figure 6.6: Comparison of the calculations and the single Flettner rotor results with respect to the double Flettner (top) and their relative percentage change (bottom). Driving (left) and heeling (right) force coefficients. Flettner rotors in tandem arrangement - Velocity ratios: $k_A = 1$ and $k_B = 1.5$. $GD = 3$

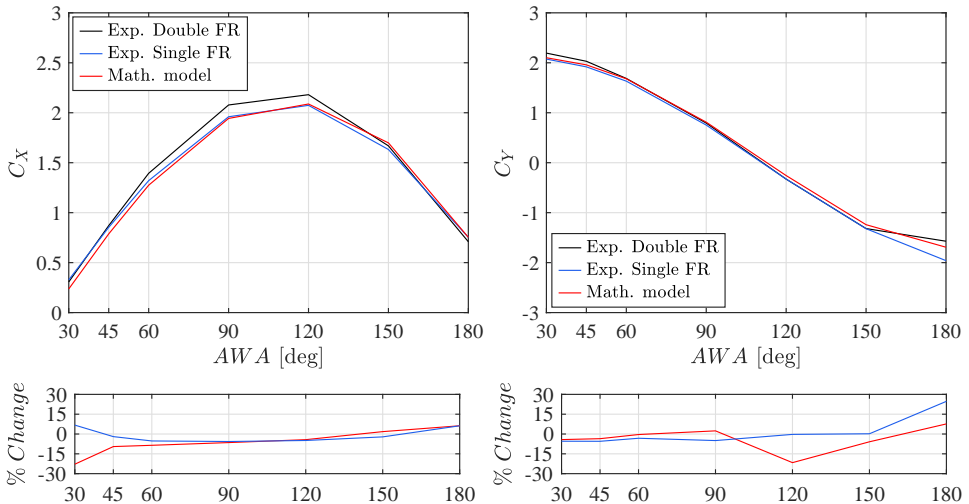


Figure 6.7: Comparison of the calculations and the single Flettner rotor results with respect to the double Flettner (top) and their relative percentage change (bottom). Driving (left) and heeling (right) force coefficients. Flettner rotors in tandem arrangement. Velocity ratios: $k_A = 1.5$ and $k_B = 1$. $GD = 3$

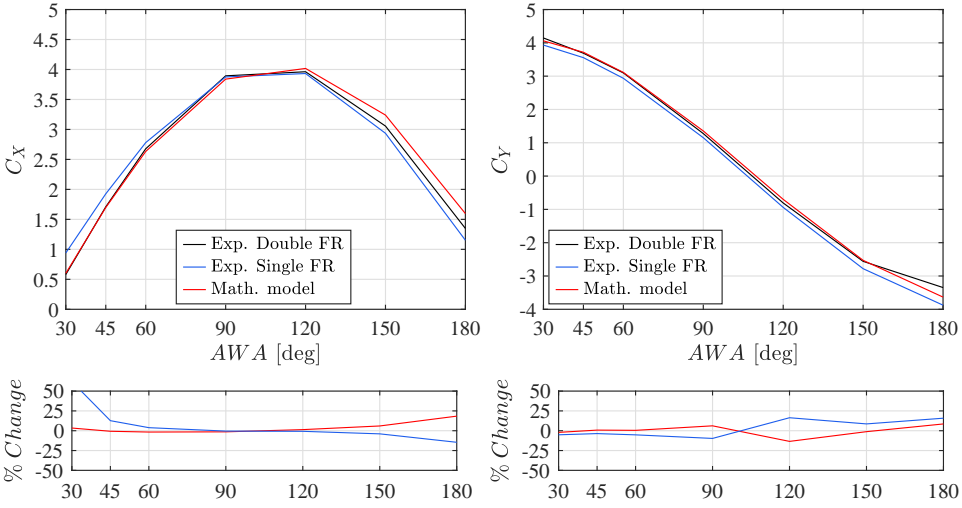


Figure 6.8: Comparison of the calculations and the single Flettner rotor results with respect to the double Flettner (top) and their relative percentage change (bottom). Driving (left) and heeling (right) force coefficients. Flettner rotors in tandem arrangement. Velocity ratios: $k_A = 2$ and $k_B = 2$. $GD = 3$

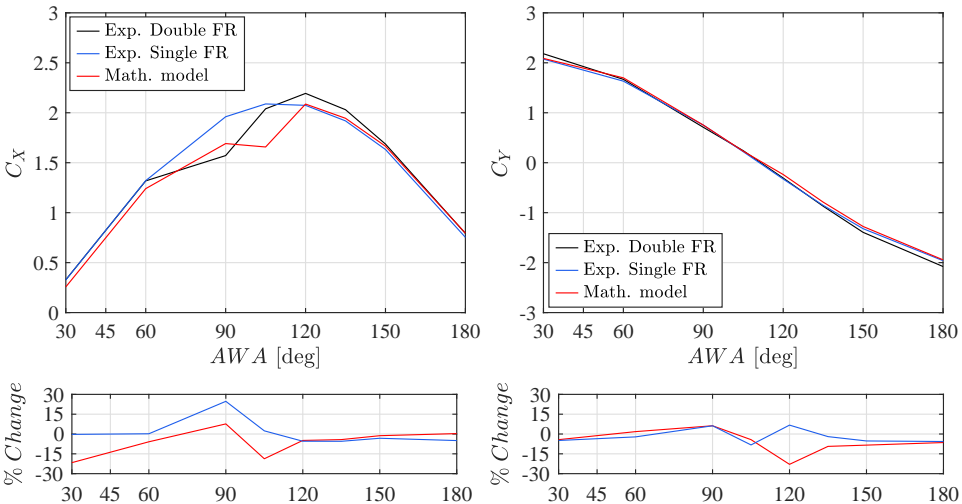


Figure 6.9: Comparison of the calculations and the single Flettner rotor results with respect to the double Flettner (top) and their relative percentage change (bottom). Driving (left) and heeling (right) force coefficients. Flettner rotors in side-by-side arrangement. Velocity ratios: $k_A = 1$ and $k_B = 1.5$. $GD = 3$

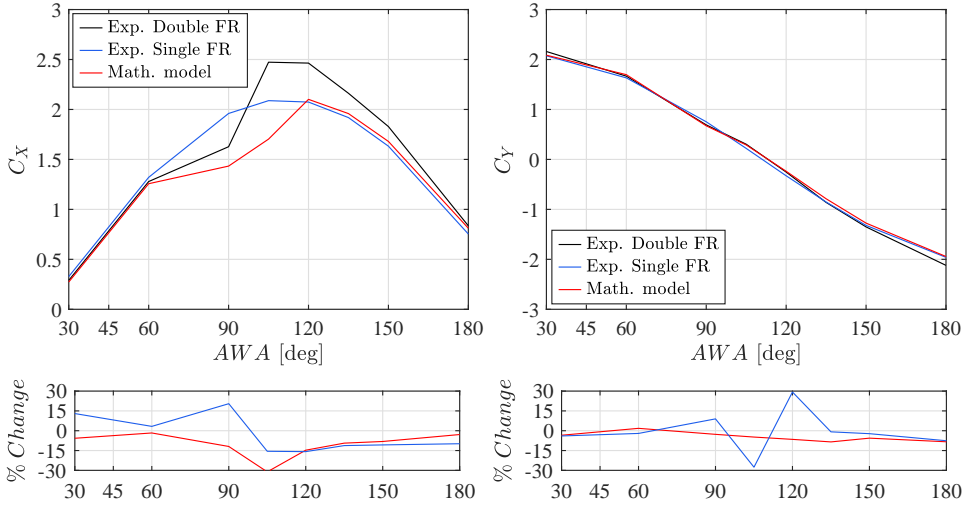


Figure 6.10: Comparison of the calculations and the single Flettner rotor results with respect to the double Flettner (top) and their relative percentage change (bottom). Driving (left) and heeling (right) force coefficients. Flettner rotors in side-by-side arrangement. Velocity ratios: $k_A = 1.5$ and $k_B = 1$. $GD = 3$

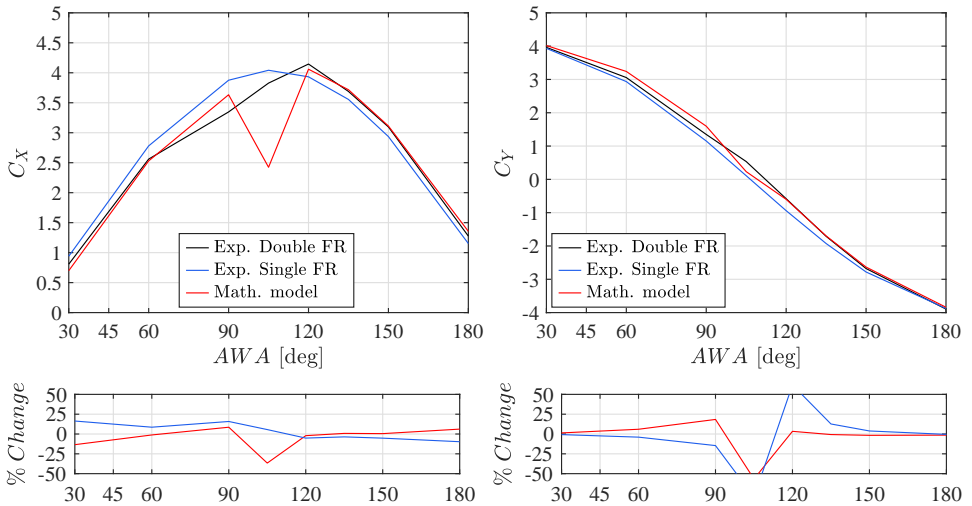


Figure 6.11: Comparison of the calculations and the single Flettner rotor results with respect to the double Flettner (top) and their relative percentage change (bottom). Driving (left) and heeling (right) force coefficients. Flettner rotors in side-by-side arrangement. Velocity ratios: $k_A = 2$ and $k_B = 2$. $GD = 3$

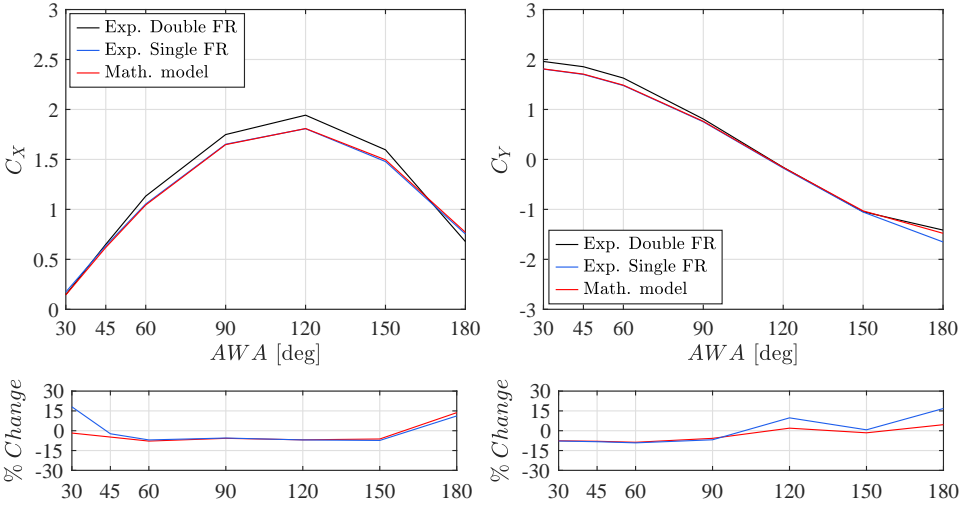


Figure 6.12: Comparison of the calculations and the single Flettner rotor results with respect to the double Flettner (top) and their relative percentage change (bottom). Driving (left) and heeling (right) force coefficients. Flettner rotors in tandem arrangement. Velocity ratios: $k_A = 1$ and $k_B = 1$. $GD = 7.5$

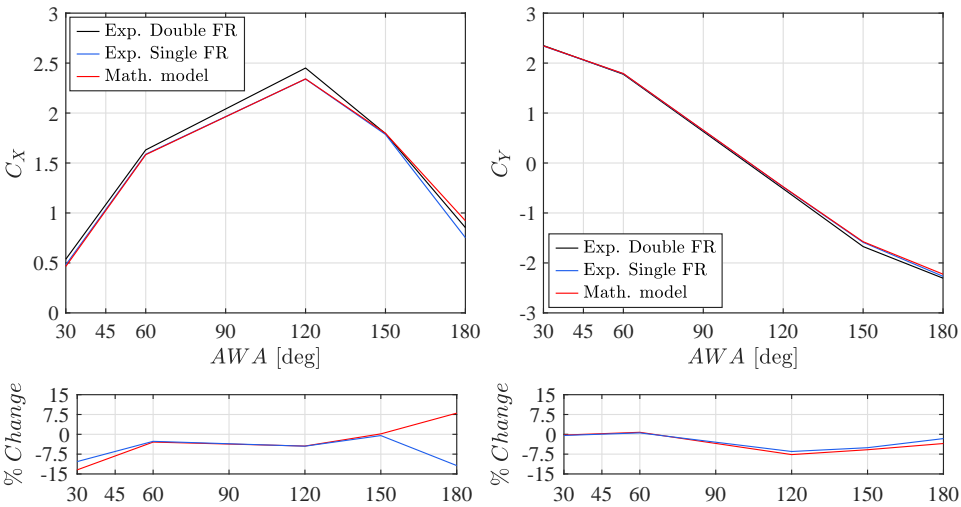


Figure 6.13: Comparison of the calculations and the single Flettner rotor results with respect to the double Flettner (top) and their relative percentage change (bottom). Driving (left) and heeling (right) force coefficients. Flettner rotors in tandem arrangement. Velocity ratios: $k_A = 1.5$ and $k_B = 1.5$. $GD = 15$

Analogous conclusions can be drawn by looking at the results of the heeling force coefficient C_Y . In fact, it appears that, in some cases, the mathematical model introduces a general improvement compared to the results of the single Flettner rotor (Exp. Single FR, see Figure 6.8, Figure 6.10 and Figure 6.12) whereas, for other velocity ratio combinations, the benefits of using the mathematical model versus neglecting the effects of the

aerodynamic interaction are questionable (see, for example, Figure 6.6, Figure 6.7 and Figure 6.9).

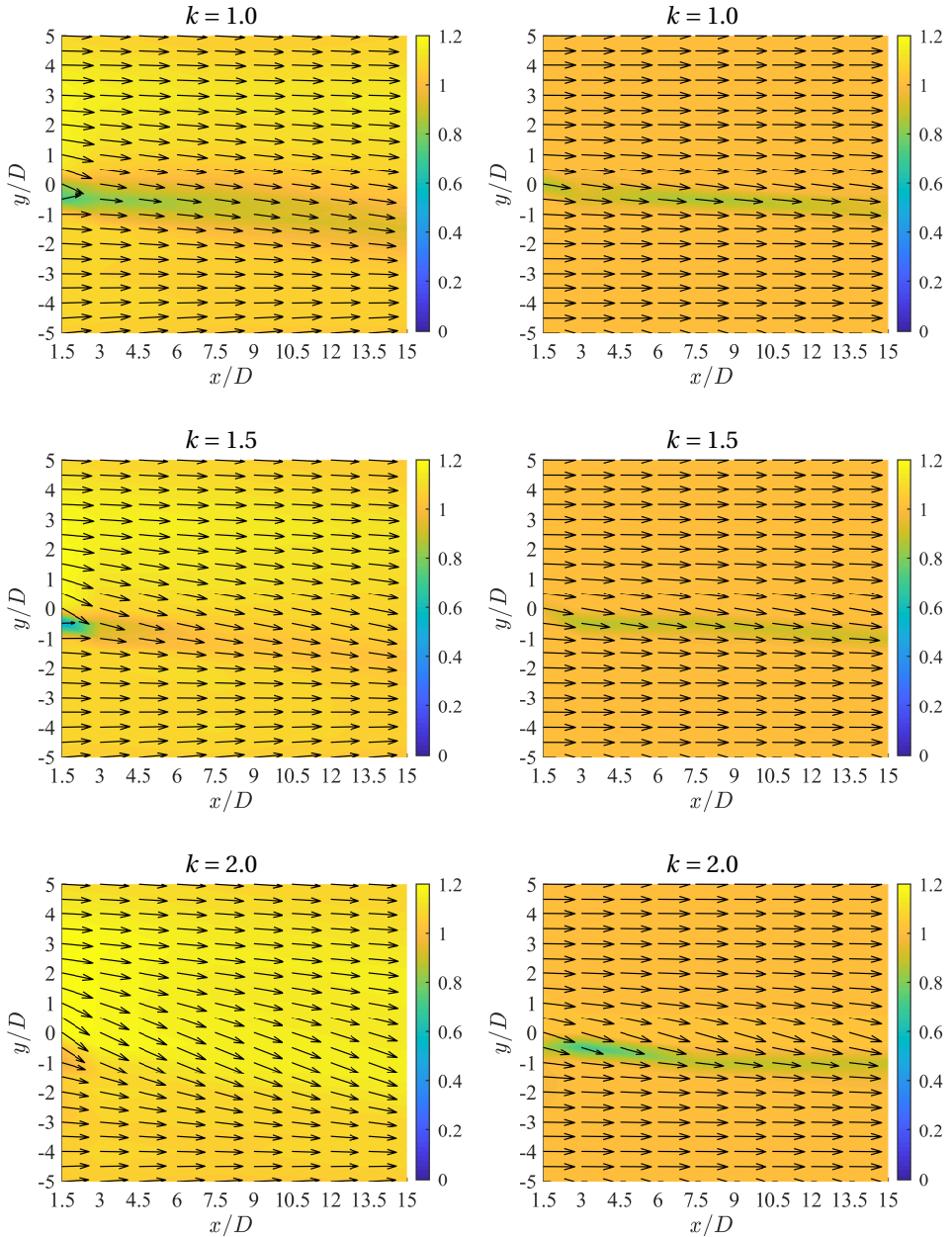


Figure 6.14: Velocity field past the Flettner rotor at different velocity ratios: experimental results (left) and calculations (right). The experimental results were taken with Cobra probe 2 at a height of 1.24 m from the ground

As for the Dynarig study reported in the previous section, also for Flettner rotors a better understanding of the results can be gained by comparing the velocity fields obtained using the mathematical model and measured during the experiments on the single Flettner rotor. The results of this comparison, reported in Figure 6.14, indicate that calculations underestimate the magnitude of the wake for velocity ratio $k = 1.0$. On the other hand, for $k = 1.5$ and, especially for $k = 2.0$, the opposite is true. In particular, for this latter case, the flow speed reduction predicted by the mathematical model is the reason behind the abrupt decrease of C_X and C_Y at $AWA = 105^\circ$ when both Flettner rotors spin at $k = 2.0$ (see Figure 6.11). Another remarkable difference between the experimental results and the calculations is that the mathematical model fails to predict the considerable flow speed increase that occurs when the Flettner rotor spins at $k = 1.5$ and $k = 2.0$. Arguably, the most noticeable effect of this discrepancy is that mathematical model is not able to predict the rise of C_X and C_Y measured during the experiments when $k_A = 1.5$ and $k_B = 1.0$ (Figure 6.10).

6.4. FORCES FROM VELOCITY FIELD MEASUREMENTS

In Section 6.3 it was shown that the considered mathematical model is currently not able to provide satisfactory results when compared to the experimental force measurements. It was argued that this is because the mathematical model fails to accurately predict the velocity field used to calculate the aerodynamic forces. To understand whether a more detailed description of the velocity field would lead to an improved agreement between the calculated and measured forces, in this section the velocity field measurements taken in the wake of the single Dynarig and Flettner rotor are used to derive the aerodynamic forces that a second device would generate in a given location downstream the perturbing wind-propulsion system. The results obtained with this method are compared with force measurements carried out in comparable conditions.

6.4.1. DYNARIG CASE

During the Dynarig experimental campaign, a series of tests was carried out especially to measure aerodynamic forces that could be compared to those derived from the velocity field measurements. To achieve this goal, two conditions had to be met. The first condition is that the force measurements have to be taken in locations at which velocity field data are available. The second condition is that the upstream (perturbing) Dynarig has to generate a velocity field comparable to that one measured during the single-sail experiments.

This particular series of tests was carried out using the same setup described in Chapter 3 and that, for convenience, is again shown in Figure 6.15. To fulfill the first condition above discussed, only a limited number of the turntable angles were tested (see Figure 6.15). In fact, depending on the gap distance between the two sails, the selected angles have to be small enough to ensure that the location of the downstream Dynarig is kept within the boundaries of the velocity field measurements, i.e. $y/c = \pm 2$ and $1.5 < x/c < 4$ (see Figure 6.5 and Figure 6.16). Complying with this condition means that, by interpolation, it is possible to calculate the velocity field at any point within these boundaries.

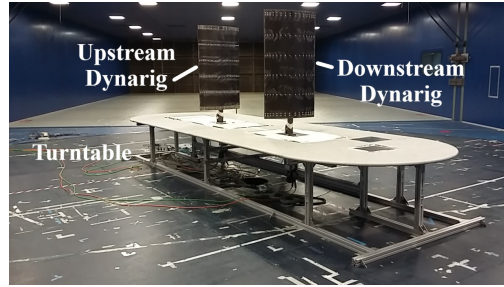


Figure 6.15: Dynarig setup in the wind-tunnel experiments

To meet the second condition, the angles of attack of the upstream Dynarig were set at $AOA = 5^\circ$, $AOA = 45^\circ$ and $AOA = 90^\circ$ which were the same angles of attack for which the velocity field was measured during the single-sail tests. Finally, differently from the experiments presented in Chapter 3, in the present case the downstream Dynarig was not trimmed to optimize its aerodynamic performance. Instead, the downstream Dynarig was set at the same angle of attack of the upstream sail. In the light of this, the aerodynamic forces of the downstream Dynarig were calculated according to the procedure described in Section 6.2 with one exception: the downwash obtained from the velocity field measurements is, in this case, used to calculate the change in the angle of attack of the downstream sail. The resulting angle of attack is then used in a lookup table to find the corresponding lift and drag coefficients. Due to this procedure, it was decided to use the lift and drag coefficients instead of the driving and heeling force coefficients to compare the measured and calculated results.

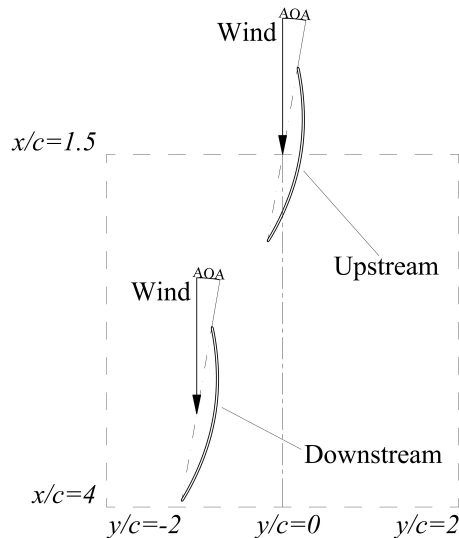


Figure 6.16: Position of the upstream and downstream Dynarig in relation to the boundaries in which the velocity field measurements were taken

The results of the present study are shown in Figure 6.17 to Figure 6.22. The aerodynamic forces derived from the velocity field measurements are obtained in two different manners. In one case, only the measurements of Cobra Probe 2 (see Figure 6.5) are used, while, in the other case, the results all four Cobra Probes (see Appendix A.1) are employed. For the sake of comparison, the results of the mathematical model are also reported. The investigation shows that, in general, a more accurate description of the velocity field leads to an improved agreement between the measured and the calculated aerodynamic force coefficients. This can be noticed by looking at the results obtained with the mathematical model, those derived using the measurements of Cobra Probe 2 alone and those achieved using all four Cobra Probes. These three methods represent an increasingly accurate description of the velocity field and, in this order, they show an improved agreement with the force measurements.

Analyzing the results depicted in Figure 6.17 to Figure 6.22, it can be noticed that the best match between the calculated and the measured forces is achieved for the lift coefficient when the Dynarigs are set at $AOA = 5^\circ$. Conversely, for the same angle of attack the results derived from the velocity field measurements and those obtained with the mathematical model are not able to capture the trend of the drag coefficient registered in the experiments (see Figure 6.17 and Figure 6.20).

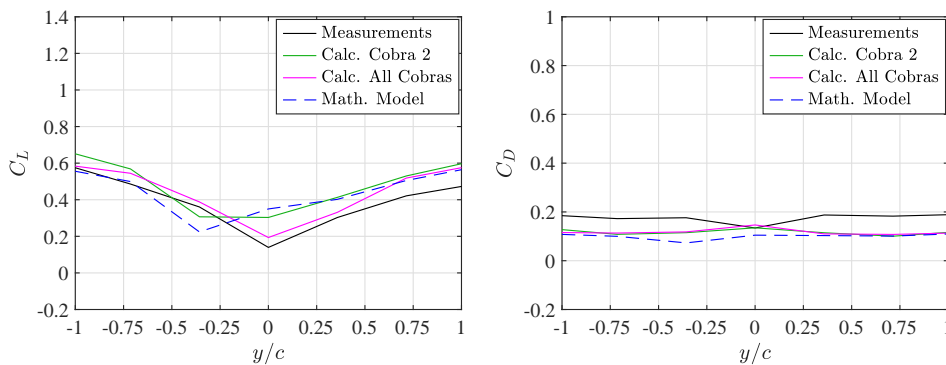


Figure 6.17: Comparison of the force measurements, the results derived from the measured velocity field and the results of the mathematical model. Lift (left) and drag (right) coefficients. Upstream and downstream Dynarig set at $AOA = 5^\circ$. Gap distance $GD = 2.5$

An opposite trend is found when the two Dynarigs are set at $AOA = 90^\circ$. In this case, in fact, C_D is better predicted than C_L . This is particularly so for the largest gap distance between the two sails (Figure 6.22). Conversely, when the Dynarigs are closer to each other, both the results derived from the velocity field measurements and those obtained with the mathematical model fail to predict a negative drag coefficient at $y/c = 0$ (Figure 6.19). For the Cobra Probe measurements, this is because the Cobra Probe has a limited functioning range and, thus, it could not measure the velocity field associated with a recirculating flow. Similarly, the mathematical model, due to the nature of its viscous component, is not able to predict the effects of such a flow type. Regarding the lift coefficient, on the other hand, it appears that the results of the mathematical model outperform those derived from the velocity field measurements (see Figure 6.19

and 6.22). This can be explained by looking at the measured and calculated velocity fields relative to $AOA = 90^\circ$ shown in Figure 6.5. For this condition, the mathematical model only predicts a change in flow velocity. Conversely, the measurements indicate that the flow after being separated (and decelerated) tends to rejoin and this causes a change in the flow direction. Since the force measurements show that at $AOA = 90^\circ$ the Dynarig is insensitive to these local changes in flow direction, it appears that, in this case, a less accurate prediction of the velocity field (mathematical model) leads to better results than using a more sophisticated method (forces derived from the Cobra Probe measurements).

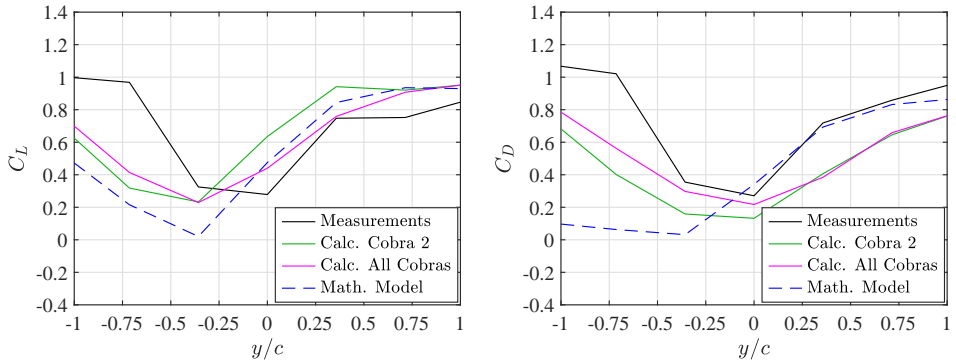


Figure 6.18: Comparison of the force measurements, the results derived from the measured velocity field and the results of the the mathematical model. Lift (left) and drag (right) coefficients. Upstream and downstream Dynarig set at $AOA = 45^\circ$. Gap distance $GD = 2.5$

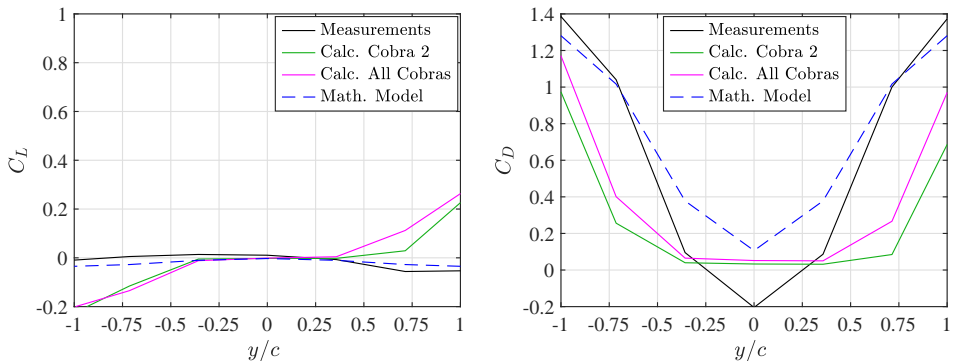


Figure 6.19: Comparison of the force measurements, the results derived from the measured velocity field and the results of the the mathematical model. Lift (left) and drag (right) coefficients. Upstream and downstream Dynarig set at $AOA = 90^\circ$. Gap distance $GD = 2.5$

Finally, the results relative to $AOA = 45^\circ$ show even more clearly the limitations of the proposed method when applied to Dynarigs or other similar wind-assist devices. In fact, for this case, the results of the lift and drag coefficients show that even using

an accurate description of the velocity field does not lead to a satisfactory prediction of the aerodynamic forces. This can be seen in Figure 6.18 and Figure 6.21 looking at the aerodynamic coefficients derived from the Cobra Probe measurements. Arguably, when the flow is still (partially) attached to the sail but separation plays an important role, the method used in this chapter to calculate the aerodynamic forces is too simplistic. In this condition, in fact, complex effects due to turbulence, neglected in the proposed method, might have a considerable influence on the flow characteristics around the sails and, eventually, on the aerodynamic forces they generate.

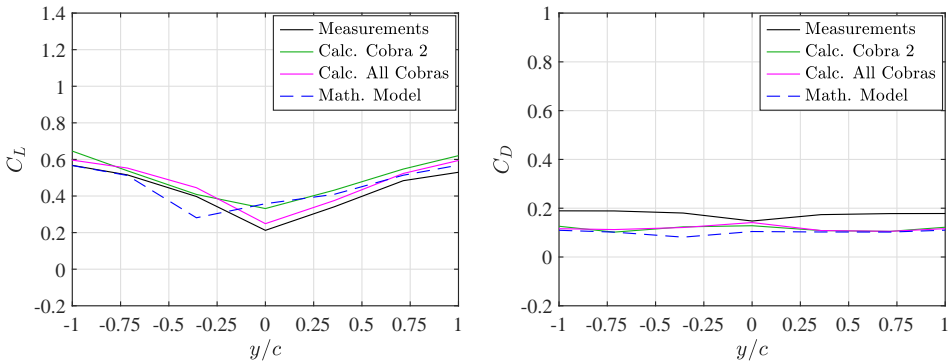


Figure 6.20: Comparison of the force measurements, the results derived from the measured velocity field and the results of the the mathematical model. Lift (left) and drag (right) coefficients. Upstream and downstream Dynarig set at $AOA = 5^\circ$. Gap distance $GD = 4$

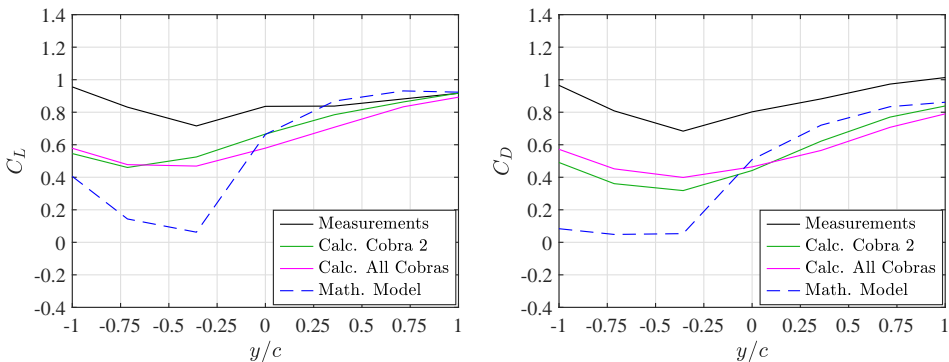


Figure 6.21: Comparison of the force measurements, the results derived from the measured velocity field and and the results of the the mathematical model. Lift (left) and drag (right) coefficients. Upstream and downstream Dynarig set at $AOA = 45^\circ$. Gap distance $GD = 4$

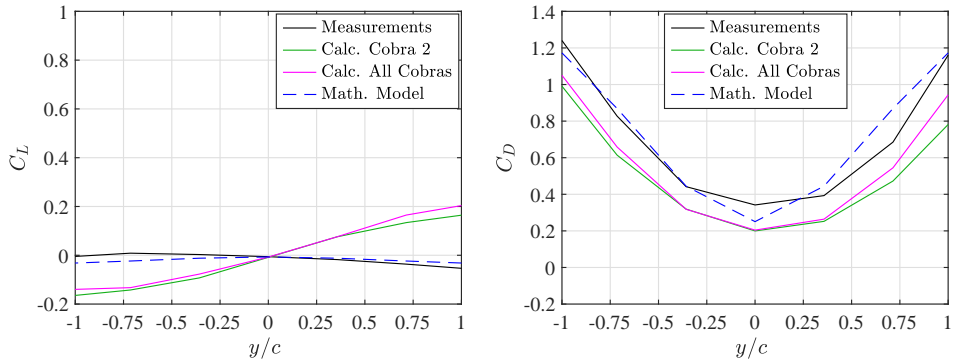


Figure 6.22: Comparison of the force measurements, the results derived from the measured velocity field and the results of the mathematical model. Lift (left) and drag (right) coefficients. Upstream and downstream Dynarig set at $AOA = 90^\circ$. Gap distance $GD = 4$

6.4.2. FLETTNER ROTOR CASE

In order to ensure a fair comparison between the force measurements and the results derived from the velocity field, the same two conditions described in Section 6.4.1 need to be applied also to Flettner rotors: the force measurements have to be taken in locations at which velocity field data are available and the upstream (perturbing) Flettner rotor has to generate a velocity field comparable to that one measured during the single-rotor tests. In this case, however, no additional force measurements were carried out. Instead, depending on the gap distance between the two Flettner rotors and the apparent wind angle (see Figure 6.23), some of the experiments described in Chapter 5 are already compliant with the above requirements. In particular, the apparent wind angles for which it is possible to establish a comparison between the measured and the calculated forces have to be such that the location of the downstream Flettner rotor is kept within the boundaries of the velocity field measurements, i.e. $y/D = \pm 5$ and $1.5 < x/D < 15$ (see Figure 6.14). Complying with this condition means that, by interpolation, it is possible to calculate the velocity field at any point within these boundaries.

Table 6.1: Results of Flettner rotor A or B used in the calculations depending on the apparent wind angle

Gap distance (GD)	Apparent Wind Angle (AWA)						
	[deg]						
	60	45	30	15	180	150	120
$3D$	B	B	B	B	A	A	A
$7.5D$	-	B ²	B	B	A	A	-
$15D$	-	-	-	B	A	-	-

Depending on the apparent wind angle, the results of Flettner rotor A or B are used. These are provided in Table 6.1.

²For this gap distance, $AWA = 45^\circ$ leads to a lateral position of the downstream Flettner rotor of $y/D = 5.3$. This was approximated to $y/D = 5.0$ and the associated velocity field data were used.

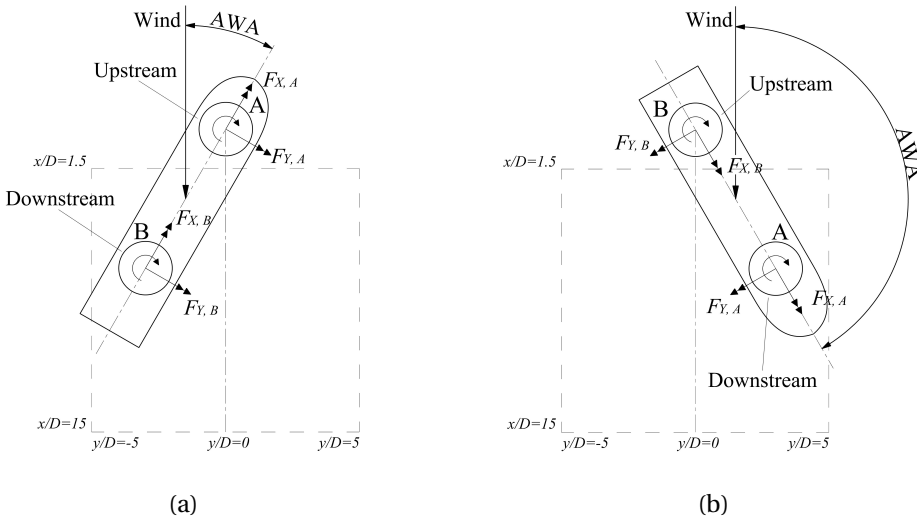


Figure 6.23: Positions of the upstream and downstream Flettner rotor, for $AWA < 90^\circ$ (a) and $AWA > 90^\circ$ (b), in relation to the boundaries in which the velocity field measurements were taken

The experiments on the two Flettner rotors discussed in Chapter 5 were carried out setting the two devices at velocity ratios $k = 1$, $k = 1.5$ and $k = 2$, leading to a matrix of nine combinations. In this section, just the most significant results are provided. The full results can be found in Appendix D.2.

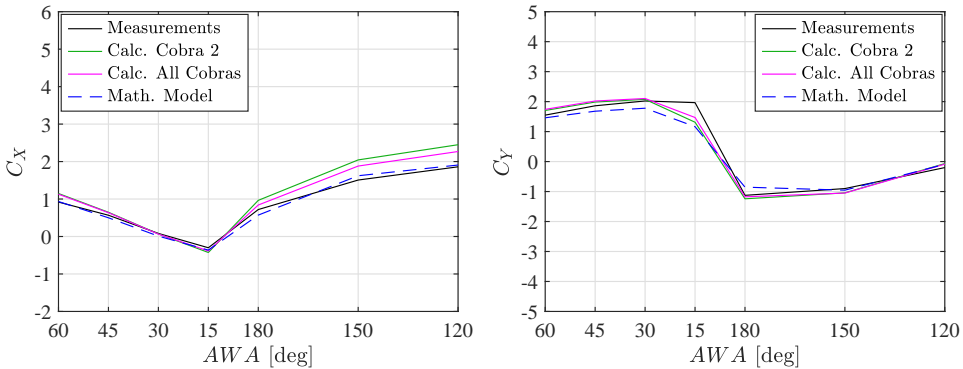


Figure 6.24: Comparison of the force measurements, the results derived from the measured velocity field and the results of the the mathematical model. Driving (left) and heeling (right) force coefficients. Upstream Flettner rotor set at $k = 1$ and downstream Flettner rotor set at $k = 1$. Gap distance $GD = 3$

In Figure 6.24 to Figure 6.31 the Flettner rotor force measurements are compared with the results derived from the velocity field measurements and those obtained with the mathematical model. Similarly to the Dynarig case previously analysed, also for the Flettner rotor the aerodynamic forces are derived from the measurements of Cobra Probe 2 alone (see Figure 6.14) as well as using the results of all four Cobra Probes (see

Appendix C.1). The aerodynamic coefficients are then obtained following the procedure described in Section 6.2. In this section, the results of the driving and heeling force coefficients are used for the comparison.

The results reported in Figure 6.24 to Figure 6.31 show that, apart from some exceptions, a more detailed description of the velocity field leads to an improved agreement between the measured and the calculated aerodynamic forces. This can be seen by comparing the results obtained with the mathematical model, those derived using the measurements of Cobra Probe 2 alone and those achieved using all four Cobra Probes. The latter are based on the most accurate description of the velocity field available and they show a satisfactory agreement with the measured forces for all conditions analysed.

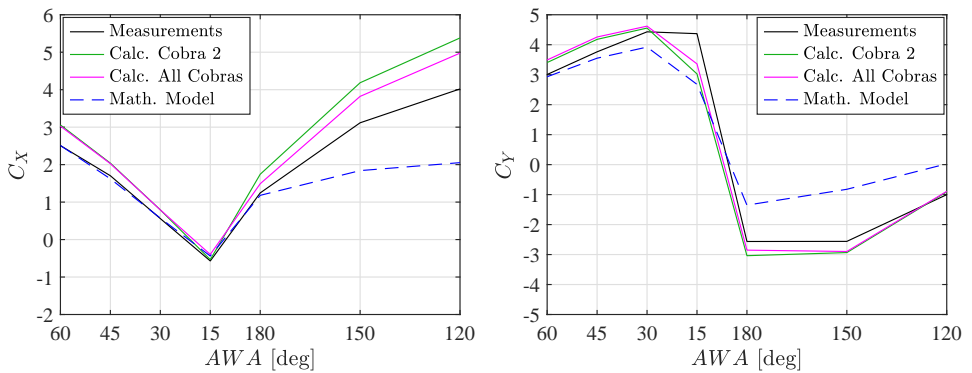


Figure 6.25: Comparison of the force measurements, the results derived from the measured velocity field and the results of the mathematical model. Driving (left) and heeling (right) force coefficients. Upstream Flettner rotor set at $k = 1$ and downstream Flettner rotor set at $k = 2$. Gap distance $GD = 3$

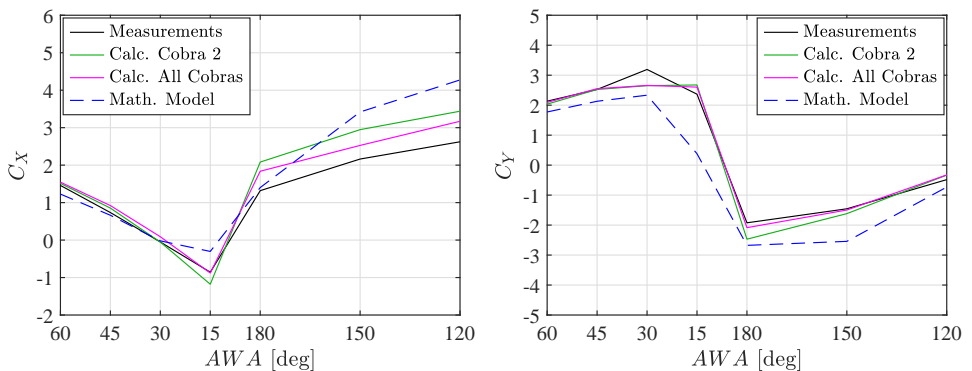


Figure 6.26: Comparison of the force measurements, the results derived from the measured velocity field and the results of the the mathematical model. Driving (left) and heeling (right) force coefficients. Upstream Flettner rotor set at $k = 2$ and downstream Flettner rotor set at $k = 1.5$. Gap distance $GD = 3$

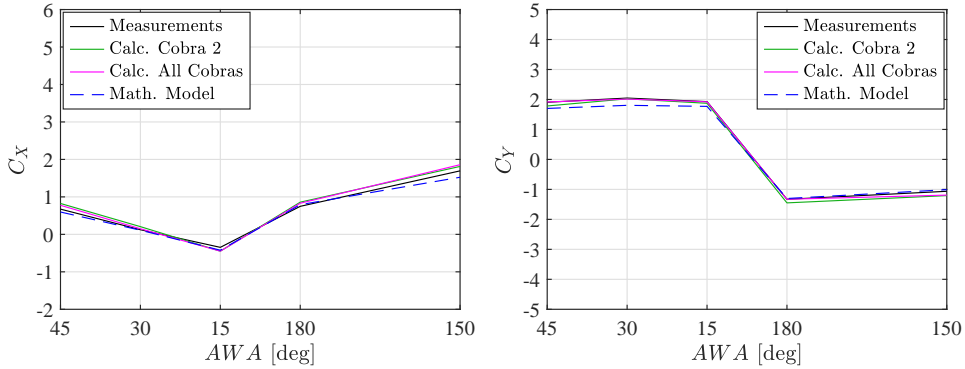


Figure 6.27: Comparison of the force measurements, the results derived from the measured velocity field and the results of the the mathematical model. Driving (left) and heeling (right) force coefficients. Upstream Flettner rotor set at $k = 1$ and downstream Flettner rotor set at $k = 1$. Gap distance $GD = 7.5$

This is a significant difference compared to the Dynarig results discussed in the previous section. For Flettner rotors, in fact, it appears that the proposed method to derive the aerodynamic forces from velocity field data is able to provide meaningful results for any operating condition.

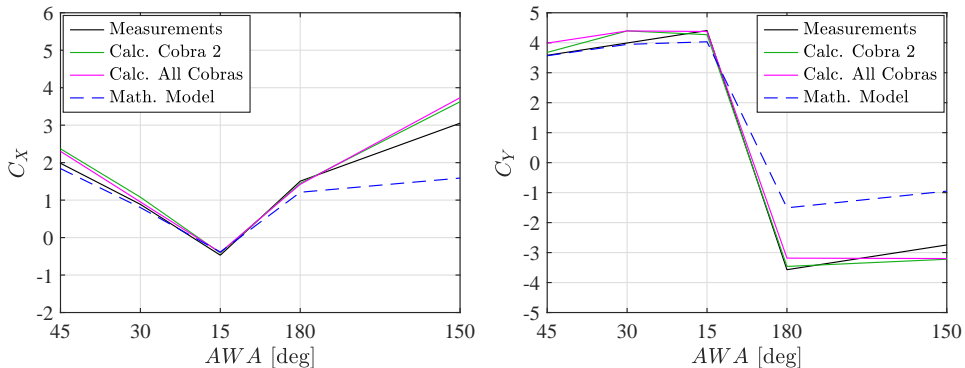


Figure 6.28: Comparison of the force measurements, the results derived from the measured velocity field and the results of the the mathematical model. Driving (left) and heeling (right) force coefficients. Upstream Flettner rotor set at $k = 1$ and downstream Flettner rotor set at $k = 2$. Gap distance $GD = 7.5$

Although the results discussed herewith deal with a limited number of apparent wind angles, and it was only possible to apply the present method to the downstream Flettner rotor, this investigation indicates that a more refined version of the mathematical model could be a feasible approach to predict the interaction effects occurring between multiple Flettner rotors. In this respect, arguably the most necessary improvement to the mathematical model is a more refined discretisation of the vortex system, i.e. implement a line of horseshoe vortices instead of the single vortex currently in use. Regarding the viscous component of the model, on the other hand, a change that is likely to lead to a better agreement between the measured and calculated velocity fields is to include

the velocity ratio k into the semi-empirical formula of Eq. 6.4. In particular, it would be necessary to establish an inverse proportional relationship between the drag-dependent flow speed decrease and the Flettner rotor velocity ratio (see Figure 6.14). However, considering that the final aim of the mathematical model is to deal with the interaction effects of full-scale Flettner rotors this modification might not be needed. As shown in Section 5.3.4, in fact, it appears that, for the velocity ratios considered, the velocity field generated by a Flettner rotor at a high Reynolds number does not show any relevant decrease in flow speed with respect to the undisturbed flow.

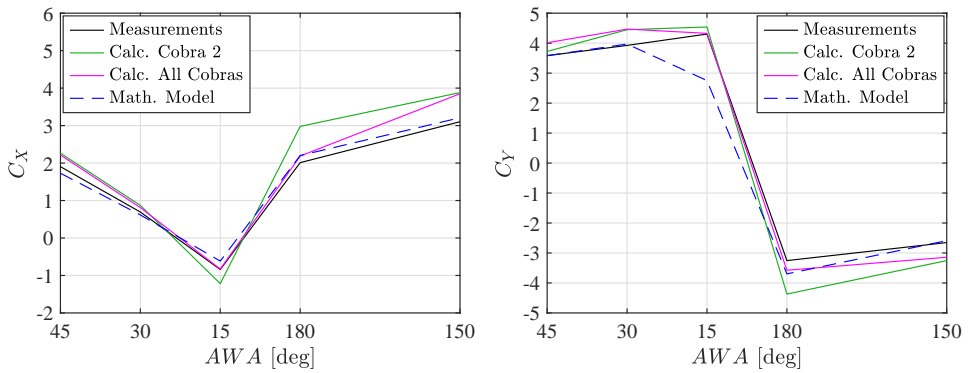


Figure 6.29: Comparison of the force measurements, the results derived from the measured velocity field and the results of the the mathematical model. Driving (left) and heeling (right) force coefficients. Upstream Flettner rotor set at $k = 2$ and downstream Flettner rotor set at $k = 2$. Gap distance $GD = 7.5$

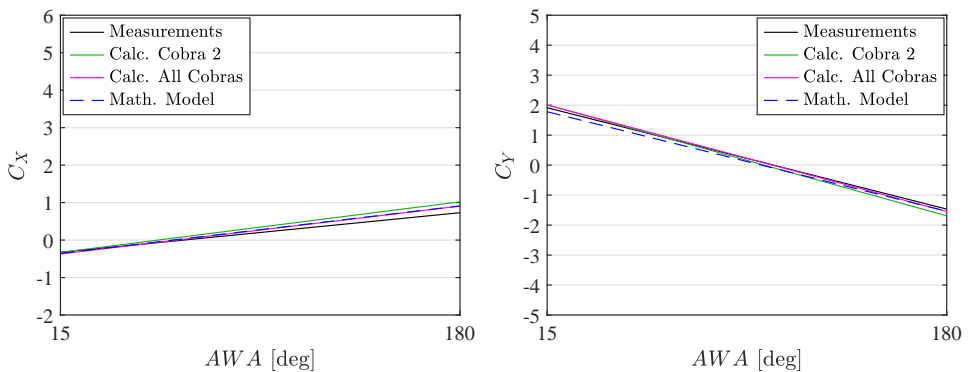


Figure 6.30: Comparison of the force measurements, the results derived from the measured velocity field and the results of the the mathematical model. Driving (left) and heeling (right) force coefficients. Upstream Flettner rotor set at $k = 1$ and downstream Flettner rotor set at $k = 1$. Gap distance $GD = 15$

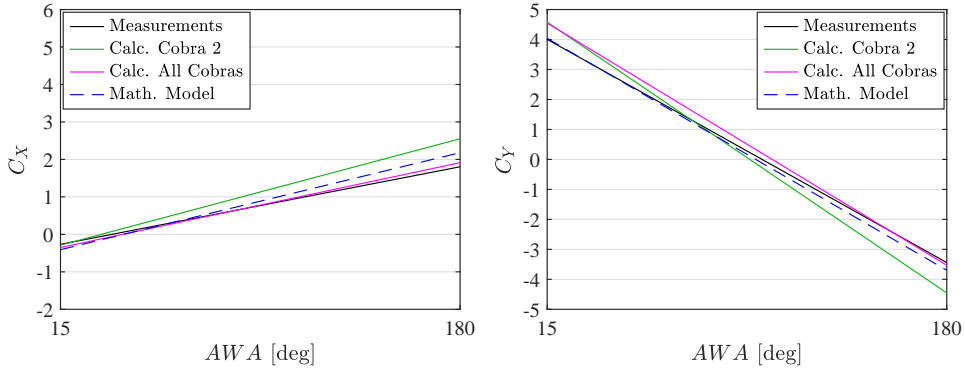


Figure 6.31: Comparison of the force measurements, the results derived from the measured velocity field and the results of the the mathematical model. Driving (left) and heeling (right) force coefficients. Upstream Flettner rotor set at $k = 2$ and downstream Flettner rotor set at $k = 2$. Gap distance $GD = 15$

6.5. CONCLUSIONS

In this chapter, a mathematical model that could contribute to the development of the aerodynamic module of the Sail Assist Performance Prediction Program was validated against the experimental results presented in the previous chapters of this dissertation. The model, found in the literature and originally employed to study the effects of the aerodynamic interaction on two competing sailing yachts, is sufficiently simple to assure quick and inexpensive calculations as underlined in the requirements of the performance prediction tool. Moreover, due to its nature, the considered model could, theoretically, deal with any set of wind propulsion systems whose performance can be assumed to be dependent solely on the amount of lift and drag generated for a given wind condition.

The results of the validation indicate that the mathematical model, in its current state, is able to properly predict some effects caused by the aerodynamic interaction while, more often, it fails to accurately replicate the trends emerged in the experiments. Arguably, this is most noticeable for the validation of the sail interaction effects. In this case, in fact, for a large range of apparent wind angles ($45^\circ < AWA < 165^\circ$), the results obtained by using the mathematical model and by neglecting the effects of the aerodynamic interaction do not show any considerable difference, meaning that the benefits brought by the use of the mathematical model to the improvement of the performance prediction are negligible. Conversely, regarding the validation with the Flettner rotor experiments, it appears that the computational results and the results obtained considering no-interaction effects are, in general, distinguishable but the trends predicted by the mathematical model often deviate from those registered during the tests.

From the comparison of the computed and measured velocity fields past the Dynarig and the Flettner rotor, it is possible to identify several discrepancies which could limit the capabilities of the analysed mathematical model to properly predict the effects of the aerodynamic interaction on the overall driving and heeling force coefficients. In order to investigate whether a more accurate description of the velocity field would lead to a better prediction of the aerodynamic forces, the velocity field measurements carried

out in the wake of the Dynarig and the Flettner rotor were used to derive the aerodynamic forces that a second device would generate in a given location downstream the perturbing wind-propulsion system. These results were then compared with force measurements taken in comparable conditions. The investigation indicates that, in general, a more detailed description of the velocity field leads to a better agreement between the measured and the calculated aerodynamic forces. For the Dynarig case, however, when the flow is still (partially) attached to the sail but separation plays a significant role (results obtained at $AOA = 45^\circ$), the proposed method, as it does not take into account the effects of turbulence in any form, appears to be too simplistic and arguably not suitable to predict the interaction effects between Dynarigs or similar wind-assist devices. To investigate whether turbulence does, in fact, play an important role in these conditions, experiments at different turbulence intensity levels could be carried out. On the other hand, within the limits of the present study, the Flettner rotor results do not indicate a particular condition in which the proposed method fails to deliver a meaningful outcome.

In view of these considerations, it can be concluded that the mathematical model analysed in this chapter, in its current form, is not able to properly predict the interaction effects occurring between two Dynarigs or two Flettner rotors. In the case of Flettner rotors, however, it was proven that a more refined version of the mathematical model is likely to deliver satisfactory results. In this respect, the most necessary improvement to the mathematical model appears to be a more refined discretisation of the vortex system.

7

CONCLUSIONS AND RECOMMENDATIONS

7.1. CONCLUSIONS

ANSWERS TO THE RESEARCH QUESTIONS

The answers to the research questions formulated in Section 2.3 are provided herewith.

- The results of the experiments carried out on two similar rigid sails indicate that the aerodynamic interaction has a considerable influence on their overall performance. Whether the interaction has a positive or negative effect, as well as its magnitude, depends on the apparent wind angle at which the ship is sailing and the gap distance between the two sails. It was proven that, for a large range of apparent wind angles, regardless from the gap distance, the aerodynamic interaction causes a considerable increase of the driving and heeling force coefficient with respect to an analogous single sail in similar conditions.
- The experimental campaign undertaken on the large-scale Flettner rotor proved that its aerodynamic coefficients are influenced by scale effects. The results of the investigation denote that the Reynolds number affects the lift coefficient in the critical flow regime and until velocity ratio $k = 2.5$. On the other hand, in the velocity ratio range $1 < k < 2.5$, it is found that scale effects influence the drag coefficient both in the critical and the supercritical flow region. Furthermore, the results of the same experiments indicate that the power coefficient is insensitive to the Reynolds number and on whether the cylinder is rotated in an air stream or in still air.
- The wind-tunnel tests on two similar Flettner rotors prove that, depending on their layout on the ship's deck, their gap distance and the apparent wind angle at which the ship is sailing, the aerodynamic interaction may have a marked influence on their overall performance. In particular, it is found that the interaction

effects are most relevant when the Flettner rotors are set closer to each other and when they come close to being aligned with the wind direction. In general, the aerodynamic interaction has a detrimental effect on the overall performance of the two Flettner rotors. Nonetheless, for one of the arrangements tested (side-by-side arrangement), and for a certain range of apparent wind angles, it is found that the interaction occurring between the two Flettner rotors increased their overall aerodynamic efficiency (higher C_X and lower C_Y). Whether this occurs depends on the velocity ratio of each of the two devices. More generally, the Flettner rotor velocity ratio, like the sail angle of attack, appears to be a key parameter that can be adjusted to improve the aerodynamic performance of the entire Flettner rotor arrangement.

- The validation of a simple mathematical model, with features compatible with the requirements of the aerodynamic model of the Sail Assist Performance Prediction Program, proves that, in its current form, it is not able to properly assess the effects of the aerodynamic interaction occurring between two rigid sails or two Flettner rotors. In the case of sails, it was shown that the use of velocity field measurements to calculate the aerodynamic forces did not significantly improve the agreement between the calculations and the force measurements. This suggests that, due to its simplifying assumptions, the considered mathematical model is not suitable to study the aerodynamic interaction effects occurring between Dynarigs or similar wind-propulsion systems (sails and wingsails). On the contrary, an analogous study conducted on Flettner rotors indicates that in case a more accurate estimate of the velocity field is attained, the working principles of the analysed mathematical model are suited to deal with two interacting Flettner rotor devices.

CONCLUSIONS ON THE SAIL ASSIST PROJECT

From the perspective of the Sail Assist project, since the considered mathematical model proved to be unfit to be employed in its current form, the aerodynamic force coefficients derived from the experiments carried out in the present doctoral work were directly included in the aerodynamic model of the Performance Prediction Program described in Chapter 1. Regarding the results of the Flettner rotor tests, engineering approximations were necessary to extend the experimental results to higher velocity ratios. The Performance Prediction Program, that comprises the results of the present dissertation and the results of an analogous doctoral effort on the hydrodynamics of wind-assisted ships, was successfully used to carry out studies on various wind-assisted ship designs. For example, the study reported by [Bordogna et al. \(2019\)](#), conducted in collaboration with Damen Shipyards and Norsepower Oy Ltd, investigates the benefits of using one or two Flettner rotors on a general cargo ship. The considered ship was 86-meter long (deadweight tonnage of 5150 tons) and the installed Flettner rotors had diameter $D = 3$ m and span $H = 18$ m. In the study, the vessel was assumed to sail in the Baltic Sea on a North-South route (Lulea - Gdansk) and on an East-West route (St Petersburg - Stockholm). The penalties introduced by the sailing condition, i.e. an increased hydrodynamic resistance and non-optimal engine operating point, were considered in the overall performance prediction.

The results of the study showed that average fuel savings of 6.0% and 13.4%, with

respect to an identical ship without wind propulsors, were achieved in case one or two Flettner rotors were used respectively. These results refer to the case in which the ship sailed along the shortest route, i.e. the Great Circle Route (GCR). In case fuel-optimised routing was employed, i.e. the ship was allowed to deviate from the shortest route to find more favourable wind conditions, fuel savings of 6.7% (one Flettner rotor) and 14.8% (two Flettner rotors) were achieved, at the price of a maximum increase in total voyage time of 1.6% with respect to the GCR. It should be noticed that the modest performance increase brought by fuel-optimised routing is due to the limited sea space proper of the Baltic Sea. Considerably higher benefits can be obtained by weather routing on routes with a larger amount of open sea and by introducing speed optimisation, i.e. allowing the ship speed to vary to maximise the wind-generated thrust. This will ensure to find the best compromise between fuel savings and ship utilisation.

7.2. RECOMMENDATIONS FOR FUTURE WORK

Here below, a number of recommendations for future work are provided.

- To predict the interaction effects between Flettner rotors, an improved version of the mathematical model is likely to deliver satisfactory results. In this regard, the most necessary improvement to the aerodynamic interaction model appears to be a more refined discretisation of the vortex system: implement a line of horseshoe vortices instead of the single vortex currently in use. Moreover, a series of CFD computations should be carried out to study the interaction effects between two full-scale Flettner rotors. Following a procedure analogous to that one described in this work to derive the aerodynamic forces from the velocity field measurements, this study will indicate whether, at high Reynolds numbers, the viscous component of the mathematical model is still necessary for this purpose.
- In the experiments on the two Flettner rotors, the velocity ratio was limited to $k = 2$ for the reasons explained in Appendix C.3. Nonetheless, full-scale Flettner rotors often spin at higher velocity ratios. Since it was proven that the velocity ratio plays a key role in the determination of the aerodynamic interaction effects, it is likely that higher velocity ratios entail a more prominent influence of the interaction on the overall Flettner rotor performance. In this respect, a new series of wind-tunnel tests should be carried out in which the analysed Flettner rotors are allowed to spin at velocity ratios $k > 2$.
- To keep pace with ever stringent environmental regulations, as well as to increase the fuel-savings potential of the ship, it is arguable that in the foreseeable future the number of Flettner rotors installed aboard a ship will increase. In order to understand whether the trends measured during the tests presented in this work will hold true also in case a larger number of Flettner rotors is employed, experiments should be conducted on arrangements comprised by three (or more) Flettner rotors. A similar reasoning also applies to rigid sails.
- At the beginning of this work, it was decided to focus on the “sail-sail” interaction effects as the available literature suggested they are the most influential for the

overall aerodynamic performance of the vessel. The same literature, however, indicates that the aerodynamic interaction occurring between the wind-propulsion systems and the ship itself is also relevant and it deserves to be further investigated. In this regard, a series of systematic experiments or CFD simulations should be undertaken on different ship types. Following the same rationale applied in this dissertation to study the “sail-sail” interaction, velocity field data should be used to calculate the change in the wind propulsors’ aerodynamic forces due to the “ship-sail” interaction effects. With this aim, for each ship variation, the velocity field on the ship’s deck (where the wind propulsors would be installed) should be measured. The experimental data should then be used to build adequate regression formulas capable to estimate the velocity field generated on the deck of a given ship. Given the results presented in this dissertation, this method could be applied to ships equipped with Flettner rotors. Conversely, in case the considered ship deploys Dynarigs or other similar wind-assist devices, dedicated experiments or CFD simulations should be carried out on the whole wind-assisted ship.

A

DYNARIG EXPERIMENTS

This chapter is partially based on the journal article: G. Bordogna, J.A. Keuning, R.H.M. Huijsmans and M. Belloli. Wind-tunnel experiments on the aerodynamic interaction between two rigid sails used for wind-assisted propulsion. *International Shipbuilding Progress*, 65(1):93-125, 2018.

A.1. MEASUREMENTS OF THE VELOCITY FIELD

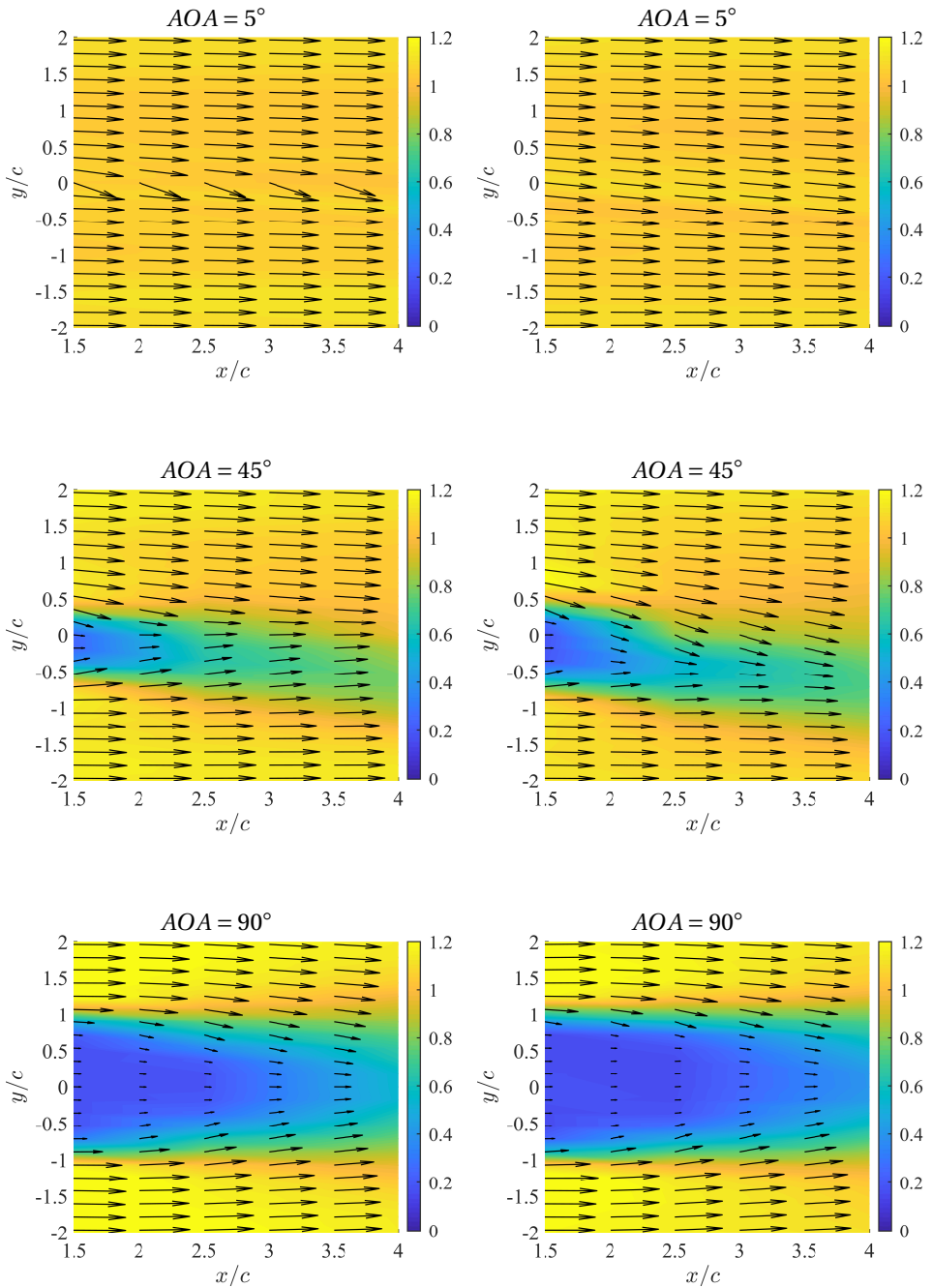


Figure A.1: Velocity field past the Dynarig at different angles of attack. Measurements of Cobra Probe 1 (left) and Cobra Probe 2 (right). The measurements were taken at a height of 1.45 m (Cobra 1) and 1.05 m (Cobra 2) from the ground. The results show the velocity field in a plane parallel to the floor

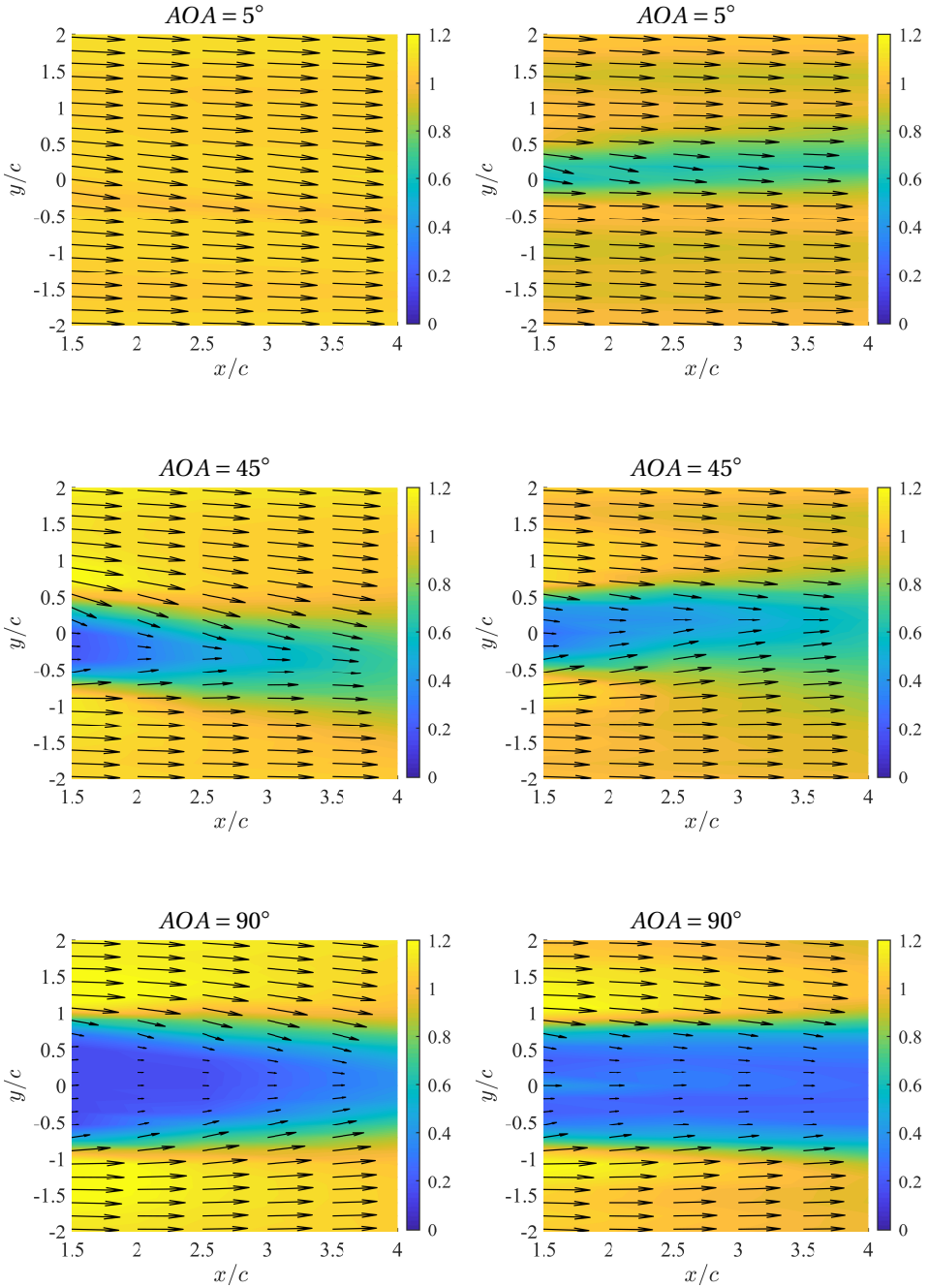


Figure A.2: Velocity field past the Dynarig at different angles of attack. Measurements of Cobra Probe 3 (left) and Cobra Probe 4 (right). The measurements were taken at a height of 0.65 m (Cobra 3) and 0.25 m (Cobra 4) from the ground. The results show the velocity field in a plane parallel to the floor

A.2. MEASUREMENT UNCERTAINTY

During the experimental campaign, it was possible to carry out a limited number of test repetitions to check the precision of the measurement setup. The only case considered was the single Dynarig set at $AOA = 20^\circ$ (that is the stall angle). For this condition, three repeated tests were conducted at the same nominal wind speed of 10 m/s and, before each measurement, the angle of attack of the sail was set anew by turning the wind-tunnel turntable. Due to a measurement problem, unfortunately, only the pressures relative to one of the three experiments were recorded, whereas the forces were measured for all repetitions.

To increase the population of the uncertainty analysis, it was decided to include the results relative to the study of the Reynolds number effects on the single Dynarig performance. This is justifiable since it was proven that for a given angle of attack, the influence of the Reynolds number on the sail aerodynamic coefficients is marginal. The experimental uncertainty was determined according to the ISO Guide to the Expression of Uncertainty in Measurements (ISO, 2008). In Table A.1 the data set used to estimate the precision of the measurement setup is given.

Table A.1: Measurement uncertainty data set and precision of the measurement setup

AOA [deg]	N experiments	Wind speed (V) [m/s]	σC_L [-]	σC_D [-]	$\sigma C_{p_{min}}$ [-]	$\sigma C_{p_{max}}$ [-]
5	3	6, 10, 12	0.0043	0.0358	0.0088	0.0028
20	3	10, 10, 10	0.0108	0.0117	-	-
45	3	6, 10, 12	0.0257	0.0172	0.0095	0.0242
90	3	6, 10, 12	0.0130	0.0387	0.0126	0.0290

The pooled variance of the data set is calculated according to:

$$\sigma^2 = \frac{\sum_{i=1}^N (N_{exp_i} - 1) \cdot \sigma_i^2}{\sum_{i=1}^N (N_{exp_i} - 1)} \quad (A.1)$$

and thus, the standard uncertainty related to the measurement precision reads:

$$u_{pr} = \sqrt{\frac{\sigma^2}{N}} \quad (A.2)$$

where N is the number of tests considered in the analysis.

The standard uncertainty u_{pr} was calculated for C_L , C_D , $C_{p_{min}}$ and $C_{p_{max}}$.

Regarding the bias errors of the measurement instruments, as per specification, the accuracy of the RUAG 192 force balance is $FB_{err} = \pm 1.27$ N while the accuracy of the ESP pressure scanner is $PS_{err} = \pm 1.50$ Pa. To calculate the standard uncertainty u_{bias} related to the measurement instrument bias errors, the sensitivity of the instrument bias errors on the quantity of interest needs to be calculated. This is done by taking the partial derivative of the bias errors FB_{err} and PS_{err} with respect to the quantity of interest, which, in this case, are C_L , C_D , $C_{p_{min}}$ and $C_{p_{max}}$. The standard uncertainties related to the experiment precision errors and the standard uncertainties related to the

measurement instrument bias errors are combined as uncorrelated quantities into the expanded uncertainty with 95% confidence level according to:

$$u_{95} = kf \cdot \sqrt{u_{pr}^2 + u_{bias}^2} \quad (\text{A.3})$$

where the coverage factor kf is set to $kf = 2$.

Finally, the expanded uncertainties of C_X and C_Y are calculated as:

$$u_{95C_X} = u_{95C_Y} = \max(u_{95C_L}, u_{95C_D}) \quad (\text{A.4})$$

The results of the measurement uncertainty analysis are reported in Table A.2, and they should be assumed to hold true for both the single-Dynarig as well as for the double-Dynarig experiments. The expanded uncertainties u_{95} were used for the error bars of the results of Chapter 3.

Table A.2: Measurement uncertainties

Coefficient	u_{pr}	u_{bias}	u_{95}
C_L	0.0045	0.0081	0.0186
C_D	0.0082	0.0081	0.0230
C_X	-	-	0.0230
C_Y	-	-	0.0230
$C_{p_{min}}$	0.0035	0.0248	0.0500
$C_{p_{max}}$	0.0073	0.0248	0.0518



B

DELFT ROTOR EXPERIMENTS

Section [B.1](#) and Section [B.2](#) are based on the article: G. Bordogna, S. Muggiasca, S. Giappino, M. Belloli, J.A. Keuning, R.H.M. Huijsmans and A.P. van 't veer. Wind-tunnel experiments on a large-scale Flettner rotor. In: Ricciardelli E, Avossa A. (eds) Proceedings of the XV Conference of the Italian Association for Wind Engineering. IN VENTO 2018. Lecture Notes in Civil Engineering, vol 27. Springer, Cham.

Section [B.3](#) is based on the journal article: G. Bordogna, S. Muggiasca, S. Giappino, M. Belloli, J.A. Keuning, R.H.M. Huijsmans and A.P. van 't veer. Experiments on a Flettner rotor at critical and supercritical Reynolds numbers. *Journal of Wind Engineering and Industrial Aerodynamics*, 188:19-29, 2019.

B.1. FURTHER INFORMATION ON THE EXPERIMENTAL SETUP

The Delft Rotor is a rotating cylinder with diameter $D = 1.0$ m and span $H = 3.73$ m and it is comprised of three main parts: a static structure, a rotating frame and an outer skin. The static structure consisted of a lower and an upper steel assembly made of four M30 threaded bars screwed into four bases, that were bolted to the wind-tunnel ground and ceiling I-section beams. To improve the stiffness of the static assemblies, four oblique steel bars were connected to the threaded bars and the force balance (Figure B.2). Two aluminum purpose-built force balances were placed at the extremity of the threaded bars, on top of which the bearing housings were bolted (Figure B.1 and Figure B.2).

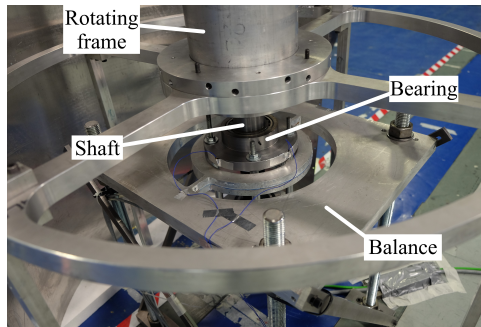


Figure B.1: Lower assembly of the Delft Rotor's static structure

To compensate for a possible misalignment, it was chosen to use two self-aligning spherical roller bearings. The reason to position the balances close to the bearings was to reduce to the minimum the bending moment. By doing so, it was possible to use a three-component force balance: only lift, drag and torque were measured.

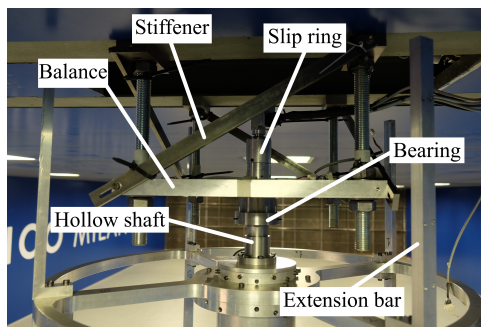


Figure B.2: Upper assembly of the Delft Rotor's static structure

Each force balance was carved out of 30 mm thick aluminum slab and it consisted of two concentric circles connected by four strips on which the lift, drag and torque extensometers were placed (Figure B.3). The force balances were purposely built for the Delft Rotor experiments to withstand the large aerodynamic forces expected to act on the cylinder ($F_{L_{max}} = 2500$ N).

The rotating frame of the Delft Rotor consisted of a 5 mm thick aluminum tube to which three equal aluminum wheels were bolted. The wheels were connected with eight vertical bars. Four extra lower (Figure B.1) and upper (Figure B.2) bars were used as an extension so that the internal frame matched the height of the outer skin. The extremities of the internal tube were plugged with lids into which two steel shafts were screwed. The shafts were then fitted into the bearings. The Delft Rotor's outer skin was composed of four calendered aluminum sheets. The sheets were 2 mm thick and they were bolted to the internal frame with more than 250 countersunk head screws. The high number of screws used to secure the calendered sheets to the rotor's internal frame was necessary to achieve a safety factor of 2 while expecting a maximum centrifugal force of 15 kN (the total weight of the rotating components was 170 kg). The frame was rotated using an electric engine that was hung to the lower bearing housing through four threaded bars, and a flexible coupling was used to connect the engine shaft with the lower shaft of the internal frame (Figure B.1).

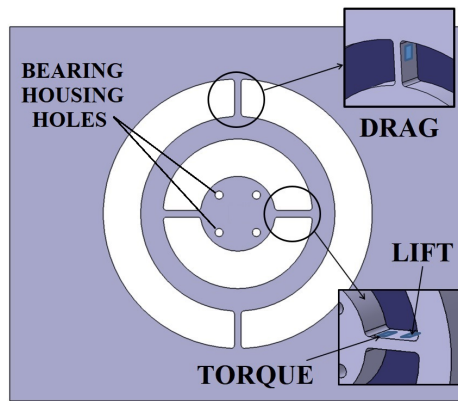


Figure B.3: Three-component force balance used during the experiments

B.2. PRESSURE MEASUREMENT CORRECTION

The pressure tube length and inner diameter influence the pressure frequency response as they act as a filter on the signal. This effect is generally relevant in experiments in which the pressures on a moving object need to be measured, and it becomes more noticeable as the speed of the moving object increases. Since the tubes of the 32 pressure taps had to be connected to one single scanner, inevitably they had a considerable length. For this reason, the pressures measured by the ESP scanner had to be corrected to account for the frequency response of the tubing system. During the first series of tests, it was chosen to use tubes of 1.02 mm inner diameter whereas during the second experimental campaign larger tubes with an inner diameter of 1.50 mm were employed. From the analysis of the pressure data, it appeared that the tubes with larger diameter had a better frequency response when compared to the data of the AMS4711 sensor.

Another correction that needs to be applied is to consider the centripetal acceleration acting upon the air column enclosed inside the pressure tubes or acting directly

upon the measurement instrument. In the first case, the effect of the acceleration on the air column is dependent on the length of the pressure tubes in the radial direction (not on the total length of the tubes). In the second case, the effect of the acceleration on the measurement instrument is dependent on the distance of the device from the axis of rotation. This means that, due to the way the pressure measurement systems were mounted on the Delft Rotor, the pressures measured by the ESP scanner need to be corrected to account for the effect of the acceleration on the air column enclosed in the pressure tube connecting the scanner and the pressure tap. Conversely, the pressures measured by the AMS4711 sensor need to be corrected for the effect of the acceleration acting on the sensor itself. As reported by Pollack et al. (1972), the effect of the acceleration on the air column can be estimated according to:

$$p_A - p_B = \frac{\rho \cdot \omega^2}{2} \cdot (r_A^2 - r_B^2) \quad (\text{B.1})$$

where $p_A - p_B$ is the pressure difference between the measurement instrument and the pressure tap, ρ is the air density, ω is the angular velocity and r_A and r_B are the radial distances of the measurement instrument and the pressure tap from the axis of rotation. To provide an example of the effect of the centripetal acceleration on the pressure measurements, Figure B.4 shows the pressure on the cylinder measured at increasing angular velocities in still air.

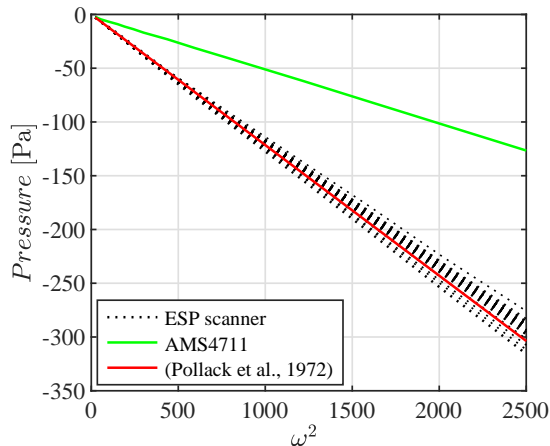


Figure B.4: Measured pressure in still air as a function of the square of the angular velocity

From the results of Figure B.4 it can be seen that the effect of the acceleration is similar for all 32 sensors of the ESP scanner, although the lengths of the pressure tubes are considerably different from one another ($390 < L_{tube} < 2500$ mm). The results of the AMS4711 sensor, on the other hand, do not follow the same trend as the measured pressure is due to the acceleration acting on the sensing membrane. An estimate of the magnitude of the acceleration effect on a generic piezoresistive pressure sensor is provided by Kurtz et al. (2003), and it depends on the magnitude of the acceleration and the full-scale pressure range of the measurement instrument. To overcome the issues

here discussed, during the experiments the rotor was spun in still air at the corresponding angular velocity of each subsequent actual measurement (rotation + wind switched on). This procedure was repeated for all tests performed. The pressures measured with both instrumentations were, therefore, corrected according to:

$$p_{corrected} = [p_{rot.\&wind} - \Delta p_{rot.\&wind}] - [p_{rot.} - \Delta p_{rot.}] \quad (B.2)$$

where $p - \Delta p$ is the pressure measured during experiments with wind switched on (rot.&wind) or with wind switched off and just the rotation (rot.), corrected for the difference in static pressure between inside and outside the cylinder for the corresponding test. By applying this correction, the effects of the centrifugal acceleration were eliminated irrespective of whether they affected the tubing system or the measurement instrument itself. The inconvenience of this correction method, however, is that it also eliminates the pressure experienced by the cylinder due to the rotation only but, according to [Thom \(1931\)](#), this effect appears to be marginal.

B.3. MEASUREMENT UNCERTAINTY

The experimental uncertainty was calculated according to the ISO “Guide to the Expression of Uncertainty in Measurement” ([ISO, 2008](#)). The expanded uncertainty with 95% confidence level, u_{95} , was calculated from the standard uncertainty related to the measurement precision, u_{pr} , and the standard uncertainty of the bias errors of the measurement instruments, u_{bias} . For each quantity of interest, u_{pr} was obtained using the data of repeated experiments as well as data of one same experiment but measured with different instruments. These are the force balances and the ESP pressure scanner for the overall C_L and C_D , the ESP pressure scanner and the AMS4711 sensor for the sectional C_l , C_d and C_p , and the force balances and the engine controller for the power consumption P . The standard uncertainty related to the measurement precision reads:

$$u_{pr} = \sqrt{\frac{\sigma^2}{N}} \quad (B.3)$$

where σ is the standard deviation of the N considered data points. Conversely, the standard uncertainty related to the bias errors of the measurement instrument is the sensitivity of the measurement instrument accuracy (as per specification of the manufacturer or, in case of the in-house built force balances, it was measured during the calibration tests) respect to the quantity of interest. u_{bias} can then be calculated by taking the partial derivative of the instrument accuracy with respect to the quantity to be analysed. The expanded uncertainty with 95% confidence level is thus calculated according to:

$$u_{95} = kf \cdot \sqrt{u_{pr}^2 + u_{bias}^2} \quad (B.4)$$

where the coverage factor kf is set to $kf = 2$.

The measurement uncertainties with 95% confidence level reported in [Table B.1](#) (overall C_L and C_D), [Table B.2](#) (sectional C_l and C_d), [Table B.3](#) ($C_{p_{min}}$ and $C_{p_{max}}$), and [Table B.4](#) (P_w and P_{nw}) refer to the mean value of the results reported in [Section 4.3](#).

Table B.1: Overall lift and drag coefficients - measurement uncertainties u_{95} with 95% confidence level

Coeff.	Re [$\cdot 10^5$]	Velocity ratio k										
		0	0.5	1.0	1.5	2.0	2.5	3.0	3.5	4.0	4.5	5.0
C_L	1.8	0.212	0.266	0.241	0.235	0.235	0.262	-	-	-	-	-
	2.5	0.135	0.184	0.234	0.224	0.204	0.182	0.142	0.153	0.119	0.117	0.128
	3.6	0.068	0.089	0.084	0.112	0.098	0.166	0.102	0.098	0.087	0.086	0.132
	10.0	0.081	0.065	0.157	0.115	0.049	-	-	-	-	-	-
C_D	1.8	0.213	0.259	0.221	0.216	0.269	0.328	-	-	-	-	-
	2.5	0.113	0.477	0.374	0.233	0.210	0.114	0.112	0.124	0.308	0.421	0.556
	3.6	0.072	0.161	0.068	0.085	0.062	0.111	0.181	0.218	0.275	0.384	0.523
	10.0	0.050	0.007	0.080	0.055	0.098	-	-	-	-	-	-

Table B.2: Sectional lift and drag coefficients - measurement uncertainties u_{95} with 95% confidence level

Coeff.	Re [$\cdot 10^5$]	Velocity ratio k										
		0	0.5	1.0	1.5	2.0	2.5	3.0	3.5	4.0	4.5	5.0
C_l	1.8	0.241	0.139	0.115	0.198	0.237	0.157	-	-	-	-	-
	2.5	0.154	0.105	0.101	0.112	0.105	0.172	0.363	0.456	0.440	0.395	0.419
	3.6	0.140	0.051	0.143	0.191	0.142	0.142	0.356	0.469	0.474	0.446	0.435
	10.0	0.125	0.078	0.356	0.025	0.223	-	-	-	-	-	-
C_d	1.8	0.197	0.104	0.128	0.112	0.159	0.146	-	-	-	-	-
	2.5	0.105	0.101	0.120	0.111	0.100	0.108	0.104	0.143	0.164	0.101	0.148
	3.6	0.054	0.048	0.082	0.067	0.079	0.059	0.047	0.099	0.119	0.052	0.148
	10.0	0.097	0.011	0.084	0.111	0.144	-	-	-	-	-	-

Table B.3: Sectional pressure coefficients - measurement uncertainties u_{95} with 95% confidence level

Coeff.	Re [$\cdot 10^5$]	Velocity ratio k										
		0	0.5	1.0	1.5	2.0	2.5	3.0	3.5	4.0	4.5	5.0
$C_{p_{min}}$	1.8	0.445	0.754	0.767	0.732	0.737	0.737	-	-	-	-	-
	2.5	0.149	0.369	0.374	0.379	0.380	0.396	0.547	0.496	0.437	0.457	0.411
	3.6	0.153	0.189	0.177	0.179	0.247	0.306	0.374	0.398	0.364	0.309	0.329
	10.0	0.121	0.105	0.101	0.075	0.038	-	-	-	-	-	-
$C_{p_{max}}$	1.8	0.224	0.730	0.732	0.735	0.755	0.730	-	-	-	-	-
	2.5	0.153	0.375	0.390	0.375	0.375	0.375	0.376	0.375	0.390	0.376	0.383
	3.6	0.092	0.178	0.178	0.176	0.199	0.176	0.179	0.193	0.189	0.176	0.179
	10.0	0.036	0.033	0.059	0.063	0.025	-	-	-	-	-	-

Table B.4: Flettner rotor power consumption measured in an air stream (P_w) and in still air (P_{nw}) - measurement uncertainties u_{95} with 95% confidence level

Re		Rotational velocity rpm										
[$\cdot 10^5$]		50	100	150	200	250	300	350	400	450	500	550
P_w [kW]	1.8	0.003	0.006	-	-	-	-	-	-	-	-	-
	2.5	0.005	0.007	0.010	0.015	0.021	0.030	0.049	-	-	-	-
	3.6	0.003	0.006	0.010	0.024	0.029	0.032	0.056	0.070	0.097	0.131	-
	10.0	-	-	0.037	-	-	0.057	-	-	0.178	-	0.303
P_{nw} [kW]	1.8	0.003	0.006	-	-	-	-	-	-	-	-	-
	2.5	0.005	0.008	0.010	0.013	0.016	0.021	0.037	-	-	-	-
	3.6	0.004	0.006	0.010	0.018	0.023	0.019	0.033	0.040	0.058	0.082	-
	10.0	-	-	0.009	-	-	0.019	-	-	0.094	-	0.173



C

DOUBLE FLETTNER ROTOR EXPERIMENTS

This chapter is partially based on the journal article: G. Bordogna, S. Muggiasca, S. Giappino, M. Belloli, J.A. Keuning and R.H.M. Huijsmans. The effects of the aerodynamic interaction on the performance of two Flettner rotors. *Journal of Wind Engineering and Industrial Aerodynamics*, (2019), doi.org/10.1016/j.jweia.2019.104024

C.1. MEASUREMENTS OF THE VELOCITY FIELD

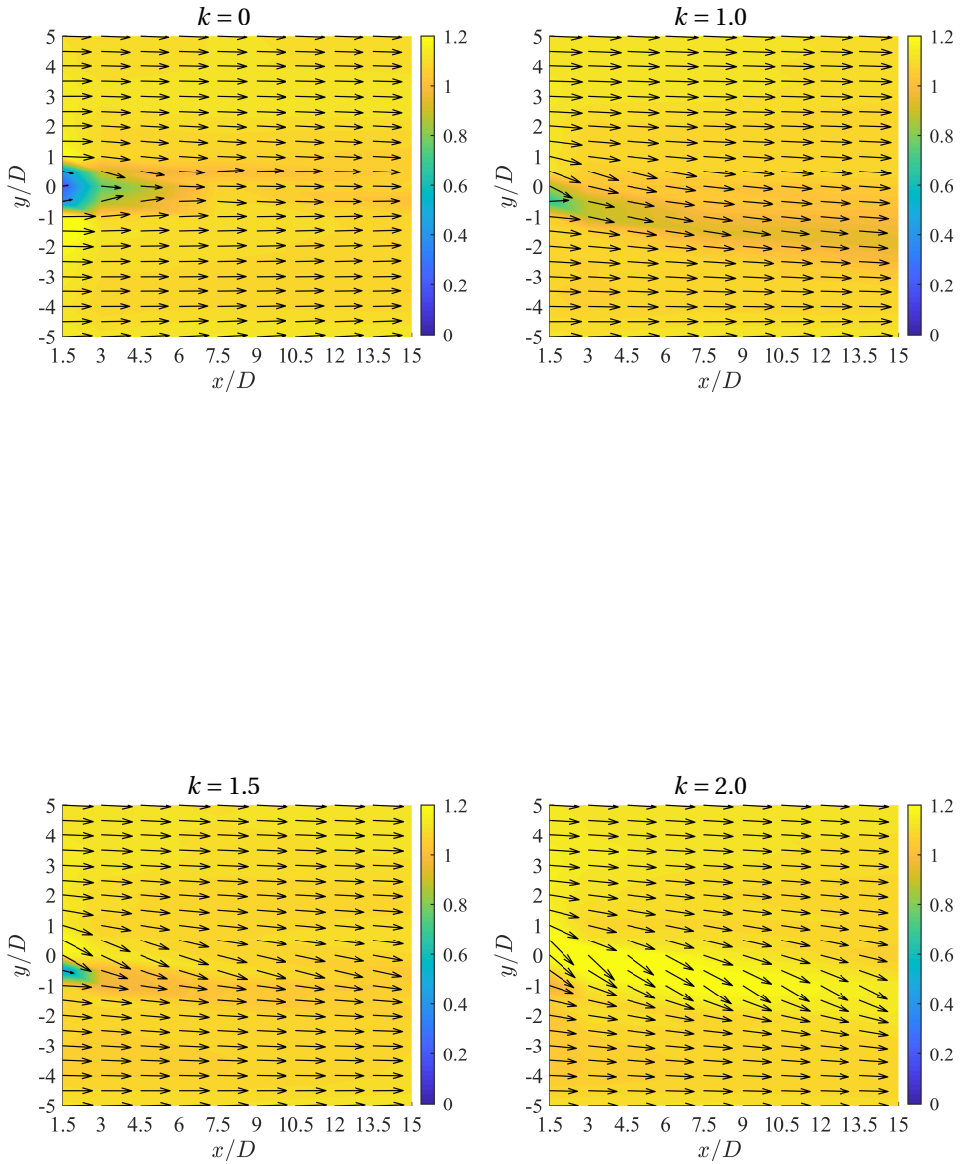


Figure C.1: Velocity field past the Flettner rotor at different velocity ratios. Measurements of Cobra Probe 1 taken at a height of 1.62 m from the ground. The results show the velocity field in a plane parallel to the floor

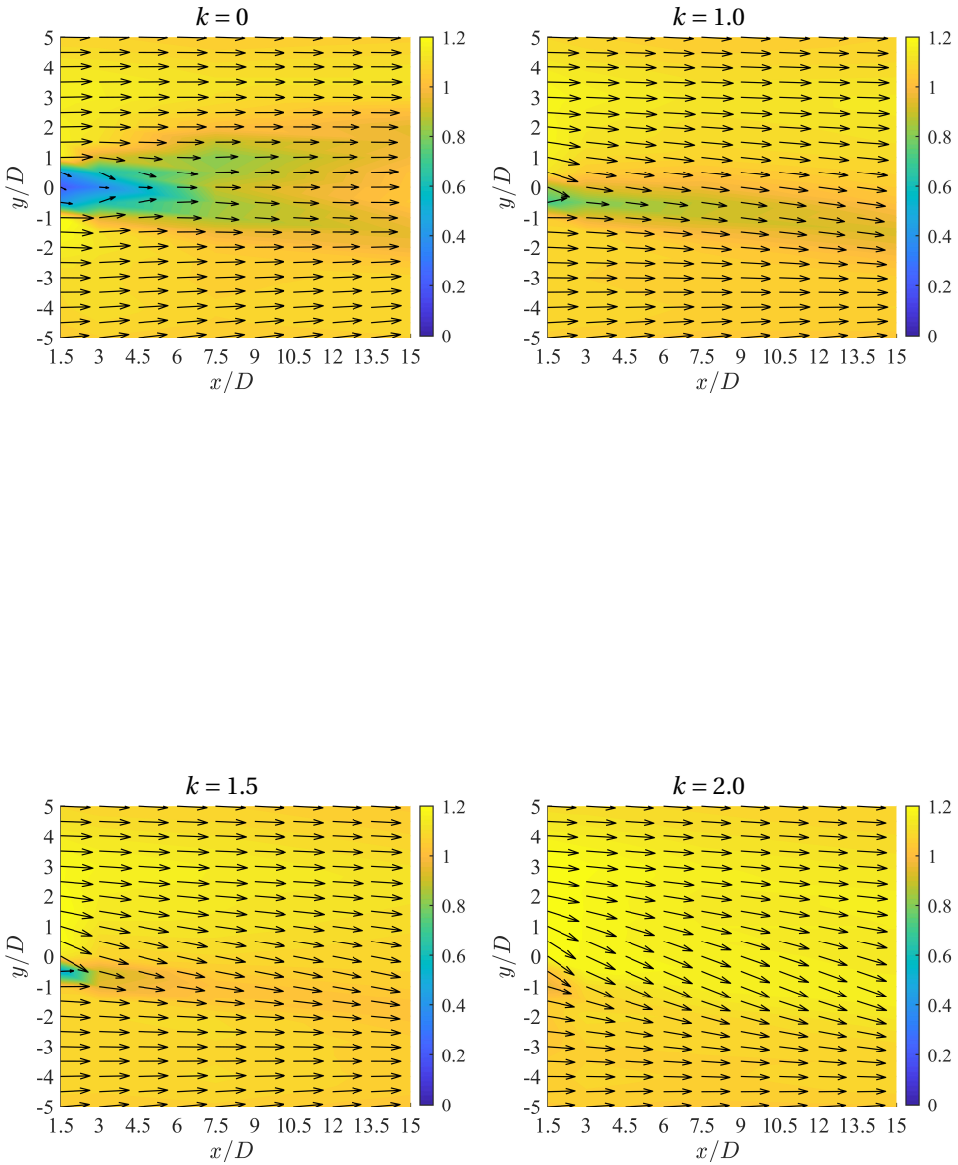


Figure C.2: Velocity field past the Flettner rotor at different velocity ratios. Measurements of Cobra Probe 2 taken at a height of 1.24 m from the ground. The results show the velocity field in a plane parallel to the floor

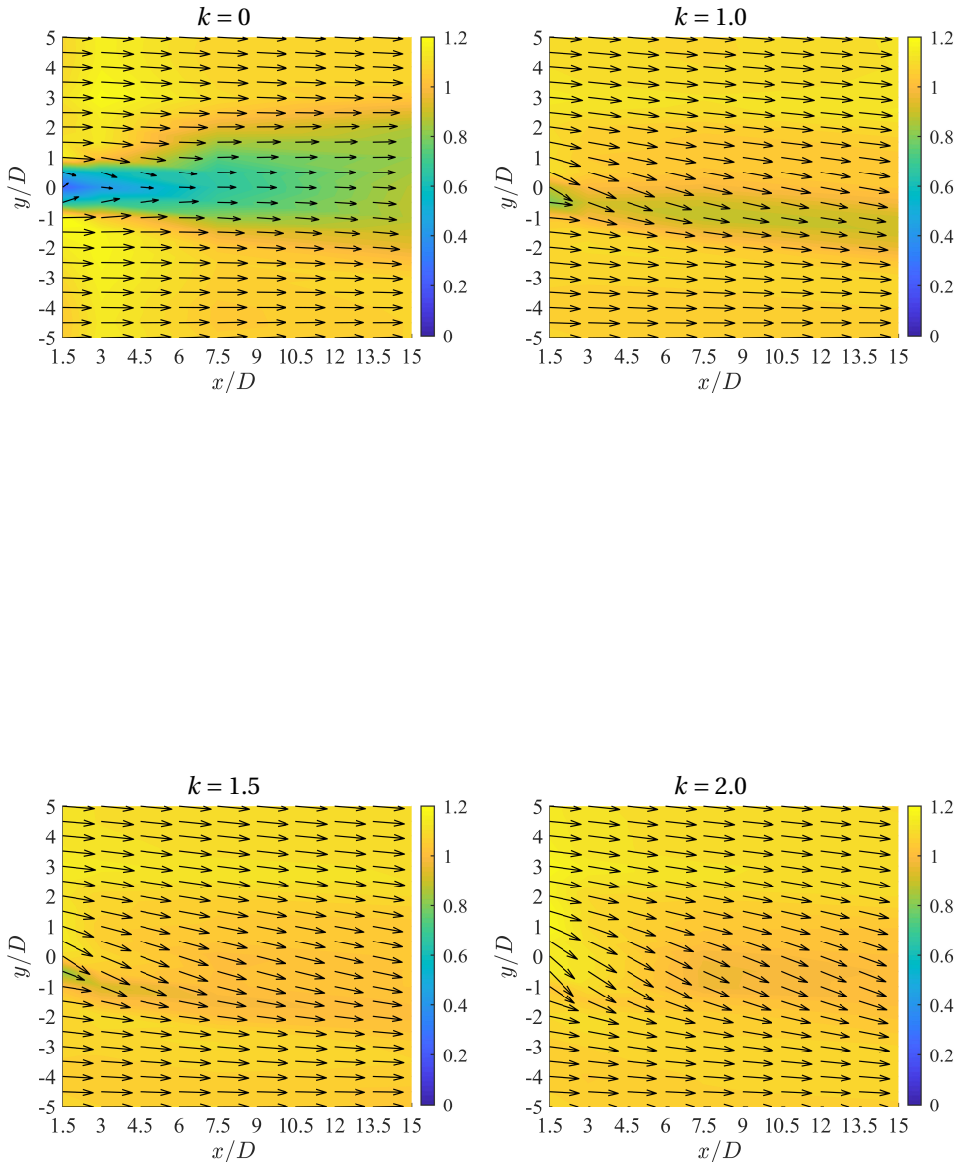


Figure C.3: Velocity field past the Flettner rotor at different velocity ratios. Measurements of Cobra Probe 3 taken at a height of 0.85 m from the ground. The results show the velocity field in a plane parallel to the floor

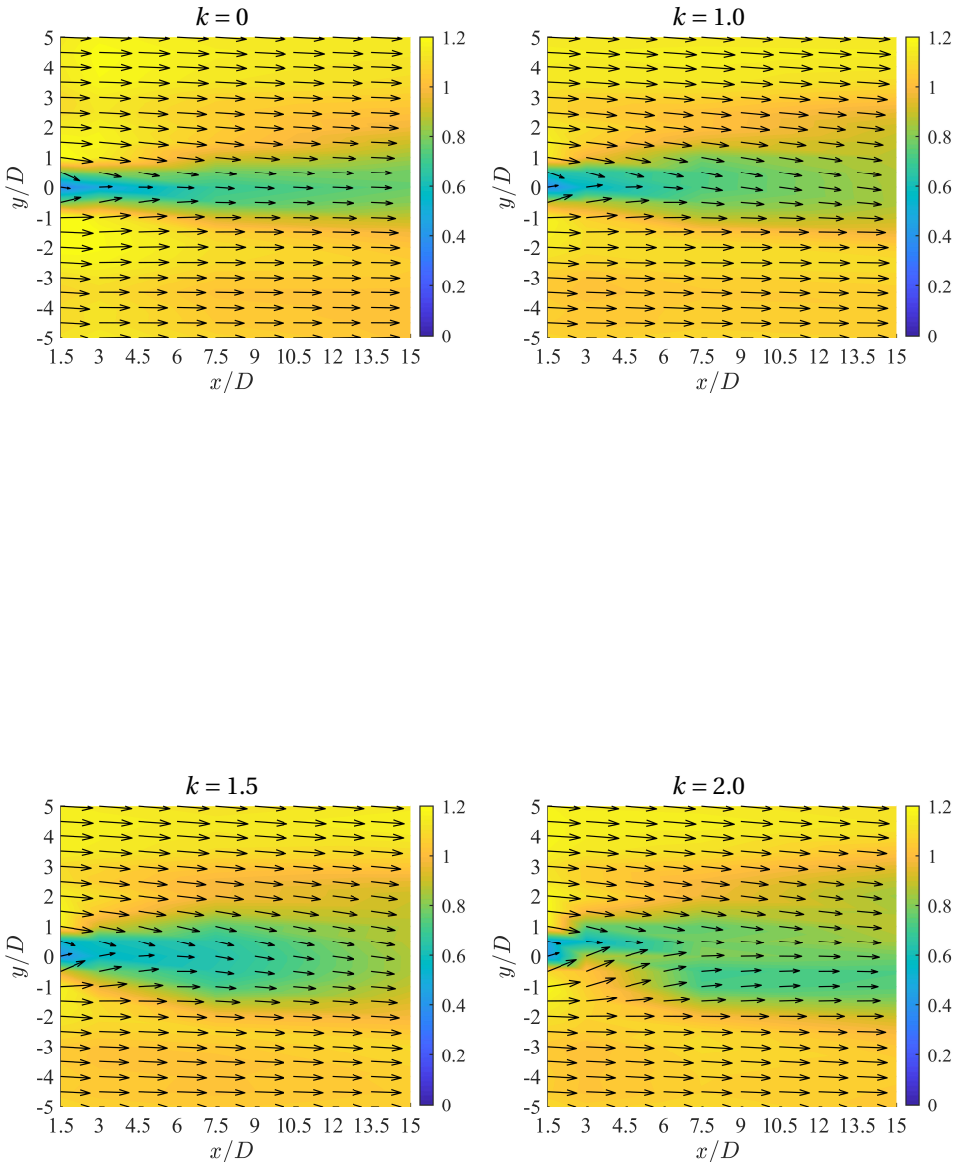


Figure C.4: Velocity field past the Flettner rotor at different velocity ratios. Measurements of Cobra Probe 4 taken at a height of 0.47 m from the ground. The results show the velocity field in a plane parallel to the floor

C.2. DRIVING AND HEELING FORCE COEFFICIENTS

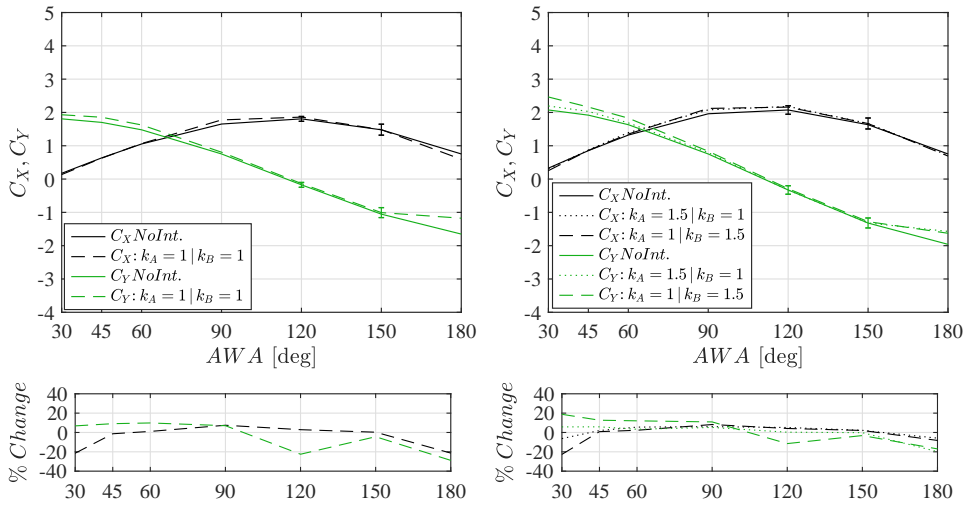


Figure C.5: Driving and heeling force coefficients (top) and the percentage change of the double Flettner rotor results with respect to two non-interacting Flettner rotors (bottom). Velocity ratios: $k = 1, k = 1$ (left) and $k = 1.5, k = 1$ (right). Devices installed in tandem arrangement at gap distance $GD = 3$

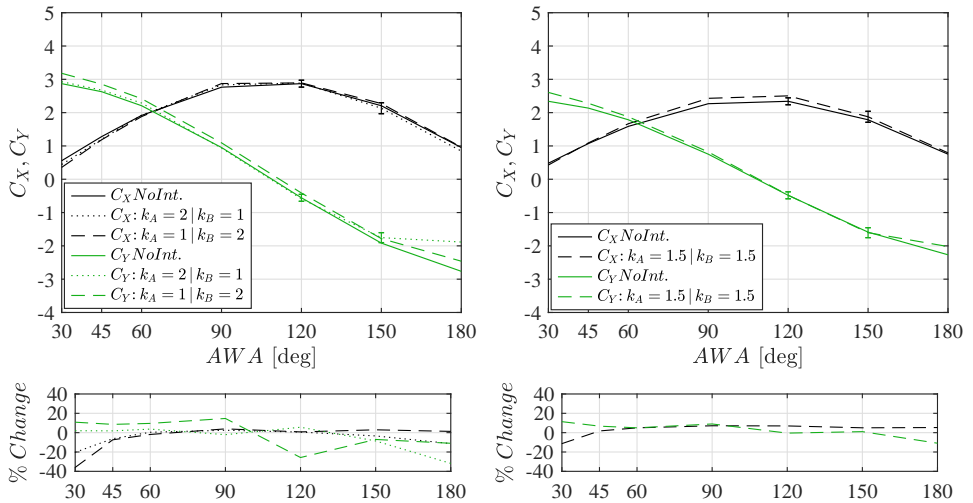


Figure C.6: Driving and heeling force coefficients (top) and the percentage change of the double Flettner rotor results with respect to two non-interacting Flettner rotors (bottom). Velocity ratios: $k = 1, k = 2$ (left) and $k = 1.5, k = 1.5$ (right). Devices installed in tandem arrangement at gap distance $GD = 3$

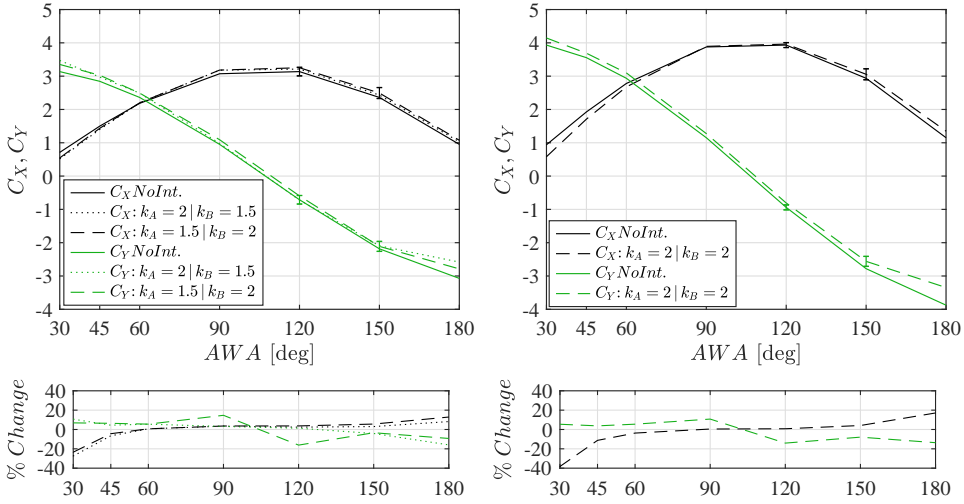


Figure C.7: Driving and heeling force coefficients (top) and the percentage change of the double Flettner rotor results with respect to two non-interacting Flettner rotors (bottom). Velocity ratios: $k = 1.5, k = 2$ (left) and $k = 2, k = 2$ (right). Devices installed in tandem arrangement at gap distance $GD = 3$

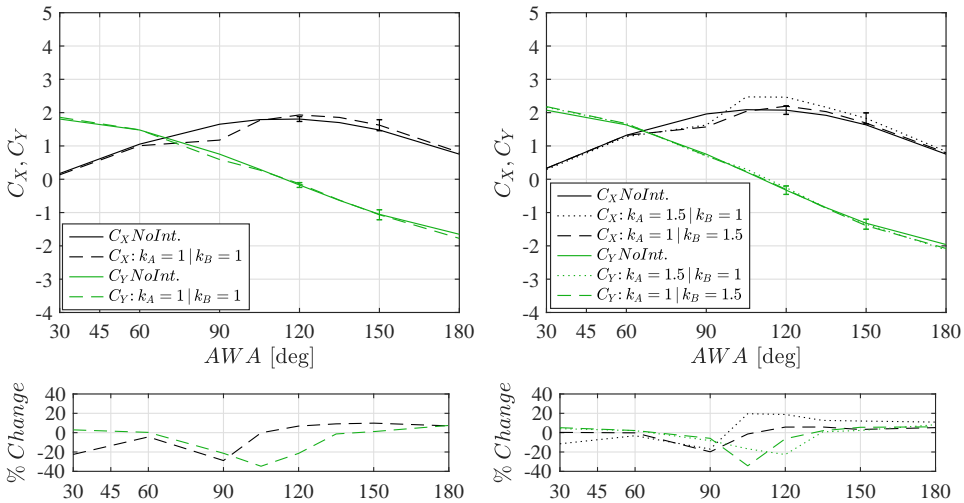


Figure C.8: Driving and heeling force coefficients (top) and the percentage change of the double Flettner rotor results with respect to two non-interacting Flettner rotors (bottom). Velocity ratios: $k = 1, k = 1$ (left) and $k = 1, k = 1.5$ (right). Devices installed in side-by-side arrangement at gap distance $GD = 3$

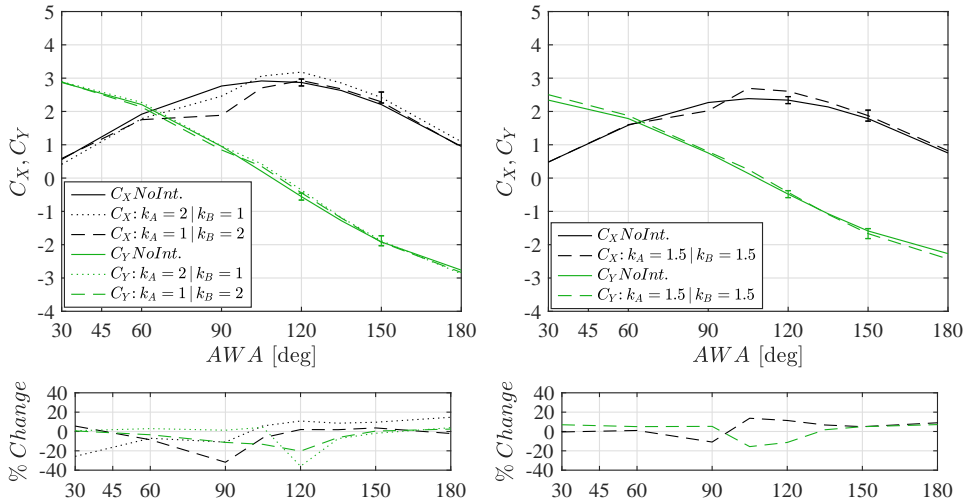


Figure C.9: Driving and heeling force coefficients (top) and the percentage change of the double Flettner rotor results with respect to two non-interacting Flettner rotors (bottom). Velocity ratios: $k = 1, k = 2$ (left) and $k = 1.5, k = 1.5$ (right). Devices installed in side-by-side arrangement at gap distance $GD = 3$

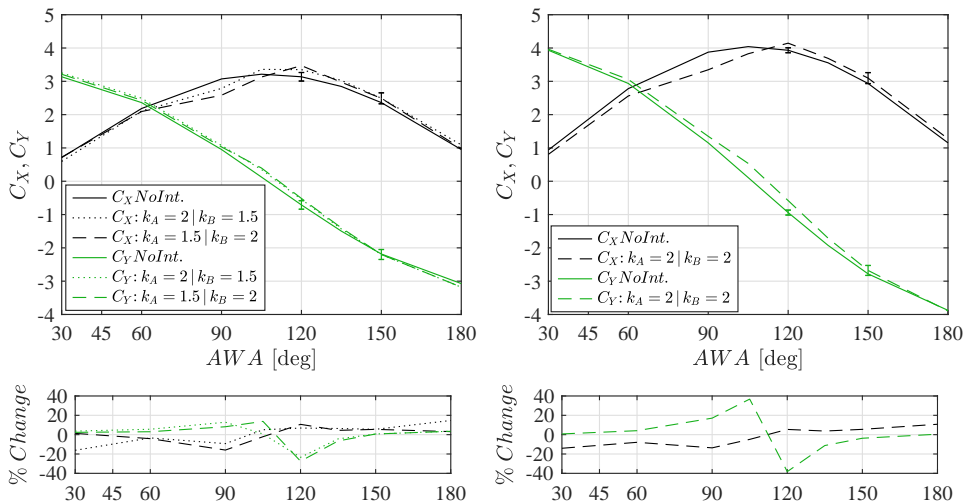


Figure C.10: Driving and heeling force coefficients (top) and the percentage change of the double Flettner rotor results with respect to two non-interacting Flettner rotors (bottom). Velocity ratios: $k = 1.5, k = 2$ (left) and $k = 2, k = 2$ (right). Devices installed in side-by-side arrangement at gap distance $GD = 3$

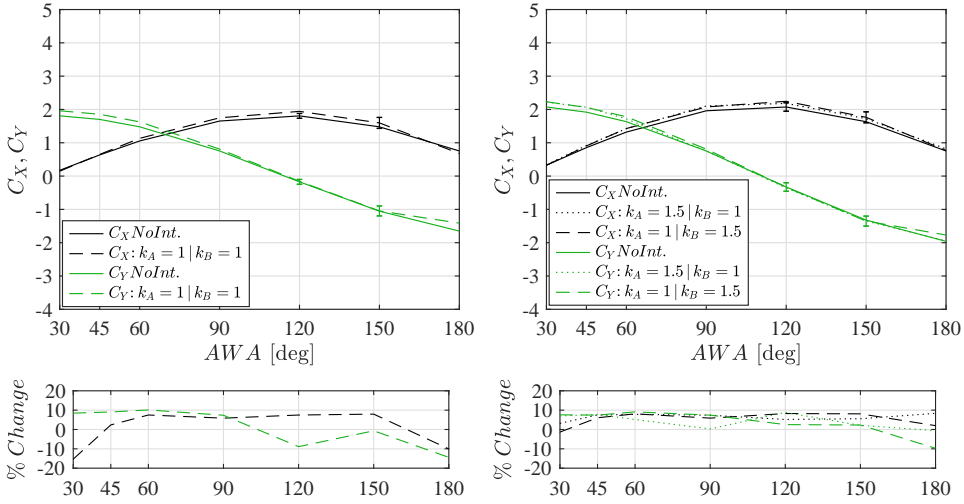


Figure C.11: Driving and heeling force coefficients (top) and the percentage change of the double Flettner rotor results with respect to two non-interacting Flettner rotors (bottom). Velocity ratios: $k = 1, k = 1$ (left) and $k = 1, k = 1.5$ (right). Devices installed in tandem arrangement at gap distance $GD = 7.5$

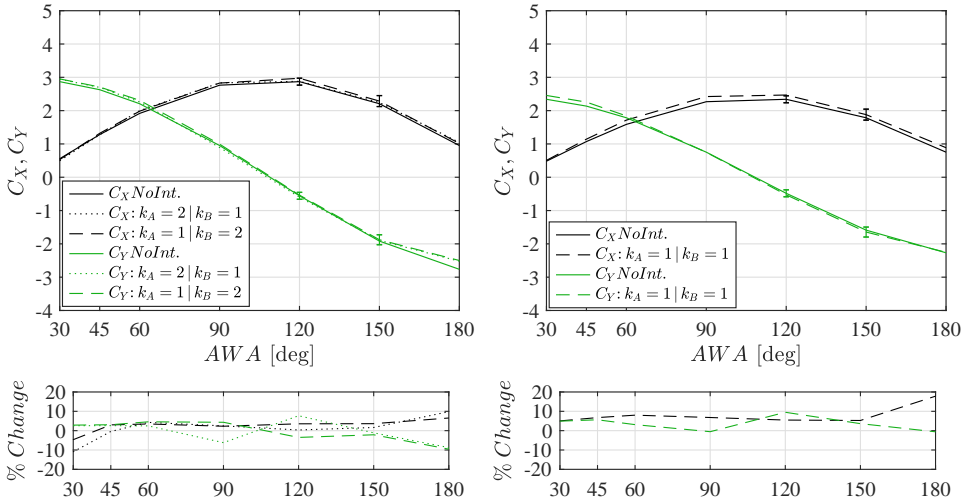


Figure C.12: Driving and heeling force coefficients (top) and the percentage change of the double Flettner rotor results with respect to two non-interacting Flettner rotors (bottom). Velocity ratios: $k = 1, k = 2$ (left) and $k = 1.5, k = 1.5$ (right). Devices installed in tandem arrangement at gap distance $GD = 7.5$

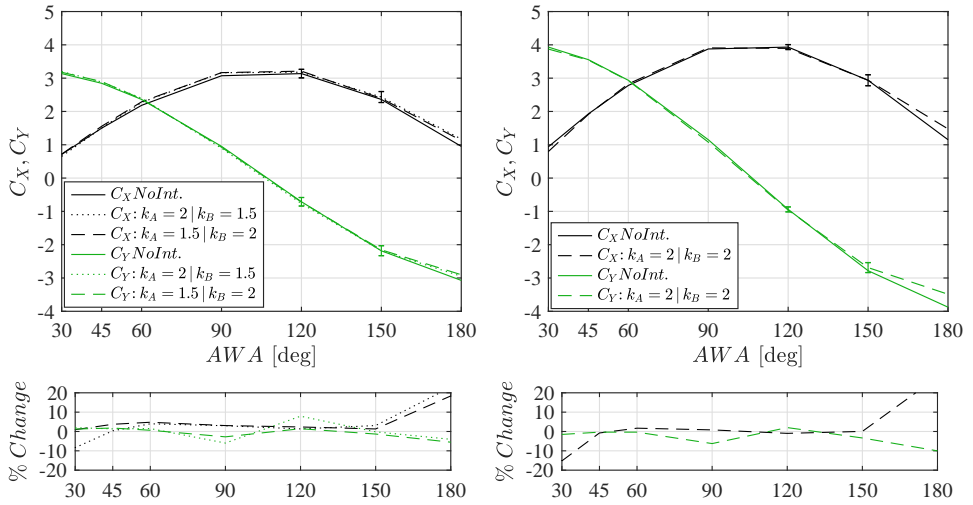


Figure C.13: Driving and heeling force coefficients (top) and the percentage change of the double Flettner rotor results with respect to two non-interacting Flettner rotors (bottom). Velocity ratios: $k = 1.5$, $k = 2$ (left) and $k = 2$, $k = 2$ (right). Devices installed in tandem arrangement at gap distance $GD = 7.5$

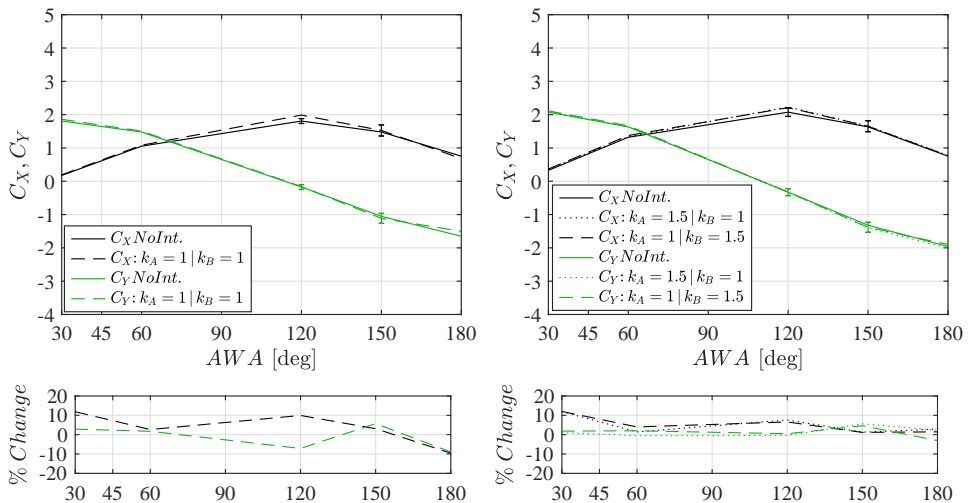


Figure C.14: Driving and heeling force coefficients (top) and the percentage change of the double Flettner rotor results with respect to two non-interacting Flettner rotors (bottom). Velocity ratios: $k = 1$, $k = 1$ (left) and $k = 1$, $k = 1.5$ (right). Devices installed in tandem arrangement at gap distance $GD = 15$

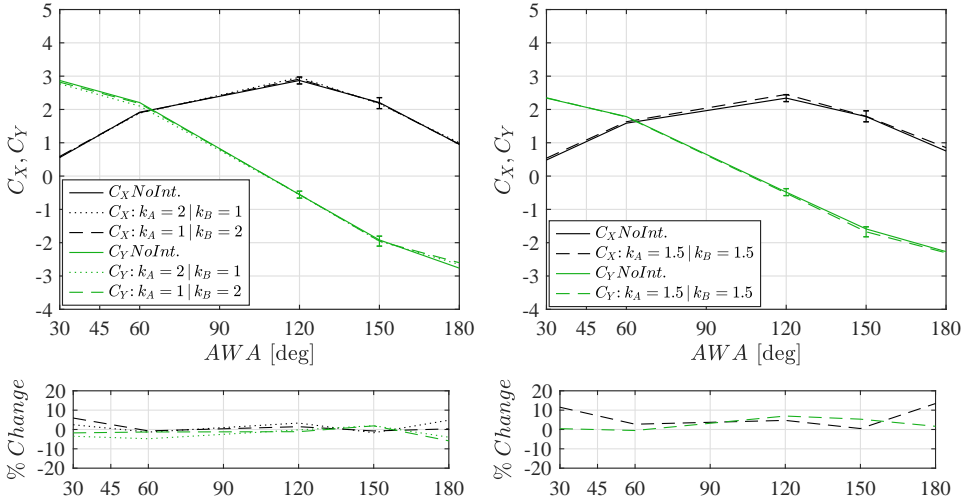


Figure C.15: Driving and heeling force coefficients (top) and the percentage change of the double Flettner rotor results with respect to two non-interacting Flettner rotors (bottom). Velocity ratios: $k = 1, k = 2$ (left) and $k = 1.5, k = 1.5$ (right). Devices installed in tandem arrangement at gap distance $GD = 15$

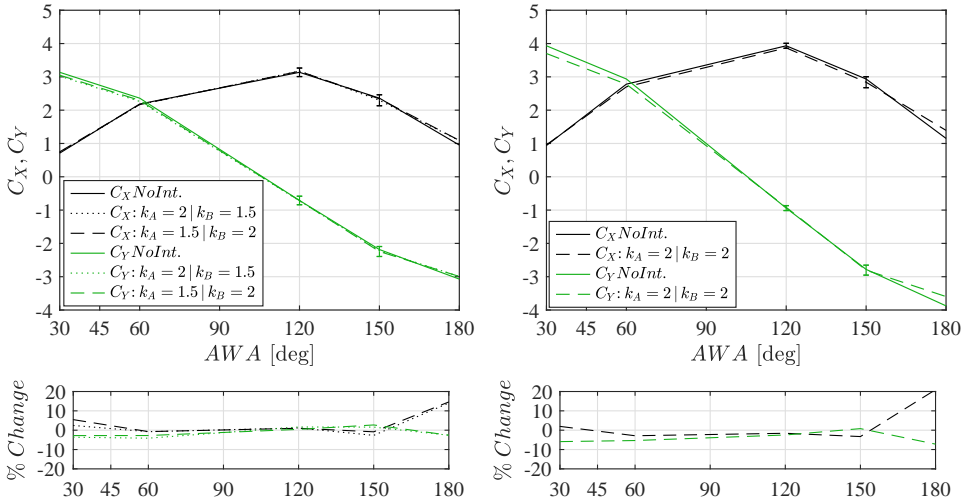


Figure C.16: Driving and heeling force coefficients (top) and the percentage change of the double Flettner rotor results with respect to two non-interacting Flettner rotors (bottom). Velocity ratios: $k = 1.5, k = 2$ (left) and $k = 2, k = 2$ (right). Devices installed in tandem arrangement at gap distance $GD = 15$

C.3. MEASUREMENT UNCERTAINTY

The uncertainty of the experimental study was calculated according to ISO “Guide to the Expression of Uncertainty in Measurement” (ISO, 2008). The expanded uncertainty with 95% confidence level, u_{95} , was calculated from the standard uncertainty related

to the measurement precision, u_{pr} , and the standard uncertainty of the bias errors of the measurement instruments, u_{bias} . During the experiments, repetitions were carried out exclusively for $k = 1$, $k = 1.5$ and $k = 2$, and for Reynolds number $Re = 1.0 \cdot 10^5$. The measurement uncertainties were therefore calculated for these conditions. The standard uncertainty related to the measurement precision reads:

$$u_{pr} = \sqrt{\frac{\sigma^2}{N}} \quad (\text{C.1})$$

where σ is the standard deviation of the N considered data points. On the other hand, the standard uncertainty related to the bias errors of the measurement instrument is the sensitivity of the measurement instrument accuracy, obtained by means of calibration tests, respect to the quantity of interest. u_{bias} can then be calculated by taking the partial derivative of the instrument accuracy with respect to the quantity to be analysed. The value of u_{bias} differ for the ATI balance and the HBM load cell. The expanded uncertainty with 95% confidence level is thus calculated according to:

$$u_{95} = kf \cdot \sqrt{u_{pr}^2 + u_{bias}^2} \quad (\text{C.2})$$

where the coverage factor kf is set to $kf = 2$.

Regarding the tests on the two Flettner rotors, it should be pointed out that repetitions were not carried out for the entire set of gap distances and flow angles analysed. In fact, for each considered velocity ratio, the tests were repeated only for one gap distance and one flow angle. The assumption is that the measurement uncertainties calculated for those conditions can also be applied to all other comparable conditions, i.e. same velocity ratio but different gap distance and different flow angle. This is justifiable because the measurement precision error appears to be marginal compared to the bias error of the measurement instrument. This is particularly the case for the HBM load cells, for which the bias error appears to be considerably large. The reason of a large bias error is because the measurement instruments chose for the current experiments had to have a sufficiently large load range along the vertical axis to withstand the weight of the Flettner rotor but, consequently, the load range along the lift and drag axes resulted to be over-dimensioned. One possibility to reduce the measurement instrument bias error would have been to increase the wind speed at which the experiments were carried out. However, in the current experimental campaign, this was not feasible because, to reach the desired velocity ratios, the Flettner rotors should have spun at considerably higher rotational speeds, and this was a concern for the structural limits of the Flettner rotor assembly with respect to vibrations. It was decided, in fact, to establish a safety limit of 11 Hz (the lowest eigenfrequency of the Flettner rotor assembly was 16 Hz), meaning that to reach velocity ratio $k = 2$ the highest achievable wind speed was $V = 5$ m/s.

In case of the double Flettner rotor experiments, the ATI balances, as well as the HBM load cells, were mounted on the wind-tunnel turntable in such a way that the driving and the heeling forces were measured along the force balances' main axes regardless from the wind angle. Therefore, u_{95} was measured for C_X and C_Y while for C_L and C_D was calculated as follows:

$$u_{95C_L} = u_{95C_D} = \max(u_{95C_X}, u_{95C_Y}) \quad (\text{C.3})$$

The uncertainties derived with the method described above are reported in Table C.1 and Table C.2. These are included in the results of Chapter 5 in the form of error bars. For the sake of clarity, the error bars are given just for one data point for each setup (single and double Flettner rotor setup) and for each quantity of interest (C_L , C_D , C_X and C_Y). This is sufficient to understand the magnitude of the uncertainties with respect to the relative measurements because, as previously explained, the standard uncertainty related to the measurement precision u_{pr} , that depends on the different testing conditions (i.e. wind angle, gap distance, velocity ratio), is typically about one order of magnitude smaller than u_{bias} .

Regarding the driving and heeling force coefficients, for which the results are presented for the entire Flettner rotor arrangement (Flettner rotor A + Flettner rotor B), the measurement uncertainties were calculated as the summation in quadrature of u_{95} of Flettner rotor A and u_{95} of Flettner rotor B. On the other hand, the measurement uncertainties of the case of two non-interacting Flettner rotors are derived using the results relative to the ATI balance (that is the measurement instrument used in the single Flettner rotor tests, Table C.1) according to:

$$u_{95C_X} = u_{95C_Y} = \max(u_{95C_L}, u_{95C_D}) \quad (\text{C.4})$$

Table C.1: Measurement uncertainties for single Flettner rotor tests

Instrument	Coefficient	u_{pr}			u_{bias}	u_{95}		
		$k = 1$	$k = 1.5$	$k = 2$		$k = 1$	$k = 1.5$	$k = 2$
ATI balance	C_L	0.0177	0.0415	0.0019	0.0318	0.0728	0.1045	0.0741
	C_D	0.0019	0.0260	0.0093	0.0093	0.0189	0.0552	0.0262
	C_X	-	-	-	-	0.0728	0.1045	0.0741
	C_Y	-	-	-	-	0.0728	0.1045	0.0741

Table C.2: Measurement uncertainties for double Flettner rotor tests

Instrument	Coefficient	u_{pr}			u_{bias}	u_{95}		
		$k = 1$	$k = 1.5$	$k = 2$		$k = 1$	$k = 1.5$	$k = 2$
ATI balance	C_L	-	-	-	-	0.0640	0.0636	0.0652
	C_D	-	-	-	-	0.0640	0.0636	0.0652
	C_X	0.0021	0.0036	0.0045	0.0093	0.0190	0.0198	0.0206
	C_Y	0.0038	0.0013	0.0073	0.0318	0.0640	0.0636	0.0652
HBM cell	C_L	-	-	-	-	0.1634	0.1635	0.1637
	C_D	-	-	-	-	0.1634	0.1635	0.1637
	C_X	0.0021	0.0035	0.0057	0.0817	0.1634	0.1635	0.1637
	C_Y	0.0065	0.0014	0.0048	0.0674	0.1355	0.1349	0.1352



D

AERODYNAMIC MODEL

D.1. HORSESHOE VORTEX METHOD

According to the work of Bertin and Smith (1998), the velocity induced by a horseshoe vortex system as defined in Figure D.1, can be calculated at a generic point in space C as follows:

$$\mathbf{V}_{HSV} = \mathbf{V}_{AB} + \mathbf{V}_{A\infty} + \mathbf{V}_{B\infty} \quad (\text{D.1})$$

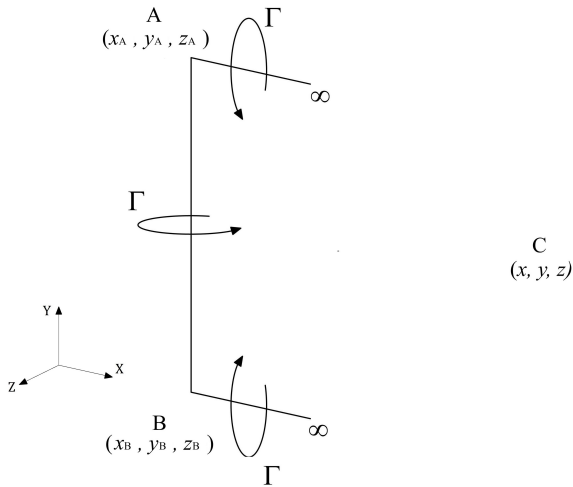


Figure D.1: The horseshoe vortex system in its reference system

The velocity induced by the bound vortex \mathbf{V}_{AB} can be computed according to:

$$\mathbf{V}_{AB} = \left(\frac{\Gamma}{4\pi} \cdot \Omega \right) \cdot \Psi \quad (\text{D.2})$$

The vectorial portion Ψ of Eq. D.2 reads:

$$\Psi = \frac{\mathbf{r}_A \times \mathbf{r}_B}{|\mathbf{r}_A \times \mathbf{r}_B|} \quad (\text{D.3})$$

while the scalar portion Ω :

$$\Omega = \left(\mathbf{r}_{AB} \cdot \frac{\mathbf{r}_A}{|\mathbf{r}_A|} - \mathbf{r}_{AB} \cdot \frac{\mathbf{r}_B}{|\mathbf{r}_B|} \right) \quad (\text{D.4})$$

The vectors \mathbf{r}_{AB} , \mathbf{r}_A and \mathbf{r}_B are defined as:

$$\mathbf{r}_{AB} = (x_B - x_A) \mathbf{i} + (y_B - y_A) \mathbf{j} + (z_B - z_A) \mathbf{k} \quad (\text{D.5})$$

$$\mathbf{r}_A = (x - x_A) \mathbf{i} + (y - y_A) \mathbf{j} + (z - z_A) \mathbf{k} \quad (\text{D.6})$$

$$\mathbf{r}_B = (x - x_B) \mathbf{i} + (y - y_B) \mathbf{j} + (z - z_B) \mathbf{k} \quad (\text{D.7})$$

On the other hand, the velocities induced by the horseshoe trailing vortices $\mathbf{V}_{A\infty}$ and $\mathbf{V}_{B\infty}$ can be calculated according to:

$$\mathbf{V}_{A\infty} = \frac{\Gamma}{4\pi} \cdot \left\{ \frac{(z - z_A) \mathbf{j} + (y_A - y) \mathbf{k}}{[(z - z_A)^2 + (y_A - y)^2]} \right\} \cdot \left[1 + \frac{x - x_A}{\sqrt{(x - x_A)^2 + (y - y_A)^2 + (z - z_A)^2}} \right] \quad (\text{D.8})$$

$$\mathbf{V}_{B\infty} = -\frac{\Gamma}{4\pi} \cdot \left\{ \frac{(z - z_B) \mathbf{j} + (y_B - y) \mathbf{k}}{[(z - z_B)^2 + (y_B - y)^2]} \right\} \cdot \left[1 + \frac{x - x_B}{\sqrt{(x - x_B)^2 + (y - y_B)^2 + (z - z_B)^2}} \right] \quad (\text{D.9})$$

The vortex strength Γ is defined as:

$$\Gamma = \frac{F_L}{\rho \cdot H \cdot V_\infty} \quad (\text{D.10})$$

where F_L is the lift force generated by the wind-propulsion system of span H .

D.2. FLETTNER ROTOR COEFFICIENTS FROM VELOCITY FIELD

GAP DISTANCE $GD = 3$

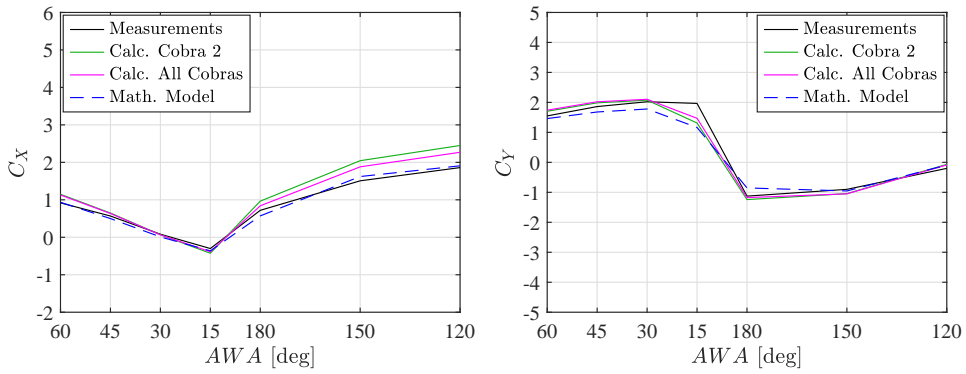


Figure D.2: Comparison of the force measurements, the results derived from the measured velocity field and the results of the mathematical model. Driving (left) and heeling (right) force coefficients. Upstream Flettner rotor set at $k = 1$ and downstream Flettner rotor set at $k = 1$. Gap distance $GD = 3$

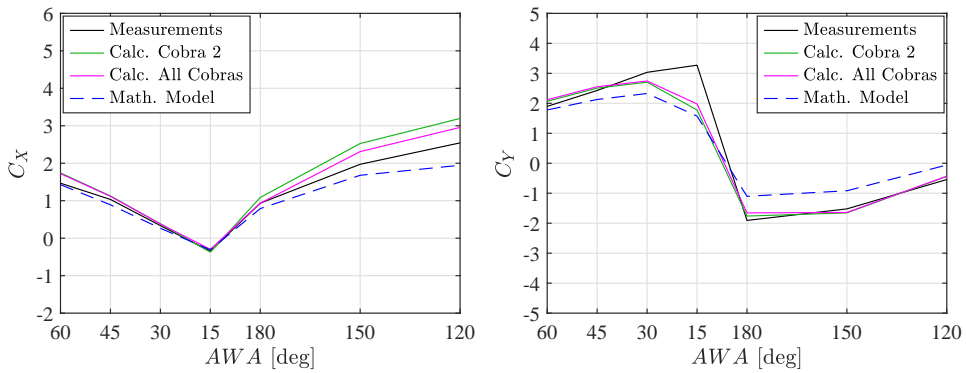


Figure D.3: Comparison of the force measurements, the results derived from the measured velocity field and the results of the mathematical model. Driving (left) and heeling (right) force coefficients. Upstream Flettner rotor set at $k = 1$ and downstream Flettner rotor set at $k = 1.5$. Gap distance $GD = 3$

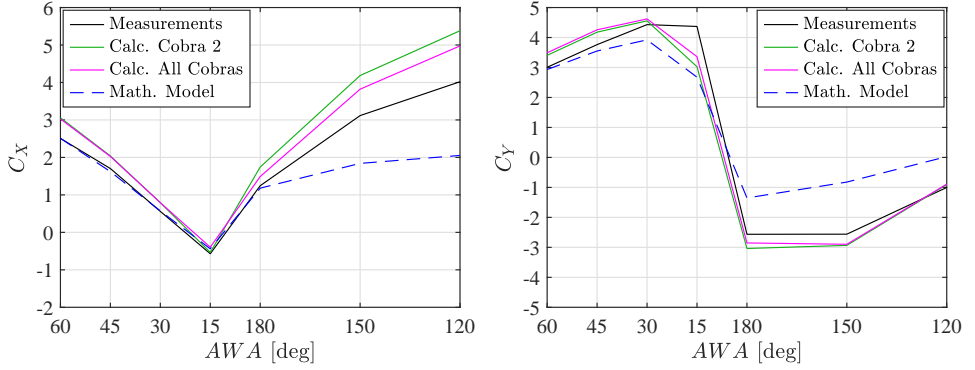


Figure D.4: Comparison of the force measurements, the results derived from the measured velocity field and the results of the mathematical model. Driving (left) and heeling (right) force coefficients. Upstream Flettner rotor set at $k = 1$ and downstream Flettner rotor set at $k = 2$. Gap distance $GD = 3$

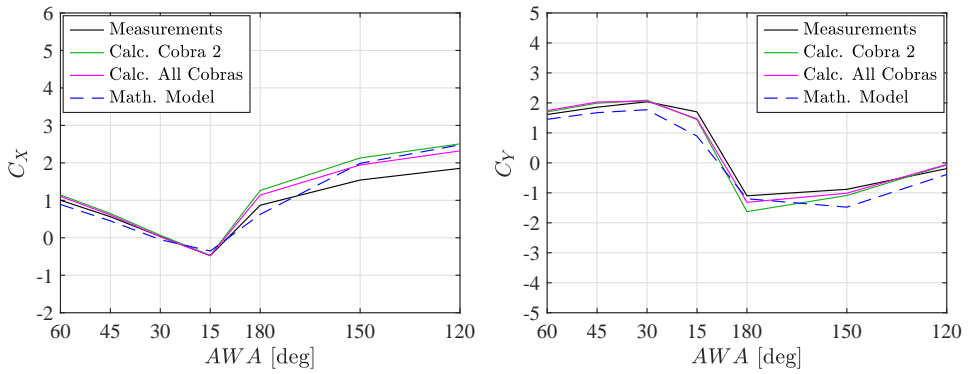


Figure D.5: Comparison of the force measurements, the results derived from the measured velocity field and the results of the mathematical model. Driving (left) and heeling (right) force coefficients. Upstream Flettner rotor set at $k = 1.5$ and downstream Flettner rotor set at $k = 1$. Gap distance $GD = 3$

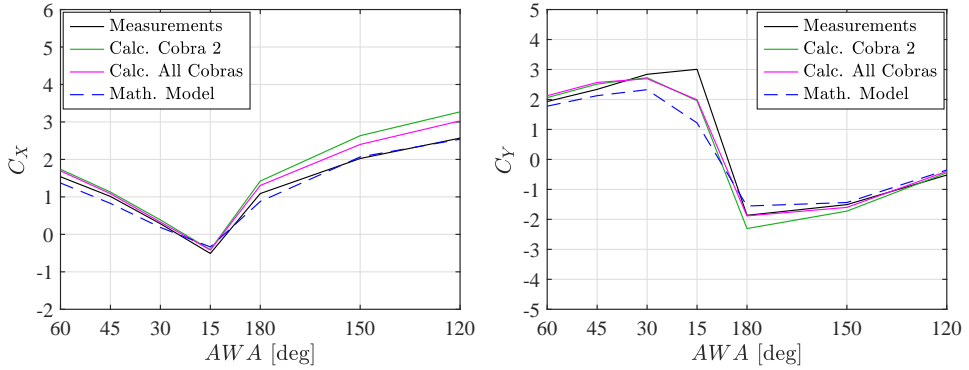


Figure D.6: Comparison of the force measurements, the results derived from the measured velocity field and the results of the mathematical model. Driving (left) and heeling (right) force coefficients. Upstream Flettner rotor set at $k = 1.5$ and downstream Flettner rotor set at $k = 1.5$. Gap distance $GD = 3$

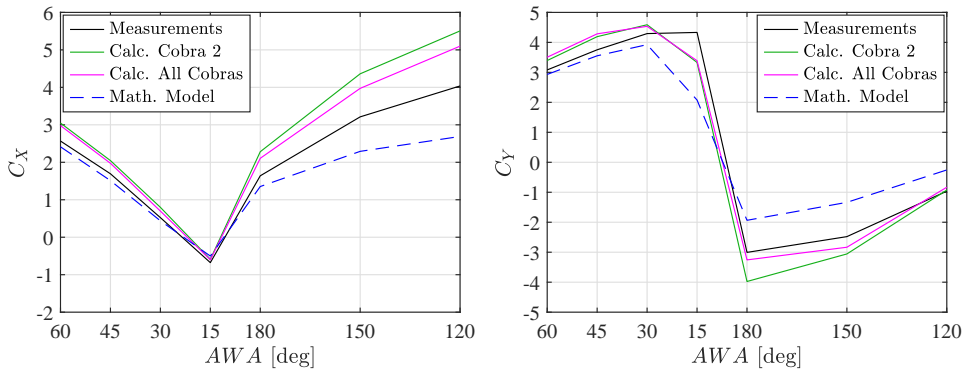


Figure D.7: Comparison of the force measurements, the results derived from the measured velocity field and the results of the mathematical model. Driving (left) and heeling (right) force coefficients. Upstream Flettner rotor set at $k = 1.5$ and downstream Flettner rotor set at $k = 2$. Gap distance $GD = 3$

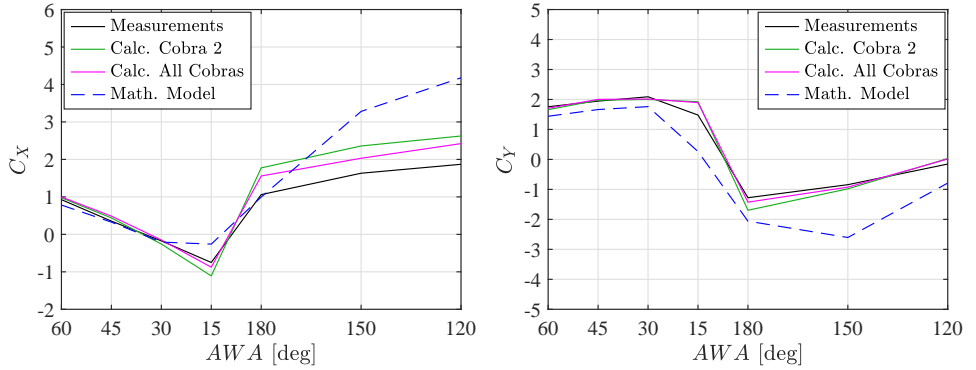


Figure D.8: Comparison of the force measurements, the results derived from the measured velocity field and the results of the mathematical model. Driving (left) and heeling (right) force coefficients. Upstream Flettner rotor set at $k = 2$ and downstream Flettner rotor set at $k = 1$. Gap distance $GD = 3$

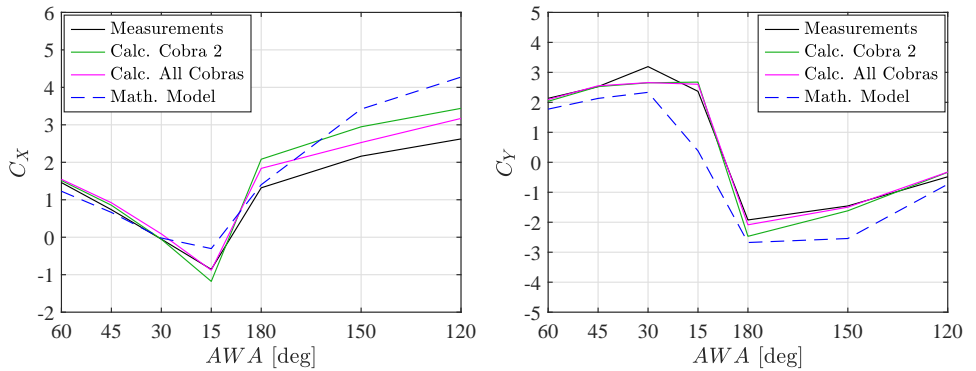


Figure D.9: Comparison of the force measurements, the results derived from the measured velocity field and the results of the mathematical model. Driving (left) and heeling (right) force coefficients. Upstream Flettner rotor set at $k = 2$ and downstream Flettner rotor set at $k = 1.5$. Gap distance $GD = 3$

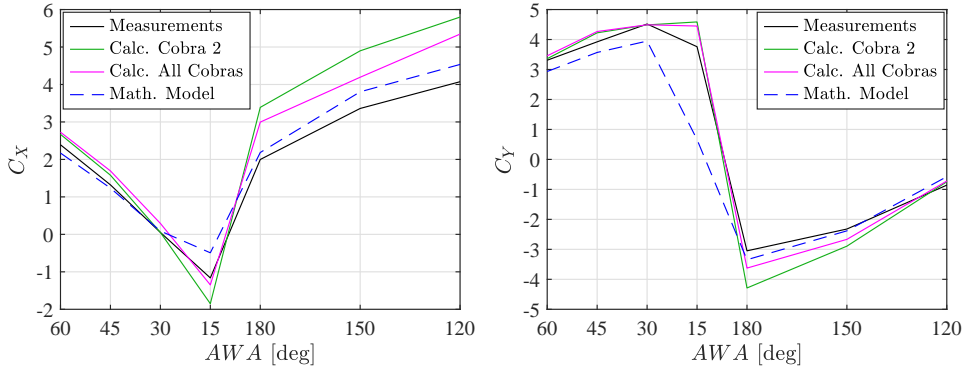


Figure D.10: Comparison of the force measurements, the results derived from the measured velocity field and the results of the mathematical model. Driving (left) and heeling (right) force coefficients. Upstream Flettner rotor set at $k = 2$ and downstream Flettner rotor set at $k = 2$. Gap distance $GD = 3$

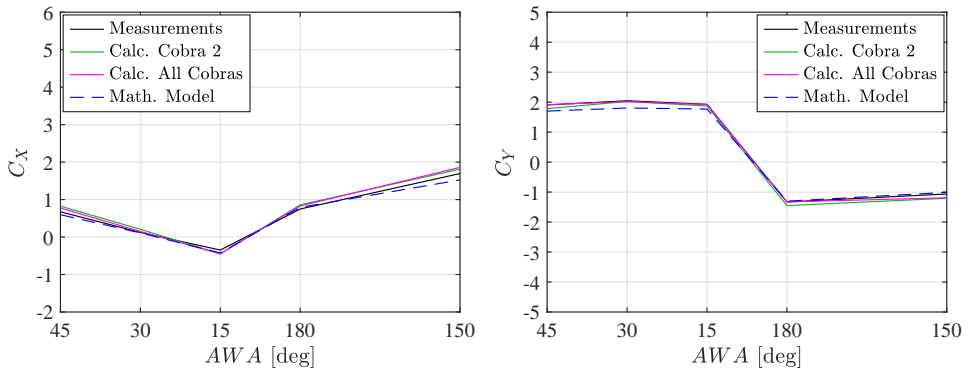
GAP DISTANCE $GD = 7.5$ 

Figure D.11: Comparison of the force measurements, the results derived from the measured velocity field and the results of the mathematical model. Driving (left) and heeling (right) force coefficients. Upstream Flettner rotor set at $k = 1$ and downstream Flettner rotor set at $k = 1$. Gap distance $GD = 7.5$

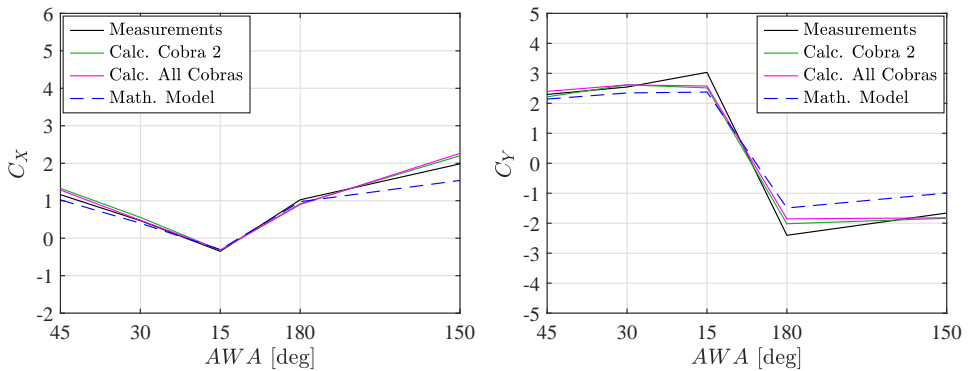


Figure D.12: Comparison of the force measurements, the results derived from the measured velocity field and the results of the mathematical model. Driving (left) and heeling (right) force coefficients. Upstream Flettner rotor set at $k = 1$ and downstream Flettner rotor set at $k = 1.5$. Gap distance $GD = 7.5$

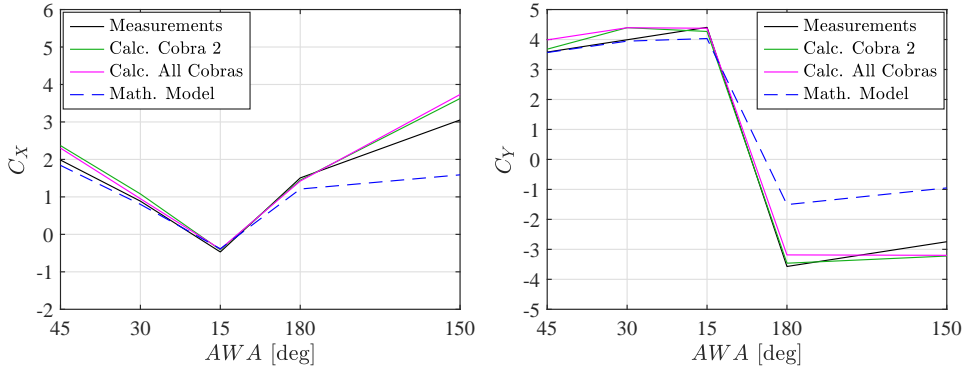


Figure D.13: Comparison of the force measurements, the results derived from the measured velocity field and the results of the mathematical model. Driving (left) and heeling (right) force coefficients. Upstream Flettner rotor set at $k = 1$ and downstream Flettner rotor set at $k = 2$. Gap distance $GD = 7.5$

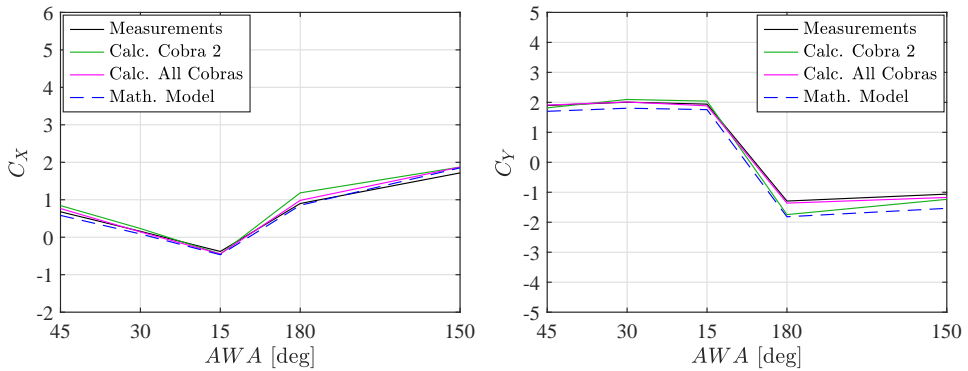


Figure D.14: Comparison of the force measurements, the results derived from the measured velocity field and the results of the mathematical model. Driving (left) and heeling (right) force coefficients. Upstream Flettner rotor set at $k = 1.5$ and downstream Flettner rotor set at $k = 1$. Gap distance $GD = 7.5$

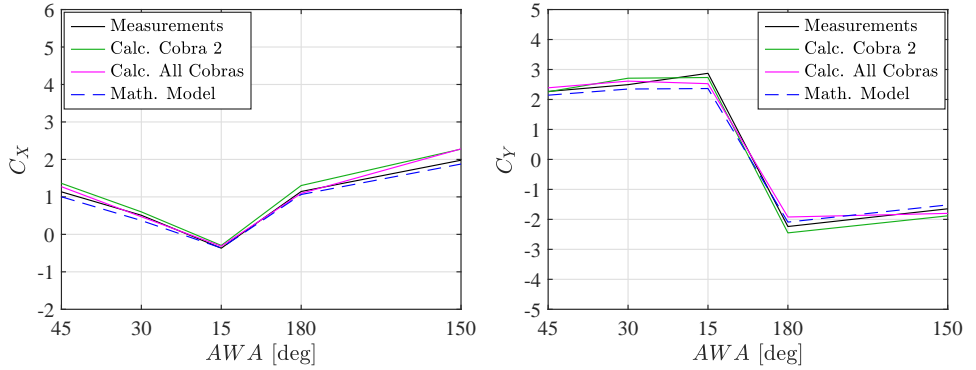


Figure D.15: Comparison of the force measurements, the results derived from the measured velocity field and the results of the mathematical model. Driving (left) and heeling (right) force coefficients. Upstream Flettner rotor set at $k = 1.5$ and downstream Flettner rotor set at $k = 1.5$. Gap distance $GD = 7.5$

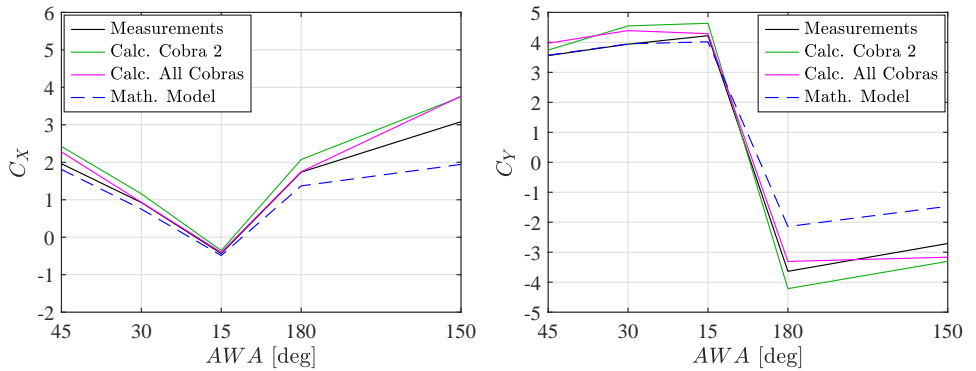


Figure D.16: Comparison of the force measurements, the results derived from the measured velocity field and the results of the mathematical model. Driving (left) and heeling (right) force coefficients. Upstream Flettner rotor set at $k = 1.5$ and downstream Flettner rotor set at $k = 2$. Gap distance $GD = 7.5$

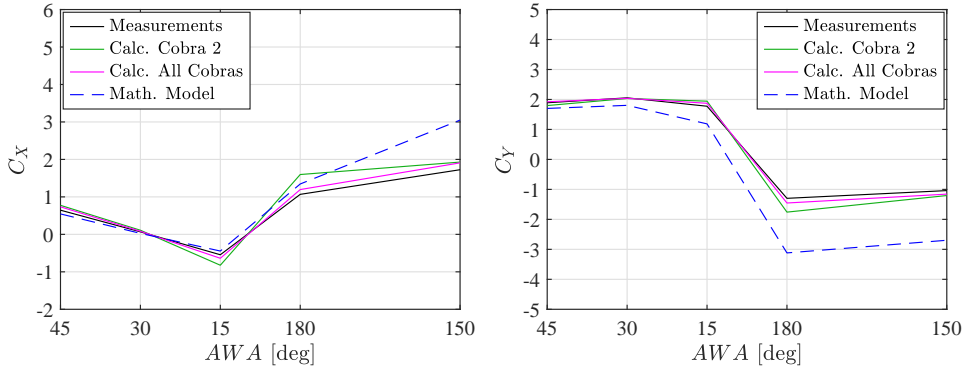


Figure D.17: Comparison of the force measurements, the results derived from the measured velocity field and the results of the mathematical model. Driving (left) and heeling (right) force coefficients. Upstream Flettner rotor set at $k = 2$ and downstream Flettner rotor set at $k = 1$. Gap distance $GD = 7.5$

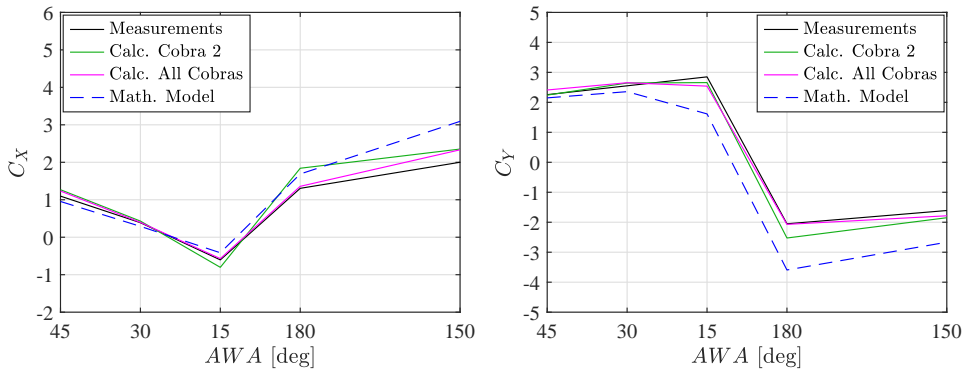


Figure D.18: Comparison of the force measurements, the results derived from the measured velocity field and the results of the mathematical model. Driving (left) and heeling (right) force coefficients. Upstream Flettner rotor set at $k = 2$ and downstream Flettner rotor set at $k = 1.5$. Gap distance $GD = 7.5$

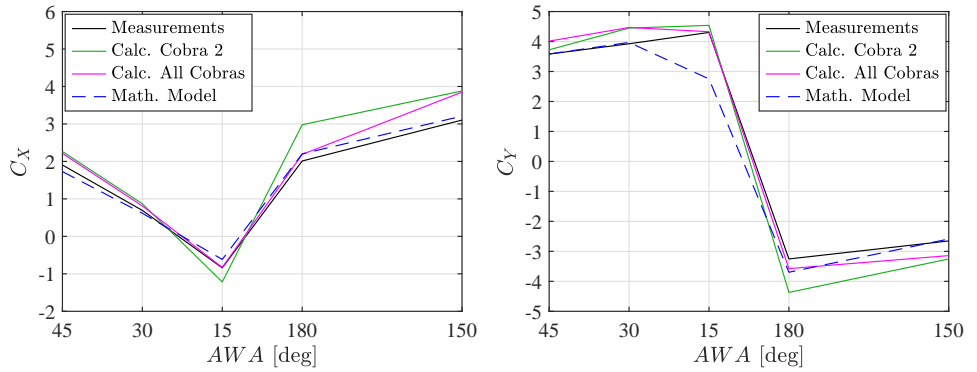


Figure D.19: Comparison of the force measurements, the results derived from the measured velocity field and the results of the mathematical model. Driving (left) and heeling (right) force coefficients. Upstream Flettner rotor set at $k = 2$ and downstream Flettner rotor set at $k = 2$. Gap distance $GD = 7.5$

GAP DISTANCE $GD = 15$

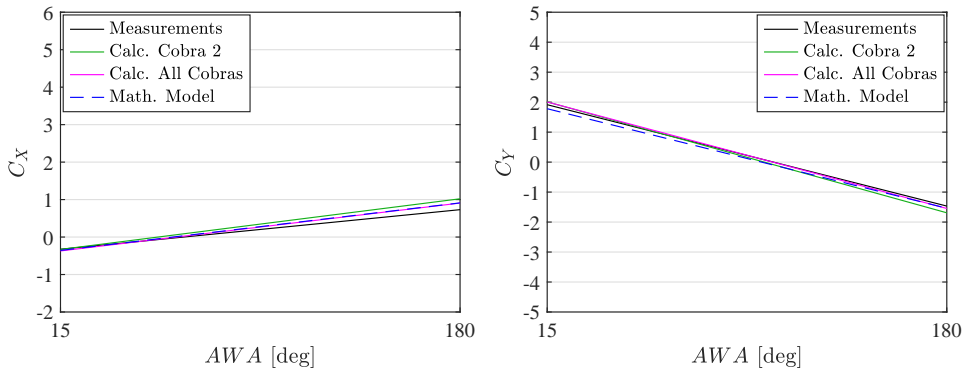


Figure D.20: Comparison of the force measurements, the results derived from the measured velocity field and the results of the mathematical model. Driving (left) and heeling (right) force coefficients. Upstream Flettner rotor set at $k = 1$ and downstream Flettner rotor set at $k = 1$. Gap distance $GD = 15$

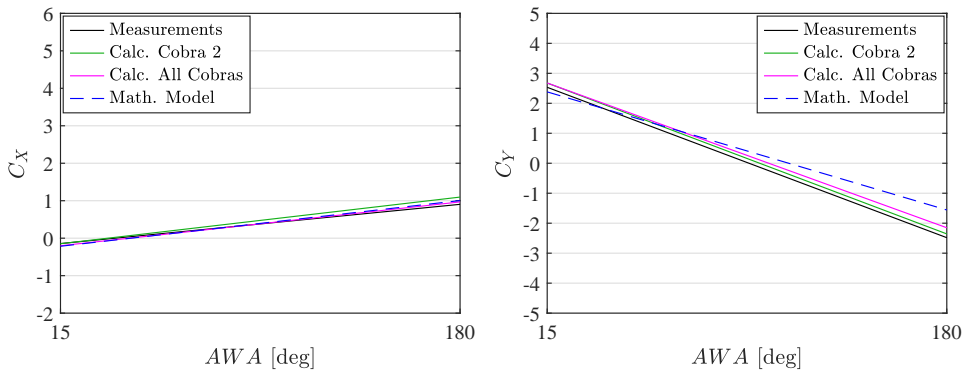


Figure D.21: Comparison of the force measurements, the results derived from the measured velocity field and the results of the mathematical model. Driving (left) and heeling (right) force coefficients. Upstream Flettner rotor set at $k = 1$ and downstream Flettner rotor set at $k = 1.5$. Gap distance $GD = 15$

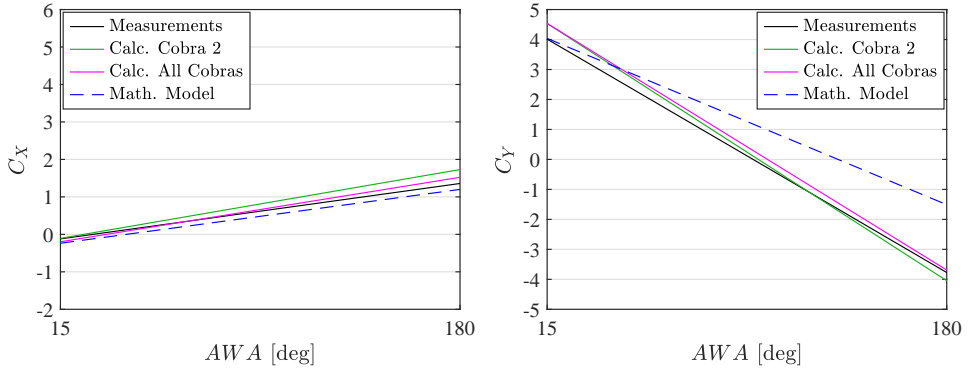


Figure D.22: Comparison of the force measurements, the results derived from the measured velocity field and the results of the mathematical model. Driving (left) and heeling (right) force coefficients. Upstream Flettner rotor set at $k = 1$ and downstream Flettner rotor set at $k = 2$. Gap distance $GD = 15$

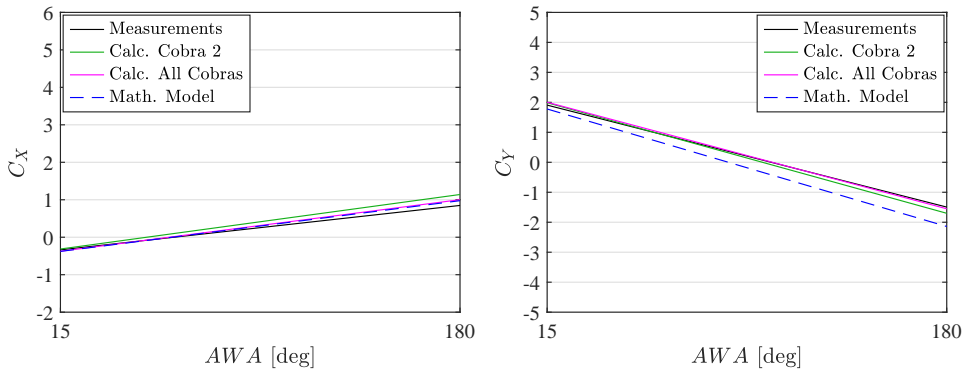


Figure D.23: Comparison of the force measurements, the results derived from the measured velocity field and the results of the mathematical model. Driving (left) and heeling (right) force coefficients. Upstream Flettner rotor set at $k = 1.5$ and downstream Flettner rotor set at $k = 1$. Gap distance $GD = 15$

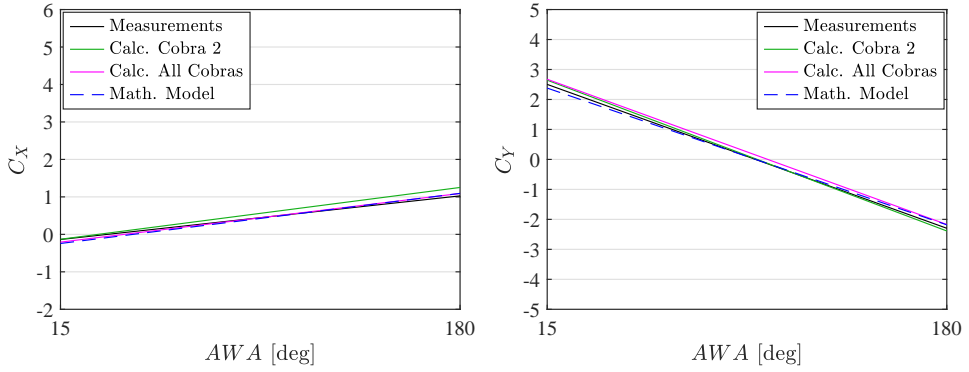


Figure D.24: Comparison of the force measurements, the results derived from the measured velocity field and the results of the mathematical model. Driving (left) and heeling (right) force coefficients. Upstream Flettner rotor set at $k = 1.5$ and downstream Flettner rotor set at $k = 1.5$. Gap distance $GD = 15$

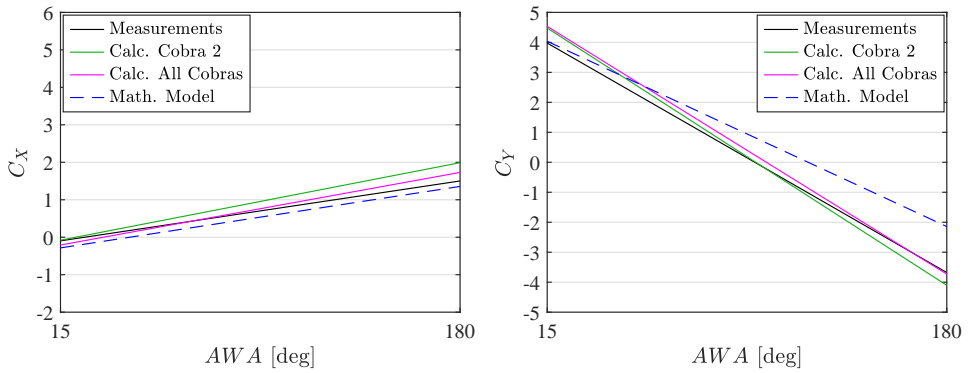


Figure D.25: Comparison of the force measurements, the results derived from the measured velocity field and the results of the mathematical model. Driving (left) and heeling (right) force coefficients. Upstream Flettner rotor set at $k = 1.5$ and downstream Flettner rotor set at $k = 2$. Gap distance $GD = 15$

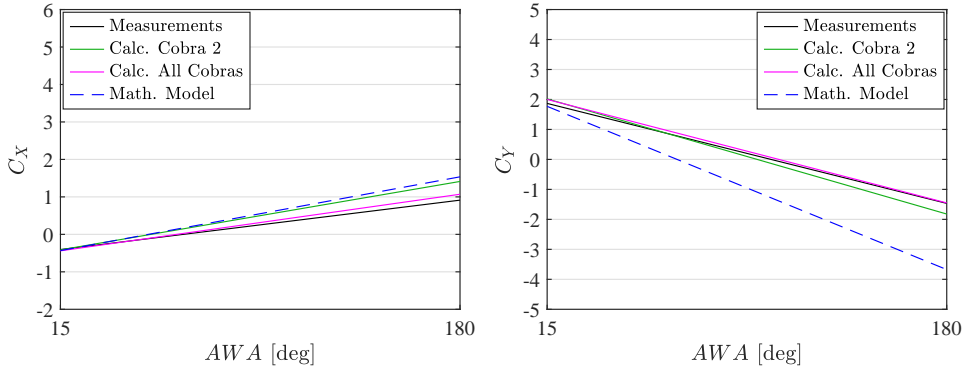


Figure D.26: Comparison of the force measurements, the results derived from the measured velocity field and the results of the mathematical model. Driving (left) and heeling (right) force coefficients. Upstream Flettner rotor set at $k = 2$ and downstream Flettner rotor set at $k = 1$. Gap distance $GD = 15$

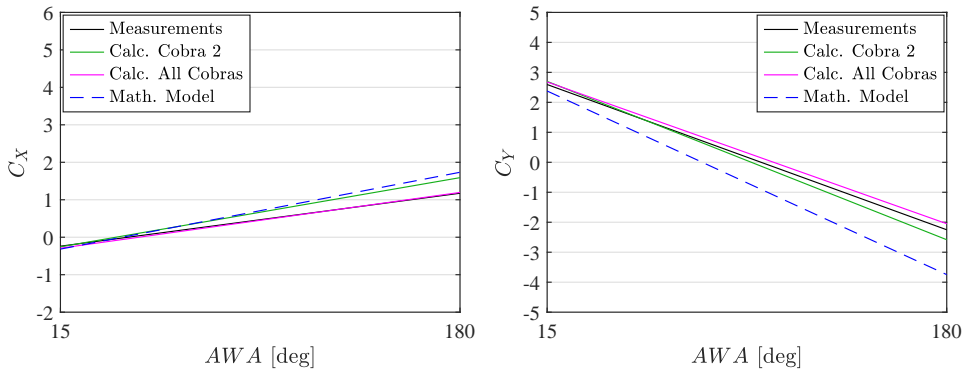


Figure D.27: Comparison of the force measurements, the results derived from the measured velocity field and the results of the mathematical model. Driving (left) and heeling (right) force coefficients. Upstream Flettner rotor set at $k = 2$ and downstream Flettner rotor set at $k = 1.5$. Gap distance $GD = 15$

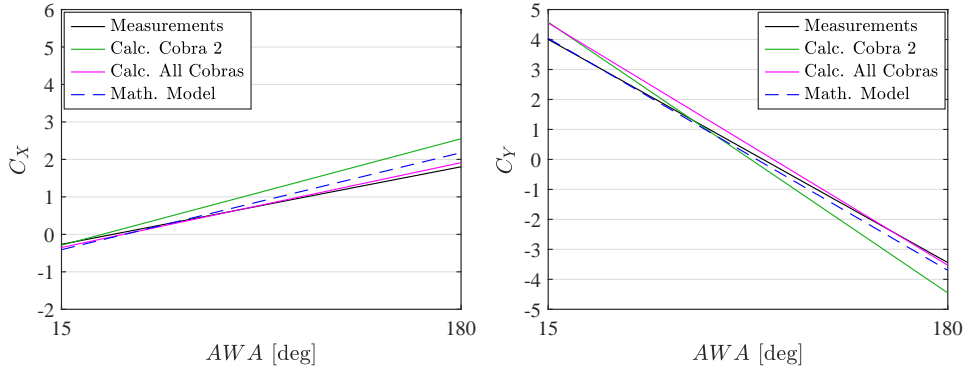


Figure D.28: Comparison of the force measurements, the results derived from the measured velocity field and the results of the mathematical model. Driving (left) and heeling (right) force coefficients. Upstream Flettner rotor set at $k = 2$ and downstream Flettner rotor set at $k = 2$. Gap distance $GD = 15$



BIBLIOGRAPHY

- K. Aoki and T. Ito. Flow characteristics around a rotating cylinder. *Proceedings of the School of Engineering of the Tokai University*, 26:29–34, 2001.
- D. Argyros. Wind-powered shipping: a review of the commercial, regulatory and technical factors affecting uptake of wind-assisted propulsion. Technical report, Lloyd's Register, 2015.
- G. R. S. Assi, P.W. Bearman, and J. R. Meneghini. On the wake-induced vibration of tandem circular cylinders: the vortex interaction excitation mechanism. *Journal of Fluid Mechanics*, 661:365–401, 2010.
- C. Badalamenti. *On the application of rotating cylinders to micro air vehicles*. PhD thesis, City University of London, 2010.
- C. Badalamenti and S.A. Prince. The effects of endplates on a rotating cylinder in crossflow. In *Proceedings of the 26th AIAA Applied Aerodynamics Conference*, 2008.
- H.M. Badr, S.C.R. Dennis, and P.J.S. Young. Steady and unsteady flow past a rotating circular cylinder at low Reynolds numbers. *Computers and Fluids*, 17:579–609, 1989.
- P.W. Bearman. Circular cylinder wakes and vortex-induced vibrations. *Journal of Fluids and Structures*, 27:648–658, 2011.
- L. Bergeson and C.K. Greenwald. Sail assist developments 1979-1985. *Journal of Wind Engineering and Industrial Aerodynamics*, 19:45–114, 1985.
- J.J. Bertin and M.L. Smith. *Aerodynamics for engineers*. Prentice-Hall, Inc., 1998.
- B.L. Blackford. Windmill thrusters: a comparison of theory and experiment. *Journal of Wind Engineering and Industrial Aerodynamics*, 20:267–281, 1985.
- G. Bordogna, N.J. van der, J.C. Mason, J.M. Bonello, and A. Vrijdag. Wind-assisted ship propulsion performance prediction, routing, and economic modelling - a corrected case study. In *Proceedings of the RINA Wind Propulsion Conference*, 2019.
- N. Bose. Windmills-propulsion for a hydrofoil trimaran. In *Proceedings of the Symposium on Wind Propulsion of Commercial Ships*, 1981.
- N. Bose and G.H. Small. Wind turbine drives - test results from the "falcon". *Journal of Wind Engineering and Industrial Aerodynamics*, 20:283–295, 1985.
- W.M.S. Bradbury. An investigation of graduated trim for an aerofoil rig. In *Proceedings of the Symposium on Wind Propulsion of Commercial Ships*, 1981.

- A.B. Burden, G.E. Hearn, T.S. Lloyd, S. Mockler, L. Mortola, I.B. Shin, and B. Smith. Concept design of a fast sail assisted feeder container ship. In *Proceedings of the Marine Unconventional Design Symposium*, 2010.
- M. Caponnetto. The aerodynamic interference between two boats sailing close-hauled. *International Shipbuilding Progress*, 44:241–256, 1997.
- V. Chapin and R. Neyhousser. Analysis, design and optimization of navier-stokes flows around interacting sails. In *Proceedings of the 6th Symposium on Yacht Design and Production*, 2006.
- B. Charrier, J. Constans, J. Cousteau, A. Daïf, L. Malavard, and J. Quinio. Fondation cousteau and windship propulsion 1980 – 1985 system cousteau - pechiney. *Journal of Wind Engineering and Industrial Aerodynamics*, 20:39 – 60, 1985.
- Y.T. Chew, M. Cheng, and S.C. Luo. A numerical study of flow past a rotating cylinder using hybrid vortex scheme. *Journal of Fluid Mechanics*, 229:35–71, 1995.
- B.R. Clayton. Bwea initiative on wind assisted ship propulsion WASP. *Journal of Wind Engineering and Industrial Aerodynamics*, 19:251–276, 1985.
- T.J. Craft, H. Iacovides, N. Johnson, and B.E. Launder. Back to the future: Flettner-Thom rotors for maritime propulsion? In *Proceedings of the 7th International Symposium on Turbulence Heat and Mass Transfer*, 2012.
- A. De Marco, S. Mancini, and C. Pensa. Preliminary analysis for marine application of Flettner rotors. In *Proceedings of the 2nd International Symposium on Naval Architecture and Maritime*, 2014.
- A. De Marco, S. Mancini, C. Pensa, G. Calise, and F. De Luca. Flettner rotor concept for marine applications: a systematic study. *International Journal of Rotating Machinery*, 2016:12 pages, 2016.
- G. Diana, M. Belloli, S. Giappino, A. Manenti, L. Mazzola, S. Muggiasca, and A. Zuin. Wind tunnel tests on two cylinders to measure subspan oscillation aerodynamic forces. In *Proceedings of the IEEE Transactions on Power Delivery, Vol. 29, No. 3*, 2014.
- R. Eggers. Operational performance of wind assisted ships. In *Proceedings of the 10th Symposium on High-Performance Marine Vehicles*, 2016.
- M. Everts, R. Ebrahim, J.P. Kruger, E. Miles, M. Sharifpur, and J.P. Meyer. Turbulent flow across a rotating cylinder with surface roughness. In *Proceedings of the 10th International Conference on Heat Transfer, Fluid Mechanics and Thermodynamics*, 2014.
- K. Fallah, A. Fardad, N. Sedaghatizadeh, E. Fattahi, and A. Ghaderi. Numerical simulation of flow around two rotating circular cylinders in staggered arrangement by multi-relaxation-time lattice boltzmann method at low reynolds numbers. *World Applied Sciences Journal*, 15:544–554, 2011.

- A. Fiorentino, L. Lecce, A. D'Antonio, G. Del Core, A. Maglione, and F. Marulo. Proposal of a sail system for the propulsion of a 25000 tdw bulk-carrier. *Journal of Wind Engineering and Industrial Aerodynamics*, 20:115–137, 1985.
- A. Flettner. The flettner rotorship. *Engineering*, 19:117–120, 1925.
- T. Fujiwara, K. Hirata, M. Ueno, and T. Nimura. On aerodynamic characteristics of a hybrid-sail with square soft sail. In *Proceedings of the 13th International Offshore and Polar Engineering Conference*, 2003.
- T. Fujiwara, G.E. Hearn, F. Kitamura, and M. Ueno. Sail-sail and sail-hull interaction effects on hybrid sail-assisted bulk carrier. *Journal of Marine Science and Technology*, 10:82–95, 2005.
- F. Garzon and A. Figueroa. The study on the flow generated by an array of four flettner rotors: theory and experiment. *Applied Mathematics*, 8:1851–1858, 2017.
- A. Gentry. The aerodynamics of sail interaction. In *Proceedings of the 3rd AIAA Symposium on the Aero/Hydronautics of Sailing*, 1971.
- A. Gentry. The double head rig. *Sail magazine*, 1973.
- A. Gentry. A review of modern sail theory. In *Proceedings of the 11th AIAA Symposium on the Aero/Hydronautics of Sailing*, 1981.
- E.W.H. Gifford. Improvement of sailing techniques in tropical countries. In *Proceedings of the Symposium on Wind Propulsion of Commercial Ships*, 1981.
- X. Guo, J. Lin, C. Tu, and H. Wang. Flow past two rotating circular cylinders in a side-by-side arrangement. *Journal of Hydrodynamics*, 21:143–151, 2009.
- D.B. Ingham and T. Tang. A numerical investigation into the steady flow past a rotating circular cylinder at low and intermediate reynolds numbers. *Journal of Computational Physics*, 8:91–107, 1990.
- P. Ingham and O. Terslov. Wind tunnel tests and manoeuvre simulator tests with different types of sails and ships. *Journal of Wind Engineering and Industrial Aerodynamics*, 20: 169–185, 1985.
- ISO. *ISO/IEC 98-3:2008. Guide to the expression of uncertainty in measurement (GUM)*. International Organization for Standardisation, 2008.
- M.A. Jaquemin. A multi-purpose tuna fishing boat with combined propulsion. In *Proceedings of the Symposium on Wind Propulsion of Commercial Ships*, 1981.
- Y. Jo, H. Lee, and S. Choi. Aerodynamic design optimization of wing-sails. In *Proceedings of the 31st AIAA Applied Aerodynamics Conference*, 2013.
- S.J. Karabelas. Large eddy simulation of high-Reynolds number flow past a rotating cylinder. *International Journal of Heat and Fluid Flow*, 31:518–527, 2010.

- S.J. Karabelas, B.C. Koumroglou, C.D. Argyropoulos, and N.C. Markatos. High Reynolds number turbulent flow past a rotating cylinder. *Applied Mathematical Modelling*, 36: 379–398, 2012.
- J.E. Kerwin. A velocity prediction program for ocean racing yachts. In *Proceedings of the New England Sailing Yacht Symposium*, 1976.
- A.D. Kurtz, R.W. Ainsworth, S.J. Thorpe, and A. Ned. Further work on acceleration insensitive semiconductor pressure sensor for high bandwidth measurements on rotating turbine blades. In *Proceedings of NASA Propulsion Measurement Sensor Development Workshop*, 2003.
- H. Lee, Y. Lo, and S. Choi. Surrogate model based design optimization of multiple wing sails considering flow interaction effect. *Ocean Engineering*, 121:422–436, 2016.
- D. Li. A new type of collapsible wing sail and its aerodynamic performance. In *Proceedings of the 36th International Conference on Ocean, Offshore and Arctic Engineering*, 2017.
- D.Q. Li, M. Leer-Andersen, and B. Allenström. Performance and vortex formation of Flettner rotors at high Reynolds numbers. In *Proceedings of the 29th Symposium on Naval Hydrodynamics*, 2012.
- Q. Li, Y. Nihei, T. Nakashima, and Y. Ikeda. A study on the performance of cascade hard sails and sail-equipped vessels. *Ocean Engineering*, 98:23–31, 2015.
- C. Luyu, C. Shunhuai, and W. Yigong. Analysis on sail selection and energy conservation of a panamax bulk carrier. In *Proceedings of the International Conference on Advances in Energy Engineering*, 2010.
- S. Mittal and B. Kumar. Flow past a rotating cylinder. *Journal of Fluid Mechanics*, 476: 303–334, 2003.
- T. Nakashima, Y. Yamashita, Y. Nihei, and Q. Li. A basic study for propulsive performance prediction of a cascade of wing sails considering their aerodynamic interaction. In *Proceedings of the 21st International Offshore and Polar Engineering Conference*, 2011.
- C.T. Nance. Wind power for ships - a general survey. In *Proceedings of the Symposium on Wind Propulsion of Commercial Ships*, 1981.
- D. Nelissen, M. Traut, J. Köhler, W. Mao, J. Faber, and S. Ahdour. Study on the analysis of market potentials and market barriers for wind propulsion technologies for ships. Project report, CE Delft, 2016. URL https://www.cedelft.eu/publicatie/study_on_the_analysis_of_market_potentials_and_market_barriers_for_wind_propulsion_technologies_for_ships/1891.
- P. Nuttall, A. Newell, B. Prasad, J. Veitayaki, and E. Holland. A review of sustainable sea-transport for oceania: Providing context for renewable energy shipping for the pacific. *Marine Policy*, 43:283 – 287, 2014.

- K. Ouchi, K. Uzawa, and A. Kanai. Huge hard wing sails for the propulsor of next generation sailing vessel. In *Proceedings of the 2nd International Symposium on Marine Propulsors*, 2011.
- K. Ouchi, K. Uzawa, A. Kanai, and M. Katori. "wind challenger" the next generation hybrid sailing vessel. In *Proceedings of the 3rd International Symposium on Marine Propulsors*, 2013.
- J.C. Padrino and D.D. Joseph. Numerical study of the steady-state uniform flow past a rotating cylinder. *Journal of Fluid Mechanics*, 557:191–223, 2006.
- D. Pearson. The use of flettner rotors in efficient ship design. In *Proceedings of the Influence of EEDI on Ship Design Conference*, 2014.
- F.G. Pollack, C.H. Liebert, and V.S. Peterson. Rotating pressure measuring system for turbine cooling investigations. Technical memorandum x-2621, NASA, 1972.
- L. Prandtl. Application of the magnus effect to the wind propulsion of ships. Technical memorandum no. 367, NACA, 1926.
- R.C.T. Rainey. The wind turbine ship. In *Proceedings of the Symposium on Wind Propulsion of Commercial Ships*, 1981.
- E.G. Reid. Tests of rotating cylinders. Technical report tn-209, NACA, 1924.
- P.J. Richards and D.J. Le Pelley. The interaction between sailing yachts in fleet and match race situations. In *Proceedings of the 23rd International HISWA Symposium*, 2014.
- RINA. *Proceedings of the Symposium on Wind Propulsion of Commercial Ships: London, November 4-6, 1980*. Royal Institution of naval architects, 1981.
- K. Roncin and J.M. Kobus. Dynamic simulation of two sailing boats in match race. *Sports Engineering*, 7:139–152, 2004.
- C.J. Satchwell. Aerodynamic design of marine aerofoils. *Journal of Wind Engineering and Industrial Aerodynamics*, 20:1–22, 1985a.
- C.J. Satchwell. *Proceedings of the International Symposium on Windship Technology (WINDTECH '85), Southampton, U.K., April 23-25, 1985*. Elsevier Science Publishers B.V., 1985b.
- C.J. Satchwell. Preliminary analysis of log data from the fiji windship 'Cagidonu'. Project report, 1986. URL <https://eprints.soton.ac.uk/43588/>. ISSN 0140-3818.
- G.W. Schaefer and K. Allsopp. Kite-sails for wind-assisted ship propulsion. In *Proceedings of the Symposium on Wind Propulsion of Commercial Ships*, 1981.
- P. Schenzle. Estimation of wind assistance potential. *Journal of Wind Engineering and Industrial Aerodynamics*, 20:97–110, 1985.
- H. Schlichting. *Boundary layer theory*. Mc Graw-Hill, 1979.

- H.F. Morin Scott. A full scale experiment in commercial auxiliary sail. In *Proceedings of the Symposium on Wind Propulsion of Commercial Ships*, 1981.
- P. Shenze. Standardised speed prediction for wind propelled merchant ships. In *Proceedings of the Symposium on Wind Propulsion of Commercial Ships*, 1981.
- P.C. Shukla and K. Gosh. Revival of the modern wing sails for the propulsion of commercial ships. *International Journal of Mathematical, Computational, Physical, Electrical and Computer Engineering*, 3:5–10, 2009.
- T. Smith, P. Newton, G. Winn, and A.G. La Rosa. Analysis techniques for evaluating the fuel savings associated with wind assistance. In *Proceedings of the Low Carbon Shipping Conference*, 2013.
- T. Smith, J.J. Corbett, L. Johansson, and C. Raucci. Third imo GHG study 2014: Executive summary and final report. Project report, International Maritime Organization, 2015. URL <http://www.imo.org/en/OurWork/Environment/PollutionPrevention/AirPollution/Pages/Greenhouse-Gas-Studies-2014.aspx>.
- F. Smulders. Exposition of calculation methods to analyse wind-propulsion on cargo ships. *Journal of Wind Engineering and Industrial Aerodynamics*, 20:187–203, 1985.
- M. Sofiev, J.J. Winebrake, L. Johansson, E.W. Carr, and M. Prank. Cleaner fuels for ships provide public health benefits with climate tradeoffs. *Nature Communications*, 9(406), 2018. doi: 10.1038/s41467-017-02774-9.
- K. Stewart. The use of inflated sails for ship propulsion. *Journal of Wind Engineering and Industrial Aerodynamics*, 20:317–334, 1985.
- K. Subramanya. *1000 solved problems in fluid mechanics*. Tata McGraw-Hill, 2005.
- D. Sumner. Two circular cylinders in cross-flow: a review. *Journal of Fluids and Structures*, 26:849–899, 2010.
- S. Sungnul and N.P. Moshkin. Effect of rotation rates and gap spacing on the structure of low reynolds number flow over two rotating circular cylinders. In *Computational Fluid Dynamics 2008*, Springer, 2009.
- W.M. Swanson. The Magnus effect: a summary of investigations to date. *Journal of Basic Engineering*, 83:461–470, 1961.
- H. Tennekes and J.L. Lumley. *A first course in turbulence*. The MIT Press, 1974.
- A. Thom. Experiments on the flow past a rotating cylinder. Reports and memoranda no. 1410, Aeronautical Research Committee, 1931.
- A. Thom. Effects of discs on the air forces on a rotating cylinder. Reports and memoranda no. 1623, Aeronautical Research Committee, 1934.
- P.T. Tokumaru and P.E. Dimotakis. The lift of a cylinder executing rotatory motions in a uniform flow. *Journal of Fluid Mechanics*, 255:1–10, 1993.

- M. Traut, A. Bows, P. Gilbert, S. Mander, P. Stansby, C. Walsh, and R. Wood. Low c for the high seas: Flettner rotor power contribution on a route brazil to uk. In *Proceedings of the Low Carbon Shipping Conference*, 2012.
- M. Traut, P. Gilbert, C. Walsh, A. Bows, A. Filippone, P. Stansby, and R. Wood. Propulsive power contribution of a kite and a flettner rotor on selected shipping routes. *Applied Energy*, 113:362–372, 2014.
- Y. Ueda, A. Sellier, T. Kida, and M. Nakanishi. On the low-reynolds-number flow about two rotating circular cylinders. *Journal of Fluid Mechanics*, 495:255–281, 2003.
- F. van Walree and E. Willemsen. Wind loads on offshore structures. In *Proceedings of BOSS-88 Conference*, 1988.
- I.M. Viola, M. Sacher, J. Xu, and F. Wang. A numerical method for the design of ships with wind-assisted propulsion. *Ocean Engineering*, 105:32–42, 2015.
- J.G. Walker. A high performance automatic wingsail auxiliary propulsion system for commercial ships. *Journal of Wind Engineering and Industrial Aerodynamics*, 20:83–96, 1985.
- E.J. Watson. The rotation of two circular cylinders in a viscous fluid. *Mathematika*, 42:105–126, 1995.
- J.F. Wellicome. Some comments on the relative merits of the various wind propulsion devices. *Journal of Wind Engineering and Industrial Aerodynamics*, 20:111–142, 1985.
- H.S. Yoon, H.H. Chun, J.H. Kim, and I.L.R. Park. Flow characteristics of two rotating side-by-side circular cylinder. *Computers and Fluids*, 38:466–474, 2009.
- M.M. Zdravkovich. *Flow around circular cylinders - Vol 2: applications*. Oxford University Press, 2003.
- W. Zhang and R. Bensow. Numerical simulation of high-Reynolds number flow around Flettner rotors. In *Proceedings of the 14th Numerical Towing Tank Symposium*, 2011.
- W. Zhang, R. Bensow, M. Golubev, and V. Chernoray. Flow past a rotating finite length cylinder: numerical and experimental study. In *Proceedings of the 51st AIAA Aerospace Sciences Meeting including the New Horizons Forum and Aerospace Exposition*, 2013.



ACKNOWLEDGEMENTS

First of all, I would like to express my gratitude to my supervisors Rene' Huijsmans and Lex Keuning for having offered me the opportunity to work on this exciting subject. They had the vision to research wind-assisted propulsion when it was still not a popular topic. I am very grateful for this. Their guidance, support and understanding, especially during the difficult times, made me realize that finishing this thesis was the right thing to do.

I would like to dedicate a special thought to the late prof. Fabio Fossati. This doctoral research started as a double-degree agreement between TUDelft and Polytechnic University of Milan, where Fabio Fossati was my co-promotor. He embraced with passion the topic of wind-assisted propulsion to supervise me during the experimental work at Polytechnic University of Milan wind tunnel. His sudden passing in November 2015 was a tragic moment for all of us.

I want to thank my current co-promotor, Ido Akkerman, for providing me with insightful comments that improved the quality of this work. I am also grateful to the members of the examination committee for taking the time to read this dissertation and providing valuable feedback.

This work was made possible with the contribution of Damen Shipyards, Dykstra Naval Architects and Maritime Research Institute Netherlands (MARIN), parties in the Sail Assist project, and the financial support of De Bijlboeg Fonds and De Samenwerkende Maritieme Fondsen. I wish to thank all the research sponsors and contributors for their kind support.

I want to thank my fellow colleagues of the Ship Hydromechanics Laboratory. We had fun times and several broodjes haring together. In particular, I want to thank Nico, who was working on the hydromechanics of wind-assisted ships, for the work done together and the reciprocal motivation to get this thesis done.

Since December 2015, I have worked from Polytechnic University of Milan wind tunnel, where I have carried out the experiments discussed in this dissertation. I would like to thank Marco Belloli for taking up the collaboration with TUDelft on the Sail Assist project and for hosting me at the wind tunnel for all this time. He and the rest of the staff welcomed me in the best way possible and made feel at home since the first moment. In particular, I want to thank Sara Muggiasca and Stefano Giappino for assisting me with the preparation, the execution and the post-processing of the experiments. I am also grateful to Luca Ronchi and Alessandro Brambilla for their assistance with the test setups.

I am very grateful to my friends living in The Netherlands who patiently hosted me every time I was back there. Ani, Lubo, Edo, Fra and Marco thank you! Likewise, I want to thank Mo, who hosted me for "two weeks" in Milan, and my friend Jack. They never stopped providing me with moral support whenever needed. I am very thankful to Carmen for her continuous encouragement and for bearing with me during the last part of this work. Lastly, I wish to thank my parents. This thesis is the result of their everlasting support.



CURRICULUM VITÆ



Giovanni Bordogna was born on April 24th 1987 in Como, Italy. He attended high school at Paolo Giovio college in Como. During this period, he spent six months at the Kerikeri high school, New Zealand, as an exchange student. In 2006, he commenced his study in Nautical Engineering at University of Genoa. In 2007, he spent his second year of bachelor's degree at Universitat Politècnica de Catalunya as ERASMUS student and in 2009 he stayed at the Ship Science department of University of Southampton for a three-month internship to study the performance of Volvo Ocean Race sailing yachts. After receiving his bachelor's degree in 2010, he began his master's degree in Marine Technology, specialization in ship hydromechanics, at Delft University of Technology. In 2012 he conducted a

six-month internship at the Yacht Research Unit of University of Auckland working on the development of a dynamic velocity prediction program for sailing yachts. He obtained his master's degree in July 2013 with a thesis on the aero/hydrodynamic performance of yachts sailing upwind in waves. In November of the same year, he commenced a double-degree PhD project at the section Ship Hydromechanics and Structures of Delft University of Technology and at the department of Mechanical Engineering of Polytechnic University of Milan. In January 2016 he decided to continue his doctoral appointment only at Delft University of Technology, although he carried out the experimental work of his research at Polytechnic University of Milan wind tunnel. The PhD project was aimed at the development of the aerodynamic model of a performance prediction program for wind-assisted commercial ships. The results of this work are presented in this thesis. Since November 2019 he works as a consultant for the company he co-founded, Blue Wasp, intending to provide clients with expert and independent advice to make informed investments in wind-assist technologies.



LIST OF PUBLICATIONS

JOURNAL ARTICLES

- **G. Bordogna**, S. Muggiasca, S. Giappino, M. Belloli, J.A. Keuning, R.H.M. Huijsmans. The effects of the aerodynamic interaction on the performance of two Flettner rotors. *Journal of Wind Engineering and Industrial Aerodynamics* (2019), doi.org/10.1016/j.jweia.2019.104024.
- **G. Bordogna**, S. Muggiasca, S. Giappino, M. Belloli, J.A. Keuning, R.H.M. Huijsmans, A.P. van't Veer. Experiments on a Flettner rotor at critical and supercritical Reynolds numbers. *Journal of Wind Engineering and Industrial Aerodynamics*, 188: 19-29, 2019.
- **G. Bordogna**, J.A. Keuning, R.H.M. Huijsmans, M. Belloli. Wind-tunnel experiments on the aerodynamic interaction between two rigid sails used for wind-assisted propulsion. *International Shipbuilding Progress*, 65: 93-125, 2018.

CONFERENCE PAPERS

- **G. Bordogna**, N.J. van der Kolk, J.C. Mason, J.M. Bonello, A. Vrijdag. Wind-assisted ship propulsion performance prediction, routing and economic modelling - a corrected case study. In *Proceedings of the RINA Wind Propulsion Conference*, 2019.
- N.J. van der Kolk, **G. Bordogna**, J.C. Mason, P. Despraires, A. Vrijdag. Case study: wind-assisted ship propulsion performance prediction, routing and economic modelling. In *Proceedings of the RINA Power and Propulsion Alternatives for Ships Conference*, 2019.
- **G. Bordogna**, S. Muggiasca, S. Giappino, M. Belloli, J.A. Keuning, R.H.M. Huijsmans, A.P. van't Veer. *Wind-tunnel experiments on a large-scale Flettner rotor*. In: Ricciardelli F, Avossa A. (eds) Proceedings of the XV Conference of the Italian Association for Wind Engineering. IN VENTO 2018. Lecture Notes in Civil Engineering, vol 27. Springer, Cham., 2018.
- **G. Bordogna**, J.A. Keuning, R.H.M. Huijsmans, F.V. Fossati, M. Belloli. Validation of a simple aerodynamic model capable to predict the interaction effects occurring between two generic wind-propulsion systems. In *Proceedings of the 12th International Conference on Hydrodynamics*, 2016.
- **G. Bordogna**, D.J. Markey, R.H.M. Huijsmans, J.A. Keuning, F.V. Fossati. Wind-assisted ship propulsion: a review and development of a performance prediction program for commercial ships. In *Proceedings of the 11th International Conference on Hydrodynamics*, 2014.